



HAL
open science

Highly efficient solar cells in low dimensionality based on Cu(In,Ga)Se₂ chalcopyrite materials

Myriam Paire

► **To cite this version:**

Myriam Paire. Highly efficient solar cells in low dimensionality based on Cu(In,Ga)Se₂ chalcopyrite materials. Chemical Physics [physics.chem-ph]. Sorbonne Universités, UPMC Univ Paris 06, 2012. English. NNT : 2012PA066439 . tel-01393784

HAL Id: tel-01393784

<https://hal.science/tel-01393784>

Submitted on 8 Nov 2016

HAL is a multi-disciplinary open access archive for the deposit and dissemination of scientific research documents, whether they are published or not. The documents may come from teaching and research institutions in France or abroad, or from public or private research centers.

L'archive ouverte pluridisciplinaire **HAL**, est destinée au dépôt et à la diffusion de documents scientifiques de niveau recherche, publiés ou non, émanant des établissements d'enseignement et de recherche français ou étrangers, des laboratoires publics ou privés.



Distributed under a Creative Commons Attribution - NonCommercial 4.0 International License



**THESE DE DOCTORAT DE
L'UNIVERSITE PIERRE ET MARIE CURIE**

Spécialité

Physique et Chimie des Matériaux
(Ecole doctorale 397)

Présentée par

Melle PAIRE Myriam

Pour obtenir le grade de

DOCTEUR de l'UNIVERSITÉ PIERRE ET MARIE CURIE

Sujet de la thèse :

**Highly efficient solar cells in low dimensionality based on
Cu(In,Ga)Se₂ chalcopyrite materials**

soutenue le 28 septembre 2012

devant le jury composé de :

M. LINCOT Daniel M. GUILLEMOLES Jean-François	Directeurs de thèse
Mme. EDOFF Marika M. KLEIDER Jean-Paul	Rapporteurs
M. RAU Uwe M. SHUKLA Abhay M. WEISBUCH Claude	Examineurs
M. PELOUARD Jean-Luc	Invité



**THESE DE DOCTORAT DE
L'UNIVERSITE PIERRE ET MARIE CURIE**

Spécialité

Physique et Chimie des Matériaux
(Ecole doctorale 397)

Présentée par

Melle PAIRE Myriam

Pour obtenir le grade de

DOCTEUR de l'UNIVERSITÉ PIERRE ET MARIE CURIE

Sujet de la thèse :

**Cellules solaires à haut rendement en basse dimensionnalité à
partir de matériaux chalcopyrites $\text{Cu}(\text{In},\text{Ga})\text{Se}_2$**

soutenue le 28 septembre 2012

devant le jury composé de :

M. LINCOT Daniel M. GUILLEMOLES Jean-François	Directeurs de thèse
Mme. EDOFF Marika M. KLEIDER Jean-Paul	Rapporteurs
M. RAU Uwe M. SHUKLA Abhay M. WEISBUCH Claude	Examineurs
M. PELOUARD Jean-Luc	Invité

ACKNOWLEDGEMENTS

A meeting over a coffee near the Luxembourg gardens in February 2009 was all it took for Daniel Lincot to have faith in me and open up the doors of his laboratory for this thesis. I would like to thank him for his great support throughout these three years, for his endless enthusiasm, bright and numerous ideas, although it is sometimes challenging to keep the pace! I would like to thank Jean-François Guillemoles for always finding time to discuss in an overbooked schedule, for his dedication to bring to light the physics of photovoltaic devices and thus give meaning and science to any measurement. I would like to thank both of them for writing recommendation letters, sometimes on short notice, for entrusting me with articles writing or the supervision of internships, and for giving me the chance to travel a lot and present this research in various conferences. I would also like to thank them for all the inspiring extra-work conversations. I was lucky to have them as supervisors. A special thank to Yves Schlumberger, deputy director of IRDEP, for your discreet presence, always wise advice and nice encouragements. I would like to thank the Laboratoire de Photonique et Nanostructures for their warm welcome, and for giving me access to their cleanroom. I would like to thank Jean-Luc Pelouard, for his interest in my work, his enthusiasm, his efficiency in patent filing and for accepting to be part of my jury, and Stéphane Collin for his help and advice, the review of our articles, even on short notice, and for always finding time to discuss microcells or anything else.

I would like to thank Prof. Marika Edoff and Dr. Jean-Paul Kleider for making me the honor to review this thesis. I deeply appreciated their throughout reading and wise suggestions. I would like to thank all the jury members, Prof. Dr. Uwe Rau, Dr. Abhay Shukla, Dr. Claude Weisbuch, Dr. Jean-Luc Pelouard for their interest in my work and presence at my PhD defense, in spite of busy schedules and sometimes long travels. It was very nice to comment and discuss my work with you.

I would like to thank the graduate school of the Ecole Polytechnique for selecting my candidature and the French Ministry for Higher Education and Research for financing this thesis. I would like to thank the University Pierre and Marie Curie for welcoming me and giving me a teaching assistant position. Even if it was not always easy to accommodate my research and my educational activities, teaching was a great experience.

I would like to thank the Institut Lavoisier de Versailles, the PROMES and CERMICS laboratories for their collaborations in this thesis.

I would like to thank the UNESCO-L'OREAL Fellowships Program for Young Women in Science that awarded me a fellowship for this thesis in 2011.

J'aimerais remercier mes collègues de l'IRDEP, du LPN et d'ailleurs. Laurent Lombez, mon soutien face aux fibres optiques, lasers ou programmes Labview, et grâce à qui je connais maintenant l'entière biographie de « Bob ». Nicolas Péré-Laperne, qui m'a appris qu'en process patience et longueur de temps font plus que force ni que rage, et qui a toujours relu en détails nos diverses publications. Christophe, MacGyver des salles blanches, lithographe, microscopiste, métalliseur, sauveteur d'échantillons, bref « Technologue ». Frédérique, pour une franchise et une spontanéité agréables au quotidien, les biscuits au vin italiens (hum !) et la découverte d'un certain resto rue Montorgueil. Marie, fournisseuse officielle de caramel au beurre salé, alliée du freestyle à la coinche, et avec qui j'ai pu deviser quinoa vs. boulgour ou Malava vs. Debby. Jean, exilé comme moi à Dache, fier de ses Birks, toujours prêt à s'engager avec un(e) supporter(trice) du PSG, tchatcheur, qui peut de moins en moins saquer l'esquichade du RER. Arthur, soutien dans les moments de tension avec MATLAB, qui a quand même réussi à trafiquer une Wii pour remporter les championnats « Just Dance ». Zac, sociologue de terrain, qui aura animé l'open-space et jamais reconnu que le handball, c'est bien plus physique que le taekwondo. Nathanaëlle, ma voisine, qui milite comme moi pour les afterworks dans le XVII^{ème}, qui a toujours eu un mot d'encouragement pour moi dans les derniers mois de cette thèse. Merci à Elisabeth pour sa contribution à cette thèse dans les expériences d'électrodépôts et de recuits, et de façon générale une présence bienveillante au laboratoire. Nicolas L. et Valérie, pour leur disponibilité et leur aide en chimie apportée à une novice comme moi. Negar, toujours de bonne humeur, et fournisseuse officielle de substrats. Gilles pour avoir pris le temps d'accueillir une petite sœur et lui avoir appris un peu ce qu'est la pulvérisation cathodique. Alain pour les nombreux dépôts de ZnO, les journaux du matin et la machine à café toujours en état de marche. Enrique pour être toujours prêt à aider lors d'une mesure IV, EQE ou à écrire un programme Labview à la demande. Un grand merci à Stéphane G. pour son aide sur l'IBE et la RIE et à Xavier pour les dépôts de SiO₂. Nathalie pour son aide en litho et les conversations à déjeuner, Fabrice sans qui je serais restée plusieurs fois impuissante devant une platine de mesure IV récalcitrante. Gulnar et Simon toujours prêts à me donner des conseils ou un coup de main. Grégory S., avec qui j'ai pu passer de longs moments à discuter politique d'innovation. Anne-Laure, ma référente à l'IRDEP avec qui je n'ai finalement jamais rempli le fameux formulaire. Sana, que je n'aurai croisé finalement que peu entre deux heureux événements, pour sa bonne humeur. Sébastien, qui m'a embauchée pour des résumés de conférence pour sa revue, et qui m'a appris que les comptes-rendus c'était quand même beaucoup plus simple quand on les tapait en direct sur un mini-PC. Philippe, rempart contre les difficultés de communication avec le « 12 ». Christian, à qui jusqu'à ce jour, je n'ai pas fait remplir de fiche de presque-accident. Jacqueline, toujours un bon mot, toujours de bonne humeur, et que j'admire pour son art d'assortir ses collants et ses pulls, ainsi que Claire et Nicole pour leur aide et leur patience dans les démarches administratives.

Une pensée toute spéciale pour Servane, Pascal et Aurélien mes compagnons de bungalow, lancés avec moi dans l'aventure du doctorat, avec qui j'ai partagé bonbons, discussions stratégiques sur la meilleure façon d'avoir une réunion avec Daniel, moments de découragement ou de succès. Mes remerciements aussi à Artabaze et Florian pour avoir vaillamment supporté ma tyrannie, et essayer les plâtres de mes « techniques managériales ».

Dans le désordre, mes remerciements à Lydie, Amaury, Corentin, Thibaud, Jean, Hugo, Jorge, Torben, Moussa, Felix, Christian, Romain, Clément, Ines, Charlie, Tarik, Benjamin, Emilie, Grégory, Pierre, Benoit, Johnny, Florian, compagnons d'open-space ou de salle blanche, qui font qu'une journée de travail est loin d'être solitaire et ennuyeuse.

Cette thèse ne s'est pas faite qu'au sein de l'IRDEP ou du LPN, un grand merci donc à Isabelle pour sa gentillesse et son aide dans la préparation de solutions KBr, Tony et Eric pour leurs éclaircissements sur les schémas de relaxation et autres matrices de rigidité, Alain D. et Arnaud pour nous avoir donné accès à leur parabole et héliostat.

Je remercie le CCAS de Chatou pour m'avoir rendue presque végétarienne ces trois dernières années avec des bols de légumes à un prix défiant toute concurrence. Je ne remercie pas vraiment la RATP de me donner si régulièrement la possibilité d'effectuer des « grands chelems »...

Parce qu'un travail de thèse, aussi passionnant soit-il, ne doit pas éclipser ce qu'il y a de plus important dans la vie, je tiens à remercier ceux qui m'ont soutenu « à l'extérieur ». Les mots me manquent pour Do et Marinette, amies, complices, embarquées comme moi dans l'aventure de la thèse. Vous avoir eu à mes côtés ces trois (et aussi/surtout sept) dernières années a été une chance incroyable. On y est arrivées !!! A Yann et Clem, amis, famille, un peu des deux en même temps, qui m'auront accueillie pour des weekends au grand air, pleins de meringue double-crème ou de fondue suisse. Une pensée pour Corentin, mon filleul, arrivé il y a peu. A Marie, une amie avec qui j'ai pu partager mes rêves et mes doutes, oreille attentive et disponible depuis le foyer Marengo jusqu'à aujourd'hui ! A toutes les handiablées : Clem, Anlor , Nikaa, Caro, Helo, Lydia, Claire, Co, Laeti, Marie, Fanny, Do, Marinette, de belles amitiés nées sur le plâtal, qui ont grandi en rando, en coloc, au resto, à Marseille, à Barcelone, à Chamonix, à Vienne, à Aujac, à la Palmyre, à Quiberon ... A Vincent, Sylvain et Ben, qui supportent vaillamment des soirées un peu trop aigues. A Antoine, Tibz, Alex et Oliv' qui auront suivi de près ou de loin ces années de recherche.

A Angel, Laure, Mag, Bibine, Aglaé, Anne-Cé, Fanny, Marie, Karen, Caro(s), Clémence, Coralie, Pris, Jess, Philou, Guillaume, Zouzou, Chef, Hippo, et tou(te)s les autres, des coéquipières, coachs, pour se dépasser, s'aérer et se défouler ! Vive le PSC !

A Charlotte, Diane, Sarah, Myriam, Joël, Thibault, Cyrille ou Jean-Michel... que de temps passé depuis Darius Milhaud, ou Michelet !

Un immense merci à ma famille, qui m'a toujours soutenue et entourée. Merci à mes parents bien sûr, et ma sœur qui auront vaillamment tenté de relire ma prose. A ma grand-mère, toujours soucieuse de mon bonheur, qui n'aura malheureusement pas pu être le témoin des derniers mois de mon doctorat. A ma tante Brigitte, qui a accepté de relire et corriger l'anglais de certains chapitres de cette thèse. A mes oncles, tantes, cousins, cousines qui ont gentiment proposé de mettre à disposition de la Science les toitures de leurs hangars (ca viendra un jour, ca viendra !).

Un grand merci enfin à tous ceux qui se sont déplacés pour venir m'écouter le jour J !

INDEX OF SYMBOLS

Symbol	Unit	
a	%	Absorptivity
A	cm^2	Ideality factor Area of a solar cell
AM1.5		Air Mass 1.5
B_{rad}	cm^3s^{-1}	Radiative recombination coefficient
c	ms^{-1}	Light velocity
C		Illumination concentration factor (ratio)
C_n, C_p	cm^6s^{-1}	Auger recombination coefficient for electron and hole
CBD		Chemical bath deposition
d_i	cm	Thickness of the semiconducting layer i ($i = a$: absorber, b : buffer, w : window)
ΔD	eV	Electrostatic potential difference induced by a dipole at an heterointerface
D_n, D_p	cm^2s^{-1}	Diffusion coefficient of electron and hole
E	Vcm^{-1} eV	Electric field Photon energy
EL		Electroluminescence
$E_{c,i}, E_{v,i}$	eV	Conduction and valence band edge of semiconductor i
E_d	eV	Energy level of defect states
E_f	eV	Fermi level
E_{fn}, E_{fp}	eV	Quasi-fermi level of electrons and holes
$E_{g,i}$	eV	Energy bandgap of semiconductor i
$\Delta E_c^{i,j}$	eV	Conduction band offset between semiconductor i and j . ΔE_c correspond to the conduction band offset between the absorber and buffer
$\Delta E_v^{i,j}$	eV	Valence band offset between semiconductor i and j . ΔE_v correspond to the valence band offset between the absorber and buffer
EQE	%	External quantum efficiency
f		Occupancy of defect states
F	C.mol^{-1}	Faraday constant
F_0	V.cm^{-1}	Electric field at the heterointerface
F_m	V.cm^{-1}	Maximum electric field
FEM		Finite Element Method
FF	%	Fill factor
G	$\text{cm}^{-3}\text{s}^{-1}$	Generation rate

I	A	Current
J	A.cm ⁻²	Current density
J_{sc}	A.cm ⁻²	Short-circuit current density
J_{ph}	A.cm ⁻²	Photocurrent density
J_0	A.cm ⁻²	Saturation current density Bessel function of the first kind of order 0
J_1		Bessel function of the first kind of order 1
J_{00}	A.cm ⁻²	Reference current density
J_{01}	A.cm ⁻²	Saturation current density for the dark current of ideality A=1
J_{02}	A.cm ⁻²	Saturation current density for the dark current of ideality A=2
J_{001}	A.cm ⁻²	Reference current density for the dark current of ideality A=1
J_{002}	A.cm ⁻²	Reference current density for the dark current of ideality A=2
k		Boltzmann constant
k_{th}	W.cm ⁻¹ .K ⁻¹	Thermal conductivity
L_n, L_p	cm	Diffusion length
l_n, l_p	cm	Mean drift length
n	cm ⁻³	Electron density
n_0	cm ⁻³	Electron density at thermal equilibrium
n_i	cm ⁻³	Intrinsic carrier density
$N_{A,i}, N_{D,i}$	cm ⁻³	Acceptor and donor density in the semiconductor i
N_c, N_v	cm ⁻³	Density of states in the conduction or valence band
N_d	cm ⁻³	Density of defects
ODC		ordered defect compound
PL		Photoluminescence
$PL(E)$	s ⁻¹	Photoluminescence intensity
p	cm ⁻³	Hole density
P_{max}	W	Maximum power generated by a solar cell
q	C	Elementary charge
Q	W.cm ⁻²	Heat flux
R_s	ohm or ohm.cm ²	Series resistance
R_{sh}	ohm or ohm.cm ²	Shunt resistance
R_{\square}	ohm/square	Sheet resistance
R_c	ohm or ohm.cm ²	Contact resistance
S_n, S_p	cm.s ⁻¹	Recombination velocity of electron and holes

t	cm	Absorber (Cu(In,Ga)Se ₂) thickness
U	cm ⁻³ s ⁻¹	Recombination rate
V_{oc}	V	Open-circuit voltage
V_{bi}	V	Built-in voltage
w_a	cm	Width of the space charge region in the absorber
α_i	cm	Absorption coefficient of semiconductor i
β	W ⁻¹ cm ⁻¹	Proportionality factor between photocarrier density and illumination power density
$\Delta\mu$	eV	Quasi-Fermi level splitting
ε	Fm ⁻¹	Dielectric function
ε_0	Fm ⁻¹	Vacuum permittivity
ε_r		Relative dielectric constant
χ	eV	Electron affinity
σ_n, σ_p	cm ²	Capture cross-section for electrons and holes
v_n^{th}, v_p^{th}	cm.s ⁻¹	Thermal velocity of electron and hole
ϕ	s ⁻¹	Luminescence flux
ϕ_{bb}	s ⁻¹	Spectral photon density of a black body
ϕ_n	V	Neutrality level of interface states
ϕ_b^p	V	Hole barrier
λ	cm	Wavelength
η	%	Solar cell efficiency
$\eta(V)$	%	External collection efficiency (dependence of photocurrent on voltage)
$\eta(z, V)$	%	Collection function (probability to collect a photogenerated carrier)
ρ	ohm.cm	Resistivity
ψ	V	Electric potential
κ	K.A ⁻¹ cm ²	Proportionality constant of solar cell temperature with J_{sc} (proportional to incident power)
$\mu_{n,i}, \mu_{p,i}$	cm ² .V ⁻¹ s ⁻¹	Electron and hole mobility in semiconductor i
τ_n, τ_p	s	Carrier lifetime

OUTLINE

ACKNOWLEDGEMENTS	5
INDEX OF SYMBOLS	9
OUTLINE	13
GENERAL INTRODUCTION.....	19
CHAPTER I. OVERVIEW OF PHOTOVOLTAIC TECHNOLOGIES AND MOTIVATIONS OF THIS STUDY	23
1. Introduction.....	24
2. Photovoltaics in the energy sector	24
2.1. The Energy today and tomorrow : key statistics.....	24
2.2. Photovoltaics : a solution to the energy challenges.....	25
3. Photovoltaics : a variety of technologies	28
3.1. Silicon wafers.....	29
3.2. Thin films	30
3.3. Concentrating photovoltaics	32
3.4. Other photovoltaic systems	33
3.5. Synthesis and conclusion.....	33
4. Our study: concentrator thin film photovoltaics	33
5. Memento.....	35
CHAPTER II. PHYSICS OF $\text{Cu}(\text{In,Ga})\text{Se}_2$ DEVICES.....	37
1. Introduction	38
2. Description of $\text{Cu}(\text{In,Ga})\text{Se}_2$ solar cell architecture and deposition techniques.	38
2.1. The structure of a $\text{Cu}(\text{In,Ga})\text{Se}_2$ solar cell.....	38
2.2. Molybdenum	39
2.3. CdS or alternative buffers.....	45
2.4. ZnO	45
2.5. Conclusions.....	45
3. The $\text{Mo}/\text{Cu}(\text{In,Ga})\text{Se}_2/\text{CdS}/\text{ZnO}$ heterojunction	46
3.1. Model of an heterojunction	46
3.2. Description of the $\text{Cu}(\text{In,Ga})\text{Se}_2$ heterojunction : different models.....	47
4. Current-voltage characteristic of a $\text{Cu}(\text{In,Ga})\text{Se}_2$ solar cell	51
4.1. Current-voltage curve of an ideal p-n junction	51
4.2. Non idealities, loss sources	52

4.3.	Recombination mechanisms	53
4.4.	Voltage dependence of photocurrent.....	57
4.5.	Concentration on Cu(In,Ga)Se ₂	59
5.	Conclusion	61
6.	Memento.....	62
CHAPTER III.	SCALE EFFECTS OF THIN FILM SOLAR CELLS	63
1.	Introduction.....	64
2.	Scale effects in light emitting diode and photovoltaic devices.....	64
2.1.	State of the art of light emitting diodes of reduced size.....	64
2.2.	State of the art of microcells in photovoltaics	67
3.	Modeling of sheet resistance problem	70
3.1.	Resistive sources in thin film solar cells	70
3.2.	Sheet resistance problem in equations.....	73
3.3.	Model validation: electroluminescence and I-V fit	81
3.4.	Size-dependent prediction of the behavior of solar cells under concentration.	85
3.5.	Discussion	88
4.	Thermal analysis of microcells	89
4.1.	Necessity to study thermal behavior of solar cells.....	89
4.2.	Thermal scale effect	90
5.	Conclusions.....	98
6.	Memento.....	99
CHAPTER IV.	CU(IN,GA)SE₂ MICROCELLS FABRICATION AND CHARACTERIZATION.....	101
1.	Introduction.....	102
2.	Design of proof of concept prototypes	104
2.1.	Geometry of the cells	105
2.2.	Size and contact geometry	105
2.3.	Choice of the absorber	105
2.4.	Sketch of the chosen microcells design.....	106
3.	Fabrication process step by step	107
3.1.	Fabrication process overview.....	107
3.1.	Fabrication steps in details.....	108
4.	Adaptation of the process to finished cells.....	113
5.	Behavior of microcells in standard testing conditions	114
5.1.	Statistical analysis of dark current-voltage characteristics	114
5.2.	Analysis of AM1.5 current-voltage characteristics.....	118
5.3.	Discussion	120
6.	Conclusion	127
7.	Memento.....	128

CHAPTER V. CHARACTERISATION OF MICROCELLS UNDER INTENSE ILLUMINATION.....	129
1. Introduction.....	130
2. Characterization under concentrated monochromatic illumination.....	130
2.1. Experimental setup of the monochromatic concentration experiment	130
2.2. Results : Current-voltage Characteristics and comparison to simulation models	132
2.3. Discussion	136
2.4. Temperature of microcells under concentration	139
3. Characterization under concentrated polychromatic illumination.....	144
3.1. Influence of spectral variations on the behavior of a solar cell – consequences for monochromatic illumination.....	145
3.2. Concentration experiment with a 644 nm red laser	147
3.3. Experimental setup for sunlight concentration.....	152
4. Synthesis and Conclusion.....	156
5. Memento.....	157
CHAPTER VI. ANALYSIS AND MODELING OF THE PHYSICS OF Cu(In,Ga)Se₂ MICROCELLS UNDER HIGH CONCENTRATION, OPTIMIZATION	159
1. Introduction.....	160
1.1. Analysis of concentration dependent <i>I-V</i> curves on Cu(In,Ga)Se ₂ solar cells.	160
1.2. Physics of solar cells under concentrated illumination.....	161
2. Series resistance modulation under illumination.....	163
2.1. Experimental results.....	163
2.2. Modeling of series resistance modulation.	165
3. Collection factor variations.....	171
3.1. Experimental measurements	171
3.2. Apparent shunt resistance analysis and modeling.....	174
3.3. General 1D model of collection in a semiconductor.....	179
3.4. Conclusions.....	189
4. Very high concentration experiments	189
5. Conclusions.....	191
6. Memento.....	193
CHAPTER VII. TOWARDS INDUSTRIAL APPLICATIONS: MICROCELLS WITH LOCALIZED ABSORBER.....	195
1. Introduction: localized depositions techniques.....	196
2. A top down fabrication process: study of mesa delineated microcells on co-evaporated Cu(In, Ga)Se₂ absorbers	198
2.1. The need for a model architecture.....	198
2.2. Fabrication process from a standard Cu(In, Ga)Se ₂ solar cell	198
2.3. Results : electrical characterization.....	200
2.4. Discussion	203
2.5. Conclusions.....	205
3. A bottom-up process: electrodeposition	205

3.1.	State-of-the art electrodeposition	205
3.2.	Fabrication of electrodeposited CuInSe ₂ microcells	208
3.3.	Results	210
3.4.	Discussion	213
4.	Synthesis and discussion on industrial relevance	214
5.	Memento	216
GENERAL CONCLUSIONS AND PERSPECTIVES		217
	Main results of this thesis	217
	Perspectives	220
RESUME EN FRANCAIS		223
BIBLIOGRAPHY		241
LIST OF PUBLICATIONS		261
	Publications with peer-review.....	261
	Publications without peer-review	261
APPENDICES		263
APPENDIX A. HEAT CONDUCTION EQUATIONS		265
1.	Physical problem.....	265
1.1.	Semi-infinite media	265
1.2.	Film of finite thickness.....	267
1.3.	Thermal behavior of the Cu(In,Ga)Se ₂ stack	271
2.	Average temperature increase.....	275
APPENDIX B. TRANSMISSION LINE METHOD.....		277
APPENDIX C. PHOTOLITHOGRAPHY		281
1.	Principals of photolithography.....	281
1.1.	Basis.....	281
1.2.	Chemistry of photoresist	281
1.3.	Process.....	282
APPENDIX D. OPEN-CIRCUIT VOLTAGE IN THE SHOCKLEY-QUEISSER LIMIT		285
APPENDIX E. FEM PROGRAM FOR THE STUDY OF SEMICONDUCTORS UNDER HIGH INJECTION.....		287

1. Physical problem	287
1.1. Hypothesis and context.....	287
1.2. Dimensionless problem.....	289
2. Finite-Element Method (FEM)	290
2.1. Weak formulation and stiffness matrices.....	291
2.2. Determining the potential V^{k+1} for given carrier concentrations N^k and P^k	291
2.3. Determining the electron concentration N^{k+1} for given V^{k+1} and P^k	292
2.4. Determining the hole concentration P^{k+1} for given V^{k+1} and N^{k+1}	294
3. Results	295
3.1. Validation of our model.....	295
3.2. Impact of boundary conditions.....	296
3.3. Impact of the mobilities.....	297
3.4. Non constant generation rate.....	300
APPENDIX F. MICROCELLS WITH LOCALIZED ABSORBERS	303
1. A top down fabrication process: study of mesa delineated microcells on co-evaporated Cu(In, Ga)Se₂ absorbers	303
1.1. Fabrication process.....	303
1.2. Electrical characterization.....	308
2. A bottom-up process: electrodeposition	312
Fabrication of electrodeposited CuInSe ₂ microcells.....	312
APPENDIX G. ADAPTATION OF THE MICROCELL FABRICATION PROCESS TO FINISHED CELLS	317
1. Performance of microcells fabricated on complete stacks	317
1.1. Current-voltage characteristics.....	317
1.2. Laser tests.....	318
APPENDICES BIBLIOGRAPHY	319
RESUME	322
ABSTRACT	322

GENERAL INTRODUCTION

The photovoltaic effect was discovered in 1839 by Alexandre Edmond Becquerel [1]. Since this pioneering work, the knowledge about photovoltaics has increased immensely and applications spread. Photovoltaics was first used as a source of energy in space applications, with the Vanguard satellite launched in 1958. If the idea of using solar energy to significantly power the world is not new, *“We are like tenant farmers chopping down the fence around our house for fuel when we should be using Nature's inexhaustible sources of energy — sun, wind and tide. ... I'd put my money on the sun and solar energy. What a source of power! I hope we don't have to wait until oil and coal run out before we tackle that.”* (Thomas Edison, 1931), no large scale applications emerge until the very end of the twentieth century. From 2000 to 2010 however, the growth rate of the photovoltaic industry has been as high as 40% [2]. In 2011, the cumulative installed power amounted to nearly 70 GW [3], [4]. In certain countries, photovoltaics has become in the past years a large scale electricity production source. Currently, in Germany for example, more than 10% of the daily electricity consumption is supplied by photovoltaics on sunny days.

Today solar panels have reached a record 33% efficiency [5], and coating technologies such as thin films enable high yields and low cost fabrication. The challenges that the photovoltaic community is facing are the terawatt level development, both from the point of view of material availability and fabrication facilities, in a world of finite natural and financial resources, and the competition with cheap fossil energy sources. This thesis studies the possibility of coupling two photovoltaic domains in order to meet these challenges: thin films and concentrating photovoltaics. Thin films enable easy fabrication and high throughput, whereas concentrating photovoltaics is raw material thrifty and enables high efficiencies. This axis of research has not been explored much up to now, due to resistive limitations in thin film solar cells. The originality of the present work lies in the design of a novel solar cell architecture. In order to build prototypes, we focus on the $\text{Cu}(\text{In,Ga})\text{Se}_2$ thin film technology. However general conclusions are drawn that can apply to other material families.

This thesis is organized in seven chapters. In Chapter I, we place the study in the general context of today's energy challenges, and explain our motivations to tackle concentration on thin films. In Chapter II the physics of solar cells in general, and that of $\text{Cu}(\text{In,Ga})\text{Se}_2$ in particular, will be reviewed .

As Cu(In,Ga)Se₂ solar cells are used as proof-of-concept in this thesis, the state-of-the art Cu(In,Ga)Se₂ manufacturing processes will be presented.

In Chapter III, scales effects that may impact resistive losses and thermal management of thin film solar cells under concentration are studied. Numerical simulations enable a good understanding of the phenomena at stake.

Following the guidelines highlighted in Chapter III, the fabrication process of prototype Cu(In,Ga)Se₂ microcells is described in Chapter IV and the basic photovoltaic properties of the devices outlined. In Chapter V, the prototypes are tested under concentrated illumination and the influence of the incident spectrum is analyzed. In Chapter VI the physics of Cu(In,Ga)Se₂ devices under high concentration is studied, and particular attention is drawn on characteristics specific to the high concentration regime.

Finally, in Chapter VII, we open perspectives on possible industrial applications, and devices with localized absorbers and their fabrication process are described.

At the end of each chapter a brief memento summarizes the main findings. Thus the reader interested in specific parts of this thesis can have a brief overview of the rest of the work in these captions.

This thesis is the result of numerous collaborations. I will briefly review them in order to be clear about the work I have done in person, from the help I had received from co-workers. The most part of my time was spent at the Institute of Research and Development on Photovoltaic Energy (IRDEP). I performed the characterization of the samples, as well as all of my numerical simulations there. I benefited from the support of the laboratory platform, and colleagues, especially for the deposition of Mo, Cu(In,Ga)Se₂, CdS, ZnO and Al₂O₃ layers, that I did not do myself. Raman measurements, X-Ray fluorescence spectroscopy cartographies as well as electrodepositions of CuInSe₂ were also done by co-workers. I had the opportunity to work in collaboration with the Laboratory of Photonics and Nanostructures (LPN), and access their clean-room facility. I did the photolithography experiments and structuring steps, as well as most of the SEM characterizations there. The metal and dielectric depositions, as well as high resolution SEM images were performed by LPN coworkers. Additionally the Institut Lavoisier de Versailles helped me in the preparation of bromine solutions. I also received

a great support from the CERMICS for the finite-element method program presented in Chapter VI, especially to choose and then refine the algorithm that I was developing. I also work with Würth Solar, which sent me some coevaporated $\text{Cu}(\text{In,Ga})\text{Se}_2$ samples.

CHAPTER I. OVERVIEW OF PHOTOVOLTAIC TECHNOLOGIES AND MOTIVATIONS OF THIS STUDY

1. Introduction	24
2. Photovoltaics in the energy sector	24
2.1. The Energy today and tomorrow : key statistics	24
2.2. Photovoltaics : a solution to the energy challenges.....	25
3. Photovoltaics : a variety of technologies	28
3.1. Silicon wafers.....	29
3.2. Thin films	30
3.3. Concentrating photovoltaics	32
3.4. Other photovoltaic systems	33
3.5. Synthesis and conclusion.....	33
4. Our study: concentrator thin film photovoltaics	33
5. Memento	35

1. Introduction

This PhD thesis is dedicated to photovoltaic energy. In order to place our research field in a broader context, a brief overview of the energy sector and current photovoltaic technologies is given. Our approach is then described in order to highlight the challenges we would like to address.

2. Photovoltaics in the energy sector

2.1. The Energy today and tomorrow : key statistics

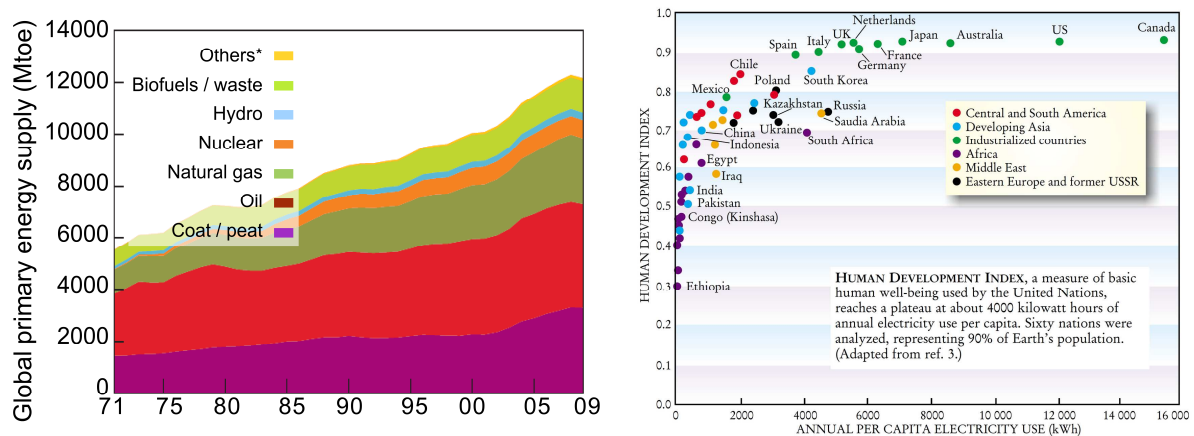


Figure I-1 : (left) Evolution of world total primary energy supply (Mtoe, i.e. mega tones of oil equivalent) from 1971 to 2009. * Others includes geothermal, solar, wind, heat etc... Reproduced from [3] (right) Human development index as a function of annual per capita electricity use. Reproduced from [6]

The energy challenge we face today has many aspects. First, the emission of green-house gases should be limited, in order to avoid a global temperature increase (compared to pre-industrial area) that could have tragic impact on climate. According to the international energy agency (IEA) we are on the track for a 6.5°C long term average temperature increase with current policies. In comparison, the temperature increase agreed on, in international energy conferences (Copenhagen 2009, United Nations 2009-2010), was 2°C. Reducing the temperature increase to 2°C would require strong political will and economical incentives [7]. Second, we will face a strong energy demand growth in the coming decades. The yearly world energy consumption amounted to 140 000 TWh in 2009 (or 12 000 mega tons of oil equivalent) and it seems reasonable to expect a 200 000 TWh consumption in 2030 if current energy policies stay in place [8]. This surplus of energy demand is driven by non-OECD countries, that account for 90% of the world population growth [7], and can only be reduced if strong incentives are put in place. Renewable energies will have a strong role to play, half of the new energy

capacity to be installed up to 2035 is expected to come from renewables (wind and hydropower mainly) [7]. The other half should come from fossil fuels, notably gas, which strengthens the issue of greenhouse gases emission. Third, the development of the energy sector is closely linked to that of human development (Figure I-1). Giving access to electricity to the 20% of the world population that are deprived from it today is a necessity [7]. “Energizing human development” is one of the main challenges of the United Nations’ program for human development, and the most part is going through off-grid micro production systems.

In this context photovoltaic energy that converts sunlight into electricity is a promising solution. It is renewable, does not emit greenhouses gases, and can easily be installed off-grid. In 2011, the photovoltaic installations worldwide produced 89 TWh per year [4]. This energy source thus only represents a minute portion of the global energy consumption today, around 0.06%. A more significant role is anticipated in the future, if current technologies evolve. It is interesting to see how they should adapt in order to play a strong role in the energy sector that we have briefly described above.

2.2. Photovoltaics : a solution to the energy challenges

2.2.1. The solar resource

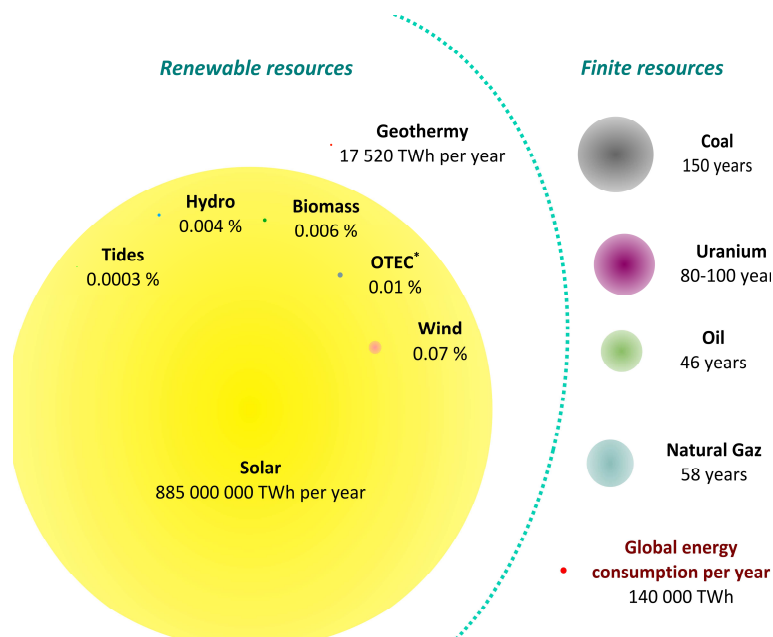


Figure I-2 : Global energy resource, the disks area is proportionate to the resource. For finite resources the data concern the total energy reserve, for renewable energy the data are yearly available energy. Note that apart from geothermal energy, the renewable sources derive from solar power, and yearly available data are expressed as percentage of the solar resource. Data from solar, coal, oil, gas resources and global yearly energy consumption [3]. Data for Uranium [9].

Other data from [10]. * OTEC stands for Ocean Thermal Energy Conversion.

Solar energy is a renewable source, from a human perspective. The solar irradiance available outside the earth's atmosphere on a surface perpendicular to the sun's flux is $1366 \text{ W}\cdot\text{m}^{-2}$. This irradiance is called Air Mass Zero (AM0). When averaged on the earth surface, and taking into account the reflection by clouds, the absorption of the atmosphere and the alternation of nights and days, the power density available on average at the earth surface is $198 \text{ W}\cdot\text{m}^{-2}$. This represents 885 000 000 TWh available per year, which is 6400 times the global human energy consumption in 2008 [3]. Thus the collection of only a small fraction of the solar energy is sufficient to cover mankind energy needs. In comparison, for non-renewable energy sources, coal reserves represent 150 years of consumption at the current annual rate, gas reserves 58 years, oil 46 years and uranium roughly 100 years [3], [9]. (These data are given as information and originate from the international energy agency. It should be noted that different numbers can be found in the literature, but the orders of magnitude are respected.)

2.2.2. The development of photovoltaics

Solar energy, even if it is still limited on the global energy market, is the fastest growing energy sector. The photovoltaic installations amounted to 40 GW by the end of 2010 (Figure I-3). Then 29.7 GW were connected to the grid worldwide in 2011, raising to the total capacity to nearly 70 GW [4]. These figures are tremendous if compared to that of the end of the 20th century, when photovoltaics was limited to off-grid applications. In some countries, where photovoltaic development was strongly supported by state policies, solar power is becoming a significant resource. In Germany on sunny 25 May 2012 for example, photovoltaic installations produced a peak 22.4 GW of power, and more importantly nearly 190 GWh throughout the day, which represented 14% of the German electricity demand that day [11]. Thus if the averaged figures on photovoltaic installations are still small on a

Box 1 :

In order to test photovoltaic modules, a reference incident spectrum is taken by convention. The most common irradiance is called Air Mass 1.5 (AM1.5). AM1.5G corresponds to $1000 \text{ W}/\text{m}^2$, or the global irradiance reaching the earth on a sunny day after going through 1.5 times the atmosphere thickness at the equator, i.e. with a zenith angle of 48° . This zenith angle corresponds to the latitude of Europe and United States. We can differentiate AM1.5 global (AM1.5G) that accounts for all the irradiance, from AM1.5 direct (AM1.5D) that only takes into account direct irradiance, i.e. not diffused by the atmosphere. This direct normal irradiance is also called DNI, and represents an incident power of $870 \text{ W}/\text{m}^2$.

global scale, regional exceptions are very promising.

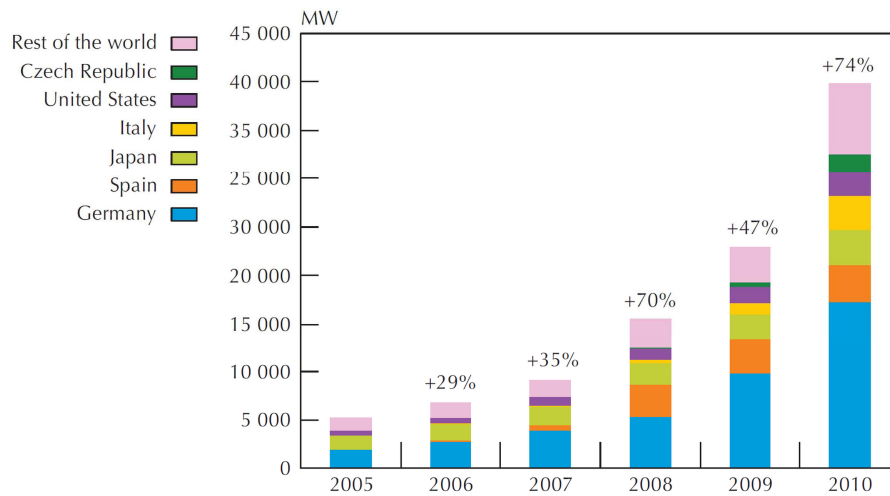


Figure I-3 : Global cumulative photovoltaic capacities by 2010. Reproduced from [3]

Grid parity for photovoltaics , i.e. the time when electricity produced by photovoltaic installations has the same price as that bought from the grid, has already been reached in some countries or regions (Italy, Hawaii, ...), and is expected to be reached for residential installations in most European countries by the end of 2020 [12]. Indeed prices are decreasing with increasing cumulative capacity (learning curve), whereas the prices of electricity by conventional means are increasing. However obtaining grid parity, if a first step, is not sufficient to ensure photovoltaics penetration in the market. Indeed, like compact fluorescent light bulbs or solar water heaters that are economical in the long run, photovoltaic installations have a high prima facie cost which gives the wrong impression of being expensive [13], [14].

Given the energy context, the photovoltaic community is facing several challenges in order to ensure its development. Before giving a brief overview of the different existing technologies, we will focus on the requirements for future photovoltaic technologies.

2.2.3. *Technological bottlenecks and challenges*

Surprisingly enough, the price of photovoltaic technologies is not necessarily the first challenge that the photovoltaic community is facing, as grid parity has already been achieved in some regions, and might be widespread by 2020 [12].

Future photovoltaic technologies will have to develop fast. In 2011, photovoltaic modules produced and installed represented more capacity than ever made up to 2009. However this trend has to

continue at a strong pace if in the coming decades photovoltaics is to represent more than the current 0.06% of the total energy consumed worldwide.

In order to achieve this manifold increase in capacity, large scale, high throughput technologies have a natural advantage. In this sense thin film technologies that originate from the coating industry have a strong leverage over traditional crystalline technologies as they can cover large areas fast. For example First Solar® claims that it takes only 2.5 hours to complete a thin film CdTe module when starting with a glass substrate. Large capacities can also only be produced if the capital expenditure (CapEx) needed to create new fabrication facilities is relatively low. Indeed a low CapEx decreases the financial risks of the investors and results in lower margins and thus more competitive prices.

Another requirement is ecological footprint. If photovoltaics is to be developed at the terawatt level, the raw material consumption has to be as limited as possible. For thin film technologies there are strong concerns about indium or tellurium for example [15], and decreasing the material consumption of actual technologies is important. The environmental impact of photovoltaics is also linked to the pollution created during the entire module life cycle. Studies have shown that photovoltaics and especially thin films, have a much smaller impact than conventional sources of energy in terms of CO₂ gases emissions or heavy metal pollutions [16]. The average energy payback time, i.e. time required by the photovoltaic installation to produce the energy needed for its manufacturing, of a thin film module today is around 1 year, and for multicrystalline silicon of 1-2 years, which are both very small compared to guaranteed operational lifetime of 20 to 30 years. For terawatt development of photovoltaics, land availability is also generally thought as a problem. However new land requirements for photovoltaics ($\approx 300 \text{ m}^2/\text{GWh}$ if ground mounted, $\approx 0 \text{ m}^2/\text{GWh}$ if building-integrated) are found comparable to coal-based fuels and less than other renewables [17]. However, if not limiting, land use has a strong impact on the photovoltaic price, and thus technologies that can easily be integrated to existing buildings are preferable.

For all technologies the efficiency of the module is critical. Efficiency gain can positively impact all the photovoltaic fabrication value chain, and ultimately decrease the price. More efficient solar panels use less raw material per watt, the land usage and thus renting cost is smaller, and more complex fabrication processes can be sustained.

3. Photovoltaics : a variety of technologies

Under the term photovoltaics, there are many different technologies that convert sunlight into electricity. Some technologies have existed for a long time now, whereas some are only emerging. Figure I-4 recall the different technologies, their maximum theoretical efficiencies and average production performances.

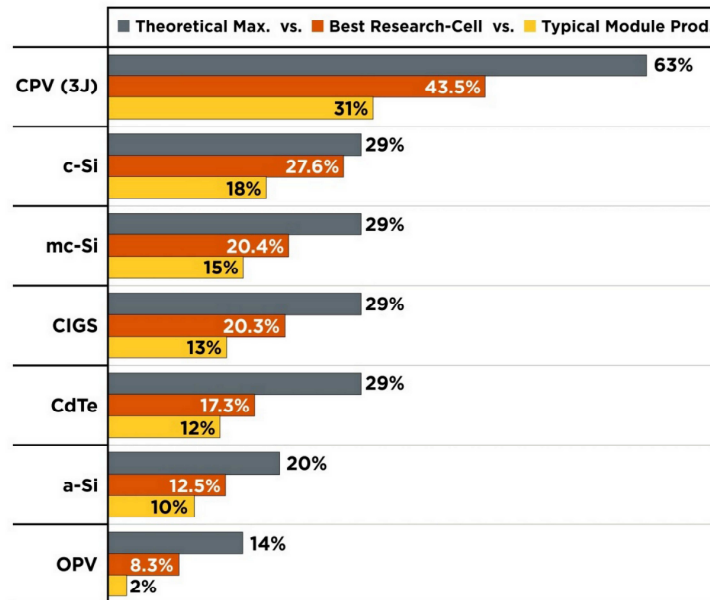


Figure I-4 : Different photovoltaic technologies, their maximum efficiency, the best research cell, and typical module efficiency. CPV (3J) stands for concentrated photovoltaic triple junction solar cells, c-Si for crystalline silicon, mc- Si for multicrystalline silicon, CIGS for Cu(In,Ga)Se_2 compounds, a-Si for amorphous silicon and OPV for organic photovoltaic. [18]

We will briefly review the technologies, focusing on advantages and drawbacks, in order to place this PhD thesis in its context.

3.1. Silicon wafers

Crystalline and polycrystalline silicon modules accounted for 85% of the market in 2010 [2]. Mono- or polycrystalline modules are fabricated by consecutive steps. Purified silicon ingots are grown and then sliced into wafers. The wafers are then turned into solar cells before being assembled in a module by interconnection and encapsulation. Silicon technologies have the advantage to work with the most abundant material in the Earth' crust. However silicon modules are currently connected with silver paste, for which shortage is foreseen. Thus copper-nickel replacements are under investigation [18].

In a silicon module the silicon material accounts for 60% of the module price, thus reduced material usage is needed to drive the costs down. However due to the poor absorption of crystalline silicon,

silicon wafers have to be thick, and strategies are implemented to trap light and increase the optical path. Typical module price for multicrystalline silicon was 1.5 – 2\$/W in 2010 (even if some producers such as Trina Solar claimed lower prices 1.1\$/W) [18]. These prices are estimated extremely low, and do not generate sufficient margins to be sustainable. Thus there is a doubt on possible cost reduction of c-Si in the future, in a market being relatively mature now, with vertically integrated manufacturers.

3.2. Thin films

3.2.1. Thin films : advantages and drawbacks

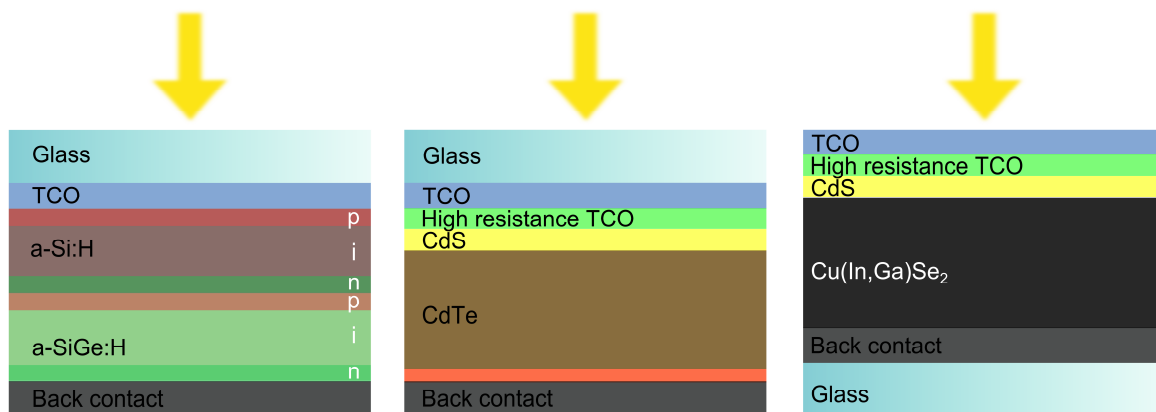


Figure I-5 : Thin film solar cells structures (left) a-Si:H/a-SiGe:H tandem thin film solar cells (middle) CdTe/CdS solar cell (right) Cu(In,Ga)Se₂/CdS solar cell

Thin films photovoltaic modules are deposited on substrates by coating techniques such as sputtering, printing or evaporation. Thus large areas can be covered fast. These coating techniques are already widespread in the automobile or glass industry. If the substrate is flexible, the module can be flexible too, enabling new applications [19], [20]. Contrary to wafer based technologies, the thin film modules are directly fabricated on a substrate, without the need for prior cells fabrication and then module assembly, which eases the process. Solar cells and module fabrication are done at the same facility, which reduces the intermediaries, and thus margins and prices. Thin films can be deposited by a variety of techniques, ranging from high vacuum to atmospheric processes. Thus the CaPex varies a lot among the different technologies.

Efficiencies of thin film modules are still lower than those of c-Si technologies (Figure I-4). On a thin film module the active material cost amounts to less than 20% of the manufacturing costs [21], thus reduction in material cost or usage will only have a limited impact on the price today compared to the lever this sector has on c-Si, but this sector can become of prime importance if certain element become scarce. Obtaining high efficiencies is thus very important to lower the impact of the balance-

of-system cost. For example on a Cu(In,Ga)Se_2 module, an absolute gain in efficiency of 0.5% , from 12.5% to 13.0 % , results in a 5% decrease in module manufacturing costs [21].

3.2.2. *a-Si : good absorption but limited efficiencies*

Contrary to wafer based silicon, amorphous silicon has a high absorption coefficient, and thin films are sufficient to collect the incident sunlight efficiently. However a-Si is highly defective and the efficiencies reached to date are rather small. Indeed the best a-Si laboratory cells reach a 10.1% conversion efficiency [22]. Tandem cells with amorphous and microcrystalline silicon or a-SiGe are also used (Figure I-5) and reach slightly higher efficiencies of 12.3% [22]. Due to high throughput, the prices of a-Si modules are relatively low, but the low efficiencies limit the market outputs.

3.2.3. *CdTe : industrial maturity*

The thin films solar cells made of CdTe were the first to be industrially developed at a large scale, by the firm First Solar®. This firm confirms a record efficiency of 17.3% in 2011 on research cells [23], and reach around 12% at the industrial scale (Figure I-4). This technology has the smallest energy payback time (0.8 year) and highest throughput with 2.5 hours needed to fabricate a complete module. The manufacturing price of CdTe modules was around 0.75 \$/W in 2011 [24], which is below other technologies including c-Si, and enabled comfortable margins.

However CdTe modules cannot be commercialized for individuals in Europe due to strict regulations regarding Cd. Moreover the resources in Te are limited and the annual maximum annual throughput of CdTe is estimated lower than 38 GWp/year up to 2020 [16]. Thus coming up with new solar cell architectures that lower the Te consumption is critical for the TW development of the CdTe field.

3.2.4. *CIGS : record efficiencies, a good candidate ?*

Cu(In,Ga)Se_2 is the most efficient thin film technology to date, with a record 20.3% efficiency at the laboratory scale [25]. Highly efficient flexible cells were also demonstrated, with efficiency of 18.7% [19]. Several non-vacuum deposition approaches are studied with efficiencies of 17.1% achieved on a laboratory cell with printing technologies [26] or 13.4% with electrodeposition on a flexible module [20]. These methods are very promising due to the lower CapEx needed for installing new production capacities, and the relatively high conversion efficiencies. Cu(In,Ga)Se_2 is at the beginning of its industrial development with firm like Solar Frontier (0.98 GW/year), Avancis, MiaSolé, Nanosolar, Solibro or Würth Solar.

Cu(In,Ga)Se_2 modules may employ CdS buffer layers, which raises the question of Cd toxicity. However, alternative buffers, such as ZnS, are already implemented at the industrial scale, and this

should not be a limiting issue. The limitation of the Cu(In,Ga)Se_2 technology may come from the low availability of Indium, which would limit the annual production at 22 GW/year up to 2020 [16]. Thus, less consuming solar cell architecture, as well as a better material utilization, which is a strong advantage of non vacuum processes, are necessary. Ultrathin solar cells are studied, and the replacement of In by highly available elements in In-free chalcopyrites, such as $\text{Cu}_2\text{ZnSnS}_4$, is under study. However the efficiencies of In-free solar cells are to date lagging behind (10.1% conversion efficiency [27]), making the incentives for In-thrifty Cu(In,Ga)Se_2 solar cells and manufacturing processes very strong.

3.3. Concentrating photovoltaics

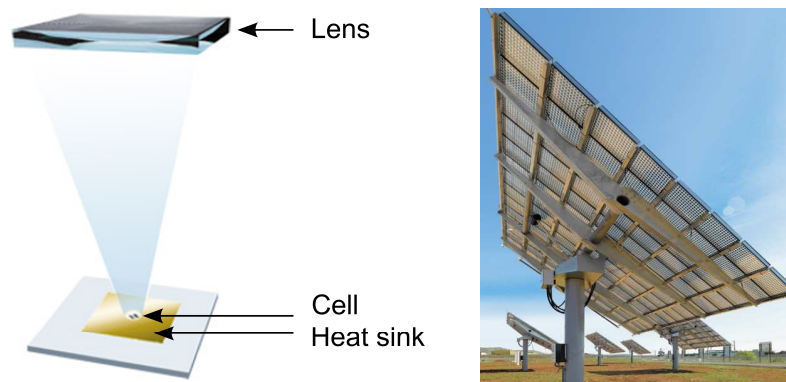


Figure I-6 : (left) Concentrating photovoltaic unit system: a lens which concentrates light on a small concentrator cell. The cell is mounted on a copper substrate to enable better heat evacuation (Reproduction from Soitec website). (right) Complete system with array of unit system of a tracker. Reproduced from Concentrix.

The term concentrating photovoltaics refers to photovoltaic systems coupling an optical system that concentrates light onto solar cells (Figure I-6). Traditionally there are two categories of concentrating photovoltaics: low or high concentration systems [28]. Low concentration systems provide concentration ratios of less than $\times 10$, i.e. the light intensity incident on the cell is inferior to ten times the light intensity incident on the optical system. High concentration systems concentrate between $\times 300$ up to more than $\times 1000$. The concentrating optics used to date are mainly Fresnel lenses and mirrors [29], [30]. In order to focus light at a given point, where the cell is mounted, throughout the day the systems need to track the sun. The complexity of the tracking system highly depends on the optical system requirements. For low concentrating systems, one axis tracking is sufficient. However for high concentration the acceptance angle is of the order of 1° , thus precise two axes tracking is necessary. As a consequence high concentration systems employ very efficient multi-junction solar cells, based on crystalline III-V materials, developed for space applications. The efficiency of the solar cell is critical to justify the use of precise, and thus expensive, optical and tracking systems.

The advantages of a concentrating system is to diminish the consumption of solar cell materials, as the solar cell covers only a fraction of a module surface, roughly equal to the inverse of the concentration ratio. This is interesting if the solar cells are very expensive, as is the case for III-V multi-junction cells. The other advantage is to increase the solar cell efficiency. Indeed the efficiency of a solar cell increases with the logarithm of the concentration ratio (See Chapter II), provided that resistances are negligible. The drawback is the need for an optical and a tracking system, which increases the costs. In addition these systems only use the direct part of the incident sunlight. Thus they can be efficiently implemented only in the regions with high DNI, such as deserts.

III-V multi-junction solar cells are grown on germanium or gallium arsenide substrates, the availability of which are limited. Several multi-junction solar cells also contain indium in the absorber materials, which resource is scarce [31]. Lift-off processes to reuse wafers and high concentration levels may be sufficient to attain a production capacity of multi-terawatt per year.

3.4. Other photovoltaic systems

The purpose of this introduction is not to give an exhaustive overview of existing photovoltaic technologies, but highlight the trends and requirements of photovoltaics to understand the point of view adopted in this study. Apart from c-Si and thin film technologies mentioned above, organic and dye-sensitized solar cells are developed, but still have efficiency and long-term stability issues. However one should note the great increase in performance of organic solar cells in the past years, coming from efficiencies below 5% in the early 2000s up to more than 10% today [22].

3.5. Synthesis and conclusion

In summary, we can conclude that several factors are important to develop photovoltaic technologies in the future energy market. High throughput is essential for large scale development, material consumption should be lowered to avoid shortages and reduce material costs, and efficiencies have to be high to ensure low prices for the overall systems.

4. Our study: concentrator thin film photovoltaics

The idea of this thesis is to use thin film solar cells under concentrated sunlight. With concentration, the material consumption can be dramatically reduced. If a concentration ratio of $\times 50$, or above, can be reached, the raw material economy would be superior to thinning Cu(In,Ga)Se₂ absorber layer from the current 2 μm to 40 nm thickness, which is far more substantial than the most optimistic studies about ultrathin solar cells [32], [33]. With a concentrating system the risk of material shortages, or sharp increase in material cost, is reduced, and maximum yearly production capacity

can be multiplied. Moreover concentration is a regime in which the conversion efficiency of solar cell increases. Thus concentrator thin film modules can give thin films the opportunity to bridge the efficiency gap with conventional c-Si technology.

The idea of using thin films instead of conventional III-V epitaxial solar cells is based on the necessity of easy and fast deposition process and thus high throughput. Current concentrator solar cells require pick-and-place assembly [34], [35] to transfer the solar cells from the wafer to their host heat sinks. With thin films, monolithic assembly seems possible and rapid fabrication of a concentration module at hand.

The idea of using thin films under concentrated sunlight seems natural, and was already presented in the literature at the beginning of this thesis [36–38]. However in the previous approaches substantial resistive losses in thin film solar cells prevented the use of middle to high concentration ratios. Thus the advantages of concentration in terms of material savings and efficiency gains were limited. Faced to the poor incentives, the research in this field faded away at the beginning of the 2000s. The novelty of the present study is to elaborate a new thin film solar cell architecture that has inherently fewer resistive sources. Thus the access to middle to high concentration for thin films is opened. For a proof-of-concept, this thesis is focused on Cu(In,Ga)Se_2 solar cells. However very general conclusions will be drawn that can impact other thin film technologies, such as CdTe.

5. Memento

This thesis is dedicated to concentrating thin film technology.

This subject was chosen as coupling thin film and concentrating approaches tackles several photovoltaic technologies requirements: high efficiency, high throughput and low material consumption.

These necessities arise directly from the energy challenge we are facing: producing more energy in the coming decades while diminishing our production of greenhouse gases.

CHAPTER II. PHYSICS OF CU(IN,Ga)SE₂ DEVICES

1. Introduction	38
2. Description of Cu(In,Ga)Se₂ solar cell architecture and deposition techniques.	38
2.1. The structure of a Cu(In,Ga)Se ₂ solar cell	38
2.2. Molybdenum	39
2.3. CdS or alternative buffers.....	45
2.4. ZnO	45
2.5. Conclusions.....	45
3. The Mo/Cu(In,Ga)Se₂/CdS/ZnO heterojunction	46
3.1. Model of an heterojunction	46
3.2. Description of the Cu(In,Ga)Se ₂ heterojunction : different models	47
4. Current-voltage characteristic of a Cu(In,Ga)Se₂ solar cell	51
4.1. Current-voltage curve of an ideal p-n junction	51
4.2. Non idealities, loss sources	52
4.3. Recombination mechanisms	53
4.4. Voltage dependence of photocurrent.....	57
4.5. Concentration on Cu(In,Ga)Se ₂	59
5. Conclusion	61
6. Memento	62

1. Introduction

The Cu(In,Ga)Se_2 solar cells are the product of a long development. In 1975, the Bell laboratory demonstrated a 12% efficient $\text{CuInSe}_2 / \text{CdS}$ solar cell, with CdS evaporated on a single crystal [39]. From then on different breakthroughs enable to reach efficiencies above 20% [25]. A chemical bath deposition for the CdS layer was developed. The control of composition was improved by the introduction of separate sources for Cu, In and Se. Bandgap engineering with the addition of Ga was introduced. The role of sodium, coming from soda-lime glass substrate was discovered. Ingenious deposition process, the three-stage process, was developed to vary stoichiometry and composition profile at will.

In this chapter we will describe in details the Cu(In,Ga)Se_2 fabrication process, material properties and device physics.

2. Description of Cu(In,Ga)Se_2 solar cell architecture and deposition techniques.

2.1. The structure of a Cu(In,Ga)Se_2 solar cell

A Cu(In,Ga)Se_2 solar cell is made of several semiconducting layers (Figure II-1). First a molybdenum back contact is deposited on a substrate, most often soda-lime glass, but that can be replaced by polyimide [19] or stainless steel [40]. Then a p-type Cu(In,Ga)Se_2 layer is deposited. At the Mo/Cu(In,Ga)Se_2 interface a thin MoSe_2 interlayer forms. The heterojunction is formed by the deposition of a n-type CdS buffer layer. An intrinsic ZnO layer is then deposited as a buffer. A window Al-doped ZnO layer is sputtered to complete the device. In order to minimize front surface reflection, an MgF_2 antireflection coating can be deposited.

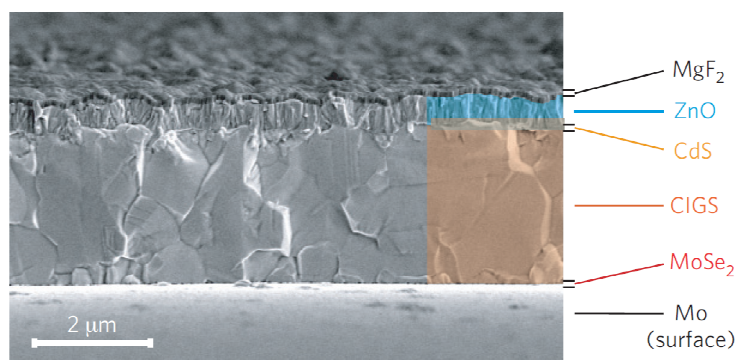


Figure II-1: Scanning electron microscope image of the cross section of a coevaporated Cu(In,Ga)Se_2 solar cell with antireflection coating. Image extracted from ref [19].

We will now briefly review the characteristics of the components of Cu(In,Ga)Se_2 solar cells. This is not an exhaustive presentation, and the interested reader is invited to refer to the different papers cited hereafter.

2.2. Molybdenum

Cu(In,Ga)Se_2 solar cells are mainly grown on molybdenum coated substrates. Mo is sputtered on soda-lime glass or flexible substrates (polyimide or stainless steel)[41–43]. The intensive usage of Mo as a back contact, compared to other alternatives [44], [45], is due to the in-situ formation at the Mo/ Cu(In,Ga)Se_2 interface of a MoSe_2 layer that favors ohmic contact [46–48]. Mo deposition is also crucial to control the incorporation of sodium, diffusing from soda-lime glass, to the absorber [49]. Sodium is an important element that diffuses to the grain boundaries, catalyzes oxygenation and passivation of Se vacancies [50], favors the formation of MoSe_2 [47] and plays a role in the growth of Cu(In,Ga)Se_2 .

2.2.1. *Description of the chalcopyrite Cu(In,Ga)Se_2*

Cu(In,Ga)Se_2 is a quaternary I-III-VI compound. It can be seen as the alloying of CuInSe_2 and CuGaSe_2 that have the tetragonal chalcopyrite structure. The chalcopyrite structure is derived from the cubic zincblende, with Se atoms in a face-centered cubic structure and Cu and In (or Ga) atoms occupying half of the tetrahedral holes. A Cu(In,Ga)Se_2 absorber is not composed of a perfect quaternary compound but most often contains ternary or binary compounds, such as In_2Se_3 or Cu_2Se . For more details on the crystallography of Cu(In,Ga)Se_2 the reader is advised to report to reference [51].

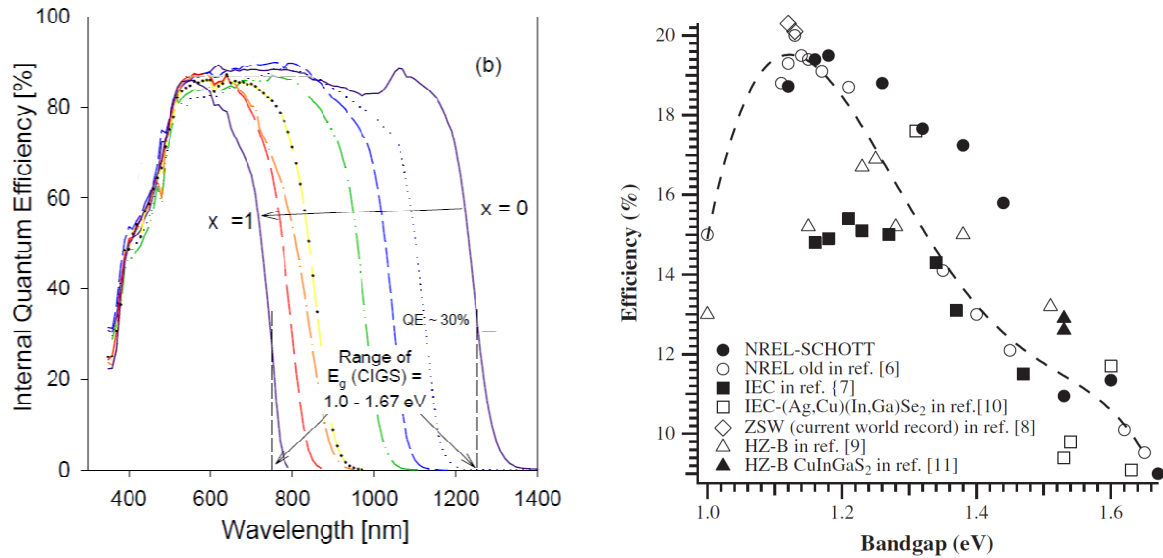


Figure II-2 : (left) Internal quantum efficiency as a function of wavelength for Cu(In,Ga)Se₂ solar with absorber having different Ga contents. The increase in bandgap with Ga content is clearly visible. Reproduced from [52].(right) Efficiency vs bandgap for Cu(In,Ga)Se₂ solar cells. Reproduced from [53].

CuInSe₂ has a bandgap of 1.02 eV and CuGaSe₂ 1.68 eV [51]. By varying the stoichiometry of the CuIn_{1-x}Ga_xSe₂ compound, i.e. adjusting $x = \text{Ga}/(\text{In}+\text{Ga})$, the bandgap can be engineered (Figure II-2). The bandgap dependence on x is of the form $E_g(x) = 1.02 + 0.67x + 0.11x(x - 1)$ [54], but differences between samples can occur and this formula has to be adjusted. The most efficient devices have a Ga content around 0.2 – 0.3 and thus bandgap energy around 1.1 – 1.2 eV [25], [53], [55].

Table II-1 : Electronic parameters of deep traps in Cu(In,Ga)Se₂. Table is reproduced from ref [56].

Electrical activity	$E_c - E_t$ (eV)	Hole capture cross section (cm ²)	Electron capture cross section (cm ²)	Assignment	Theory [57]
Donor	0.19		6×10^{-17}	$(\text{In}_{\text{Cu}} + \text{V}_{\text{Cu}})^+$	$E_c - 0.2$ eV
Donor	0.26		4×10^{-16}	In_{Cu}^+	$E_c - 0.26$ eV
Donor	0.34		4×10^{-15}	$\text{In}_{\text{Cu}}^{2+}$	$E_c - 0.34$ eV
Donor	0.47	$< 10^{-18}$	5×10^{-16}	O_{Se}	
Donor	> 0.6	5×10^{-14}	$> 5 \times 10^{-14}$	V_{Se}^0	

Cu(In,Ga)Se₂ presents a p-type conduction. The doping level of Cu(In,Ga)Se₂ is around 10^{16} cm⁻³ [58]. The shallow acceptor V_{Cu}^- is assumed to be the principal dopant, as calculated by *ab-initio* [57], but In_{Cu} antisite is a donor impurity that compensates Cu(In,Ga)Se₂. It was calculated that several neutral defect complexes exhibit low formation enthalpies, and in particular $(2\text{V}_{\text{Cu}} + \text{In}_{\text{Cu}})$ that has an enthalpy close to 0 or even negative. This is beneficial to Cu(In,Ga)Se₂ as it limits two defects, V_{Cu} and In_{Cu} , in the bandgap region. Off-stoichiometry can thus be accommodated without formation of high

amounts of electronic states in the bandgap that would be harmful for the device performance. However several donor deep defects that compensate Cu(In,Ga)Se_2 have been reported (See Table II-1). These defects are mainly studied by admittance or modulated photocurrent spectroscopies. Despite intensive study their position and exact origin in the Cu(In,Ga)Se_2 layer are still under debate [56], [59–61].

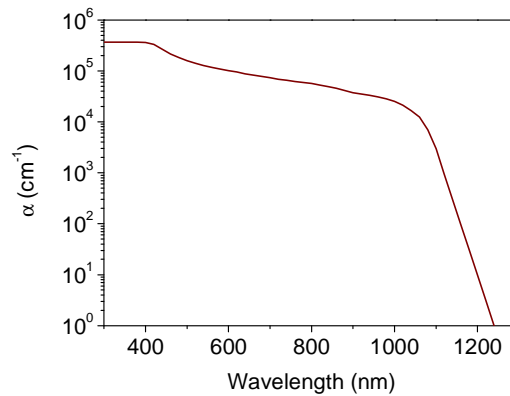


Figure II-3 : Absorption coefficient of Cu(In,Ga)Se_2 absorber of bandgap 1.15 eV according to [62]

Cu(In,Ga)Se_2 is a direct semiconductor thus the absorption coefficient is high for visible wavelengths (Figure II-3), as confirmed by spectrophotometry or ellipsometry measurements.

2.2.2. Cu(In,Ga)Se_2 grain boundaries

Solar cells are usually made of polycrystalline Cu(In,Ga)Se_2 absorbers. The typical grain size is around 0.5 - 1 μm [63]. Surprisingly the devices do not suffer from the polycrystalline character of the absorber, as polycrystalline devices are more efficient than crystalline ones [64]. There are numerous studies on the Cu(In,Ga)Se_2 grain boundaries that can be controversial, showing at least variations between samples. Independent on the composition of the film, it has been found that grain boundaries are both twin boundaries (no dangling bonds or strain), which is a favorable situation, and nontwin, "random", grain boundaries [63], [65]. The effective grain boundary recombination velocity is smaller than 10^3 cm/s at twin boundaries in highly efficient devices [66], [67]. Nontwin boundaries have higher recombination velocities, around 10^4 cm/s, which is the sign of higher density of defects [65], [68] or higher capture cross section. The low recombination velocity in twin boundaries can stem from low defect density, passivation and/or appropriate band diagram. Cu(In,Ga)Se_2 grain boundaries present a low band bending (< 200 mV), or even no bending [69], which reflects a low concentration of charged defects. Oxygenation passivates defects at grain boundaries, such as positive charges due to selenium vacancies [70], [71]. Thus post-deposition annealing can be desirable. It was shown that the presence of sodium, which diffuses from soda-lime

glass or is purposely introduced, catalyzes the oxidation of selenium vacancies [50]. It was also proposed that the twin grain boundaries present negative valence band offsets. This originates from the Cu-poor composition of twin grain boundaries [40], [72], due to Cu vacancies and In_{Cu} antisites. This valence band offset prevents holes from recombining at grain boundaries. The Cu-poor composition of grain boundaries may be due to the diffusion of Cd during chemical bath deposition and consequent Cu outdiffusion that would also lead to a strong n-type doping of the grain boundaries and thus provoke inversion. For random grain boundaries Cu depletion is not systematic, but an anticorrelation between Cu and In contents is seen [65]. Due to the negative band bending or even inversion of grain boundaries, it was proposed that Cu(In,Ga)Se₂ polycrystalline solar cells are a self-assembled nanostructured radial junction solar cell, which explains the excellent collection efficiency [69]. In this respect, the multi-stage deposition process is particularly favorable (see paragraph 2.2.4), as it leads to grain boundaries with more voids than single step preparations, due to the coalescence of Cu vacancies during the Cu diffusion between Cu-poor and Cu-rich phases. These voids help CdS to cover grain boundaries deep in the absorber (up to 500 nm under the free surface), and enhances the radial junction behavior [69].

2.2.3. *Cu(In,Ga)Se₂ free surface*

The free surface of Cu(In,Ga)Se₂ presents similarities with grain boundary surfaces. In Cu-rich Cu(In,Ga)Se₂ films the Fermi level at the surface is nearly merged with the valence band, due to the presence of Cu rich binaries on the surface. For Cu-poor compositions of the absorber, the surface presents a type-inversion, with the Fermi level closer to the conduction band than to the valence band (and the $E_f - E_v$ difference can be as large as 1.1 eV). The surface composition of Cu-poor absorbers suggests the presence of an ordered defect compound (ODC), i.e. a Cu(In,Ga)₃Se₅ phase. This compound has a higher bandgap than the bulk material (the bandgap of CuIn₃Se₅ is 1.23 eV and that of CuGa₃Se₅ is 1.8 eV) and tends to exhibit n-type conduction. However the doping of the ODC is too shallow to be the source of a buried homojunction. It is more likely that defects such as Se vacancies and In_{Cu} or Ga_{Cu} antisites at the free surface that can provide more than 10¹⁴ charges/cm² are the cause of the type-inversion [71]. It seems that the presence of such surface defects is thermodynamically favorable for the formation of the ODC, explaining their simultaneous presence on numerous samples [51]. The defects on the free surface of Cu(In,Ga)Se₂ can be passivated by oxygenation and sodium, as for grain boundaries [71].

2.2.4. *State of the art deposition method : co-evaporation*

The record Cu(In,Ga)Se₂ devices have absorbers that are made by three-stage co-evaporation [25], [55]. This is the state-of-the-art deposition technique at the laboratory scale, first introduced in 1994

[73] as an evolution from previous “Boeing” two-stage process [74]. In the industry slightly simpler deposition routines are followed [75], [76]. Co-evaporation is a physical vapor deposition technique, where Cu, In, Ga and Se are evaporated in a high vacuum chamber from elemental sources onto a heated substrate (Figure II-4). The deposition begins with the formation of $(\text{In,Ga})_2\text{Se}_3$. Then Cu is evaporated until a copper-rich compound is reached. The temperature of the substrate has to be brought to 500°C-600°C during this phase to enable a good crystallization with formation of large grains. A liquid Cu_xSe phase mediates mass transport and thus promotes grain growth. The formation of the stoichiometric $\text{Cu}(\text{In,Ga})\text{Se}_2$ compound can be detected by changes in thermal emissivity, and thus thermal power needed to maintain the substrate at high temperature. In order to avoid the formation of the highly conductive Cu_xSe binaries on the surface, a third stage is added where In and Ga are evaporated in the presence of Se overpressure. Se overpressure is favorable during the whole absorber growth in order to prevent the formation of selenium vacancies, which are active electronic defects [77]. The three-stage process naturally leads to a slightly Ga-rich compound near the back substrate and front surface. This Ga gradient is due to the low mobility of Ga compared to In and Cu, which prevents Ga from outdiffusing from the bottom copper poor phase to the surface copper rich phase during phase II [78], [79]. This gradient naturally creates a front and back surface field that are favorable for the device electronic properties and will be discussed in paragraph 3.2. Figure II-4 displays schematically the sequences of the three stage process with indications on metal fluxes and substrate temperature.

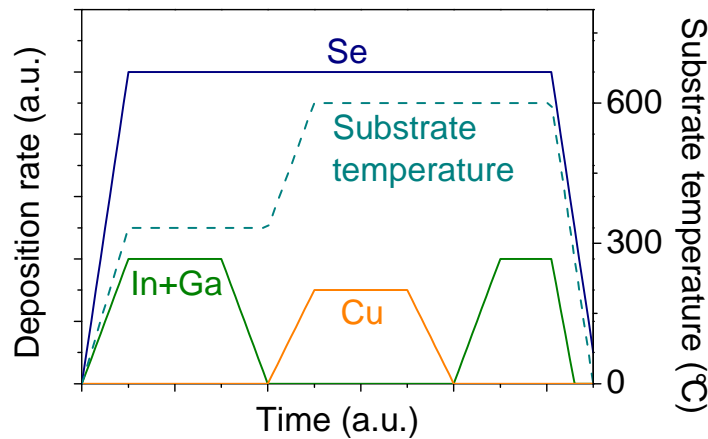


Figure II-4 : Sketch of the three-stage process. Values are given for information.

The three-stage process is a stationary process that is difficult to control, and thus a modified in-line process is usually preferred at the industrial scale. The substrate is moving through deposition

chambers and is subjected to elemental fluxes of various compositions, basically Cu-rich in a first part and then Cu-poor at the end of the growth [75]. Thus a Ga gradient is also seen in industrial samples.

2.2.5. *Other deposition methods*

If co-evaporation is the state-of-the-art deposition technique for high efficiency devices, other techniques are in development at the laboratory as well as at the industrial scale. First, another physical vapor deposition, sputtering, can be used to deposit a stack of metallic layers that is then thermally annealed in a sulfur and/or selenium atmosphere. This method is used at the industrial scale by Solar Frontier, Avancis and Sulfurcell [76]. Reactive sputtering, with direct deposition of a Cu(In,Ga)Se₂ compound is possible as well. Non vacuum methods are also developed [80]. The stack of metallic layers of In, Ga and Cu can be deposited by electro-deposition, preferably on a conductive stainless steel substrate, such as for Nexcis or Solopower. Inkjet printing approaches of Cu(In,Ga)Se₂ nano-particles inks are also developed by Nanosolar for example. Pure solution deposition also lead to high efficiency devices [81]. Table II-2 sums up the different industrial processes and corresponding conversion efficiencies.

Table II-2 : Overview of the efficiencies of different Cu(In,Ga)Se₂ fabrication processes in laboratory and industry. Cell and submodules differ from module due to the smaller area. In the absence of indication the efficiencies are given as total module efficiency. If the abbreviation AA is used, the efficiencies are relative to the module aperture area, if the sign (?) is present, the efficiency claim did not precise total or aperture area efficiency.

Company / Laboratory	Deposition method	Record cell	Record module	Reference
Flisom	Co-evaporation	18.7% (flexible)		[82]
NREL	Co-evaporation	19.9%		[55]
Solibro	Co-evaporation	17.4% (AA) (16 cm ²)	13.4% (14.7 % (AA))	[83–85]
Würth Solar/Manz	Co-evaporation		15.1% (AA)	[86]
ZSW	Co-evaporation	20.3%		[25]
Nexcis	Electrodeposition	14.9%	11.8%	[87]
SoloPower	Electrodeposition	13.8%	13.4% (AA) flexible	[20], [88]
Nanosolar	Inkjet printing	17.1% (AA)		[26]
Avancis	Sputtering	15.8% (AA) (30×30 cm ²)	12.6% (14.2% AA)	[89], [90]
Heliovolt	Sputtering	14% (?) 11.7% (?) (30×30 cm ²)		[91]
MiaSolé	Sputtering		15.7% (AA) 15.5 (AA) flexible	[92]
Solar Frontier	Sputtering	17.8% (AA) (30×30 cm ²)	13.4% (14.5% AA)	[93]
Sulfurcell	Sputtering		13.1% (AA)	[94]

2.3. CdS or alternative buffers

On the surface of Cu(In,Ga)Se₂ a buffer layer is deposited. The standard technique is the chemical bath deposition of CdS. This method is a non-vacuum process that exploits the precipitation of a CdS layer of controlled composition on a substrate [95], [96]. Due to the toxicity of cadmium, and the relatively low bandgap of CdS (2.4 eV) that causes optical losses [97], other buffers are very promising and are introduced in industrial processes, such as ZnS (3.6 eV). Chemical bath deposition is a non-vacuum method. It has the advantage to be relatively low cost but requires Cu(In,Ga)Se₂ substrates, fabricated by sputtering or co-evaporation, to break the high vacuum chain between absorber and window layer depositions. Thus other approaches aim at developing high efficiency vacuum depositions of buffer layers [98].

The electrical role of the buffer is complex and not yet completely understood [99], but the passivation and cleaning of the absorber surface by chemical bath deposition, the chemical intermixing at the interface [100] and its protecting role on the absorber surface during the sputtering of the window layer are often highlighted. Cd is also a dopant in Cu(In,Ga)Se₂, and chemical bath deposition may help the outdiffusion of Cu from the surface and grain boundaries, and the diffusion of Cd in the formed Cu vacancies, which helps type-inversion of the surface and grain boundaries [69] (see paragraph 2.2.2).

2.4. ZnO

In order to complete the device, ZnO window layers are deposited by magnetron sputtering. The window layer should be transparent to sunlight and have a good conductivity to minimize resistive losses. The ZnO deposition is done in two steps. First a thin layer of intrinsic ZnO is deposited (50 nm), which role is mainly to prevent shunts due to its high resistivity [101–103]. Then a conductive aluminum doped ZnO is sputtered (200-400 nm), to act as the window layer. Optimization of Al-doped ZnO comes from the balance between high electrical conductivity and high optical transmittance [104].

2.5. Conclusions

Growth of a complete Cu(In,Ga)Se₂ device is complex. We presented here the main aspects that will be relevant in our study, however this overview is brief and eludes certain important material properties issues. The interested reader is invited to refer to the different papers cited in this chapter.

We will now discuss in detail the electronic properties of Cu(In,Ga)Se₂ devices in the next paragraph. This presentation aims at giving a detailed overview of the current description of Cu(In,Ga)Se₂ devices, in terms of electric characteristics.

3. The Mo/Cu(In,Ga)Se₂/CdS/ZnO heterojunction

3.1. Model of an heterojunction

The Mo/Cu(In,Ga)Se₂/CdS/ZnO solar cell is a heterojunction, i.e. a junction between semiconductors of different bandgaps. The model for an ideal heterojunction has been developed by Anderson [105], which extends the p-n homojunction model to a defect-free abrupt heterojunction. In this model the valence and conduction band present discontinuities, due to the different bandgaps $\Delta E_g = E_{g2} - E_{g1}$, and different electron affinities χ (Figure II-5). The conduction band discontinuity ΔE_c is fixed by the difference of electron affinity of the two materials. $\Delta E_c = E_{c2} - E_{c1} = |\chi_2 - \chi_1|$, where the subscript 1 refers to small bandgap material and 2 to the large bandgap material. The valence band offset $\Delta E_v = E_{v1} - E_{v2}$, is a function of ΔE_c and the difference of bandgap energies : $\Delta E_v = \Delta E_g - \Delta E_c$. As a convention we speak of positive or negative band offsets. A band offset is positive when carriers have to spend energy to cross it from the small to the large bandgap semiconductor.

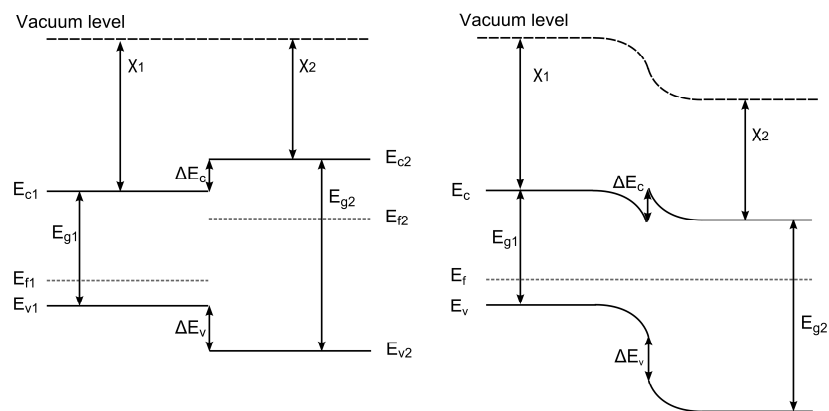


Figure II-5 : Energy band diagram in the Anderson model. (left) semiconductor seen independently before formation of the junction. (right) after the formation of the junction.

For real devices however, the assumption of a defect-free interface is no longer valid (Figure II-6). Interface states, caused by impurity atoms for instance, can add additional charges at the interface and thus modify the potential distribution. The charge created at the interface depends on the density of traps and position of the Fermi level, which determines if an interface state is charged or not. Positive (negative) charges at the interface have an effect similar to a higher doping concentration of the n-type (p-type) semiconductor layer. The influence of the interface states is high

when the charge density (cm^{-2}) becomes comparable to the semiconductor charge per area (ratio of doping density (cm^{-3}) to the respective depletion width). If the interface defects have a sufficient concentration, the Fermi level at the interface can be pinned and the semiconductor type can change at the interface.

Dipoles can also form at the heterointerface due to the reconstruction of the surfaces. The introduction of a dipole results in a voltage change between the two sides of the junction $\Delta\phi = \sigma d/\epsilon$, where the analogy with a capacitor is done, with σ the charge stored, d the distance between charged layers and ϵ the dielectric constant. It should be noted that the determination of this dielectric constant is complex. The energy difference induced by the dipole $\Delta D = q\Delta\phi$ adds to ΔE_c and subtracts to ΔE_v , or vice-versa depending on its orientation [106]. Screening dipoles are also systematically created due to the discontinuity of the dielectric constant at the heterojunction [107]. A plane of charged interface states can form at the heterointerface. If a plane of opposite charge is created in the vicinity, a dipole is formed. Dipoles can also be created by molecules at the interface. Due to the presence of interface states or dipoles the vacuum level can present discontinuities.

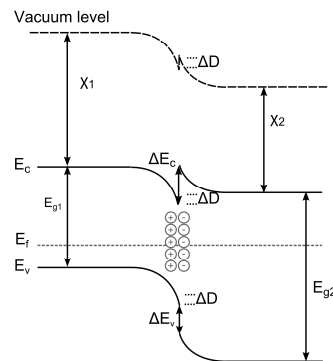


Figure II-6 : Heterojunction in presence of a dipole layer.

3.2. Description of the Cu(In,Ga)Se₂ heterojunction : different models

The Cu(In,Ga)Se₂ solar cell is a heterojunction. Determining the band diagram is not an easy task, and depends on the material properties and specific deposition processes. We will give a standard description of the cell and discuss the most interesting variants.

3.2.1. General band diagram (SCAPS)

A general description of the Cu(In,Ga)Se₂ solar cell band diagram can be calculated with SCAPS software [108] and the material parameters given in reference [58]. Figure II-7 shows the energy

band diagram in the dark under zero applied voltage. The absorber presents a bandgap gradient, from 1.34 eV at the back contact to 1.08 eV at the front contact (See paragraph 3.2.4).

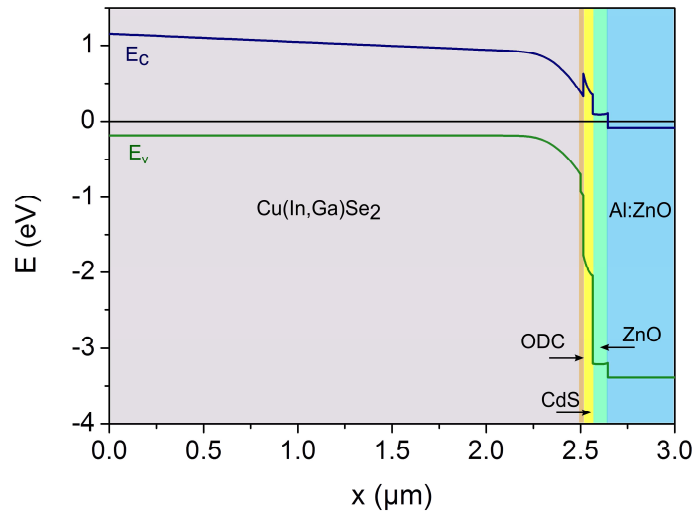


Figure II-7 : Energy band diagram of the Cu(In,Ga)Se₂ solar cell according to reference [58] at zero applied voltage in the dark. Cu(In,Ga)Se₂ bandgap shows a gradient from 1.34 eV at the back contact to 1.08 eV at the front contact. An ordered defect compound layer is included at the absorber surface.

3.2.2. *Cu(In,Ga)Se₂ absorber*

The Cu(In,Ga)Se₂ absorber can be separated in two regions : majority charge carrier depleted space-charge region and quasi neutral region. In the space-charge region the electric field due to the heterojunction is high, the conduction and valence bands are bent, and minority carriers drift towards the interface. In the quasi neutral region the carriers are subjected to diffusion. Depending on the doping level of the absorber and window layer, the width of the space-charge region varies but is usually of the order of 500 nm at zero applied voltage [109].

3.2.3. *CdS/Cu(In,Ga)Se₂ interface*

The interface between CdS and Cu(In,Ga)Se₂ is crucial for the device performance. The physics of this interface is intricate, and we will shed light on the principal mechanisms at stake.

The heterointerface is never defect free, due to lattice mismatch between Cu(In,Ga)Se₂ and CdS for example. These defects can be centers of recombination. According to the Shockley-Read-Hall model, if we note E_d the energy level of the defects, we can define the recombination rate as [110]:

$$U = S_p S_n \frac{n^{IF} p_a^{IF} - n_i^2}{S_n (n^{IF} + n_1) + S_p (p_a^{IF} + p_1)} \quad (\text{II-1})$$

Where $n_1 = N_c \exp(-(E_c - E_d)/kT)$, $p_1 = N_v \exp(-(E_d - E_v)/kT)$, with N_c and N_v the effective density of states in the conduction and valence band, n^{IF} the density of electrons at the interface and p_a^{IF} the density of holes at the interface, on the absorber side, S_p and S_n the recombination velocity for holes and electrons. The subscript of n^{IF} depend of the dominant recombination path : straight recombination between electrons and holes of the absorber, or cross-recombination if electrons from the window recombine with holes in the absorber. In the case where the density of defects at the interface N_d is substantial, the electron density at the interface (in the absorber or the buffer) is higher than the hole concentration, such that $n^{IF}/S_p \gg p_a^{IF}/S_n$, and the defect level is deep (near midgap), then $n^{IF}/S_p \gg n_1/S_p$ and $\gg p_1/S_n$, equation (II-1) becomes [111] :

$$U \approx S_p p_a^{IF} \quad (II-2)$$

Thus the recombination at the Cu(In,Ga)Se₂/CdS interface is controlled by the hole concentration p_a^{IF} . Designs that tend to decrease p_a^{IF} are thus beneficial for the device performance as they will reduce interface recombination.

When the concentration of interface states N_d is sufficiently large, the Fermi level at the interface can be pinned. The distance between the Cu(In,Ga)Se₂ conduction band and the Fermi level at the interface ΔE_{Fn} is equal to [71] :

$$\Delta E_{Fn} = \frac{\Delta\chi - \frac{qN_d d_b^2}{2\varepsilon_b} + \frac{qN_d d_b}{\varepsilon_b} (E_{g,a} - \phi_n) + \frac{qN_{A,a} d_b w_a}{\varepsilon_b}}{1 + \frac{qN_d d_b}{\varepsilon_b}} \quad (II-3)$$

where $\Delta\chi = \Delta E_C^{wb} - \Delta E_C$ and ΔE_C^{wb} is the conduction band offset between the window (subscript or superscript w) layer and buffer (subscript or superscript b), and ΔE_C is the conduction band offset between the absorber (subscript or superscript a) and the buffer. ε is the dielectric constant, $E_{g,a}$ the absorber bandgap, ϕ_n the neutrality level of the interface states with respect to the valence band edge, d_b the thickness of the buffer layer, that is supposed to be completely depleted, $N_{A,a}$ the doping level of the absorber and w_a the width of the space charge region in the absorber. It was calculated that for interface states concentration N_d superior to $10^{13} \text{ cm}^{-2} \text{ eV}^{-1}$, the Fermi level can be pinned, so that $\Delta E_{Fn} = E_{g,a} - \phi_n$ (doping levels of CdS and Cu(In,Ga)Se₂ are set to 10^{16} cm^{-3}). As a consequence of Fermi level pinning, the surface of the absorber can be inverted, and a buried homojunction is created. This homojunction is desirable as it makes electrons become majority carriers at the interface, i.e. decreases the density of holes at the interface, and thus interface recombination (equation (II-2)).

Depending on the bandgap of Cu(In,Ga)Se₂ the conduction band offset ΔE_c between buffer and absorber can be positive or negative (In Figure II-7, the band offset is positive). Positive conduction band offset occurs for bandgaps at the interface smaller than 1.3 eV, and negative conduction band offset for bandgaps higher than 1.3 eV [112]. Positive band offsets are desirable designs as the hole concentration at the interface becomes small, due to the high hole barrier ϕ_b^p (difference between valence band and Fermi level at the interface) (See Figure II-12). For a negative band offset ΔE_c the open-circuit voltage decreases proportionally to $-\Delta E_c$ [51], due to a reduced ϕ_b^p and thus increased recombination velocity at the interface. Thus most efficient cells present a positive conduction band offset at the Cu(In,Ga)Se₂/CdS interface (see Figure II-2).

As discussed in the previous section of this chapter, the surface of Cu(In,Ga)Se₂ can present a composition different from the bulk, forming an ordered defect compound that tends to be Cu-poor. This compound, that presents a high concentration of defects, is often represented by a layer of the same material properties as the bulk but with a positive valence band offset [58]. Thus this layer can improve device efficiency by an increase in the hole barrier.

Cu(In,Ga)Se₂ absorbers often present front bandgap grading. This grading is used to obtain a high open-circuit voltage, combined with a good short-circuit current density. The high open-circuit voltage is due to the decrease in interface (or space-charge region) recombination due to higher bandgap at the Cu(In,Ga)Se₂/CdS interface, and thus higher hole barrier ϕ_b^p . The good short-circuit current density is maintained due to a smaller bandgap region in the absorber. Front grading is thus highly desirable (Figure II-8).

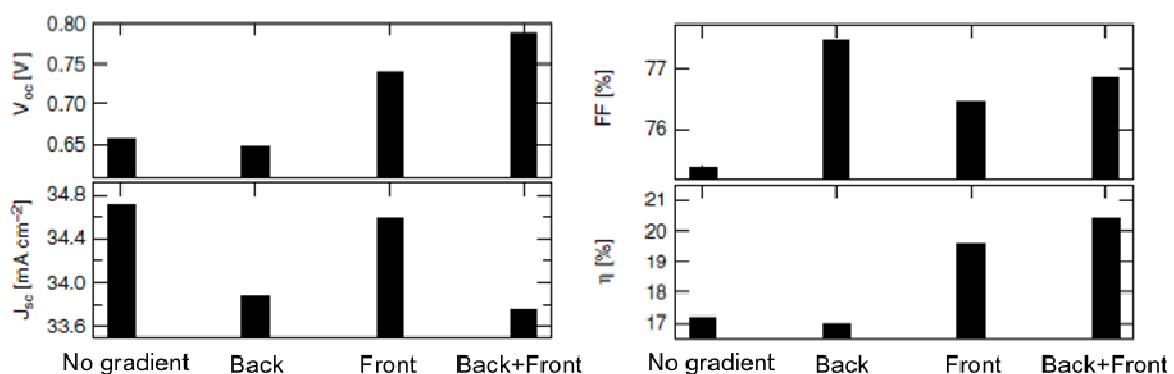


Figure II-8: Effect of back and front surface gradient on solar cell parameters, for an absorber of 500 nm thickness with 0.2 eV of gradient (front surface gradient extends 10 nm from front, back surface gradient extends on 100 nm from back). Data extracted from Figure 3.30 of ref [51]

3.2.4. Back contact

The Cu(In,Ga)Se₂ solar cell also generally features a band gap gradient at the back contact. This gradient is widely used in industrial processes, and is used to help carrier collection in the absorber by repelling electrons from the recombining back contact [19], [113], [114], and thus improve fill factor (Figure II-8). This bandgap grading is especially crucial for the thinnest devices or absorbers with large electron diffusion lengths. However, due to the grading the average bandgap is increased and thus the absorption and short-circuit current are reduced. The total effect on the solar cell performance is thus a balance between increased collection and decreased absorption. The combination of a front and back contact grading (Figure II-8) is the most efficient configuration, often referred to as V-shape. However the bandgap grading has to be controlled in order to avoid the formation of a notch, i.e. difference between minimum and maximum bandgap that is too pronounced (Figure II-9). This situation leads indeed to increased recombination, by the capture of carriers in a potential well [19].

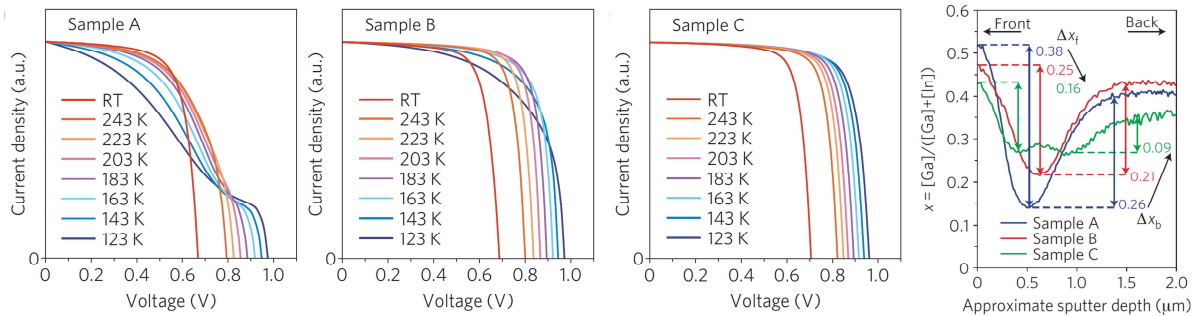


Figure II-9 : Temperature dependent current voltage characteristics of Cu(In,Ga)Se₂ solar cell with different band gap gradings, measured by SIMS and shown on the right graph. All samples present a V-shape gradient that is decreasingly pronounced from sample A to sample C. At lower temperatures, due to the decreased thermal energy of the carriers, a deep gradient notch traps the carriers and decreases collection efficiency. At higher temperature, the effect of the notch is increased recombination, i.e. smaller V_{oc} . Extracted from ref [19].

The back contact is also the location of recombination. Similarly to what we defined for the Cu(In,Ga)Se₂/CdS interface, the back contact can have a high recombination velocity.

4. Current-voltage characteristic of a Cu(In,Ga)Se₂ solar cell

4.1. Current-voltage curve of an ideal p-n junction

The current voltage curve of an ideal cell, where collection efficiency is supposed to be equal to 1 independently of the voltage, can be expressed as $J_{light}(V) = J_{diode}(V) + J_{ph}$. This is the superposition principle. The diode current is also called “dark current”, even if this terminology can be misleading when the shifting approximation is wrong. Indeed if the diode current that is flowing in

the dark is the same as the diode current under illumination, the shifting approximation holds, and $J_{diode}(V)$ is also the dark current. Unfortunately, in Cu(In,Ga)Se₂ solar cells, the diode current depends on illumination and shifting approximation is wrong.

The diode current $J_{diode}(V)$ can be expressed formally in two ways, and is the sum of different recombination currents in a cell. Thus one can choose to express the diode current as the sum of two terms that discriminate between the different recombination mechanisms having fixed ideality factors equal to 1 and 2 : $J_{diode}(V) = -J_{01}(\exp(qV/kT) - 1) - J_{02}(\exp(qV/2kT) - 1)$, where J_{01} and J_{02} are the saturation currents. This model is called the “two-diodes model”. One can also choose to write the diode current as an average term $J_{diode}(V) = -J_0(\exp(qV/AkT) - 1)$, where A is an average ideality factor. This model is referred to as the “one-diode model”.

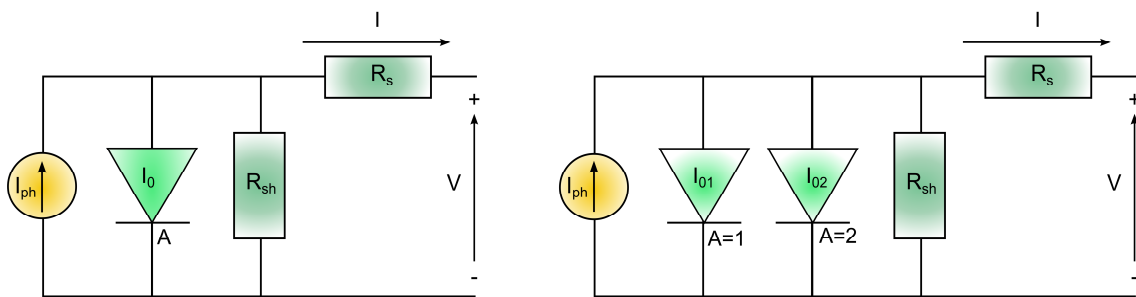


Figure II-10 : Equivalent circuit (left) one-diode model with ideality factor A . (right) two-diodes models associated with two fixed values of the ideality factor $A = 1$ and $A = 2$. Parasitic series and shunt resistance are shown.

In our study we choose the two-diodes model, as the two diode current components, with ideality factor 1 and 2 are visible on our measurements (see Chapter V). For instance these components can stem from quasi neutral region and space-charge region recombination respectively. Thus we obtain:

$$J_{light}(V) = J_{ph} - J_{01} \left(\exp\left(\frac{qV}{kT}\right) - 1 \right) - J_{02} \left(\exp\left(\frac{qV}{2kT}\right) - 1 \right) \quad (II-4)$$

4.2. Non idealities, loss sources

In a real solar cell, non idealities arise. First of all, the solar cell is resistive and an ohmic voltage drop has to be taken into account, due to series resistance R_s . Then the cell may present shunts, characterized by a shunt resistance R_{sh} . Finally the photocurrent can be voltage dependent. Thus the general current-voltage curve becomes (Figure II-10):

$$J_{light}(V) = J_{ph,max} \times \eta(V) - J_{01} \left(\exp \left(\frac{q(V + J_{light}R_s)}{kT} \right) - 1 \right) - J_{02} \left(\exp \left(\frac{q(V + J_{light}R_s)}{2kT} \right) - 1 \right) - \frac{(V + J_{light}R_s)}{R_{sh}} \quad (II-5)$$

One can define several important parameters of the cell characteristic (Figure II-11). The open-circuit voltage is the voltage when no current flows, and the short-circuit current is the current when the applied voltage is zero. The fill factor FF is the ratio of the maximum power that can be extracted from the cell P_{max} (area of the green rectangle) to the reference power $I_{sc} \times V_{oc}$ (area of the dotted rectangle), $FF = P_{max} / (I_{sc} \times V_{oc})$. The fill factor is a measure of the squareness of the current-voltage curve. High series resistance, high shunt conductance or high diode current result in poor FF . The conversion efficiency of the cell is defined as the maximum power extracted from the cell to the incident light power, $\eta = P_{max} / P_{light}$. For information, the record Cu(In,Ga)Se₂ solar cell to date has the following parameters : $\eta=20.3\%$, $V_{oc}=740$ mV, $J_{sc}=35.4$ mA/cm², $FF=77.5\%$ [25] (Figure II-11).

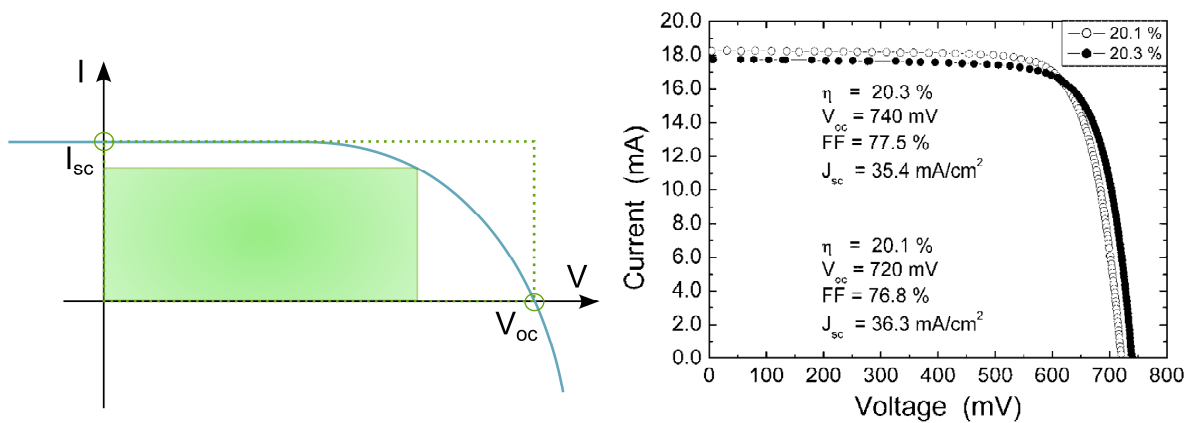


Figure II-11 : (left) Current-voltage characteristic of a solar cell (right) Current-voltage characteristic of state-of-the-art devices [25].

4.3. Recombination mechanisms

In a solar cell, the diode current is due to several recombination mechanisms.

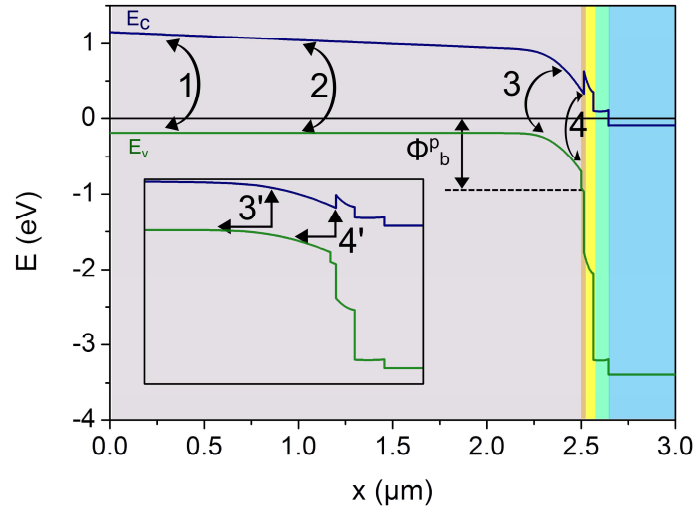


Figure II-12 : Recombination paths : 1 back surface, 2 quasi-neutral region, 3 space-charge region, 4 interface. In the inset we detail the tunneling enhanced space-charge region recombination 3' and the tunneling enhanced interface recombination 4'. Tunneling increases the density of holes that can participate in the recombination. The hole barrier ϕ_b^p at the interface is also depicted.

As stated before there are several recombination paths in a Cu(In,Ga)Se₂ solar cell (Figure II-12). The back contact (1), quasi-neutral region (2), space charge region (3) and Cu(In,Ga)Se₂/CdS absorber interfaces (4) are the principal recombination paths. Due to the high bandgap of the window layers, recombination is neglected there. Tunneling-enhanced space-charge region and interface recombination are also depicted on the inset of Figure II-12. The tunneling of holes can indeed increase both recombination rates.

The two recombination mechanisms that cannot be avoided in a solar cell are radiative recombination and Auger recombination. Radiative recombination is the inverse of optical absorption: the direct recombination of an electron and a hole that emits a photon. The radiative recombination rate is :

$$R_{rad} = B(np - n_i^2) \tag{II-6}$$

where B is the radiative recombination coefficient. This coefficient is of the order of $10^{-10} \text{ cm}^3\text{s}^{-1}$ in Cu(In,Ga)Se₂ solar cell [115]. The product np in the space-charge region or quasi neutral region is equal to $n_i^2 \exp(qV/kT)$, due to the constant separation of quasi-Fermi levels, equal to applied voltage. Thus the diode current corresponding to radiative recombination has a voltage dependence in the term $\exp(qV/kT)$, an ideality factor of 1. The activation energy of the saturation current is equal to the absorber bandgap. More generally the diode ideality factor A can be defined through the voltage dependence of carriers [51] as :

$$(np)^{1/A} = n_i^{2/A} \exp(qV/AkT) = (N_c N_v)^{2/A} \exp(-E_g/AkT) \exp(qV/AkT) \quad (II-7)$$

The saturation current density is then:

$$J_{0A} = J_{00A} \exp(-E_a/AkT) \quad (II-8)$$

with J_{00A} the reference saturation current density for the ideality factor A , and E_a the activation energy of the saturation current that in this case equals the bandgap energy E_g . In standard Cu(In,Ga)Se₂ the radiative recombination is never limiting.

The Auger recombination is also intrinsic and the corresponding recombination rate is $R_{Auger} = C_p(np^2 - n_0p_0^2) + C_n(pn^2 - p_0n_0^2)$, where C_p (C_n) is the Auger coefficient for the excitation of a hole (electron), by the recombination of a electron-hole pair. The Auger recombination is more important when the carrier concentrations are high, and thus may be substantial under intense illuminations, high forward voltages or high doping levels. Auger coefficients of Cu(In,Ga)Se₂ are unknown. An interpolation from Auger coefficients of direct bandgap III-V semiconductors as a function of bandgap [116] gives values of Auger recombination coefficient of Cu(In,Ga)Se₂ (1.1-1.2 eV) around $10^{-30} \text{ cm}^6 \text{ s}^{-1}$. Thus this mechanism is negligible in standard operation conditions. It should be noted that Auger recombination does not follow the formalism of equation (II-8).

The other recombination mechanisms are related to the presence of defects, and may be avoided by an optimum fabrication process. However in Cu(In,Ga)Se₂ solar cells, even state-of-the-art devices are subjected to such recombination. We will review briefly the diode current related to the different recombination paths of Figure II-12. The case of tunneling enhanced recombination is not treated here, and the reader is invited to refer to [51], [117].

Interface

Based on the expression of recombination rate at the interface (equation (II-1)), supposing mid-gap defects, and highly asymmetric junction ($\varepsilon_D N_D \gg \varepsilon_A N_A$) and the absence of Fermi level pinning and tunneling, the saturation current due to interface recombination is [51]:

$$J_{0,IF} = qS_p N_{A,a} \left(\frac{N_{c,w} N_{v,a}}{N_{D,w} N_{A,a}} \right) \exp\left(-\frac{E_g^{IF}}{kT}\right) \text{ for } \Delta E_c < 0 \quad (II-9)$$

$$J_{0,IF} = qS_p N_{A,a} \left(\frac{N_{c,w} N_{v,a}}{N_{D,w} N_{A,a}} \right) \exp\left(-\frac{E_{g,a}}{kT}\right) \text{ for } \Delta E_c > 0$$

It should be noted that in the case of a negative conduction band offset, E_g^{IF} is not the absorber bandgap $E_{g,a}$ but is smaller, $E_g^{IF} = E_{g,a} + \Delta E_c$ [51]. The ideality factor is 1, which is due to the fact that only the hole quasi-Fermi level can vary with applied voltage.

In the case where the Fermi Level at the interface is pinned by interface charges above midgap, and that electrons are majority carriers at the interface, the interface current density becomes [117], [118] :

$$J_{0,IF} = qS_p N_{v,a} \exp\left(-\frac{\phi_b^{p,0}}{kT}\right) \quad (\text{II-10})$$

where $\phi_b^{p,0}$ is the hole barrier at zero applied voltage, defined by the level of Fermi-level pinning, S_p is the hole recombination velocity at the interface, in the case where all interface states are empty of holes. As $\phi_b^{p,0}$ is temperature-independent, it can be assimilated to an activation energy. The diode ideality factor is 1.

Space-charge region

Equation (II-1)(VI-2) is general and describes recombination processes through traps. In the space-charge region with midgap defects, we can obtain the expression of the saturation current as [51]:

$$J_{0,SCR} = \frac{\pi/2 \times kT}{F_m} \left(\frac{N_{c,a} N_{v,a}}{\tau_{n0,a} \tau_{p0,a}}\right)^{1/2} \exp\left(-\frac{E_{g,a}}{2kT}\right) \quad (\text{II-11})$$

where F_m is the electric field at the position of maximum recombination, $\tau_{n0,a}$ and $\tau_{p0,a}$ are electrons and holes minimum lifetimes (lifetime as minority carriers in a semiconductor of the same defect density). The bandgap of the absorber $E_{g,a}$ is the activation energy and the ideality factor is 2. The physical reason behind this ideality factor is that both electron and hole quasi Fermi levels vary with applied voltage.

Quasi neutral region

In the quasi neutral region, the diode current depends on the collection of carriers that governs the minority carrier concentration. To discriminate between back contact and quasi neutral region recombination, we suppose that the absorber thickness is high compared to electron diffusion length. In the case of a deep defect, the saturation current is [51]:

$$J_{0,QNR} = q \frac{n_i^2}{\tau_{n0,a} N_{A,a}} \int_{QNR} \eta_c(z) dz \quad (II-12)$$

where $\eta_c(z)$ is the collection function, i.e. the probability for generated charge carriers to be collected at the contact, which depends on the position z in the cell. The ideality factor is 1. In the case of large applied voltages, the hypothesis of minority carrier is no longer valid and the quasi-Fermi levels of both carriers move symmetrically to the defect level, and thus the ideality factor is expected to increase and reach a value of 2 under high injection.

Back contact

Back contact recombination is a dominant path if the diffusion length of minority carriers is large compared to the quasi neutral region thickness. In this limit case, the saturation current is [51]:

$$J_{0,BC} = q \frac{D_{n,a} n_i^2}{N_{A,a}} \frac{1}{d_{QNR}} \quad (II-13)$$

where d_{QNR} is the width of the quasi-neutral region, and $D_{n,a}$ the diffusion coefficient of electrons in the absorber. This mechanism is scaled with the inverse of the absorber thickness, thus it becomes predominant for thin and ultrathin samples.

We have seen the different diode currents and their dependence on voltage. We shall discuss briefly the dependence on voltage of photocurrents.

4.4. Voltage dependence of photocurrent

In Cu(In,Ga)Se₂ solar cells the photocurrent dependence on applied voltage can be important. The photocurrent is defined as $J_{ph}(V) = -q \int (G(z) - R(z, V)) dz$, with $G(z)$ the light generation rate and $R(z, V)$ the net local recombination rate. $R(z, V)$ is dependent on carrier distribution and thus on the excitation of the cell. It is useful to use the collection function $\eta_c(z, V)$, probability of a photogenerated carrier to be collected at the contact. Thus the photogenerated current is determined by the product of generation and collection function $J_{ph}(V) = -q \int G(z) \eta_c(z, V) dz$.

The collection of carriers and thus photocurrent is voltage dependent. In the absence of interface states and transport barriers, this dependence can be analyzed as follows. The collection efficiency is 1 in the space-charge region (negligible recombination due to high electric field) and within one diffusion length $L_{n,a}$ from the space-charge region edge (with $L_{n,a}$ smaller than the absorber

thickness). The collection efficiency is set to zero elsewhere, and infinite recombination is assumed at the back contact. This model is the well known as the Gärtner model [119].

$$EQE(\lambda, V) = T(\lambda) \left(1 - \frac{\exp(-\alpha_a(\lambda)w_a(V))}{1 + \alpha_a(\lambda)L_{n,a}} \right) \quad (\text{II-14})$$

where EQE is the external quantum efficiency, T is the transmission coefficient to the absorber layer, $\alpha_a(\lambda)$ the absorption coefficient at the incident wavelength λ and $w_a(V)$ the voltage dependent space-charge width in the absorber. The external quantum efficiency is the percentage of incident photons that will result in a collected carrier. $EQE(\lambda, V) = \int G(z) \eta_c(z, V) dz$, and is a Laplace transform of $\eta_c(z, V)$. The voltage dependence of EQE is due to that of the space-charge width, and increases with longer wavelengths. It should be noted that in a Cu(In,Ga)Se₂ solar cell, it is considered that no photocurrent is extracted from the CdS layer and that collection is limited to the absorber alone. This observation, which is coherent with EQE measurements, can be explained by the presence of a buried homojunction in Cu(In,Ga)Se₂ due to surface inversion. This homojunction would significantly lower the electric field in CdS and hinder collection due to strong recombination at the interface [69].

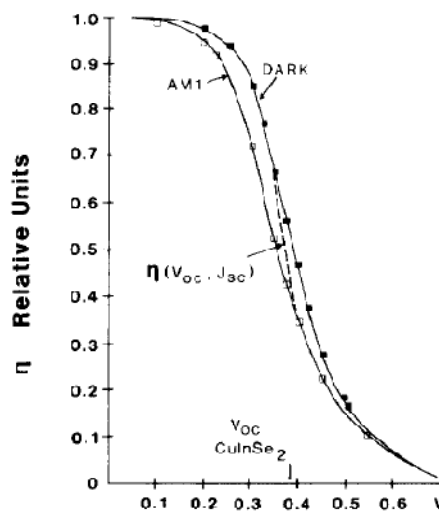


Figure II-13 : Collection function as a function of applied voltage for a CuInSe₂/CdZnS solar cell. Reproduced from [120]

At the Cu(In,Ga)Se₂/CdS interface, photogenerated carriers can recombine through deep defects. Thus the collection efficiency is:

$$\eta_{c,IF}(V) = \mu_{n,b}F / (\mu_{n,b}F + S_p) \quad (\text{II-15})$$

with $\mu_{n,b}$ the electron mobility in the buffer, F the electric field at the interface and S_p the hole recombination velocity at the interface [120]. In early CuInSe₂ solar cells $\eta_{c,IF}$ could not be

considered unity even at low applied voltages, due to highly recombining interface (Figure II-13). For state of the art Cu(In,Ga)Se₂ devices today $\eta_{c,IF}$ is considered close to 1 in most of the voltage range.

Transport barriers can impede the flow of photogenerated carriers. Positive conduction band offsets at the Cu(In,Ga)Se₂/CdS interface is a barrier for example. However the current that can pass this barrier is dependent on $\exp(-\Delta E_c/kT)$, i.e. thermal emission over the barrier, and on the density of electrons at the interface. Thus a high density of electron is favorable and is obtained if the Cu(In,Ga)Se₂ surface is inverted for example. A similar situation arises for a strong front bandgap grading (paragraphs 3.2.3 and 3.2.4).

$\eta_c(z, V)$ is modified by barrier or interface recombination. The maximum photocurrent is always found at reverse bias, but the value of the bias at which maximum photocurrent is obtained varies. Therefore a useful definition of the external collection efficiency is $J_{ph}(V) = J_{ph,max} \eta(V)$, where $\eta(V) = 1$ for a certain reverse bias.

4.5. Concentration on Cu(In,Ga)Se₂

4.5.1. Principle of light concentration onto solar cells

We have seen in the previous chapter that the use of concentrated sunlight can be interesting for solar cells as it reduces the amount of absorbing material necessary to produce a certain electric power.

If the sunlight is concentrated by a factor C , i.e. under C suns illumination also noted $\times C$, then the photocurrent should be $J_{ph} = J_{ph,1 sun} \times C$. If we neglect series and shunt resistances, and consider $\exp(qV_{oc}/kT) \gg 1$, the open-circuit voltage becomes :

$$V_{oc} = \frac{2kT}{q} \ln \left(\frac{-J_{02} + \sqrt{J_{02}^2 + 4J_{01}C \times J_{ph,1 sun}}}{2J_{01}} \right) \quad (II-16)$$

Thus the open-circuit voltage increases with the logarithm of concentration. At low illumination, the diode current of ideality factor 2 dominates and the slope of the $V_{oc} - \ln(J_{ph,1 sun})$ curve is $2kT/q$, then at higher illuminations the diode current of ideality factor 1 dominates and the slope decreases to kT/q . Due to the increased open-circuit voltage, if series resistance and temperature elevation are negligible, the efficiency under concentration increases.

However in real devices the efficiency reaches a maximum due to resistive losses that cannot be neglected when the current density is sufficiently high. This optimum concentration ratio can be calculated analytically in the one-diode formalism, and it can be shown that the maximum in efficiency occurs when $J_{ph}R_s = C \times J_{ph,1}R_s \sim AkT/q$, or $C \times J_{sc,1}R_s \sim AkT/q$, if the collection factor is close to 1 at short-circuit [121]. One can see that the maximum in efficiency occurs at a concentration ratio inversely proportional to the solar cell series resistance. Thus if the series resistance is too high, the maximum efficiency occurs at low concentration ratio and the efficiency increase that can be expected is limited. The optimization of concentrator cells towards the lowest series resistance possible is thus crucial.

4.5.2. Experiments of concentration on Cu(In,Ga)Se₂

Table II-3 : Record Cu(In,Ga)Se₂ solar cell under concentration. (*) The value of J_{sc} under 1 sun is calculated from that at 14 suns.

Concentration	V _{oc} (mV)	J _{sc} (mA/cm ²)	FF (%)	Efficiency (%)
1	647	36.4 (*)	76.3%	17.9%
14	736	510.1	80.5%	21.5%

A few experiments of concentration on Cu(In,Ga)Se₂ solar cells have been conducted [36], [38], [122–124], but maximum efficiencies were obtained at low concentration ($C < 15$). The record Cu(In,Ga)Se₂ solar cell under concentration was fabricated by NREL in 2002, its performance at $\times 1$ and $\times 14$ are given in Table II-3 and Figure II-14. This cell was 0.1cm², with a collecting grid. They claim that the efficiency at 14 suns was not yet limited by series resistance as they found the same efficiency at $\times 50$. The concentration of $\times 14$ is thus probably not the optimum efficiency, which lies between $\times 14$ and $\times 50$. The relatively low optimum concentration ratio is the sign of a series resistance of the order of 0.5 ohm.cm².

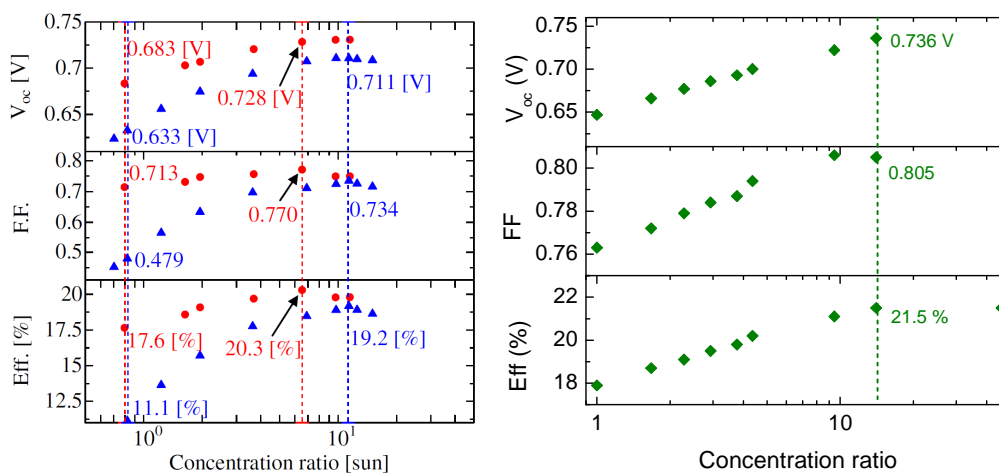


Figure II-14 : (left) Evolution of open circuit voltage, efficiency and fill factor with concentration ratio of a high performance Cu(In,Ga)Se₂ cell (red) and a poor device (blue). Reproduced from [124]. (right) Evolution of efficiency and open-circuit voltage with concentration ratio for the record Cu(In,Ga)Se₂ solar cell (0.1 cm²). Data from [36].

An interesting feature highlighted in the works of [124] and [37], is that devices that behave poorly under low light intensity benefit more from concentration than good devices because of the higher slope of V_{oc} with concentration ratio, and also lower impact of shunt resistance (Figure II-14 left).

5. Conclusion

We have seen how Cu(In,Ga)Se₂ solar cells are fabricated. Due to the quaternary character of the absorber, obtaining a desirable stoichiometry, homogeneity or doping level is difficult. From the variability of the fabricated devices follows a multitude of description models, of which we exposed the main aspects. In particular the Cu(In,Ga)Se₂/CdS interface is of critical importance for both diode current and photocurrent. This interface can be inverted or not, have a conduction band offset that can be either positive or negative, eventually present Fermi level pinning. The role of composition grading, by the adjustment of Ga content of the absorber, was also highlighted.

We have seen, from the classic one-diode or two-diode model formalisms, that sunlight concentration leads to increased open-circuit voltage. Thus efficiency can be increased, as long as series resistance is low enough. For Cu(In,Ga)Se₂ solar cells, the low concentration range was the only explored, as series resistance is too substantial to study concentrations over $\times 100$. The objective of the next chapters will therefore be to design and fabricate Cu(In,Ga)Se₂ solar cells with intrinsically low series resistance.

6. Memento

Cu(In,Ga)Se₂ solar cells are heterojunctions composed of a Mo back contact, Cu(In,Ga)Se₂ absorber, CdS and ZnO buffer layers and ZnO:Al front contact. The Cu(In,Ga)Se₂ absorber is a polycrystalline semiconductor of direct bandgap.

State-of the art Cu(In,Ga)Se₂ absorbers are fabricated by a three-stage co-evaporation process and have front and back composition, and thus bandgap, gradients.

The current in a cell is the sum of photocurrent and dark current and is usually described by a two-diodes model, that in the absence of series resistance or shunt is :

$$J_{light}(V) = J_{ph} - J_{01} \left(\exp \left(\frac{qV}{kT} \right) - 1 \right) - J_{02} \left(\exp \left(\frac{qV}{2kT} \right) - 1 \right)$$

Light concentration leads to higher open-circuit voltage and thus higher conversion efficiency, for series resistance lower than $(AkT)/(qCJ_{sc,1})$, with A the diode ideality factor.

The record conversion efficiency reported in the literature for a Cu(In,Ga)Se₂ solar cell is 21.5% under $\times 14$. Light concentration has the characteristic to be more beneficial for the low performing devices.

CHAPTER III. SCALE EFFECTS OF THIN FILM SOLAR CELLS

1. Introduction	64
2. Scale effects in light emitting diode and photovoltaic devices	64
2.1. State of the art of light emitting diodes of reduced size.....	64
2.2. State of the art of microcells in photovoltaics	67
3. Modeling of sheet resistance problem	70
3.1. Resistive sources in thin film solar cells	70
3.2. Sheet resistance problem in equations.....	73
3.3. Model validation: electroluminescence and I-V fit	81
3.4. Size-dependent prediction of the behavior of solar cells under concentration.	85
3.5. Discussion	88
4. Thermal analysis of microcells	89
4.1. Necessity to study thermal behavior of solar cells.....	89
4.2. Thermal scale effect	90
5. Conclusions	98
6. Memento	99

1. Introduction

We have described in the previous chapter the physics of Cu(In,Ga)Se_2 devices. Using concentrated sunlight is a mean to increase the conversion efficiency of solar cells, but resistive losses are strongly limiting its use on thin film solar cells to date. In this chapter, we describe strategies to find a solar cell architecture that has inherently less resistive sources. We will also discuss the thermal management of solar cells that can become crucial when large light fluxes are used. These two aspects will be discussed in the framework of scale effects. As an introduction we will review the scale effects that are known and used today in the concentrated photovoltaic community but also in the light emitting diode domain.

2. Scale effects in light emitting diode and photovoltaic devices

In the late 50s, the first monolithic integrated circuits were fabricated by Jack Kilby (Texas instrument) and Robert Noyce (Fairchild Semiconductors), out of a single piece of silicon. From that point on electronic evolved towards increasingly smaller devices, giving birth to microelectronics. The increasing miniaturization was one of the cornerstones for the continuous improvement of the devices performance in terms of speed and costs. While this thesis is focused on photovoltaic devices, some of the improvements in the field of similar electronic components, such as light emitting diodes, will be reviewed to show the synergy between the two domains.

2.1. State of the art of light emitting diodes of reduced size

Light emitting diodes functioning

Light emitting diodes (LED) are semiconducting devices based on electroluminescence. Radiative recombination between electrons and holes under forward bias leads to the emission of light that is then guided out of the device. The first LED was based on a GaAs p-n junction. More recently nitride III-V materials were employed to have access to blue and UV light emission [125]. Double heterojunction structures were developed to increase carrier densities compared to simple p-n homojunctions and therefore improve the efficiency of radiative recombination (Figure III-1 and equation (II-6)). Multi quantum well structures were also developed to confine carriers and reach higher radiative recombination efficiencies.

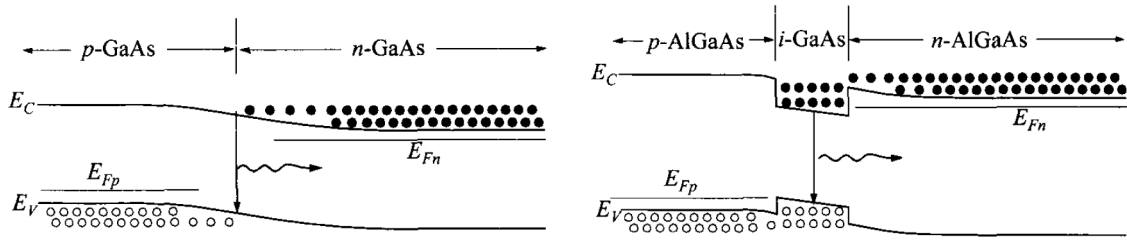


Figure III-1 : LED structures : (left) p-n homojunction, under forward bias where electrons injected from the n-side recombine with holes injected from the p-side. (right) Higher carrier densities and improved carrier confinement in a double heterostructure. Reproduced from [125].

Current crowding

For a good operation of LEDs, light emission homogeneity and thus current homogeneity is desirable. When current densities are concentrated in certain spots of the LED, current crowding is said to occur. Due to these inhomogeneities, hot spots are created in the device, especially near the contacts, and this leads to fast degradation [126]. Current crowding is known to be one of the major challenges for light emitting diodes [127]. This is especially true for high power LEDs, on which current densities can reach 50 A/cm² [128]. One difficulty is to grow current spreading window layers with high sheet conductance and optical transmittance that enable a good distribution of current over the device (transparent electrode of Figure III-2), even for high current densities.

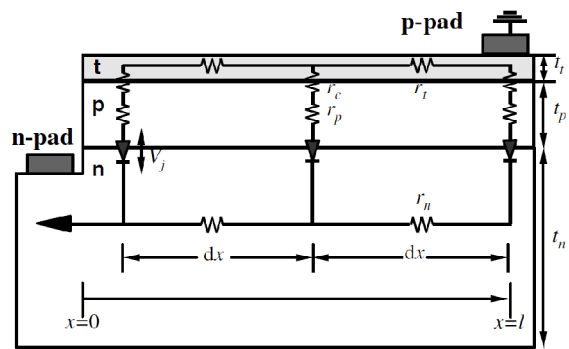
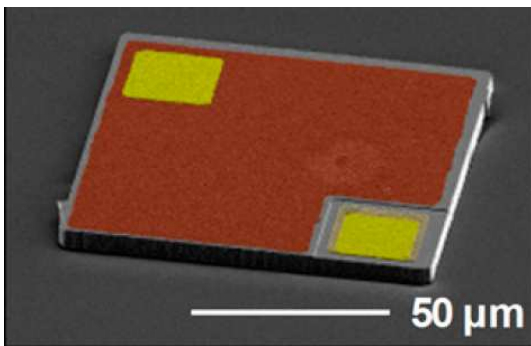


Figure III-2 : (left) Colorized scanning electron microscope image of an InGaN microLED. Yellow corresponds to contact pads and red to a thin current spreading layer. Reproduced from [129] (right) Equivalent LED circuit, with a p-pad as the physical ground that can be used to model current crowding according to references [130], [131]. In this example *t* refers to the semi-transparent electrode made of approximately 50 Å of Ti/Au, p and n layers are made of GaN.

Current spreading lengths are defined to describe the characteristic lengths associated with current density gradients. These spreading lengths highly depend on the current density ($\sim J_0^{-1/2}$) and the window layer sheet resistance ($\sim R_{\square}^{-1/2}$), and are typically in the order of 50 μm for high intensity LED. In order to maintain good homogeneity under high power operation, when the window layer conductivity becomes insufficient, two approaches emerged: the addition of an inter-digitated top contact grid [132] or the reduction of LED size [128], [133]. The latter is of particular interest with

respect to our study (Figure III-3). If the device is smaller than the characteristic spreading length, current crowding becomes negligible [133]. Micro-pixel designs, made of hundreds of interconnected micro-LEDs, were developed, and show superior performance compared to their macro-LED counterparts (Figure III-3 left). Resistive limitations are thus overcome by a well employed scaling effect that requires devices to go down to sizes in the 50 μm range.

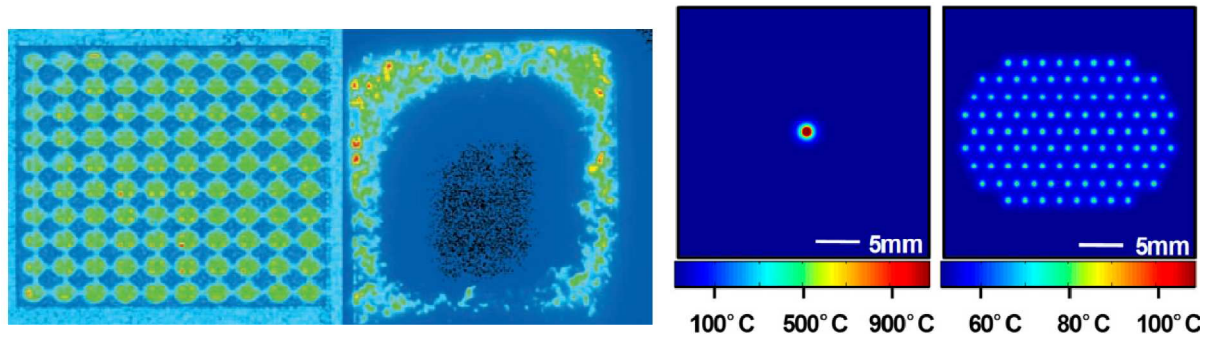


Figure III-3 : Image of UV-LED by a CCD camera (left) image of a micropixel UV LED array with total area junction $220 \mu\text{m}^2$ and of a conventional square geometry LED (total area junction $200 \mu\text{m}^2$). Image under continuous applied bias, the inhomogeneities observed are due to inhomogeneous light emission. Reproduction from [128], [134] (right) Temperature distribution of a 1 mm^2 LED and of an array of 100 micro-LEDs ($100 \times 100 \mu\text{m}$) at a spacing of 2 mm at an incident heat flux density of 400 W/cm^2 .

Thermal management

Additionally to improvements in current homogeneity, micro-LEDs show superior thermal management. In a way similar to the electric considerations, thermal resistance and spreading lengths can be defined [135], and temperature elevation is found inversely proportional to the radius of the device. Passive cooling is thus possible on distributed micro-LEDs [129]. At a power density of 400 W/cm^2 an array of 100 micro-LEDs ($100 \mu\text{m} \times 100 \mu\text{m}$) is found to operate at 100°C , compared to 1000°C for a single 1 mm^2 device that would actually cause its complete destruction (Figure III-3 right).

A good thermal management of LED is also a pre-requisite for a long life span of the device [131]. Indeed degradation is strongly dependent on the operation temperature. Therefore micro-LEDs are expected to be more reliable than their macro LED counterparts. Commonly, LED manufacturers guarantee LEDs to last for 10^5 hours.

Microelectronics has thus emerged as the best option for efficient, fast, low material consumption, electronic devices. In the past years, photovoltaic devices have adopted similar strategies.

2.2. State of the art of microcells in photovoltaics

In parallel to the trend of scaling down light emitting diodes, the photovoltaic community engaged works to evaluate the potential of small photovoltaic solar cells. This has been done especially for concentrator cells, where high illumination intensities cause problems very similar to what impacts high power light emitting diodes. Microcells, i.e. photovoltaic devices which lateral dimensions are smaller than 1 mm, have emerged in the past years.

The so called “LED-like” approach in photovoltaics is based on the assessment that LED devices and concentrator cells are very similar. In fact solar cells are often used as LED to detect defects [136–139] or check the concentrating optics alignment [140]. From a fundamental point of view, reciprocity relations can be drawn between the electroluminescence of a LED and the photovoltaic quantum efficiency of a solar cells [141]. A perfect LED is also a perfect solar cell. However in real devices significant differences may arise. For a solar cell the carrier mobility has to be sufficient to collect charges, whereas a good LED can withstand low mobility. On the contrary, a good LED needs a long radiative lifetime, whereas a solar cell is less sensitive to it.

From a practical point of view, the LEDs and the standard concentrator cells are very similar. Both devices are based on p-n junctions or heterojunctions made of the same materials, III-V semiconductors. Their fabrication processes are close, as well as their operating conditions. Therefore advances in LEDs are supposed to impact concentrator solar cells, and vice-versa. A better connection between the two domains was proposed to benefit from the synergy [35], [142]. Questions regarding high power LEDs and high concentration photovoltaic cells are indeed very much alike. Concentrator cells are designed to work under high illumination intensities, created by concentrating optics. Thus the questions regarding current homogeneity and heat dissipation that are important for high power LEDs are also crucial for concentrator cells.

2.2.1. Concentrator cells miniaturization

As a consequence of concentration, light fluxes over 10^6 W/m² are reached and current densities on concentrator cells can surpass 60 A/cm² [143], causing both thermal and resistive issues. These current densities are of the same order of magnitude as those of high power LEDs.

For high current density management, concentrator cells use a metal collecting grid to improve front contact conductivity [144–147]. The resistance associated with the structure composed of a window layer and a metallic grid is roughly proportional to $R_{\square}L^2$, where R_{\square} is the window layer sheet resistance and L is the spacing between grid fingers [146], [148–152] (the proportionality coefficient depends on the grid geometry). Therefore by diminishing the distance between two grid fingers, the

influence of front contact resistance can be controlled. For a given illumination intensity an optimum grid pitch is thus found as the balance of small lateral front contact resistance and low surface coverage. Attempts to eliminate grid shadowing, and therefore enable higher grid coverage, have been made by the use of micro-concentrator optics based on total internal reflection [153], [154]. However fabrication complexity and costs prevented its implementation in the market to date.

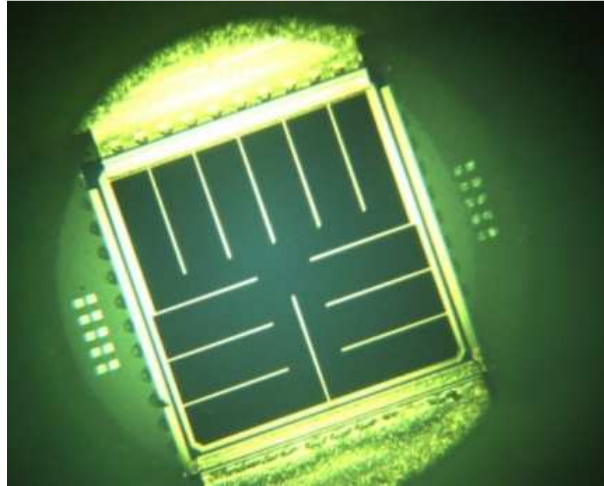


Figure III-4 : 600 × 600 μm solar cell from Sempruis. Confirmed efficiency of 41% at $\times 1000$ [155]. The collecting grid is visible.

Reducing the cell size, leads to smaller currents, and thus decreased resistive losses [146], [147], [156]. Miniaturizing concentrator cell eases resistive losses management, but also enables a better heat evacuation [35], [157], as seen for LEDs. In January 2012, miniaturized concentrator cells, which sizes were $600 \times 600 \mu\text{m}$ (Figure III-4), enabled the fabrication of a 33.9% efficient module under AM1.5 direct (active area), where each individual cell works under $\times 1100$ illumination [5]. This was the most efficient photovoltaic module at the time of its certification. The reduced size of the cell makes the use of heat sinks unnecessary, and cells are working typically at $35\text{-}40^\circ\text{C}$ above the ambient [34]. This result agrees with previous studies showing that devices smaller than 1 mm^2 should operate at a temperatures very close to those of one-sun modules [35], [158]. However the cells are still wide enough to need a collecting grid (Figure III-4).

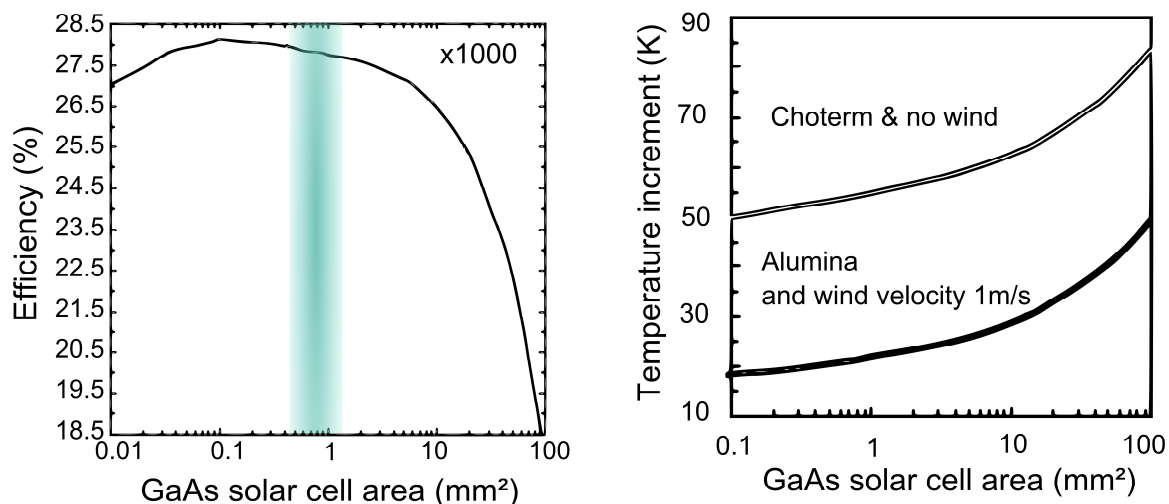


Figure III-5 : (left) Efficiency as a function of size for single junction GaAs cell under $\times 1000$. (left) The temperature increases over the ambient temperature as a function of the solar cell size under $\times 1000$ for different heat conductors (alumina, choterm) and wind velocities. Reproduced from [35]

The question of the optimum size of a concentrator cell was tackled by the group of Algora [35], [159]. It was calculated for a single GaAs junction that the optimum size range for an operation under $\times 1000$ is around 1mm^2 (Figure III-5). These calculations took into account the decreased resistive losses, the lower temperature elevation but also the increasing impact of edge recombination on small devices [35], [143], [160].

In III-V concentrator cells, and GaAs junctions in particular, the main obstacle that prevents concentrator cells from going down to grid pitch size ($100\ \mu\text{m}$) seems to be edge recombination [35]. Indeed as the size of the device is reduced, the impact of the edge recombination as compared to bulk recombination increases. In these devices, the saturation current density J_{02} , relative to the ideality factor $A = 2$, is the sum of a bulk term and of a perimeter term. $J_{02} = J_{02,bulk} + J_{02,P}$ where $J_{02,P} = qn_i s_0 L_s (P/A)$, with s_0 the edge recombination velocity, L_s the surface diffusion length and P/A the perimeter to surface ratio. Edge recombination is significant in GaAs, and even large devices ($0.25\ \text{cm}^2$) can be limited by this recombination path [161]. Edge recombination parameters taken into account for the analysis of optimum cell size of reference [35] are not published. Values for the perimeter recombination exponential prefactor in the order of $10^{-13}\ \text{A/cm}$ seems reasonable [161], which explains the conclusion that devices around $1\ \text{mm}^2$ are an optimum.

2.2.2. Optimum size for a solar cell

We have seen that there are strong incentives to miniaturize concentrator solar cells from an electrical and thermal point of view. However the study of the optimum size of a solar cell has been

limited to date to particular material systems, and no underlying physical governing equation was clearly highlighted.

For example the value of the edge recombination current in GaAs hinders the design of an efficient concentrator cell sufficiently small to prevent the need for a collecting grid. The concentrator cell size is thus set as a trade-off between on the one hand improved conductivity and heat evacuation and on the other hand increased shadowing and edge recombination. For other photovoltaic cells, such as thin films for example, edge effects may be less detrimental, and ultrasmall devices ($<100\ \mu\text{m}$) may still be efficient.

Another limit to the miniaturization is potentially increased costs. Thus it is not clear if there is an incentive to go to monocrystalline devices smaller than $100\ \mu\text{m}$. Indeed for such devices the gain in terms of resistive or thermal management may be small compared to that of larger devices ($100\ \mu\text{m} - 1\text{mm}$) [162] and costs in alignment, bonding, wafer cut wastes may increase. However if one works with self-assembly techniques and localized deposition methods, which are widespread in the thin film community, those costs can be decreased significantly. Handling small device can thus become interesting even from an economical point of view. Indeed on miniaturized solar cells, costs related to the optical system, that is expected to be much more compact, may decrease [162].

We propose to have a more general approach to the question of the optimum cell size for photovoltaics. We want to derive equations that can be applied for a variety of photovoltaic solar cells. As this thesis is dedicated to thin film polycrystalline solar cells, these cells, and especially $\text{Cu}(\text{In,Ga})\text{Se}_2$, will be used as an example. However the governing equations derived will have a broad scope.

3. Modeling of sheet resistance problem

The question of using high concentration for thin film solar cells was eluded up to now because resistive losses were thought to be an insurmountable obstacle [36–38]. However we have seen that miniaturizing concentrator cells and LEDs lead to the decrease in such losses. Before discussing in detail the possible advantages of a scale effect regarding resistive losses on thin film solar cells, we will give a brief overview of the different sources of resistance in a solar cell in order to precisely define our study.

3.1. Resistive sources in thin film solar cells

3.1.1. *Introduction: the respective contributions of the different layers*

Solar cells are based on a stack of semi-conducting layers between two metallic contacts. Semiconductor resistivity is a function of carrier concentration and mobility. In solar cells, the semiconducting layers are sources of resistive losses that cannot be neglected. This is especially true if the solar cell is designed to work under high flux illumination. Indeed significant current densities will be generated due to the intense illumination, and power losses may become critical.

The resistance of a solar cell is often described in terms of a lumped resistance that represents an average of all resistive loss mechanisms [163]. However determining the value of such a resistance for a stack containing different sources, with possibly non-uniform current flow, is not straightforward. Intricate dependence of the resistive losses on applied voltage or illumination intensity may be difficult to apprehend in a simple lumped approach.

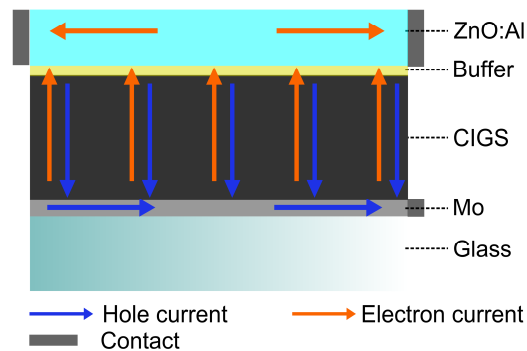


Figure III-6 : Current flow in a Cu(In,Ga)Se_2 solar cell, with an annular front contact, and a right back contact.

If we take a look at the configuration of the current flow in a Cu(In,Ga)Se_2 solar cell for example (Figure III-6), similar to that of a majority of solar cells, two types of layers have to be examined separately. First, the current flow may be perpendicular to the film plane, such as in the absorber and buffer layers. In these layers the resistive losses are well defined by a series resistance term, as the current flow is uniform in the film plane. Second, the current can flow laterally, such as in the back contact and window layers. The distributed resistance source yields a non-uniform current distribution that makes the resistive losses analysis more complex.

In the next paragraphs, we will treat these two cases separately and see the geometric parameters that can impact the resistive losses.

3.1.2. *Series resistance: vertical current flow*

Definition

For the layers where the current flow is vertical, calculating the series resistance associated to the crossing of the layer is straightforward. In general, the resistance R associated with a portion of a

material of resistivity ρ , on a length L and cross-section S is $R = \rho L/S$. Therefore in a cell of area A the resistance of a thin layer of thickness t is $R_{vertical} = \rho t/A$. Thus, the voltage drop at a given current density J , when the current is of drift nature, is :

$$\Delta V(J) = J \times A \times R_{vertical} = J\rho t \quad (III-1)$$

Scale effect

For a given thin film material, the voltage drop is controlled by its thickness (equation (III-1)) as its resistivity is set by material constraints. Everything else being unchanged, thinner devices should yield smaller resistance. However problems may arise from ultra-thin layers : apparition of shunt resistances, weak light absorption, and the influence of surface defects [164], [32].

In standard Cu(In,Ga)Se₂ solar cells, the layers associated with vertical current flow are the Cu(In,Ga)Se₂ absorber, CdS and i-ZnO buffer layers. The series resistances induced by these layers are reported in Table III-1. One can see that the predominant source of resistance is the absorber layer. In spite of thickness around 50 nm, the CdS layer can also have a non-negligible impact on the total device resistance, especially if the photosensitivity is low.

Table III-1 : Resistive losses associated with the different layers of a Cu(In,Ga)Se₂ solar cell. Note that the resistivity of CdS is varying in a very large range. The electric properties of chemical bath deposited CdS depend highly on the deposition process, and are also dependent on illumination condition.

Layer	Thickness (nm)	Resistivity (ohm.cm)	Series resistance (ohm.cm ²)	Sheet resistance (ohm/square)	References
Molybdenum	500 - 1000	10 ⁻⁵ – 10 ⁻⁴	2 10 ⁻¹⁰ – 2 10 ⁻⁸	0.1-2	[37], [41], [43], [46]
Cu(In,Ga)Se ₂	1000 - 3000	10 - 10 ³	10⁻³-10⁻¹	10 ⁵ - 10 ⁷	[37], [145], [165], [166]
CdS	50	10 ⁻² - 10 ⁴	10⁻⁷-10⁻¹	10 ³ - 10 ⁹	[167], [168]
i-ZnO	50 - 100	1 - 10	10⁻⁵-10⁻⁴	10 ⁵ - 10 ⁶	[102]
ZnO:Al	100 - 400	10 ⁻⁴ - 10 ⁻³	10 ⁻⁸ - 10 ⁻⁹	10 - 20	[169]

3.1.3. Sheet resistance

Definition

When current is flowing parallel to a thin film plane, the resistive losses are evaluated by the sheet resistance R_{\square} of a layer with a resistivity ρ , a thickness t , a width W and a length L where $R = \rho L/tW$. The sheet resistance is then defined as the resistance of a square layer, where $L = W$. Therefore the sheet resistance of a thin film is only dependent on its resistivity and thickness:

$$R_{\square} = \frac{\rho}{t} \quad (\text{III-2})$$

The sheet resistance is expressed in ohm/square.

Scale effect

In a Cu(In,Ga)Se₂ solar cell, the layers in which the current flows laterally are the molybdenum back contact layer and the ZnO:Al window layer. Given the difference between the sheet resistance of the ZnO:Al and Molybdenum layers (see Table III-1), the main source of distributed resistance loss in a Cu(In,Ga)Se₂ device is the window layer[138], [169].

From what we saw in the literature review, if the lateral dimensions of a device are limited, we can expect the resistive losses associated with lateral current flow to drop. We need a general framework to study the spreading resistance problem that can guide us to find the relevant design parameter for a low resistive thin film solar cell.

3.2. Sheet resistance problem in equations

3.2.1. Hypotheses – definition of a simple physical model

Our goal is to study a Cu(In,Ga)Se₂ solar cell. However the following analysis of sheet resistance has a general scope and may describe a wide range of thin film solar cells. This approach has been described in a published paper [170].

We study a thin film solar cell in which a layer, for example the window layer, of thickness t and resistivity ρ is the predominant source of resistance. The series resistance of the other layers are neglected, their influences being incidental compared to the spread sheet resistance as can be seen in Table III-1. Indeed for a 0.1 cm² solar cell, the lumped series resistance associated with lateral flow in the window layer is in the order of 1 ohm.cm², well above all other sources. The shunt resistances can also be neglected for high efficiency solar cells, as their values are very high [25], often above 1000 ohm.cm². Therefore, unless otherwise mentioned, R_{sh} is taken infinite in our calculations.

The thickness, resistivity as well as illumination intensity are considered uniform over the cell area. As the solar cell is supposed to have uniform characteristics, photocurrent and saturation current densities are assumed to be constant. For the sake of simplicity we will study the case of a cell with cylindrical symmetry. We choose the cylindrical coordinates (r, θ) to describe our problem and we fix the origin at the cell's center. Because of this symmetry, the potential ψ and the current densities J only have a radial component. Due to the cell homogeneity, the electric potential and the current density are also considered to have no dependence on the θ coordinate. We consider that the

window layer thickness t is much smaller than the cell radius a (in Cu(In,Ga)Se₂ solar cells, the thickness t of the window layer is approximately 400 nm). Therefore we define electric potentials and currents that have no z -dependence by estimating an average value with respect to the thickness. The temperature of the device is kept constant and the thermal voltage kT/q is set to 25.85 mV.

3.2.2. Fundamental Equation

We analyze the spreading resistance effect based on the methodology that can be found in the literature [171], [172]. The window layer is considered resistive in the sense of Ohm's law, that is:

$$\vec{J} = -\frac{1}{\rho} \overrightarrow{\text{grad}}(\psi) \quad (\text{III-3})$$

where J is the current density, ρ the window layer's resistivity and ψ the electric potential. In the absence of fixed charges in the window layer, the divergence of the current field can be determined from Gauss's law :

$$\text{div}(\vec{J}) = 0 \quad (\text{III-4})$$

The current density coming from the p-n junction is supposed to be:

$$J_z(z=0) = J_{ph} - J_0 \left(\exp\left(\frac{q\psi(z=0)}{AkT}\right) - 1 \right) - \frac{\psi(z=0)}{R_{sh}} \quad (\text{III-5})$$

where z is the altitude, which is set to 0 at the bottom of the window layer and equals t at the surface, J_{ph} , J_0 , A , kT/q , R_{sh} are respectively the photocurrent density, the diode saturation current density, the diode ideality factor, the thermal voltage, and the shunt resistance.

We define the average current density in the horizontal plane \vec{J}_{\parallel} , independent of z , as:

$$\vec{J}_{\parallel}(r, \theta) = \frac{1}{t} \int_0^t \vec{J}_{horiz}(r, \theta, z) dz \quad (\text{III-6})$$

where \vec{J}_{horiz} refers to the current density in the horizontal plane and t is the thickness of the window layer. If we integrate equation (III-4) with respect to the thickness of the film, we obtain:

$$\begin{aligned}
\frac{1}{t} \int_0^t \text{div}(\vec{J}) dz &= 0 \\
\Rightarrow \text{div}(\vec{J}_{\parallel}) + \frac{1}{t} \int_0^t \text{div}(\vec{J}_z) dz &= 0 \quad (\text{III-7}) \\
\Rightarrow \text{div}(\vec{J}_{\parallel}) + \frac{J_z(z=t) - J_z(z=0)}{t} &= 0
\end{aligned}$$

where \vec{J}_z refers to the current density along the z-direction, and J_z to its norm. Because no current flows through the upper surface, $J_z(z=t) = 0$. Combining equations (III-3), (III-4), (III-5) and (III-7) the potential ψ on the surface of the cell is the solution of the following one-dimensional equation:

$$\frac{\partial^2 \psi}{\partial r^2} + \frac{1}{r} \frac{\partial \psi}{\partial r} + R_{\square} \left(J_{ph} - J_0 \left(\exp\left(\frac{q\psi}{AkT}\right) - 1 \right) - \frac{\psi}{R_{sh}} \right) = 0 \quad (\text{III-8})$$

In order to solve equation (III-8), appropriate boundary conditions are needed. The first boundary condition corresponds to the electric contact between the window layer and the external circuit: the potential ψ equals the applied potential V . The second condition depends on the geometry. Two different geometries are studied (Figure III-8). First we consider that the electric contact on the window layer is taken with a probe of radius b , placed at the center of the cell of radius a . Therefore the probe perimeter is an equipotential at the applied voltage V , $\psi(b) = V$ and in the absence of surface charge or recombination at the cell perimeter, we have the Neumann condition $\frac{\partial \psi}{\partial r}(a) = 0$. This contact geometry will be designated as a “dot contact”. Second, we consider the case where the contact is taken by the deposition of an annular electrode at the periphery of the cell (designated as “ring contact”). In this case, $\psi(a) = V$, and due to the circular symmetry there is no net current at the centre of the cell, i.e. $\frac{\partial \psi}{\partial r}(0) = 0$.

With these boundary conditions, we do not take into account edge recombination effects. In order to take them into account we should consider a surface current, i.e. impose a gradient of the potential at the edge. However, as will be seen in Chapter VII edge recombination is not a limiting factor for a Cu(In,Ga)Se₂ solar cells and this is why we neglect it in our study. However as seen in the introduction, this approximation cannot be made for other types of materials.

3.2.3. Multiple sheet resistance sources

It should be noted that if we want to take into account the influence of several layers in which spreading resistance is significant, the present approach can easily be extended. For example, if we

want to take into account the influence of both window and back contact layers, we can proceed as follows.

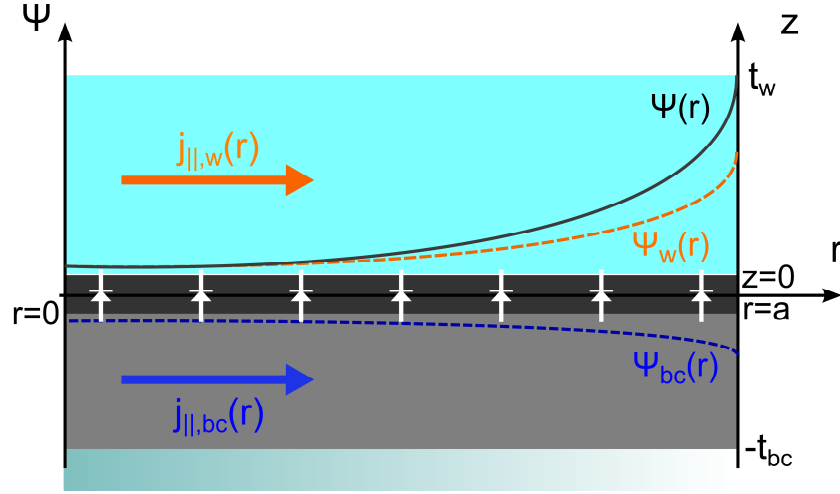


Figure III-7 : The total local potential difference ψ across the solar cell is the difference between potential at the back and front surface $\psi_w - \psi_{bc}$. Due to the sheet resistance they are position dependent. The figure is drawn in the ring contact geometry.

Equation (III-7) for the window (subscript w) and back contact (subscript bc) layers becomes :

$$\begin{aligned} \text{div}(\vec{J}_{\parallel,w}) + \frac{J_z(z = t_w) - J_z(z = 0)}{t_w} &= 0 \\ \text{div}(\vec{J}_{\parallel,bc}) + \frac{J_z(z = 0) - J_z(z = -t_{bc})}{t_{bc}} &= 0 \end{aligned} \quad (\text{III-9})$$

where 0 denotes the position of the junction, which thickness is neglected. Because no current flows through the upper or back surface, in this case $J_z(z = t_w) = J_z(z = -t_{bc}) = 0$. Thus the potential of the upper ψ_w and back surface ψ_{bc} are given by :

$$\begin{aligned} \frac{\partial^2 \psi_w}{\partial r^2} + \frac{1}{r} \frac{\partial \psi_w}{\partial r} + R_{\square,w} \left(J_{ph} - J_0 \left(\exp \left(\frac{q\psi_w}{AkT} \right) - 1 \right) - \frac{\psi_w}{R_{sh}} \right) &= 0 \\ \frac{\partial^2 \psi_{bc}}{\partial r^2} + \frac{1}{r} \frac{\partial \psi_{bc}}{\partial r} - R_{\square,bc} \left(J_{ph} - J_0 \left(\exp \left(\frac{q\psi_{bc}}{AkT} \right) - 1 \right) - \frac{\psi_{bc}}{R_{sh}} \right) &= 0 \end{aligned} \quad (\text{III-10})$$

Then we can derive the solution for the total potential $\psi = \psi_w - \psi_{bc}$. We find :

$$\frac{\partial^2 \psi}{\partial r^2} + \frac{1}{r} \frac{\partial \psi}{\partial r} + (R_{\square,w} + R_{\square,bc}) \left(J_{ph} - J_0 \left(\exp \left(\frac{q\psi}{AkT} \right) - 1 \right) - \frac{\psi}{R_{sh}} \right) = 0 \quad (\text{III-11})$$

Thus we can see that equation (III-8) is a general equation in which the different sheet resistance contributions are summed.

It should be noted that if the contacts for the front and back surface are not at the same position r then the potential drops due to front and back contact can experimentally be distinguished. Indeed with different contact position, the front and back contact will influence the total potential ψ at different spatial position, and their respective influence can be decorrelated [138]. This is the case for example in interconnected modules.

3.2.4. Simulation results: distribution of potential on a cell's surface

The system of equation (III-8) and its boundary conditions is not solvable analytically. We therefore developed a MATLAB program to obtain a numerical solution for chosen parameter values. Equation (III-8) is transformed in a system of two differential equations of the first order. The system is then solved with MATLAB function bvp4c (solver of boundary value problem for first order differential equations). The inputs of our calculations are the diode characteristics of the record NREL solar cell (area 0.419 cm², $A = 1.14$, $J_0 = 2.1 \cdot 10^{-9}$ mA/cm², $J_{sc} = 35.5$ mA/cm²) [55], [173]. We assumed the ZnO:Al sheet resistance to be 10 ohm/square and, in the case of a probe contact, we consider a probe of radius 3.5 μm. After calculation we obtain the potential distribution and thus the current density over the cell's surface for a given size, illumination intensity and applied voltage. A 500 points mesh is used to get enough precision especially close to the contacts.

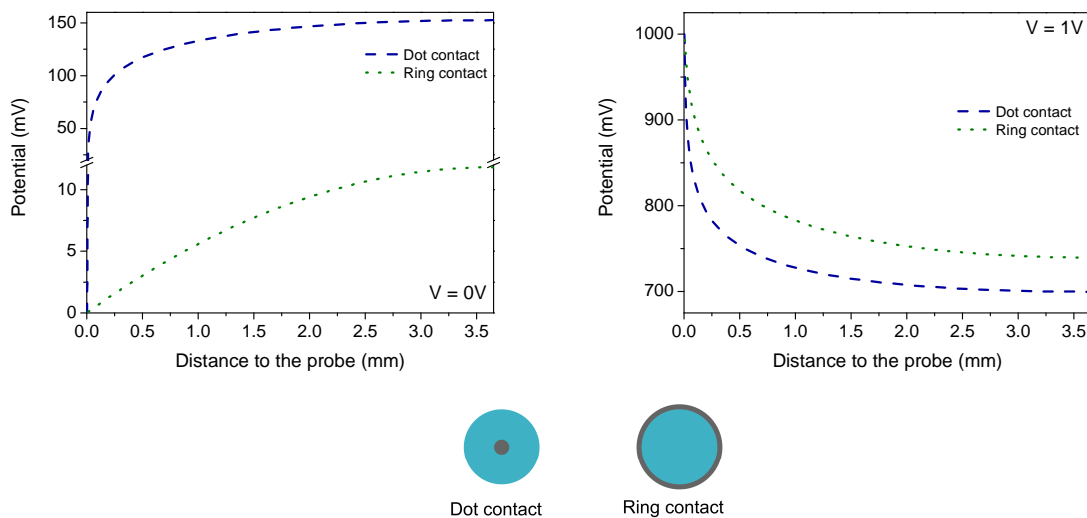


Figure III-8 : Effective applied voltage to the cell with respect to the distance to the probe, $R_{\square} = 10$ ohm/square. Blue dashed line corresponds to a dot contact, the green dotted line to a ring contact. a) Short-circuit current conditions under AM1.5 b) $V = 1V$ in the dark.

Two situations are given in Figure III-8 for both dot contact and ring contact geometry. One can see that the potential varies on the cell surface, even for a relatively low sheet resistance (10

ohm/square). The potential variation, i.e. voltage drop, increases with current density (see equation (III-1)). We can thus conclude that the ring contact geometry, which lowers voltage drops, results in a better distribution of the current than the dot contact one, avoiding current crowding effects (Figure III-8b). It should be noted however that with a larger dot, the dot contact could be improved. However on small devices, in order to avoid shading, dot contacts are constraint to be very small. Therefore ring contacts, that imply no shading, are regarded as highly desirable to connect cells under intense illumination.

Before analyzing further the performances of thin film solar cells, we will study equation (III-8) to get more insight in the physics controlling spreading resistance phenomena.

3.2.5. *Scaling effect*

In order to get more insight in the physical meaning of equation (III-8), we derive its dimensionless equivalent, in the case where the shunt resistance can be considered infinite:

$$\frac{\partial^2 v}{\partial R^2} + \frac{1}{R} \frac{\partial v}{\partial R} + \alpha(1 - j_0(\exp(v) - 1)) = 0 \quad (\text{III-12})$$

where the dimensionless variables are $\alpha = R_{\square} a^2 C J_{ph}(1 \text{ sun}) q / AkT$, $j_0 = J_0 / C J_{ph}(1 \text{ sun})$, $j_{ph} = 1$, $R = r/a$ and $v = q\psi/nkT$. C represents the concentration factor, defined as the ratio of the incident light power density by the light power density at one sun (100 mW/cm², see box n°1 page 26). $J_{ph}(1 \text{ sun})$ is the photocurrent density at one sun. From the dimensionless factor α we can derive two characteristic lengths:

$$l_{illumination} = \sqrt{\frac{AkT}{qR_{\square} C J_{ph}(1 \text{ sun})}} \quad (\text{III-13})$$

$$l_{dark} = \sqrt{\frac{AkT}{qR_{\square} J_0}} \quad (\text{III-14})$$

l_{dark} has an expression close to the spreading length defined in the LED community [127], [132] and is also called a screening length in the study of solar cell non-uniformity [174]. (In fact our factor J_0 is the saturation current and not the dark current). This term controls the length over which the potential be decreased due to spreading resistance effects.

$l_{illumination}$ is the counterpart of l_{dark} for solar cells, where current spreading is controlled by the current density under illumination and thus intensity of the incident light flux. $l_{illumination}$ is inversely proportional to $C J_{ph}(1 \text{ sun}) \approx C J_{sc}(1 \text{ sun}) \approx C J_{mpp}(1 \text{ sun})$, where $C J_{mpp}$ is the current

density at the maximum power point. Therefore it decreases when illumination increases. As a consequence, in order to maintain a good homogeneity of the current in a device and avoid resistive losses (i.e. maintaining voltage drop across the surface smaller than the thermal voltage kT/q) the device area should be close to $l_{illumination}^2$. In this case, spreading resistance losses will be negligible and high flux operation of thin film devices possible.

The miniaturization of thin film solar cells maintains high efficiency under concentrated light flux. This miniaturization does not require a change in the classic structure of the solar cell, as it is purely a scale effect. Therefore miniaturized thin film solar cells can rely on standard materials already developed in the community.

3.2.6. *Generalization to other geometries*

In the preceding section, we studied a cell of cylindrical symmetry. In the case of cells that are rectangular for example, the same approach applies. Indeed if we considered cells that are extended in a direction, for example y, a one dimensional analysis along the x-axis is valid. Equation (III-8) for a cell of width L , thus becomes:

$$\frac{\partial^2 \psi}{\partial x^2} + R_{\square} \left(J_{ph} - J_0 \left(\exp \left(\frac{q\psi}{AkT} \right) - 1 \right) - \frac{\psi}{R_{sh}} \right) = 0 \quad (III-15)$$

$$\frac{\partial^2 v}{\partial X^2} + \alpha' (1 - j_0 (\exp(v) - 1)) = 0$$

where $\alpha' = R_{\square} L^2 C J_{ph} (1 \text{ sun}) q / AkT$. Equation (III-15) has a form that is analog to equation (III-8). In order to limit resistive losses the width of the cell has to be smaller than $l_{illumination}$.

Thus the principal of scaling down solar cells to avoid spreading resistance losses is general. It can be applied to circular, rectangular or any other shaped cell, as long as one of the lateral dimensions of the cell is kept close to the spreading length.

3.2.7. *Simulation of a current-voltage curve*

Once the potential is determined on the cell surface by solving equation (III-8), the current density can be obtained by (III-3). In order to generate a complete J-V curve, this step has to be repeated for each voltage of the desired characteristic.

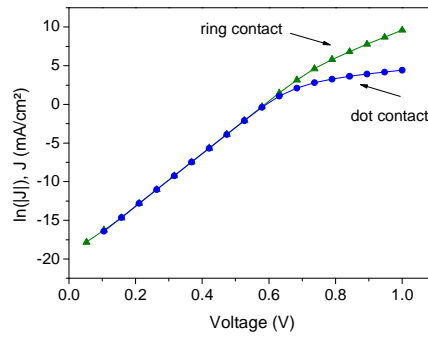


Figure III-9: $\ln(|J|)$ as a function of applied voltage, for 0.419 cm^2 NREL solar cell with sheet resistance of 10 ohm/square

We simulate the dark $J - V$ characteristic of the record NREL cell for both ring and dot contact geometry. One can see the influence of spreading resistance at high voltages with the saturation of the current. As could be predicted from our analysis of Figure III-8, the ring contact geometry leads to reduced resistance compared to the dot one.

$J - V$ curves under illumination can be simulated likewise. The AM1.5 $J - V$ curve for the same cell is plotted on Figure III-10 (green curve). On this figure is also displayed the $J - V$ curve based on a “lumped” series resistance approach: the $J - V$ curve simulated from our model is fitted with a least-square regression to determine the series resistance that results in the same maximum power point. As one can see in the inset, the two approaches are very close in the first quadrant. However at higher voltages, where resistive losses are more important, the differences are noticeable. This is due to the fact that the lumped resistance is a constant over the explored voltage range, highlighting the need for a spreading model.

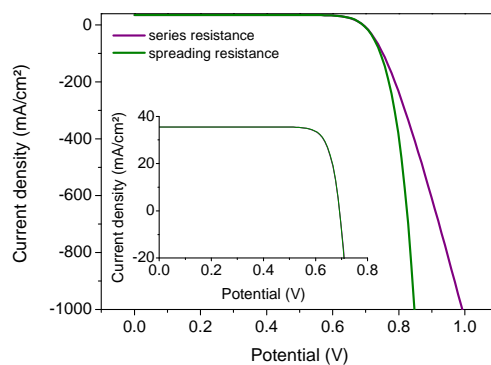


Figure III-10 : Current voltage curve of a 0.419 cm^2 solar cell with 10 ohm/square window layer sheet resistance (green). The purple curve is a least-square regression for a series resistance analysis that leads to the same maximum power point (see inset).

3.3. Model validation: electroluminescence and I-V fit

Before using our model to predict the behavior of thin film solar cell in various conditions, we assess its correctness. To validate the model, we compare the calculated potential distribution to that extracted from experimental electroluminescence images [175].

3.3.1. Basis of electroluminescence

Electroluminescence (EL) is the emission of light induced by radiative recombination of carriers in a semiconductor, under an applied bias. The luminescence intensity emitted normal to the surface at a distance r from the contact is related to the voltage V across the junction by:

$$\phi(r) = \phi_0(r, E) \exp\left(\frac{qV(r)}{kT}\right) \quad (\text{III-16})$$

where ϕ_0 is a factor that depends on the emitted photon energy E , and local properties. If the window layer is the only source of resistance, V is equal to the voltage applied to the device, otherwise voltage drops due to losses between the junction and the contacts have to be subtracted. Based on the detailed balance theory, a reciprocity relation between a solar cell and a LED can be defined [141]. Thus equation (III-16) becomes [138] :

$$\phi(r) = EQE(E, r)\phi_{bb}(E) \exp\left(\frac{qV(r)}{kT}\right) \quad (\text{III-17})$$

where $EQE(E, r)$ is the local external quantum efficiency, and ϕ_{bb} the spectral photon density of a black-body, $\phi_{bb} = \frac{2\pi E^2/h^3 c^2}{\exp(E/kT)-1}$ with c the light velocity and h the Planck constant.

The intensity recorded camera pixel is then:

$$\begin{aligned} \phi_{cam}(r) &= \exp\left(\frac{qV(r)}{kT}\right) \times \int Q_{cam}(E)EQE(E, r)\phi_{bb}(E) dE \\ &= \phi_1 \exp\left(\frac{qV(r)}{kT}\right) \end{aligned} \quad (\text{III-18})$$

where $Q_{cam}(E)$ is the sensitivity of the camera at the energy E . If at the scale of the experiment the material is homogeneous, i.e. $EQE(E, r) = EQE(E)$, ϕ_1 is independent of the position. Therefore any variation in the recorded EL intensity originates from potential variation across the device.

Analyzing spatially resolved EL images is therefore a mean to measure potential variations. We use EL to ensure that our simulation model is working properly.

3.3.2. *Experimental setup*

A homemade EL setup is used. A solar cell is contacted in the two point probe geometry, and connected to a Keithley 2635A sourcemeter. The setup is placed in the dark. After applying a sufficient voltage, the luminescence is intense enough to be recorded by a CCD camera, through a microscope objective. After spatial calibration with a grating of known period, the camera provides a spatially resolved image of the EL.

3.3.3. *Analysis of EL imaging with sheet resistance model*

EL images are recorded on Cu(In,Ga)Se₂ solar cells, with a 400 nm thick ZnO:Al window layer. The solar cells are made with an absorber provided by Würth Solar, and the junction is completed at IRDEP. Solar cells are mechanically scribed on the same substrate to create solar cells of different sizes: 0.1 cm² and 0.3 cm².

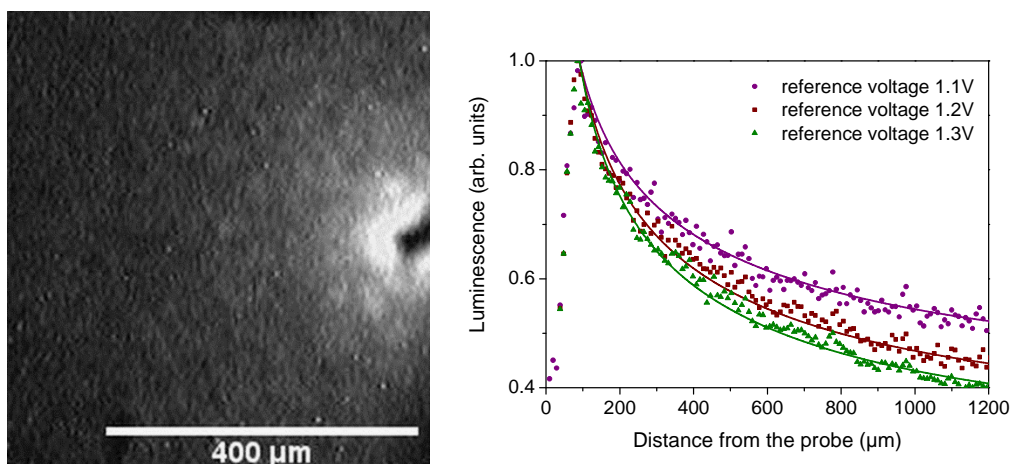


Figure III-11 : (left) EL image recorded on a 0.1cm² cell under an applied voltage 0.76V. (right) EL data (dots) and fit (solid line) at three different reference voltages applied to a 0.3cm² solar cell.

Figure III-11 shows an EL image on the 0.1 cm² cell. It can be seen that the EL intensity drops with distance to the contacting probe (on the right side of the image) indicating an important voltage drop. The luminescence signal from the EL image is obtained as the average over a 180° angular sector, centered at the probe tip, in order to minimize the influence of material inhomogeneity. In order to compare the luminescence signal from our simulated data with the experimental ones, we normalize both luminescence signals by their maximum value. Prior to the EL experiment, dark current-voltage characteristic of the cells are measured, and fitted to extract the values of saturation current and ideality factor. For the 0.3 cm² solar cell we find $I_0 = 5.14 \cdot 10^{-10}$ A, $A = 1.72$, and $I_0 = 2.97 \cdot 10^{-9}$ A, $A = 1.82$ for the 0.1 cm² cell. As the shunt resistance is superior to 10⁵ ohm, its contribution is neglected in the analysis. In order to fit the EL signal by our model, we also need to know precisely the effective voltage that is applied to the junction. Therefore we need to determine the contact

resistance between the probe tip and the ZnO:Al surface, as this resistance was found very important in our experimental setup due to the high contact resistance between the tungsten probe tip and ZnO surface.

Several EL images are recorded at different reference applied voltages, i.e. voltages imposed by the sourcemeter (Figure III-11). The EL signals are fitted by adjusting both sheet resistance and effective applied voltage, i.e. reference applied voltages corrected by the voltage drops. The contact resistance taking place at the interface between the probe tip and the ZnO surface, is expressed in terms of effective and reference voltages as :

$$R_{contact} = \frac{(V_{ref} - V_{eff})}{I(V_{ref})} \quad (III-19)$$

where $R_{contact}$ is the contact resistance, V_{ref} the reference voltage, V_{eff} the effective voltage, and $I(V_{ref})$ the intensity measured on the in-situ dark $I - V$ measurement at the reference voltage. We verify that the difference between the experimental reference voltages and fitted effective voltages is due to a constant contact resistance that we evaluate. The fits give a sheet resistance of 30 +/- 1 ohm/square for the three experiments and the three effective applied voltages (0.72V, 0.74V, 0.75V). From this we can deduce a value for the contact resistance that is 79 ohm (see Table III-2).

Table III-2 : Reference voltage, corresponding effective applied voltage and current intensity for the three signals of Figure III-11

Reference voltage (V)	Effective voltage (V)	Intensity at the reference voltage (mA)	Contact resistance (ohm)	Sheet resistance (ohm/square)
1.1 +/- 0.1%	0.72 +/- 5%	4.81 +/- 0.1 %	79 +/- 5%	30 +/- 1
1.2 +/- 0.1%	0.74 +/- 5%	5.89 +/- 0.1%	78 +/- 5%	30 +/- 1
1.3 +/- 0.1%	0.75 +/- 5%	6.94 +/- 0.1%	79 +/- 5%	30 +/- 1

It is worth noting that the sheet resistance value of 30 +/- 1 ohm/square is also coherent with the one we found in classic current-voltage experiment under AM1.5 illumination. We are able to extract from the current-voltage curves the value of the sheet resistance on cells on different sizes with our model. We find on average 31 ohm/square +/- 2 ohm/square (see Figure III-12). The coherence between the EL experiment and the illuminated current-voltage measurement confirms that the value of the sheet resistance extracted from the EL is valid and accounts for the resistive effect visible on well-known current-voltage curves. The slight differences between the two experiments originate from the two different experimental setups, especially contacting probes. It may also come from variation in photocurrent with voltage that are not taken into account in our model.

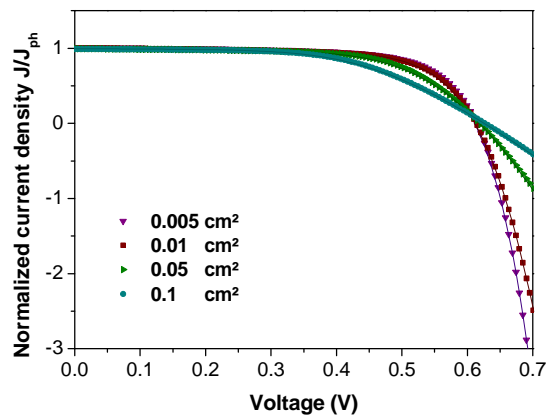


Figure III-12 : Experimental normalized I-V curves (symbols) and the corresponding fit by spreading resistance model (solid lines)

3.3.4. Discussion

EL experiments enable us to verify the correctness of our model simulation, and measure sheet resistance. The potential variations on a solar cell surface, linked with spreading resistance losses in the window layer, are in good agreement with the profiles extracted from EL images.

We compare the value of the window layer sheet resistance extracted from our images to the one available from a ZnO:Al layer deposited on glass under the same conditions. With a four point probe experiment on a ZnO:Al layer of 420 nm thickness on glass we found that the sheet resistance is 14.7 ± 0.3 ohm/square. The cells we study in the EL experiment have a ZnO:Al layer that is deposited in the same conditions, in terms of time and sputtering characteristics. Therefore it appears that the data of our fit gives a value of the sheet resistance that is higher than the one measured from ZnO:Al on glass. This can stem from different considerations. First, the ZnO:Al layer that is grown on the cell differs from the one grown on glass: the nucleation on ZnO:i and on glass is different resulting in different material properties, such as crystallites sizes and grain boundary properties for example. Therefore the lateral conductivity of the ZnO:Al should differ in the two layers. Second, the cell is rough. If the window layer is not flat the average distance to the electrode is increased by the surface roughness. In our model we suppose a flat solar cell of a given radius a . We fit the luminescence drop according to the value of the product $R_{\square}a^2$ and thus deduce R_{\square} . As a consequence, we may overestimate the sheet resistance value, as we give as input the geometrical radius a , instead of a radius corrected by the roughness factor. Thus the overestimation of R_{\square} should be close to the square root of the ratio of developed rough surface area over the flat surface area. As roughness can be very important on Cu(In,Ga)Se₂ solar cells, this factor is an important factor.

There are other approaches using spatially resolved EL image to determine window layer, as well as back contact, spreading resistances [138], [139]. Instead of solving equation (III-15) directly it is either proposed to linearize the current density around the applied voltage, or to study separately different parts of the I-V characteristic (constant, linear, exponential), in order to get analytical expressions for the voltage as a function of space variable and spreading resistances. All the methods, including ours, analyze EL images where a 1D modeling is sufficient, and [139] used the extracted sheet resistance to calculate a 2D EL map with Finite-Element Method to compare to the original data. The use of analytical solutions greatly facilitates the fit of the experimental EL signals. However, with robust simulation software (MATLAB), we did not experience too much trouble in fitting EL decay numerically. The advantage to do so is that the diode characteristic of the cell can be used directly without resorting to linearization. More advanced models and experiments can also investigate separately shunt resistance from lock-in thermography and spreading resistance from EL images [176]. The analysis of spatially resolved EL images is a robust method to study solar cells and modules and is already widely used in the industry.

The size dependence analysis of different solar cells characteristics can be done with our spreading resistance model. From the analysis of equation (III-12), we saw that maintaining the cell lateral dimension below the spreading length should limit resistive losses and enable high flux illumination of thin film solar cells. In the following section, we will quantitatively analyze the performance that can be expected from Cu(In,Ga)Se₂ cells of different sizes under various illumination intensities.

3.4. Size-dependent prediction of the behavior of solar cells under concentration.

3.4.1. Evolution of the conversion efficiency with concentration

We study the evolution of cell efficiency with concentration. We simulate $I - V$ curves under increasing concentration factor C . Then we can extract from the $I - V$ curves the open-circuit voltage, fill factor and efficiency. Figure III-13 shows the I-V curves for a 10^{-3} cm² solar cell that has the electric parameters of the NREL record cell and a window layer sheet resistance of 10 ohm/square in ring contact geometry. $I - V$ curves are normalized by the concentration factor to ease visualization. One can see that from $\times 1$ to $\times 1000$ the efficiency increases due to the increase in the open-circuit voltage. The fill factor increases too, from 83.2% to 84.9% between $\times 1$ and $\times 100$. For $\times 10\,000$, in spite of an increased V_{oc} , the efficiency decreases because of deterioration of the fill factor (68.3%). This decrease in fill factor is due to the $I - V$ curve rounding around the maximum power point, and is characteristic of spreading resistance losses [177].

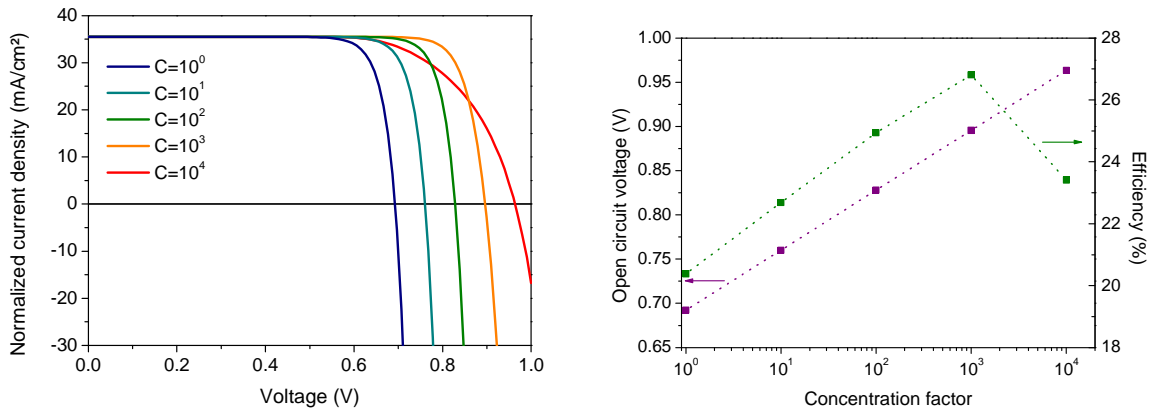


Figure III-13 : (left) normalized current density (I/C) vs. applied voltage for a cell of 10^{-3} cm^2 under 5 different illumination intensity for an annular contact. (right) corresponding open circuit voltage and efficiency vs. concentration factor

For this 10^{-3} cm^2 solar cell an important efficiency increase can be obtained: at 1000 suns the relative efficiency increase is 31% compared to the $\times 1$ value.

In order to quantitatively analyze the potential of the resistive scale effect on thin film solar cells, the performances of cells of various sizes under concentration are simulated.

3.4.2. Scaling effect – the need of microcells

We study the efficiency variations with the concentration ratio of four different cells: 10^{-1} cm^2 , 10^{-2} cm^2 , 10^{-3} cm^2 , 10^{-5} cm^2 (or 1780 μm , 564 μm , 178 μm and 18 μm of radius respectively) for a dot contact geometry (Figure III-14). The electric parameters are those of the record NREL solar cell, and the window layer sheet resistance is supposed to be 10 ohm/square.

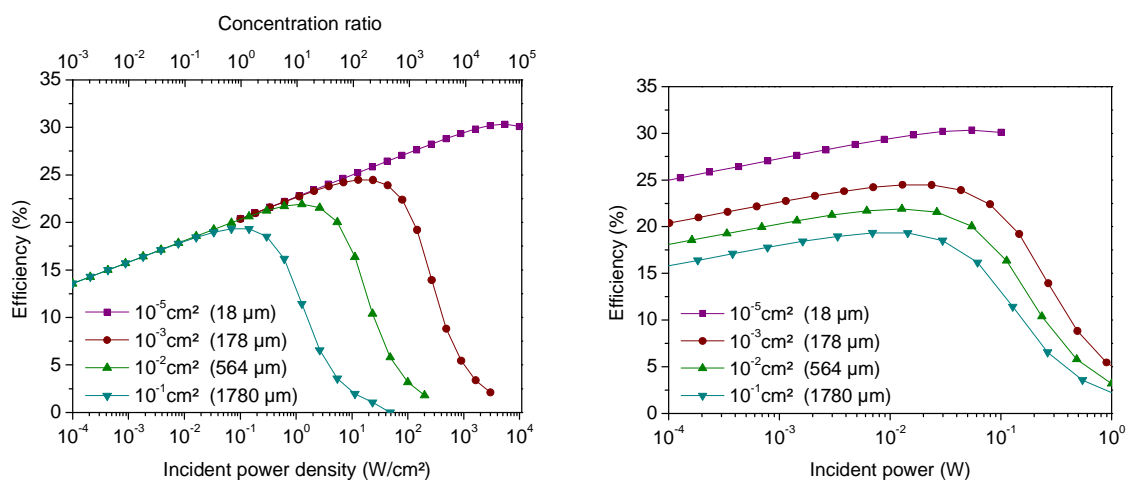


Figure III-14 : Efficiency vs. (left) incident power density or (right) incident power for four cells of radius 1780 μm (10^{-1} cm^2), 564 μm (10^{-2} cm^2), 178 μm (10^{-3} cm^2), 18 μm (10^{-5} cm^2) for a dot contact geometry. Sheet resistance 10 ohm/square.

Up to a certain incident light power, or a certain concentration ratio for a given cell area, the performance of the cells are improved by the concentration (the efficiency is proportional to the logarithm of concentration, as expected with this model) (see Chapter II), until a point where the ohmic losses induced by the sheet resistance are important enough to deteriorate the cell performance.

It is therefore possible to estimate for a certain cell, its optimum working conditions and the corresponding efficiency. Figure III-14 shows that for the same incoming power the best configuration is made by the smallest cell under the higher concentration. One can notice that the maximum efficiency for each cell occurs in first approximation for the same incident light power, as expected from the dimensionless analysis (Figure III-14 (right)). We can calculate from the dimensionless factor α , the concentration ratio at which the solar cell area is exactly the square of the spreading length $l_{illumination}$ (equation (III-13)). We find for example that for the 0.1 cm² cell this concentration ratio is 0.83, and 83 for the 10⁻³ cm² cell. These values are close to the optimum concentration ratios, i.e. concentration ratio at the maximum efficiency, that can be observed on Figure III-14 (left).

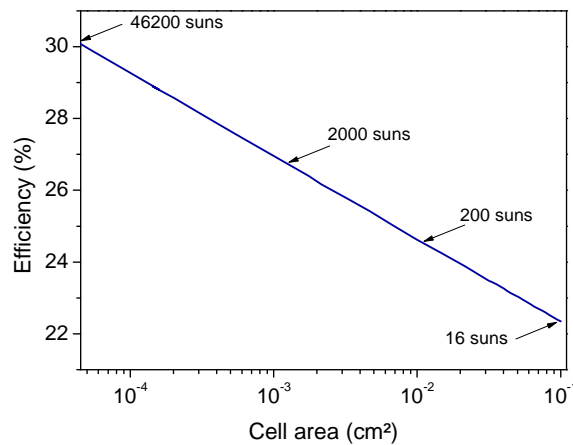


Figure III-15 : Optimum efficiency as a function of the cell size for a ring geometry. Four concentration ratios are given for information.

One important point for determining optimum cell geometry is to evaluate the optimum operating point for a given cell, and the corresponding efficiency. Figure III-15 displays the maximum efficiency expected for a given cell area. As examples, four optimum concentration ratios are placed on the line in Figure III-15. They correspond to the cells of 10⁻¹ cm², 10⁻² cm², 10⁻³ cm² and 4.5 10⁻⁵ cm² respectively. For cells which sizes are smaller than 4.5 10⁻⁵ cm², the optimum concentration ratio found in our calculations exceeds the concentration limit (in air) of 46 200 [178], indicating that the spread sheet resistance is no longer a limiting factor for the cell performance (the efficiencies for

smaller cells, with optimum concentration higher than 46 200, are irrelevant and not displayed on this graph). As expected, the ring contact method yields higher efficiency than the dot one for a given size, as the spread sheet resistance effect is diminished by a better current distribution. A 10^{-1} cm² solar cell (operated under 16 suns) will yield a 22 % efficiency, the 10^{-2} cm² solar cell (operated under $\times 200$) a 24 % efficiency, the 10^{-3} cm² solar cell (operated under $\times 2000$) a 27% efficiency and a 10^{-5} cm² solar cell (of radius 18 μ m) operated at 46 200 suns yields 31% efficiency .

3.5. Discussion

We concluded in the previous chapters that using concentrating illumination of thin film solar cells, and especially Cu(In,Ga)Se₂, can have multiple advantages. The main limitation to the realization of Cu(In,Ga)Se₂ concentrator cells was resistive losses [37]. These resistive losses are predominantly due to the ZnO:Al window layer. We developed a spreading resistance model in order to get theoretical predictions of the performance of thin film solar cells under concentration. Compared to the lumped resistance approach where the link between size and series resistance has to be calculated in advance, our model directly takes as input the cell size, as well as the diode characteristics.

We found that very important scaling benefits, associated with the decrease in cell area from the actual cm² range to a μ m² range, are to be expected, especially in terms of efficiency. It was predicted that the Cu(In,Ga)Se₂ technology, which yields 20% efficiency at one sun for cells in the cm² range, can yield up to 30% efficiency under concentrated sunlight in the μ m² range, while conserving the stacking architecture and materials properties of standard Cu(In,Ga)Se₂ technology.

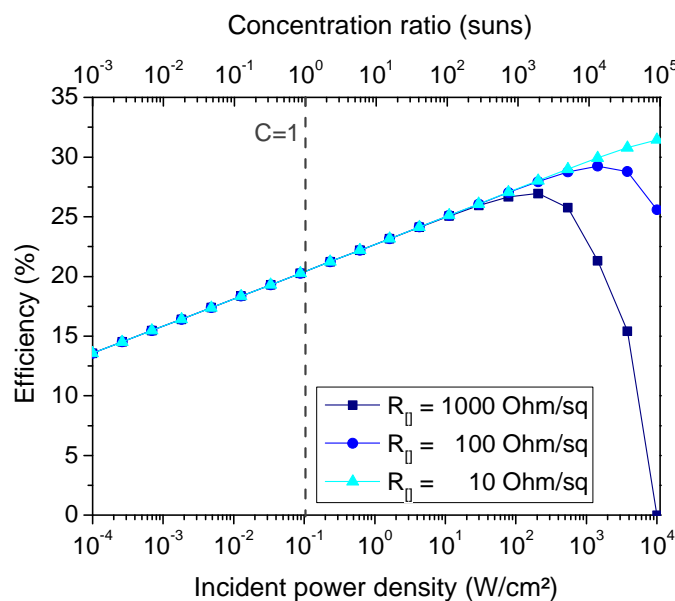


Figure III-16 : Efficiency vs. concentration for three different sheet resistances for a 10^{-5} cm² solar cell in the ring contact geometry.

We highlighted the importance of appropriate contact geometry, and ring contact has proven the most efficient due to a better distribution of current on the device. Moreover it avoids any shadowing of the cell, which results in higher photocurrent. Scaling effect can also help loosening the conductivity constraint on the window layer, enabling the use of highly transparent front contact. Indeed we study the efficiencies of cells of radius $18 \mu\text{m}$ of different sheet resistance (10 Ohm/square – 100 Ohm/square – 1000 Ohm/square) with concentration ratio for a ring contact (Figure III-16). We see that for the cell with a sheet resistance of 10 or 100 ohm/square, the resistance is hardly a limiting factor, and for the cell with sheet resistance of 1000 ohm/square, concentration effects are beneficial up to 5000 suns. Higher photocurrents are thus expected on microcells as the transparency of the window layer can be improved with greater freedom.

Our model however remains simple. No other resistive sources than the window layer were taken into account. This hypothesis is realistic given the low impact of these resistances on CIGS solar cells under AM1.5. The resolution of equation (III-8) becomes highly non-linear if a series resistance term is added to the expression on the diode current, making numerical convergence a lot more difficult. But this hypothesis will certainly be untrue at high concentration ratios for microcells. Indeed we saw that for a microcell spreading resistance can be made negligible even at high concentration. Therefore the other sources of resistance will become predominant and limit the efficiency to concentration ratio smaller than in the simulations presented above.

Our model does not take into account solar cell roughness either. Thin film solar cells are usually designed to have a non-flat surface, in order to decrease reflection and increase light trapping. Thus our model should be considered as a tool to predict the behavior of a cell under the same light power density, which surface is equal to the developed surface of a rough cell.

Our analysis has been limited to resistive scale effects. An important parameter for concentrator cell is the cell temperature that was considered constant up to now. As we scale down the solar cell, the thermal behavior of the cell can change as well. The next section is therefore dedicated to an analysis of thermal behavior of microcells under intense light fluxes.

4. Thermal analysis of microcells

4.1. Necessity to study thermal behavior of solar cells

Photovoltaic devices are heated up by the incident light flux. Under concentrated illumination the temperature increase can be very important, causing degradation. For example, Cu(In,Ga)Se_2 solar cells are stable at temperatures below 200°C . At higher temperatures the degradation can be

attributed to the diffusion of Cd in the absorber layer (or Zn in case of a ZnS buffer). This results in a shift of the space-charge region near the back contact, and thus decreases the performances of the cell [179]. In order to maintain a proper solar cell lifetime, it is crucial to ascertain that the maximum temperature increase under intense flux is below the degradation limit.

Moreover, even before the solar cell is irreversibly degraded, the increase in temperature leads to a decrease in solar cell performance, by the increase in saturation (recombination) currents [28], [180]. An increase in the intrinsic carrier concentration leads to an increase in the dark saturation current. Indeed the intrinsic carrier concentration is temperature dependent: $n_i \propto T^{\frac{3}{2}} \exp(-E_G/2kT)$, where the band gap E_G is also temperature dependent, $E_G = E_G(0) - \alpha T^2 / (T + \beta)$ (α and β are constants depending on the semiconductor) [181]. As a consequence, the open-circuit voltage drops when the temperature increases: $V_{oc}(T) = E_G(0)/q - kT/q \ln(BT^\xi / I_{sc})$, where B is a temperature independent constant, and $T^\xi \exp(-E_G(0)/kT)$ represents the temperature dependence of the saturation current. A moderate temperature increase can therefore decrease the solar cell efficiency, even if the temperature does not reach the damage threshold.

As we are planning to use intense flux on small solar cells, we have to evaluate the maximum temperature increase as a function of incident power.

4.2. Thermal scale effect

4.2.1. Thermal constants of the Cu(In,Ga)Se₂ solar cell components

The Cu(In,Ga)Se₂ solar cell thermal behavior depends on the thermal conductivity and thicknesses of each of its constituents (See numerical values in Table III-3).

Table III-3 : Thermal conductivities of the Cu(In,Ga)Se₂ solar cell layers and parameters used in the simulations

Layer	Thickness	Thermal conductivity (W/cm/K)	References
Glass	3 mm	0.009	[182]
Molybdenum	1 μ m	1.37	[183]
Cu(In,Ga)Se ₂	3 μ m	0.1 (CuGaSe ₂ : 0.11 - CuInSe ₂ : 0.086)	[184]
ZnO:Al	500 nm	0.15	[185]

The temperature gradient across a thin film is a function of the incident heat flux, film thickness and thermal conductivity. According to Fourier's law, the thermal conduction flux is $\vec{Q} = -k_{th} \vec{\nabla} T$, where Q is the heat flux, k_{th} the thermal conductivity and T the temperature. In one dimensional

analysis, for a uniform film of thickness t that receives a heat flux perpendicular to its surface, the temperature difference between front and back surface of the film is:

$$|\Delta T| = \frac{Qt}{k_{th}} \quad (\text{III-20})$$

Therefore when the film thickness is small and/or its thermal conductivity is high, the temperature difference stays rather small. One can see from this simple 1D analysis, and from the numerical values of Table III-3, that the glass substrate is the most important thermal component of a thin film solar cell. Therefore, in first approximation we will restrict our thermal study of Cu(In,Ga)Se₂ microcell to the study of a localized heating on a semi-infinite glass substrate.

4.2.2. Evolution of temperature with spot size on a homogeneous semi-infinite medium.

In order to model the local heating of a glass substrate, we will look at the general framework of local heating on a semi-infinite medium.

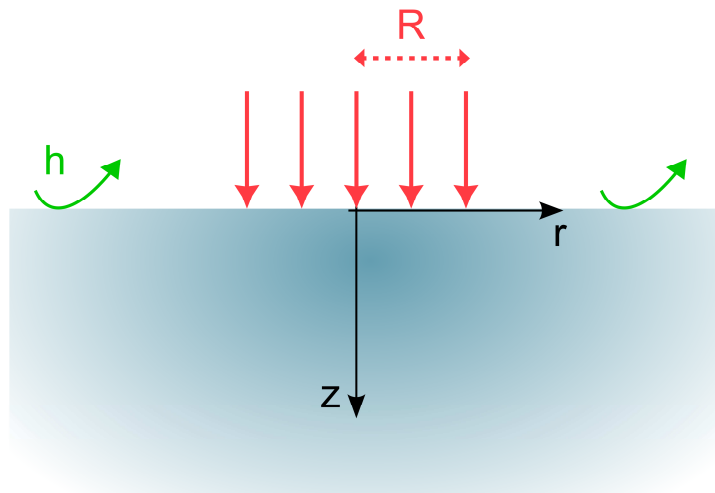


Figure III-17 : Semi-infinite medium under a localized heat flux ($r < R$), with natural convection at the surface.

We consider a semi-infinite medium that is uniformly heated on a small circular area of radius R at the surface (Figure III-17). We use a cylindrical coordinate system and neglect the variation of temperature with the angular coordinate, as we suppose a symmetry of revolution. The temperature in the media under steady-state conditions is given by the heat conduction equation [186–188]:

$$\Delta\theta = \frac{\partial^2\theta}{\partial r^2} + \frac{1}{r} \frac{\partial\theta}{\partial r} + \frac{\partial^2\theta}{\partial z^2} = 0 \quad (\text{III-21})$$

The boundary conditions are:

$$\theta \rightarrow 0, z \rightarrow \infty \quad (III-22)$$

$$h\theta - k_{th} \frac{\partial \theta}{\partial z} = \begin{cases} Q & (r \leq R) \\ 0 & (r > R) \end{cases}$$

where $\theta = T - T_{\infty}$ is the temperature elevation from the ambient, h the coefficient of natural convection, k_{th} the thermal conductivity defined in Fourier's law and Q the heat flux incident on the disk of radius R .

This equation has an analytical solution (see Appendix A):

$$\theta(r, z) = \frac{QR}{k_{th}} \int_0^{\infty} \frac{\exp(-\lambda z) J_0(\lambda r) J_1(\lambda R)}{h/k_{th} + \lambda} d\lambda \quad (III-23)$$

where J_0 and J_1 are the Bessel functions of the first kind of order 0 and 1 respectively, and λ is a mathematical variable. As Bessel functions are tabulated, this expression can be used directly in a calculation software, such as MATLAB®.

The temperature on the surface, where the temperature elevation is the highest, is :

$$\theta(r, 0) = \frac{QR}{k_{th}} \int_0^{\infty} \frac{J_0(\lambda r) J_1(\lambda R)}{h/k_{th} + \lambda} d\lambda \quad (III-24)$$

At the center, when convection is neglected, it can be shown that the temperature is [187]:

$$\theta(0,0) = \frac{QR}{k_{th}} = \frac{P}{\pi R k_{th}} \quad (III-25)$$

Where $P = Q\pi R^2$ is the total incident power. Therefore the maximum temperature is proportional to the source radius and incoming heat. This scale effect is what is observed on microelectronic devices [129].

We simulate the temperature on the surface of a semi-infinite glass substrate of thermal conductivity k_{th} ($9 \cdot 10^{-3}$ W/cm/K) (Figure III-18). We suppose that the surface is exposed to natural convection, the coefficient of natural convection h being $25 \cdot 10^{-4}$ W/cm²/K. The heat flux used in our calculation is 100 W/cm², which corresponds to a $\times 1000$ illumination at open-circuit voltage, where all the incident light power is converted to heat. We plot the temperature elevation from the ambient θ as a function of the dimensionless factor r/R , for different heat source of radii R . In agreement with equation (III-25), the maximum temperature elevation (at the heat source center) is proportional to the heat flux radius and intensity. Thus the maximum temperature elevation on a glass substrate at $\times 1000$ is 11 K for a heat source radius of 10 μ m.

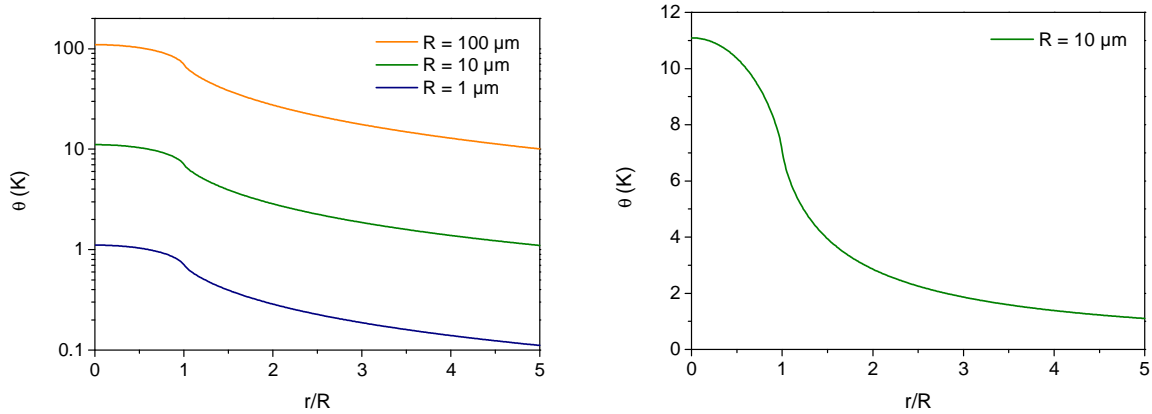


Figure III-18 : (left) Surface temperature elevation on a semi –infinite media for various heat source radii (1 μm -10 μm - 100 μm) as a function of the dimensionless variable r/R . (right) Detail of the surface temperature elevation for the 10 μm heat source. The heat source is 100 W/cm^2 ($\times 1000$), the coefficient of natural convection $25 \cdot 10^{-4} \text{ W/cm}^2/\text{K}$, and the bulk thermal conductivity $9 \cdot 10^{-3} \text{ W/cm/K}$.

For this 10 μm heat source radius, we look at the temperature elevation in the depth of the material (see Figure III-19). One can see that the temperature elevation rapidly decreases with depth, due to the exponential decrease in equation (III-23). The temperature elevation is confined near the heat source. For a material that has dimensions very large compared to the heat source, the semi-infinite approximation seems valid.

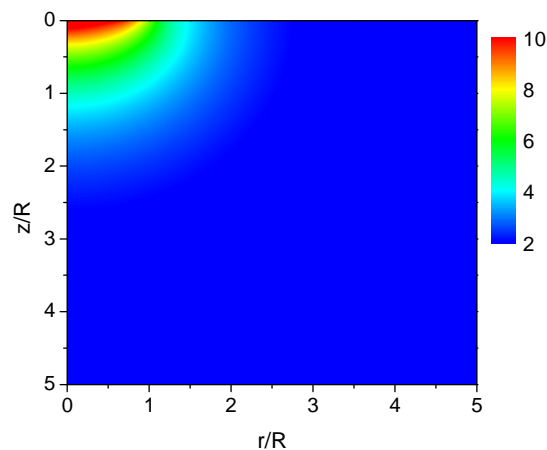


Figure III-19 : Temperature elevation on a glass substrate as a function of the dimensionless variables z/r and r/R , for $R=10 \mu\text{m}$. The position (0,0) corresponds to the center of the heat source of radius R .

Studying the behavior of a semi-infinite glass substrate gives a first insight in the thermal behavior of thin film solar cells. However for a more precise analysis, one needs to consider the stack of thin film layers of finite thickness under localized heating.

4.2.3. Prediction of temperature evolution on stratified thin film solar cells with spot size

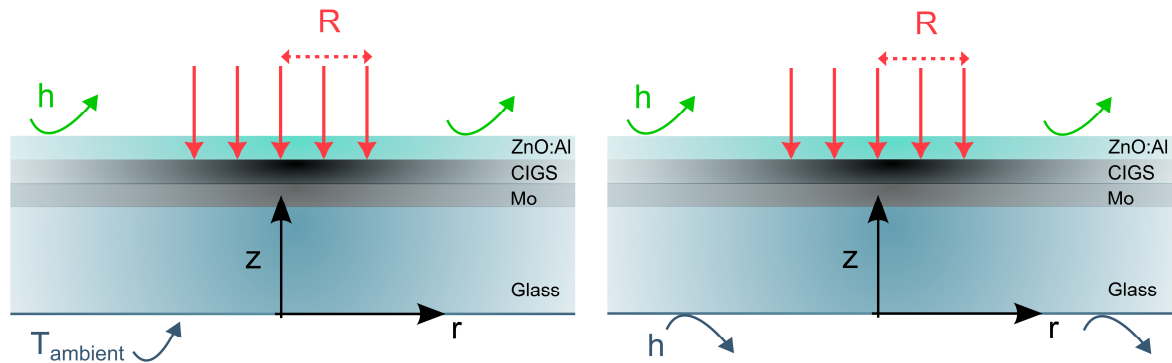


Figure III-20 : Thin film solar cell under a localized heat flux at the window/absorber interface ($r < R$), with natural convection at the upper surface and (left) the ambient temperature or (right) convection imposed at the back of the substrate

We now consider a stack of four layers: glass, molybdenum, Cu(In,Ga)Se_2 , ZnO:Al (Table III-3). The layers are considered infinite in the plane coordinate but have finite thicknesses. For each layer we define a thickness and thermal coefficient. The heat source is supposed to arrive at the ZnO:Al / absorber interface, and has a radius R . In reality the heat source is not completely localized at the interface but is distributed throughout the absorber. The back plane of the glass substrate is either kept at the ambient temperature or is prone to convection while the upper ZnO:Al surface is always prone to convection. At each of the interface we ensure the continuity of temperature and heat flux.

The temperature in each layer i can be written as :

$$\theta_i(r, z) = \int_0^{\infty} (A_i \exp(-\lambda z) + B_i \exp(\lambda z)) J_0(\lambda r) \lambda d\lambda \quad \text{(III-26)}$$

where the coefficients (A_i, B_i) are the solution of a linear problem, set by boundary conditions (see Appendix A).

We simulated a Cu(In,Ga)Se_2 solar cell under 100W/cm^2 for a source of $100\ \mu\text{m}$ radius with material parameters of Table III-3. The temperature in the stack is smaller than in the semi-infinite approximation. The role of convection at the back surface has only a limited influence. The metal, and to a lesser extent the absorber and window layers, spread the heat on the glass surface, which results in a more than two times decrease in the maximum temperature.

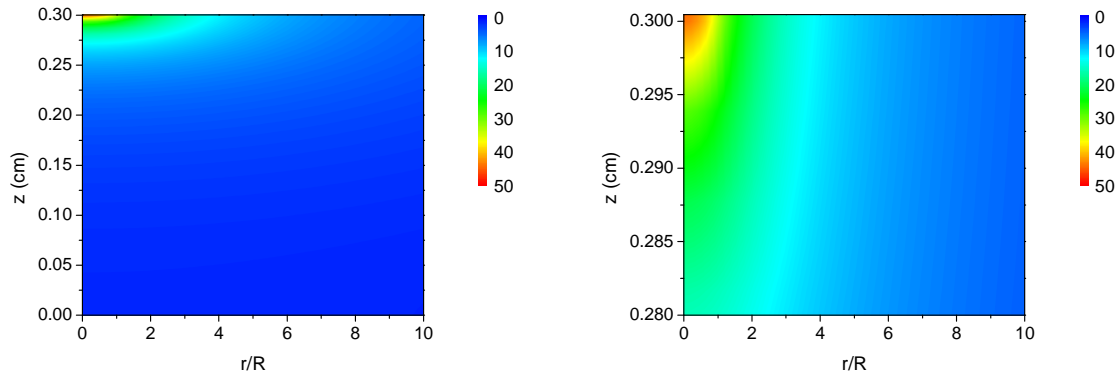


Figure III-21 : (left) Temperature increase on a Cu(In,Ga)Se_2 substrate as function of the dimensionless variable r/R , for $R=100\ \mu\text{m}$ for a $100\ \text{W/cm}^2$ heat source. (right) zoom on the surface. The thickness of the Mo is set to $1\ \mu\text{m}$, that of CIGS to $3\ \mu\text{m}$. The back surface is prone to convection.

One can see in our simulations that the maximum temperature increase from the ambient for a $100\ \mu\text{m}$ radius heat source is 44°C , even under high fluxes at $\times 1000$ ($1\ \mu\text{m}$ thick molybdenum). If the thickness of the layers that have a thermal conductivity higher than glass is decreased, the maximum temperature will rise, and ultimately reach the value for a standalone glass substrate (See Appendix A).

4.2.4. *Consequence for the illumination of a microcells array*

We have seen in the previous paragraphs that under localized radiation, the temperature elevation stays confined close to the source and decreases far from it. However in real conditions, several microcells at finite distance from each other will be illuminated simultaneously (Figure III-22). In order to deduce the temperature of the microcell array, we have to take advantage of the superposition principle, consequence of the linearity of the heat equations, and superimpose the individual solutions for localized heat generation.

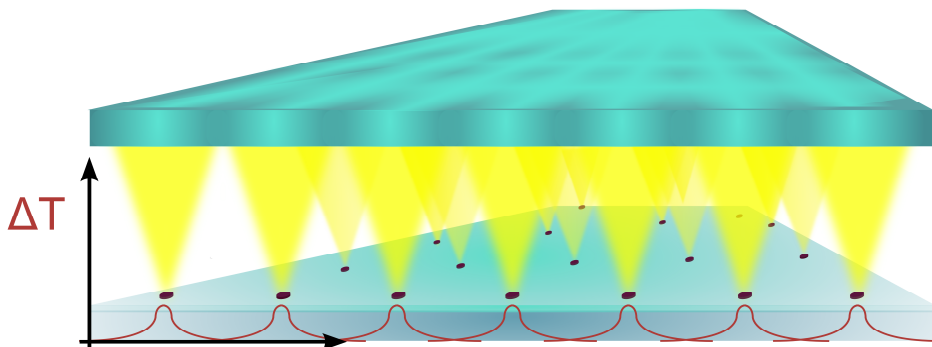


Figure III-22 : Sketch of the superposition principle for a microcells array illuminated simultaneously. The temperature of the array is given by the superposition of the temperature field of individual microcell.

Standard thin film flat plates under AM1.5G have a steady-state temperature around 50 - 60 °C. This steady – state is the equilibrium between homogeneous heat generation on the panel due to the incident sunlight and heat evacuation by convection (main heat dissipation path on a flat plate) and by radiation [28]. From an energetic point of view, the average temperature elevation on an array of microcells illuminated simultaneously should be the same as on a flat plate illuminated homogeneously with the same heat power and same boundary conditions. Therefore if the heat source is the AM1.5 spectrum (100 mW/cm²), and the microcell array is prone to convection on front and back surface, we should find an average temperature elevation around 50°C – 60°C. Thus the temperature elevation from the ambient we have calculated in the previous sections, are upper limits of the temperature difference between a microcell array and an illuminated flat plate.

One should note that on a microcell array, the best configuration in terms of material saving is to have a Cu(In,Ga)Se₂ layer that is discontinuous, with the absorber confined to the microcell location. (See Chapter VII). Thus on a microcell array, the lateral heat spreading will be conducted through the Mo back contact (and possibly front ZnO depending on the geometry), instead of being conducted by the ZnO/Cu(In,Ga)Se₂/Mo stack as in the above simulations. However the thermal conductivity of Mo being more than an order of magnitude higher than that of Cu(In,Ga)Se₂ and ZnO, a small increase in Mo thickness would compensate the loss of lateral dissipation in the Cu(In,Ga)Se₂ and ZnO layers.

4.2.5. Discussion

We used a simple analytical simulation to look at the 3D thermal behavior of a Cu(In,Ga)Se₂ solar cell. Our results are general. By adapting the thicknesses and the thermal conductivity coefficients, we can extend our work to other solar cells, either in thin film or not. Resorting to analytical solutions enabled us to show the scaling effect that is taking place for localized heating on a large medium (equation (III-25)). Indeed we found that the maximum temperature increase is proportional to the incident heat flux and to the radius of the heat source on a semi-infinite substrate when convection is neglected. To keep the cell operating temperature constant under an incident flux density increased 10 times, the heat source radius has to be 10 times smaller. In other words a 10 μm microcell under ×1000 illumination should have the same temperature as a 100 μm microcell under ×100. The use of analytical solutions is not compulsory and standard finite element method would have given similar results. In order to get the exact temperature of a particular module or microcell array, more details should be added (thermal coefficient and thicknesses of encapsulating materials, wind velocity, temperature dependence of thermal conductivity...), and numerical analysis becomes mandatory.

Our calculations suppose that the total incident light flux is transformed into heat in our device. This is indeed true at open-circuit voltage, but not at the operating point. If we take into account electricity generation roughly 20% of the incident flux should not result in heat generation at maximum power point. Therefore our temperature increase predictions are upper limits to effective temperature increase.

We have seen that the glass substrate was the most important thermal element of a thin film solar cell. However the metallic back contact lowers the temperature increase. If the devices are in the 100 μm – 10 μm range a use under ultra-high fluxes with glass substrate is possible without detrimental temperature increase. If one wants to lower the maximum temperature increase in a microcell array, the most effective leverage would be to use a metallic substrate. This field is under intense study in the thin film community and especially Cu(In,Ga)Se₂ community [40], but was not tackled in this thesis.

For a microcells array, the temperature field calculated for a microcell under illumination should be superimposed to that of the other microcells of the array. As a consequence under simultaneous illumination, the average temperature increase in a microcell array should be similar to that of a flat plate (50°C – 60°C). Locally however, the temperature elevation may differ significantly from the average flat-plate temperature. These local temperatures elevations stay smaller than those calculated above, for individual microcell with respect to the ambient temperature.

In our calculations we did the approximation of a uniform heat source. However in a concentrating system the light flux impinging on a solar cell is never perfectly homogeneous, but can be closer to a Gaussian-shape. This non-uniformity impacts the form of the temperature field, but does not change dramatically our analysis.

It should finally be noted that in this chapter, we insisted on the maximum local temperature increase, as this value is important concerning the damage threshold and device life time span. However, from an experimental point of view, the parameter that will impact current-voltage measurement for example is not the maximum but the average temperature over the microcell. Therefore it is interesting to study the average temperature as a function of microcell size. The relationship between these two parameters is not straightforward, but a departure from linearity can be observed for small devices. (See Appendix A).

5. Conclusions

We studied the potential benefits of using microscale thin film solar cells under intense illumination. The use of concentration is promising as it is a way to increase cell efficiency and lower material consumption at the same time. However due to the concentrated light fluxes resistive losses and heating are more pronounced. For thin film solar cells the increase in resistive losses on standard cells limited to date the maximum obtainable efficiency at 14 suns [36]. A new architecture was thus needed to overcome these limitations.

Miniaturizing solar cells, or electronic components in general, leads to two beneficial scale effects: the reduction of spreading resistance losses and of the temperature elevation. The resistive losses are governed by a dimensionless parameter $\alpha = R_{\square} a^2 C J_{ph}(1 \text{ sun}) q / AkT$. Thus a decrease in the solar cell area a^2 by a factor X can compensate the X -fold increase in the product of concentration ratio C by the sheet resistance R_{\square} . In our analysis R_{\square} is the sum of the sheet resistances of layers in the solar cells in which the current flows laterally. Local increase in temperature for a microcell is also dependent on the cell radius. In the limiting case of a microcell considered as a semi-infinite media heated locally without convection, the maximum temperature increase is exactly $\theta = QR/k_{th}$, where Q is the heat flux density and R the solar cell radius. For a microcell array, the temperature is found as the superposition of the temperature field for each microcell. We have seen that the average temperature on the array is that of a flat plate, with local temperature increases on the microcell that are size dependent. For $\text{Cu}(\text{In,Ga})\text{Se}_2$ in particular, going to devices with lateral dimensions smaller than $100 \mu\text{m}$ will enable ultra-high flux operation, both from a thermal and resistive point of view. As a consequence an important efficiency increase is expected.

We modeled these two scale effects numerically and highlighted the governing parameters. However the electric and thermal modelings are kept separated. No coupling effects are therefore studied. The next step could be to have a more general framework, with FEM calculations for example.

From our results we have evidenced specifications for the design of proof of concept devices. The fabrication and test of such thin film microcells and the link to simulation results is the object of the next chapters.

6. Memento

The contribution of a layer, in which currents flows laterally, to the total resistance of a solar cell decreases with the miniaturization of the cell. The dimensionless factor controlling the scale effect is $\alpha = R_{\square} a^2 C J_{ph}(1\ sun) q / AkT$, where R_{\square} is the sheet resistance, a the cell radius, A the ideality factor, $J_{ph}(1\ sun)$ the photocurrent density at 1 sun and C the concentration ratio.

For solar cells smaller than 200 μm in diameter, where the only source of resistance is the window layer of sheet resistance of 10 ohm/square, the optimum efficiency of the cell is reached at a concentration higher than $\times 100$, according to our simulation results.

The heat flux density generated by the sunlight on a solar cell leads to a temperature increase from the ambient, which diminishes with decreasing device size. The maximum temperature increase for a given heat flux density is exactly proportional to the device radius, if the cell is considered as a semi-infinite medium, and convection is neglected. Slight departure from linearity can be expected otherwise.

Maximum temperature increase on a solar cell decreases with thicker Mo layer. For a 1 μm thick Mo layer the maximum temperature increase on a $\text{Cu}(\text{In,Ga})\text{Se}_2$ solar cell of 100 μm diameter at $\times 1000$ suns is around 45°C.

Miniaturized solar cells can withstand the resistive and thermal constraints of concentrated photovoltaics.

CHAPTER IV. CU(IN,GA)SE₂ MICROCELLS FABRICATION AND CHARACTERIZATION

1. Introduction	102
2. Design of proof of concept prototypes	104
2.1. Geometry of the cells	105
2.2. Size and contact geometry	105
2.3. Choice of the absorber	105
2.4. Sketch of the chosen microcells design.....	106
3. Fabrication process step by step	107
3.1. Fabrication process overview.....	107
3.1. Fabrication steps in details.....	108
4. Adaptation of the process to finished cells	113
5. Behavior of microcells in standard testing conditions	114
5.1. Statistical analysis of dark current-voltage characteristics	114
5.2. Analysis of AM1.5 current-voltage characteristics.....	118
5.3. Discussion	120
6. Conclusion	127
7. Memento	128

1. Introduction

The previous chapter showed the benefits that can be expected from scaling down solar cells in general, and thin film Cu(In,Ga)Se₂ in particular. No thin film solar cells in the 10 - 100 μm range were fabricated, when this PhD work began. An attempt to form CuInSe₂ mesa diodes of 0.5 × 0.5 mm² in 2003 was reported [189]. Designs and appropriate fabrication processes for Cu(In,Ga)Se₂ microcells need therefore to be developed. However in 2009, an array of 10 μm × 10 μm Cu(In,Ga)Se₂ photodetectors was fabricated by structuring a co-evaporated absorber [190]. Even if photodetectors do not have the same design requirements as a solar cell, i.e. minimum dark current instead of maximum conversion efficiency, the fabrication process can be very similar. These pixels were fabricated with classic microelectronic techniques that also have been employed by others to develop micro photovoltaic devices on crystalline materials. We will briefly review these approaches to put in perspective our own fabrication processes.

Photovoltaic crystalline microcells have been designed to get flexible modules. By covering a flexible substrate by a multitude of crystalline microcells, stretchable and flexible modules are fabricated [154], [191–197], and very small devices are tested. Very low concentrations are used in these applications and the cells are not designed as concentrator cells.

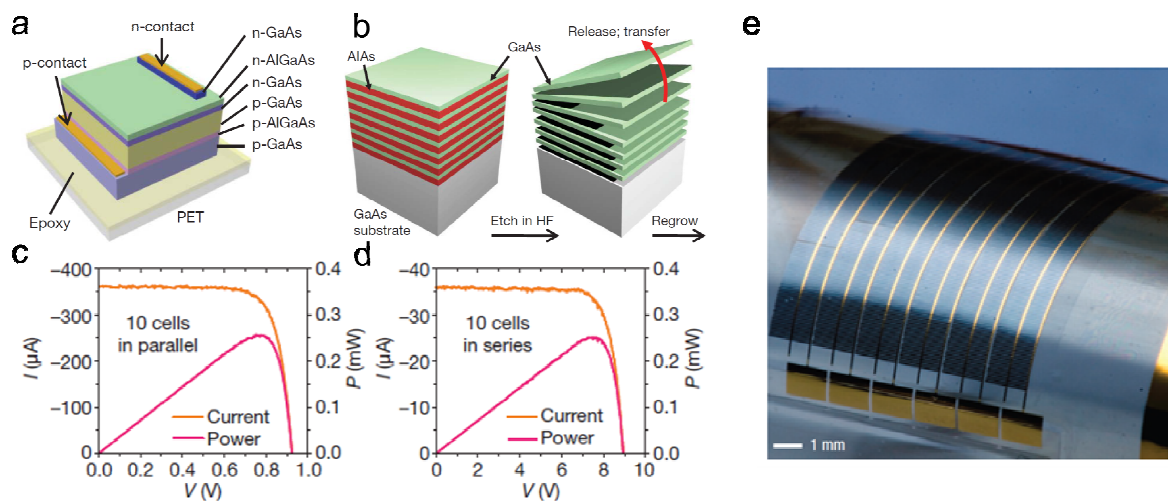


Figure IV-1: (a) Sketch of a GaAs solar cell (b) Release multilayer epitaxy principle. Current-voltage characteristics of 10 microdevices (c) in parallel, (d) in series. Reproduced from [192] (e) Optical image of a module bent along a direction parallel to the widths of the c-Si microcells (1.5 mm long and 50 μm large) [154].

Some of the studies are carried out on single junction GaAs solar cells [192], [194]. A multilayer epitaxy assembly, vertical etching and selective chemical etch of AlAs sacrificial layers release

microcells from a wafer (Figure IV-1 b). Then transfer printing or solution assembly can transfer microcells onto a host substrate. Photovoltaic devices of $500\ \mu\text{m} \times 500\ \mu\text{m}$ with efficiency of 14.5% have been reported, smaller devices have been made but efficiencies are degraded due to the relative increase in edge effects. Other microcell approaches are dedicated to Si cells. By using very similar techniques (lithography, etching and transfer printing), modules consisting of hundreds of interconnected microcells are realized (Figure IV-1 e). The weak absorption of crystalline silicon requires microcells that are at least ten times thicker than GaAs microcells. Si microcells of $250\ \mu\text{m}$ diameter have reached 14.85% efficiency ($14\ \mu\text{m}$ thick) [193]. Mini modules ($0.95\ \text{cm} \times 0.63\ \text{cm}$) based on $45\ \mu\text{m}$ wide and $1.5\ \text{mm}$ long and $15\ \mu\text{m}$ thick microcells yielded 6-8% conversion efficiencies [195] (Figure IV-1 e). A few attempts are also made to use multijunction devices. Dual junction GaInP/GaAs microcells ($<0.5\ \text{mm}^2$) transferred on a polyimide substrate led to a 12.8% efficient $24\ \text{cm}^2$ module under AM1.5G [198].

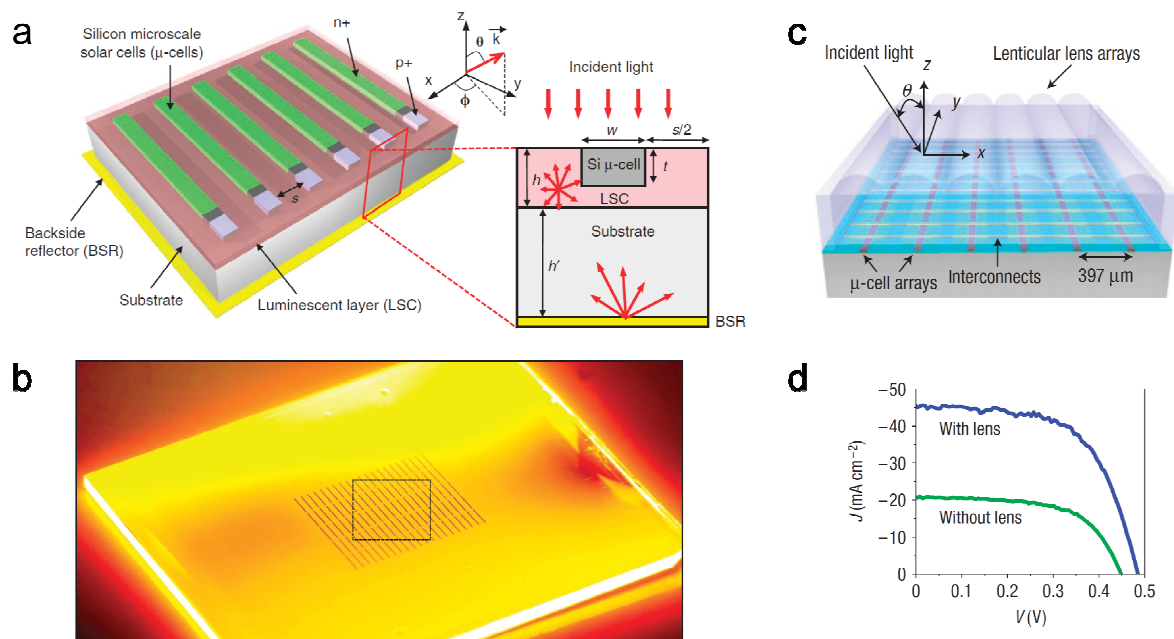


Figure IV-2 : (left) c-Si microcell array embedded in a luminescent waveguide : (a) sketch and (b) optical image Reproduced from [196] (right) (c) c-Si microcell array with lenticular lens array . (d) Current voltage curve show a 2.5 fold improve of the maximum power output for a optical concentration of x4. Reproduced from [154]

Innovative fabrication techniques are invented to make the most out of these microcells. Self-tiling techniques are developed to transfer microcells that are in solution to a host substrate in a well-defined pattern, by controlling interfacial energy. This self-assembly technique is developed for devices that are too small for robotic assembly ($<60\ \mu\text{m} \times 60\ \mu\text{m}$). For bigger devices micro-transfer printing is used to pick and place arrays of microdevices through a polymeric stamp [34], [198]. Modules made of Si bifacial microcells embedded in a luminescent waveguide increase the module

efficiency by using inter-microcell spaces as a collecting area for the luminescent concentrator (Figure IV-2 b). Threefold increase in power output is observed for this module compared to module with the same cells without concentration [196]. In order to use inter-microcell spaces, lenticular concentrator arrays can also be used and result in a 2.5 fold increase in output power compared to non-concentrated illumination (relative however to a $\times 4$ optical concentration) (Figure IV-2 c and d). A very low concentration module is thus created based on microcells. These innovative designs based on crystalline microcells show encouraging possibilities but their performances are still lagging behind those of state-of-the-art solar cells, in terms of efficiency [199].

Concerning crystalline devices, we can see that there is a gap to bridge between highly efficient concentrator cells that are designed for a use under ultrahigh fluxes and lower efficiency microdevices designed for flexible applications. For thin film concentrator cells, high efficiencies are needed on miniaturized cells. At first sight this requirement seems very ambitious, but we can reasonably expect good efficiencies of Cu(In,Ga)Se₂ devices even at small scale. Indeed $10\ \mu\text{m} \times 10\ \mu\text{m}$ Cu(In,Ga)Se₂ pixels photodetectors show small leakage currents at -1V, of the order of 10^{-7} - 10^{-8} A/cm² [190], which is the sign of limited dark current and high shunt resistance.

In this thesis we focus on Cu(In,Ga)Se₂ microcells. We want to have proof-of-concept devices, made to evaluate the potential of thin film microscale concentrator cells. Thus our fabrication process is not intended for the first generation of prototypes to be readily transferable to the industry. The aspects concerning more closely industrial applications will be discussed in Chapter VII. The elaborated fabrication process relies on thin film deposition techniques, but also transfers some microelectronic processing and structuring techniques, from which a brief overview was given here above.

This chapter is organized as follows. First, the design of thin film Cu(In,Ga)Se₂ microcells is described, then the fabrication process and its optimization are presented. Finally, electrical characterizations are carried out on the Cu(In,Ga)Se₂ photovoltaic microcells, to verify if they are good photovoltaic devices and control the fabrication process.

2. Design of proof of concept prototypes

Several parameters have to be reviewed in order to determine the most appropriate design for microscale Cu(In,Ga)Se₂ solar cells.

2.1. Geometry of the cells

We decided to fabricate solar cells that have a cylindrical symmetry. First, it is a simple geometry that enables easy comparison to the theoretical models, developed in the previous chapter. Then, as these microcells are intended to be used under concentrated illumination, it is a shape that is adapted to concentrating optics. Indeed, our concentration experiments will mainly be conducted using laser sources linked to microscopes that results in disk-shaped spots. As we have seen in Chapter III paragraph 3.2.6, this geometry will give results that can be easily generalized to various geometries.

2.2. Size and contact geometry

Our simulations show that the dimensionless factor governing the problem of spreading resistance is $\alpha = R_{\square} a^2 C J_{ph}(1 \text{ sun}) q / AkT$. We deduced that decreasing the area of the cell could compensate the losses associated with increased current density, due to light concentration. We have seen that with devices smaller than 10^{-3} cm^2 using 100 suns or more seemed reasonable. We also showed the importance of a good contact geometry. We will therefore use peripheral contact deposited outside the microcells, to avoid shadowing. In the thermal study, we found that for devices made solely of glass using 100 W/cm^2 ($\times 1000$ illumination), the temperature elevation is below 100°C for devices up to $100 \mu\text{m}$ radius. For the stack, the molybdenum layer helps heat evacuation and the temperature elevation is smaller.

These two aspects, resistive and thermal, are in good agreement. Devices with diameter varying between $500 \mu\text{m}$ down to a few micrometers will enable a good study of these scale effects. As a reference, four 0.1 cm^2 cells are present on each substrate.

2.3. Choice of the absorber

There are two solutions to design thin film Cu(In,Ga)Se_2 microcells. One can use an absorber that is selectively deposited at the microcell location. This is the preferable geometry in terms of material consumption. One can also limit the microcell area by structuring only the front side of the solar cell, and keeping the absorber on the whole substrate. This solution has the advantage of decoupling the results concerning the miniaturization of the cell to the problems linked to edge effects. We chose the latter for the first prototypes. This allows us to work on as-grown co-evaporated absorbers that are the state-of-the-art devices to date. The absorbers are coming from our laboratory that received a co-evaporation system during the second year of this thesis work, but also from the pilot line of Würth Solar. The absorbers coming from Würth Solar are referred to as "industrial" samples; the

samples with IRDEP absorber will be referred to as “IRDEP” samples. We use our own co-evaporation facility to vary some of the important absorber parameters for this study, such as resistivity.

The extension of our results to selectively deposited absorbers will be treated in Chapter VII.

2.4. Sketch of the chosen microcells design

A sketch of the prototype microscale Cu(In,Ga)Se₂ solar cells is given on Figure IV-3. The absorber and buffer layers are kept on the whole substrate. An electrically insulating layer is inserted between the buffer and front contact and structured. This layer prevents the window layer from being in contact with the rest of the junction. Given the low resistivity of intrinsic ZnO and CdS buffer layers (See Table III-1), current flow is limited to the holes patterned in the insulating layers. Indeed, we can calculate the spreading length of current in the CdS according to (Equation (III-10)). We find $l_{illumination} = \sqrt{AkT/qR_{\square}CJ_{ph}(1\ sun)}$ that can be as small as 300 nm. For cells of diameters between 5 μm and 500 μm, this current spread is negligible. However if the CdS layer properties are changed drastically, by photoconductivity for example the diode current would increase due to improved conduction and current spreading. For the current spreading due to Cu(In,Ga)Se₂ we find a length of at least 3 μm. Thus for the smallest devices, current spreading in the absorber may not be neglected.

In order to take a peripheral contact on the cells, a metal layer is deposited. The metal is deposited before the window layer in order to be structured simultaneously with the insulator. This enables a good alignment between the electric and optical part of the design (the metal is thick enough to be considered opaque). The ZnO:Al window layer is then deposited on the whole substrate, and electrically connects the solar cell to its metal front contact.

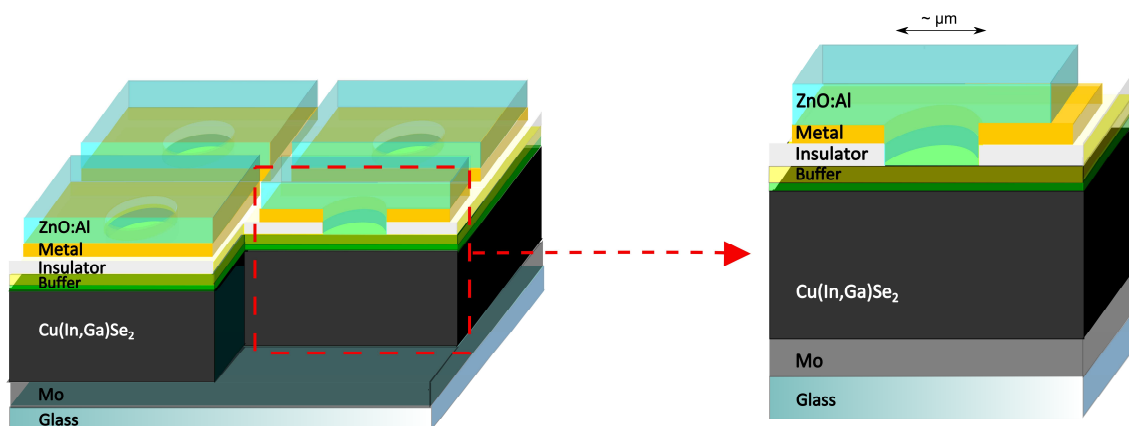


Figure IV-3 : Sketch of the cross section of a Cu(In,Ga)Se₂ prototype microcell array and zoom on an individual cell.

In order to fabricate these prototypes we have to use a structuring tool to pattern the holes in the metal and insulating layers. Different steps of the classic Cu(In,Ga)Se₂ solar cell deposition also need to be adapted. We will therefore give more details of the specific optimization of the fabrication process of microcells.

3. Fabrication process step by step

3.1. Fabrication process overview

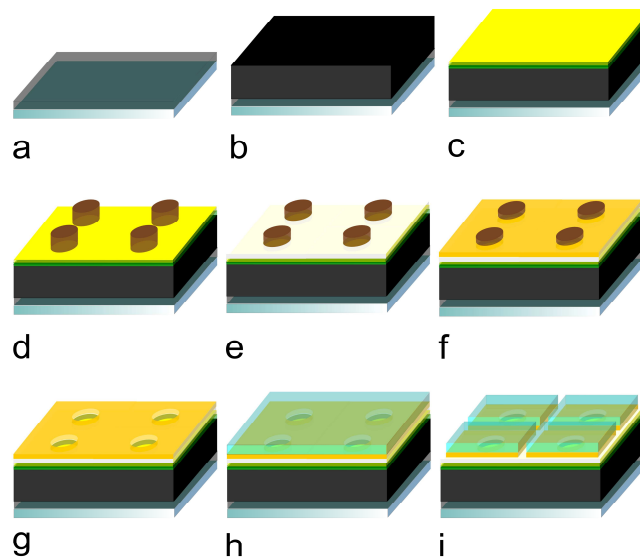


Figure IV-4 : Illustration of the microcell fabrication process

Fabricating a microcell consists in numerous steps. Figure IV-4 sums up the principal phases. The process begins with the deposition of a Mo layer on soda-lime glass (a) and the co-evaporation of a 1-3 μm thick CIGS absorber layer (b). These steps can be done in our laboratory or at Würth Solar facility for the industrial cells. Then a CdS layer is deposited in our laboratory by chemical bath deposition, and an intrinsic ZnO layer by RF sputtering (c). The microcells are defined with photolithography: a resist layer is spin-coated and illuminated through a patterned mask. After the development step, an array of cylindrical blocks (d) protects the sample during the deposition of a ~ 400 nm thick SiO₂ insulating layer (e), and a 20nm/300 nm thick Ti/Au conductive bilayer (f). The resist is removed in acetone (lift-off process) (g), and the ZnO:Al front contact is deposited by sputtering (h). The microcells are connected in parallel as they share the same back and front contact. In order to test the cells individually, we etch selectively both the ZnO:Al and Au layers on strips around the microcells (i). The microcells have therefore the same back contact but individual front contacts. Not displayed on Figure IV-4 is the selective etch of ZnO:Al, that creates gold contacting pads to electrically test the microcells.

3.1. Fabrication steps in details

3.1.1. *Cu(In,Ga)Se₂ deposition*

Cu(In,Ga)Se₂ is deposited on a Mo coated soda lime glass. Our industrial samples come from Würth Solar, where this step is done on an in-line co-evaporation system [75], [76], [200] (See Chapter II for more details on co-evaporation). Cu(In,Ga)Se₂ layer deposited at IRDEP are evaporated in a laboratory system that handles 10 × 10 cm² substrates. A classic three-stage process is followed [55], [73]. In this process the elemental rates are varied in three phases in order to create a well-controlled V-shape Ga profile in the absorber by the alternation of copper poor – copper rich – copper poor phase [79].

3.1.2. *Buffer layers deposition*

CdS is deposited at IRDEP by chemical bath deposition (CBD) [95], [98]. The bath is composed of cadmium acetate (Cd(CH₃CO₂)₂), thiourea (SC(NH₂)₂) and ammonia (NH₃) in aqueous solution. The deposition is done at 65°C under constant agitation during approximately 5 minutes. The samples are then rinsed in distilled water and any parasitic particle (Figure IV-5) is removed by ultrasonic agitation. The thickness of the CdS layer is around 50 nm.

The ultrasonic step is needed to have the samples as clean as possible. CBD is based on the precipitation of the desired layer from a solution. If there are any particles in the solution, precipitation can initiate on them, making these particles grow and deposit on the substrate (Figure IV-5). Such particles can come from the Teflon tank in which the CBD is done, which degrades slowly under intense use releasing small parts, or from an external source. On standard, large area solar cells, these particles have only a very limited influence, as they have a negligible surface coverage. However, for our process these particles can create ruggednesses on the surface that will perturb lithography (Figure IV-6). Therefore we decided to systematically clean the substrate by immersion in distilled water and exposure to ultrasound for 3 mn after CdS deposition to remove those particles.

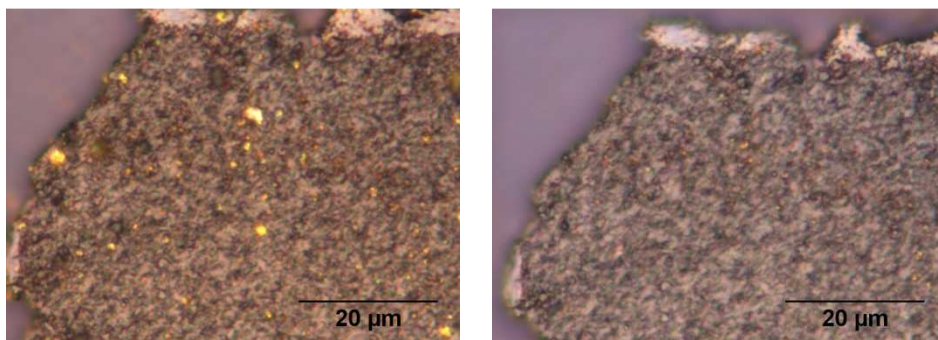


Figure IV-5 : Particles on a CdS layer on Cu(In,Ga)Se₂ before (left) and after (right) cleaning in ultrasounds.

Intrinsic ZnO is deposited on top of CdS by magnetron sputtering (Plassys) from a ZnO target. The deposited layer is around 50 nm.

3.1.3. *Photolithography*

Photolithography is an extensively used technique in microelectronics. As patterns in the 5 μm – 500 μm range are needed, this technique is especially suited for our microdevices. Photolithography is used to transfer a pattern created on an optical mask to a desired substrate, using specific resins that are light-sensitive. A photolithographic process consists in a series of steps: cleaning the substrate, spin-coating a photoresist, pre-baking the resist, illuminating it through a mask, finally developing it with an appropriate solvent called “developer”. There are two ways to use the photoresist pattern to structure the substrate: one can etch the substrate through the resist mask, or deposit a new layer and then dissolve the resist (this technique is called lift-off). More details on photolithography can be found in the Appendix C

After CBD, the samples are structured by photolithography. They are coated with a photoresist (AZ[®]2070 resist, AZ Electronics Materials) and spun at 4000 rpm (Karl Süss CT62) for 30 s. The resist is pre-baked at 105°C, exposed (365nm - 435nm light, through Karl Süss MJB mask aligner), baked at 105°C and then developed (developer MF 26A). An array of cylindrical blocks is thus created. Their profile show a slight undercut, necessary for the lift-off (See figure in Appendix C).

Photolithography is of standard use on flat crystalline surfaces. In this thesis we used it on rough polycrystalline Cu(In,Ga)Se₂ substrates (up to 200 nm of rms) [201]. The peak-to-valley height can be more than 1 μm on the industrial samples. Such a roughness is an obstacle for photolithography. Indeed if the resist that is spin-coated is too thin, there is a high probability that some of the peaks emerge from the resist, and thus perturb the structuring (Figure IV-6).

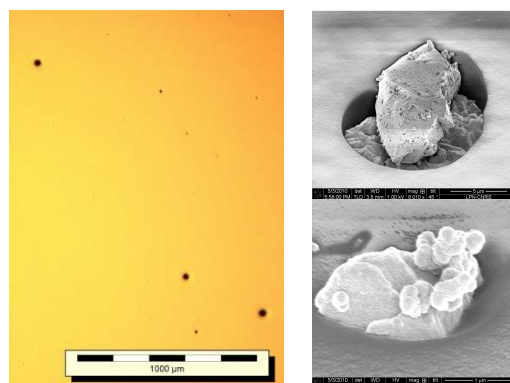


Figure IV-6 : (left) optical microscope image of the photoresist AZ2070 on Mo/CIGS/CdS/ZnO:i. One can see dark spots on the resist that are holes in the layer. (right) SEM image of various defects emerging from the resist.

One of the most intensively used photoresist is the AZ®5214 image reversal resist, i.e. it can either be positive or negative depending on illumination and baking. The reversible characteristic greatly eases the fabrication processes. However AZ®5214 is thin, typically 1.5 μm thick. To avoid peaks emerging from the resist during the process, we used the AZ® 2070 as structuring resist, which is 5.5 μm thick in the same spin-coating conditions. However it can happen that even with those precautions, the resist cannot perfectly cover the surface (Figure IV-6). In order to have the best photolithography, it is necessary to have the smoothest substrate, which explains our optimization of buffer deposition.

3.1.4. *Insulating layer deposition*

A 400 nm thick SiO₂ layer is deposited by electron beam evaporation under high vacuum as the insulating layer (Plassys MEB 400). The thickness of the layer is controlled by in-situ ellipsometry on an industrial wafer. This deposition tends to be isotropic, therefore the sidewalls of the photoresist structures would be covered if their profiles did not show a pronounced undercut.

3.1.5. *Metallization*

Metallization is done to get a good electrical peripheral contact with the ZnO:Al layer that will be deposited afterwards. As microcells are designed for use under concentration, each resistive source should be optimized. To determine the metal that shows the lowest contact resistance with ZnO:Al, we conducted transmission line measurements for different metals: Au, Al, Pt and Ti. Transmission line method consists in measuring the resistance between metal electrodes in contact with a thin film at varying distance (Figure IV-7), in order to determine the film/metal contact resistivity. More details on this technique and our TLM experiments can be found in Appendix B.

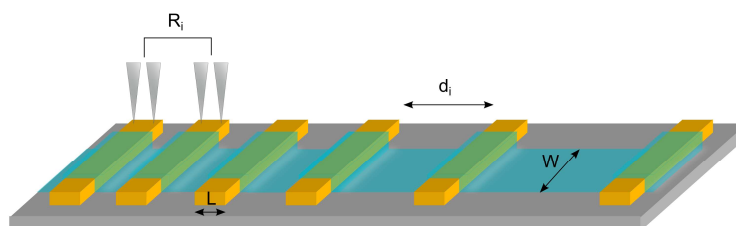


Figure IV-7 : (left) Sketch of the TLM structure. The metal is deposited prior to ZnO:Al sputtering. Metal pads width is L , and the width of the ZnO:Al deposit is W . The resistance R_i for a given spacing d_i is $R_i = 2 \times R_c + R_{\square}(d_i/W)$, where R_c is the contact resistance between the Au and ZnO:Al layers, and R_{\square} the ZnO:Al layer sheet resistance [202], [203].

Table IV-1 : Transfer length and contact resistivity between 5 metals and sputtered ZnO:Al. The contact Al/ZnO:Al is so resistive that a proper analysis of the TLM was made impossible.

Metal	Au	Al	Ni	Pt	Ti
L_T (μm)	2	/	7	7	16
ρ_c (ohm.cm^2)	$5 \cdot 10^{-7}$	/	$7 \cdot 10^{-6}$	$9 \cdot 10^{-6}$	$6 \cdot 10^{-5}$

From our data, it is clear that gold is the best contact to ZnO:Al (Table IV-1). Resistance is found linear with inter-electrode spacing and the statistical distribution of the measures shows small standard deviation. We chose gold as the front contact metal for microcells for the rest of our study. The contact resistance of the front contact, $R_{c,microcell}$, for a microcell of diameter $50 \mu\text{m}$ is 0.2 ohm or $4 \cdot 10^{-6} \text{ ohm.cm}^2$ (see Appendix B). The front contact has therefore a resistance that is sufficiently low to be neglected compared to the other sources of resistance in the solar cell. (see Chapter III). Therefore with gold the front contact resistance is never limiting the device performance.

The metallic front contact layer is deposited by e-beam evaporation (Plassys MEB 550 SL). A Ti/Au bilayer is chosen. The Ti layer is necessary for a good adhesion on SiO_2 , and Au enables a good contact with the ZnO:Al that will be sputtered afterwards. The thicknesses of the layers are respectively 20 nm and 300 nm. This deposition is more directive than that of SiO_2 and gold is not deposited in the undercut of the resist, preventing shunts between gold and ZnO (Figure IV-8).

3.1.6. Lift-off

The samples are then immersed in acetone to dissolve the photoresist. The lift-off is a critical point of the process. Depending on the quality of the lithography, especially the undercut profile of the structures, this step is problematic or not. In some cases, ultrasounds were used to remove badly defined sectors.

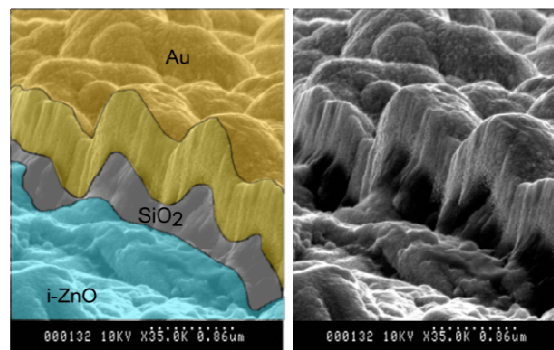


Figure IV-8 : ZnO:i/SiO₂/Ti/Au on Cu(In,Ga)Se₂ substrate after lift-off at the edge of a microcell. It can be seen that the SiO₂ layer extends laterally more than gold, due to less directive deposition. This geometry is desirable to avoid parasitic contacts between Au and i-ZnO.

3.1.7. Front contact deposition

After lift-off, aluminum doped zinc oxide is deposited on the whole sample by magnetron sputtering. The standard thickness of this layer is 400 nm. Sheet resistance is around 15 ohm/square (resistivity $6 \cdot 10^{-4}$ ohm.cm) and optical transmission is high (70% on average between 280 nm and 1100 nm), although important free carrier absorption occurs after 1000 nm.

3.1.8. Creation of individual front contacts

In order to test microcells individually, it is important to etch the front contact. Indeed ZnO:Al and gold layers are sputtered on the whole substrate, as the back contact is. Therefore microcells are connected in parallel as long as the ZnO:Al and gold layers are not structured. We found that chemical etch of the ZnO:Al layer in an acidic solution was highly suitable. In a $5 \cdot 10^{-2}$ mol/L hydrochloric acidic solution we found that the etching rate of ZnO:Al on glass was 8 nm/s and 15 nm/s on Cu(In,Ga)Se₂ substrate. This difference is most probably due to the effect of roughness on etching rate. The high etch rate permits a complete etch of a 400 nm thick ZnO:Al layer in less than 1 min. The under-etching is significant, in the range of 5 μ m for a 400 nm vertical etch, but is not a limitation in this process step. Moreover the acidic etch is selective and does not deteriorate the gold contact. This enables us to selectively remove the ZnO:Al layer from defined regions to create gold pads for easier contacting with electric probes (Figure IV-9 left). These pads are 100 μ m \times 200 μ m.

In order to etch the gold layer, Ion Beam Etching (IBE) was chosen. The IBE system, IonSys 500 - Roth&Rau, is equipped with a mass spectrometer that tracks the etched elements. Therefore one can detect the end of the etching when both gold and Ti adhesion layer signals decrease. This bilayer is etched on strips around the cells (Figure IV-9 left).

To create individual front contacts, two lithographic steps are done: one to etch zinc oxide, one to etch the metallic front contact. For these steps we use the photoresist AZ[®]5214, spin coated at 4000 round per minute during 30s. The resist is then pre-baked at 128°C for 3 min, insolated for 5 seconds, post-baked at 128 °C for 3 min and flooded for 35 seconds. The structures are then developed in MIF 726 developer for 30 seconds.

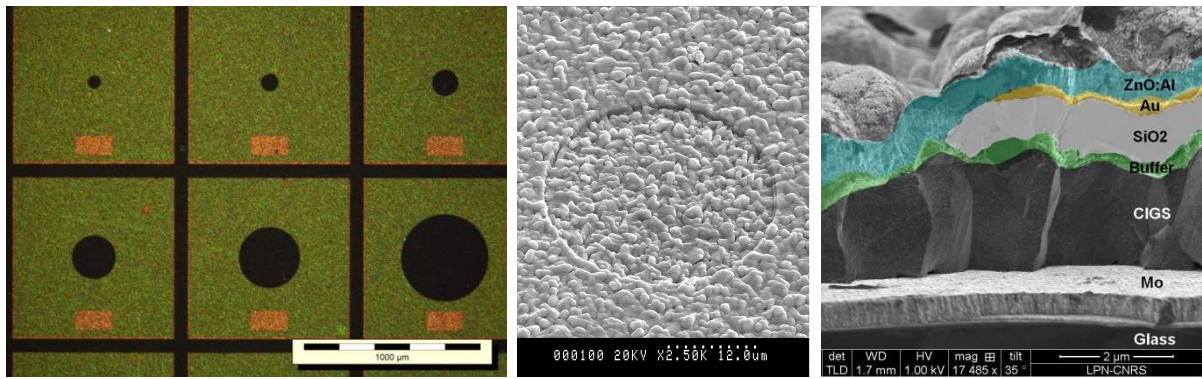


Figure IV-9 : (left) Optical microscope image of a sample at the end of the process. Black strips are the zones where ZnO and Au are etched, orange zones are zones where ZnO is selectively etched on gold, green zones are zones where ZnO is intact. The black disks are the microcells. (middle) SEM image of a finished sample. (right) Colorized SEM cross section image of a microcell.

3.1.9. Connection of the cells

In order to perform electric measurements, two electric wires are connected on the Mo, with an indium welding alloy. Front contacts are connected with micro-probes on the Au pads that are visible in Figure IV-9 (left).

4. Adaptation of the process to finished cells

The process described above is not suitable when starting from a finished cell. However it can be interesting to get information by testing substrates that have followed a classic fabrication process. The process from a finished cell has to be marginally adapted from our reference process (Figure IV-10). For finished substrates photolithography is used in to create the photoresist structure (d). The zinc oxide is etched either chemically or in IBE. None of these methods enable to distinguish between intrinsic ZnO and aluminum doped ZnO, thus both layers are removed. Chemical etch results in an under-etching of 5 μm whereas IBE does not create under-etch. Then the resist is kept on the substrate and the SiO₂ layer (f) and Ti/Au bilayer (g) are deposited. A lift off is performed to remove the photoresist and ZnO:Al is sputtered on the substrate (h). The individualization of the cells is done similarly to the reference process.

The principal difference between the two processes is the cleanness of the microcell edges. In the modified process SiO₂ and Ti/Au are deposited next to ZnO:Al, which is protected on its top by the resist. It may happen that these depositions slightly damage the ZnO:Al edges, and they are most probably not perfectly adjacent to the ZnO:Al columnar grains. Therefore when ZnO:Al is deposited on the whole substrate at step h, ZnO:Al may be directly in contact with CdS at the microcell edges,

creating zones of bad quality. (More details on the results of such microcells can be found in Appendix G.)

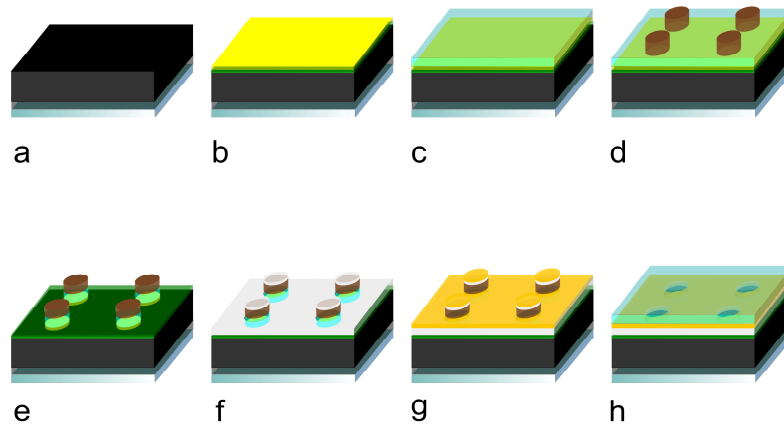


Figure IV-10 : Sketch of the fabrication process adapted for finished cells.

5. Behavior of microcells in standard testing conditions

At the end of the process, 244 microcells are created on a $2.5 \times 2.5 \text{ cm}^2$ substrate (16 cells of 15 different diameters between $5 \mu\text{m}$ and $500 \mu\text{m}$, and four 0.1 cm^2 cells). In order to verify if the fabrication process was successful, we proceed to standard tests: dark and AM1.5G current voltage measurements and external quantum efficiency.

5.1. Statistical analysis of dark current-voltage characteristics

5.1.1. Measurement setup

Current-voltage curves of the microcells are measured on a semi-automatic setup. Four terminal configuration is used with two wires welded on the Mo and two probes on the Au front contact. A Keithley 236 SMU source-meter acquires the measurement data. The setup is kept in the dark. A motorized chuck enables automatic measurement of all microcells.

5.1.2. Two-diodes model

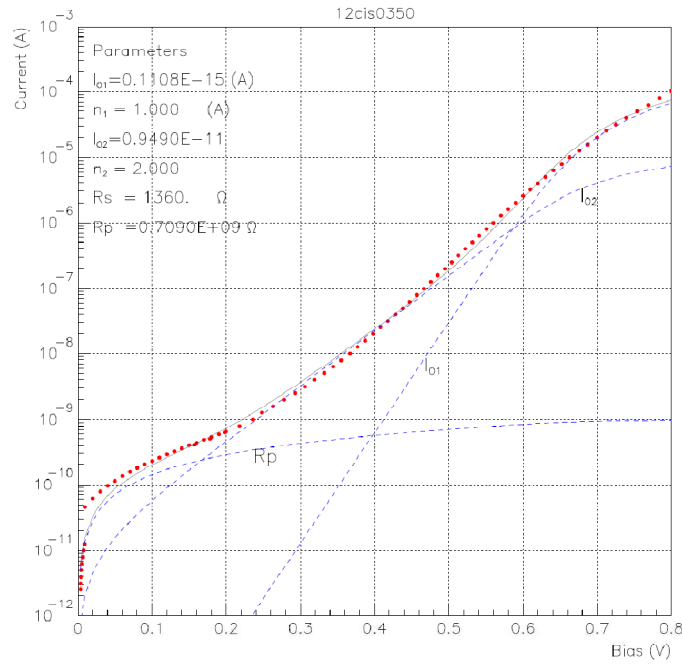


Figure IV-11 : Dark I-V curve for a 350 μm diameter solar cell of an industrial sample. Red dots are the experimental data, black line the fit and in dotted blue lines are displayed the components of the two diode model.

Dark current-voltage curves are fitted by a two-diode model (See Chapter II). Dark saturation currents J_{01} and J_{02} , series and shunt resistances are measured. This fitting model was preferred because the influence of the two recombination currents was detected on $V_{oc} - J_{sc}$ curves (See Chapter V).

5.1.3. Saturation currents

The saturation current densities J_{01} are found to be very small, around 10^{-10} mA/cm². However the large fluctuation of the results highlights numerical difficulty to determine this value. The saturation current densities J_{02} are within 10^{-5} to 10^{-4} mA/cm². These results show that the saturation currents found on our samples are nearly two orders of magnitude higher than those of state-of-the-art devices [25]. This is in agreement with the fact that this industrial sample comes from an in-line process, which results in more defects than state-of-the-art laboratory devices. However, the variation range of the dark current, more than an order of magnitude, is typical for Cu(In,Ga)Se₂ devices and observed even in these state-of-the-art devices [25].

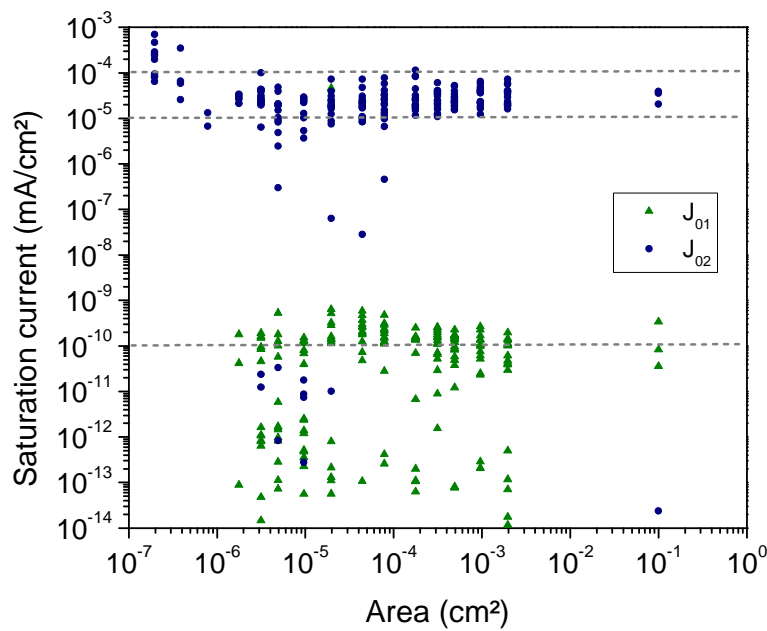


Figure IV-12 : Saturation currents J_{01} and J_{02} as a function of microcell size for an industrial sample. Dotted lines are guides for the eye.

It should be noted that these values do not vary much with microcell size (Figure IV-12). This means that in our devices the dark current is proportional to the cell surface. In other words the electric dimensions of the device are similar to the geometric ones. Current spreading in the CdS, i:ZnO and Cu(In,Ga)Se₂ is therefore very limited for a cell with a diameter above 10 μm and microcells are cylindrical from an electrical point of view. Notable exceptions are the 5 μm and 7 μm devices, where an increase in dark current is visible.

5.1.4. Series resistance

Series resistance of the microcells can also be estimated. It is found that series resistances, expressed in ohm.cm^2 , are of the same order of magnitude for all devices, and vary between 0.1 and 1 ohm.cm^2 (Figure IV-13). This resistance is of the same order of magnitude as for gridded laboratory 0.5 cm^2 devices, which is around 0.3 ohm.cm^2 , but generally below [25].

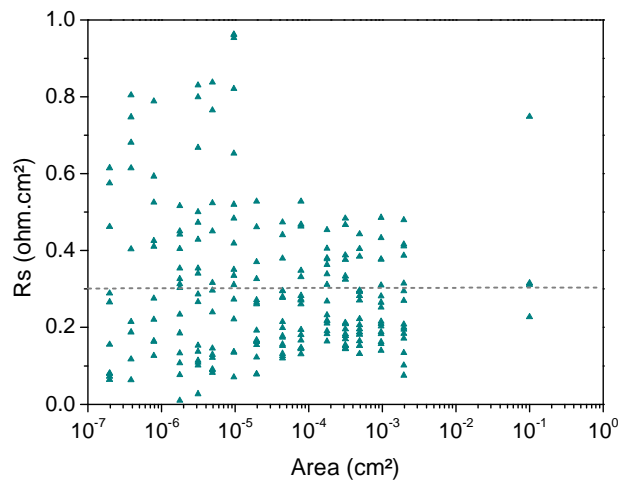


Figure IV-13 : Series resistance as a function of microcell size for an IRDEP sample. The dotted line corresponds to the average of series resistance on state-of-the art gridded samples.

5.1.5. Shunt resistance

The shunt resistance expressed in ohm, is found independent of the cell size and in the order of 10^8 - 10^9 ohm (Figure IV-14). This indicates that the shunt values are fixed by the area around the cell and not by the cell itself. If a cell is of area A, the substrate around the cell is $1 \text{ mm}^2 - A$. As a result values of shunt resistance as high as 10^7 ohm.cm² are found, and can be explained by the limitation of the SiO₂ layer to prevent shunt path formation.

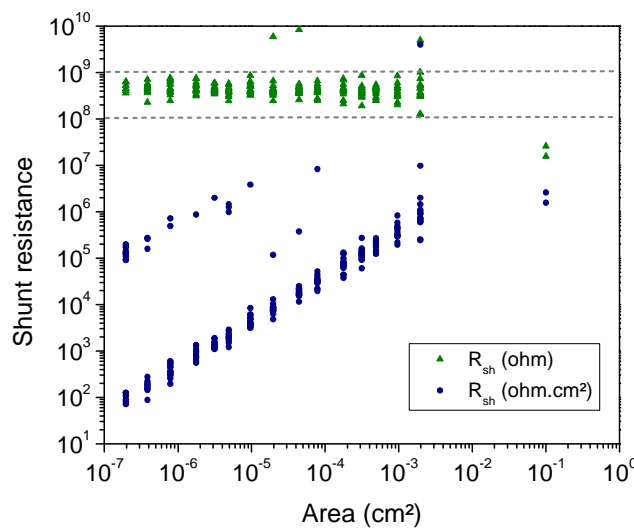


Figure IV-14 : Shunt resistance in ohm or in ohm.cm² as a function of microcell size for an industrial sample. Dotted lines are guides to the eye.

5.1.6. Reproducibility

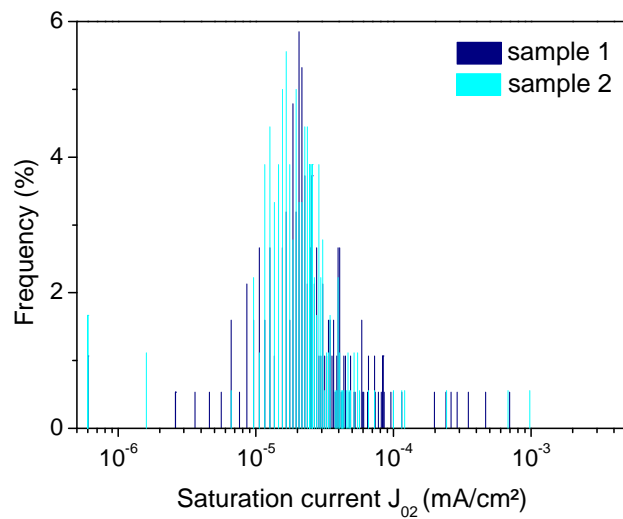


Figure IV-15 : Statistical distribution of the saturation current J_{02} for two industrial samples made with the same absorber.

The microcell fabrication process is a succession of numerous steps, and the reproducibility issue is important. We fabricated two microcell samples from the same industrial absorber coming from Würth Solar. On Figure IV-15 we show for example the distribution of saturation current J_{02} for two samples. One can show that the results are very much alike, indicating good reproducibility. (The frequency is counted as the number of devices represented by a bin divided by the total number of devices in the sample.)

5.2. Analysis of AM1.5 current-voltage characteristics

5.2.1. Measurement setup

We perform AM1.5G measurement with a class AAA solar simulator (Spectra Nova or Newport). The cells are contacted in two-terminal configuration: one wire on the Mo and one probe on the surface. As this setup is not linked to a microscope, it is not possible to position the probe on the Au pad, and the contact was taken on ZnO:Al. A motorized chuck was acquired in the last year of this PhD. Early samples were measured manually (it concerns industrial samples, where absorber comes from Würth Solar). Therefore only a few microcells of each size were measured. For the last samples automatic measurements were performed and more statistical results could be extracted (IRDEP samples).

5.2.1. Short-circuit current density J_{sc} and open-circuit voltage V_{oc}

Short-circuit current densities are measured on current-voltage curves. We can see that this current density is constant over a wide size range (six orders of magnitude). It should be noted that the area of the microcell that is taken into account here is not the theoretical one - that of the photomask -

but takes into account a slight deviation. Indeed microcells do not have exactly the size of the photomask structure but are slightly smaller, with a deviation of the diameter varying between 2 μm for the biggest microcells down to less than 0.5 μm for the smallest.

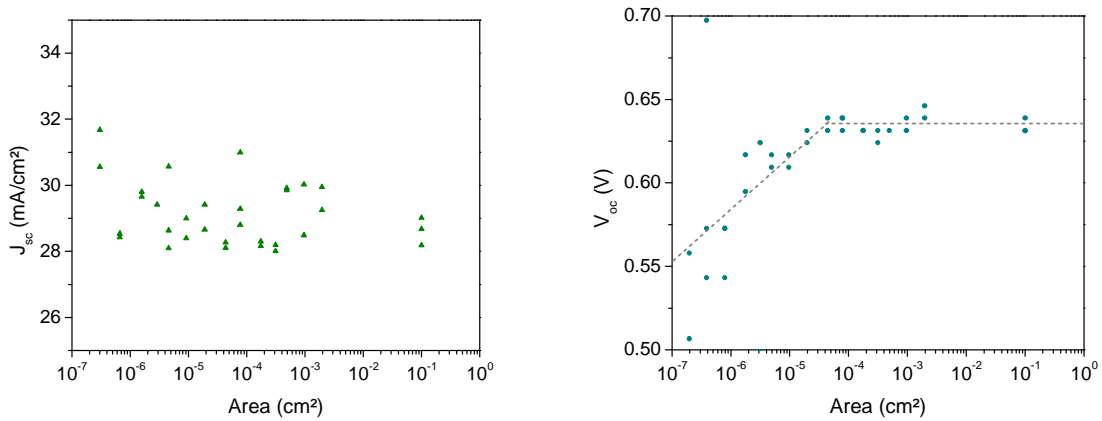


Figure IV-16 : (left) Short-circuit current density under AM1.5G for an industrial sample as a function of cell size. (right) Open circuit voltage under AM1.5G for an industrial sample as a function of cell size. Dotted line is a guide to the eye.

Open circuit voltages are also measured. We can see a decrease in V_{oc} with cell size for devices under 10⁻⁵ cm². This decrease is most likely due to the increased influence of shunts for smaller devices. Indeed we have seen that the shunts are mainly due to the space surrounding a microcell (of area 1 mm² - that of the cell). The influence of shunts is therefore increasingly important for the smallest devices.

5.2.2. Conversion efficiency η

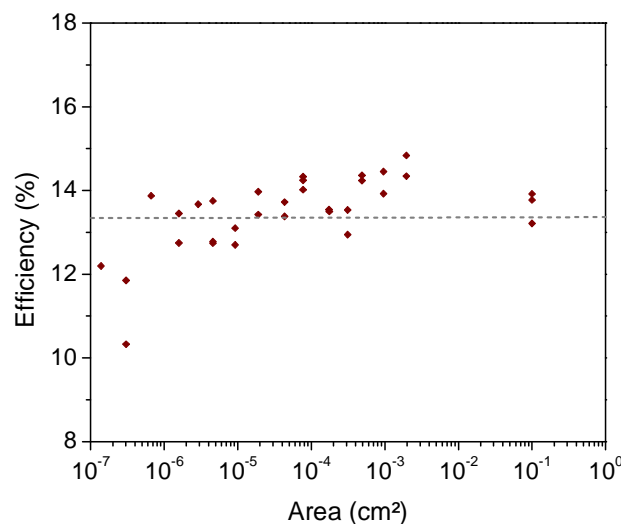


Figure IV-17 : Efficiency under AM1.5G for an industrial sample as a function of cell size. The average efficiency is given by the dotted line.

The microcell efficiencies can be extracted from their current-voltage curves, and we found 13.2% efficiency on average and no visible trend with cell size, on the industrial sample of Figure IV-17. These efficiencies are in line with what is observed on industrial absorbers [75], [204].

5.2.3. External quantum efficiency

We measured external quantum efficiency with a homemade spectral response setup. As our light source has a diameter of approximately 2 mm, no measurement on microcells was possible. Therefore we tested industrial cells of 0.1 cm², with a wavelength step of 10 nm. The photocurrent that can be extracted from this measure under AM1.5G spectrum is 28.1 +/- 0.25 mA/cm² on average.

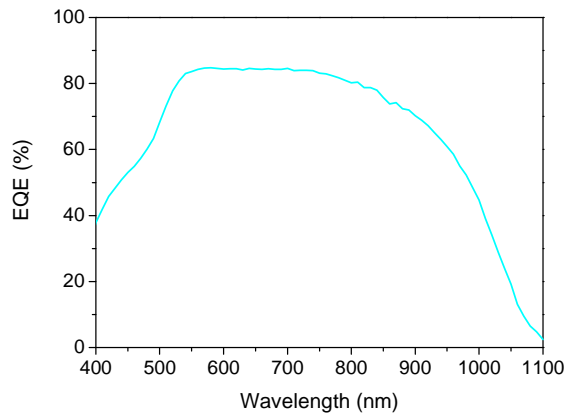


Figure IV-18 : External quantum efficiency of a cell of 0.1 cm² on an industrial sample.

5.3. Discussion

Having the possibility of creating hundreds of cells of various sizes on a 2.5 × 2.5 cm² sample gives us the chance to use statistical data on a single substrate. Statistical analyzes of the performance of Cu(In,Ga)Se₂ devices are seldomly published [25], [174], [200], [204]. This is surprising because a lot of information and more confidence in the data can be drawn out of statistical analyses.

In the next paragraphs of this discussion, we use our statistical data to analyze opto-electronic properties of the devices. We evaluate how the solar cell characteristics (J_{SC} , V_{OC} , ..) evolve with changing diode parameters (dark current,...). We will also try to use our data to get ideas on the homogeneities of our samples in paragraph 5.3.3.

5.3.1. Size-dependent analysis of microcells under standard conditions

The large size range of our micro-device is particularly interesting to study scale effects. We have seen that series resistance was not dependent on solar cell size in our measurements (Figure IV-13). Considering our analysis of size dependent contributions of the window layer, this can seem

surprising. We simulate dark or illuminated $I - V$ curves with our model for microcells between 10^{-7} and 0.1 cm^2 (Figure IV-19). We found that the $I - V$ curves differ only for applied voltages above 0.7 V. We usually measured our devices between -0.3 and 0.8 - 1V. Therefore the influence of window resistance is very weak at these applied potentials, and no size dependence can be extracted from the fitted values. Moreover the FF of the illuminated diodes are nearly constant, indicating that at this illumination level, the spreading resistance has a negligible influence. This shows therefore that our microcells have a series resistance that is set by other sources than the window layer. It explains that this value of series resistance is close to that of standard laboratory cells [25], which collecting grids also make window layer spreading resistance negligible at AM1.5. It is visible that standard deviation of the measured values increases with decreasing cell size (Figure IV-13). This seems more a numerical artifact due to the difficulty to adjust the series resistance parameter on $I - V$ curves on which series resistance has a small influence due to low currents.

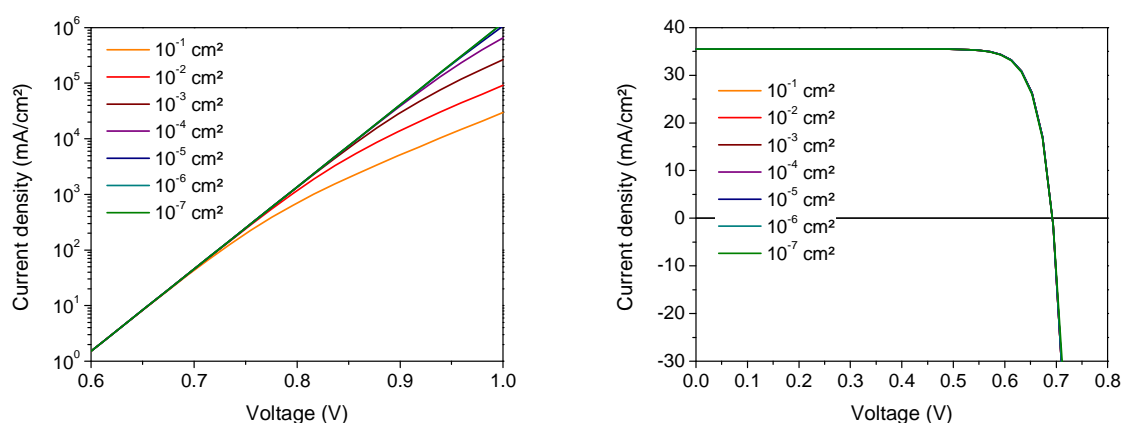


Figure IV-19 : Calculated current-voltage curves for cells of different sizes (10^{-7} to 10^{-1} cm^2) according to the spreading resistance model in dark condition (left) or under AM1.5g illumination (right). Diode characteristic of the cell are that of the NREL record cell and the ZnO:Al sheet resistance is set to 10 ohm/square.

In our design a microcell is electrically connected to the rest of the mesa by the Mo, Cu(In,Ga)Se₂, CdS and i:ZnO layers. Moreover if the SiO₂ layer is not continuous, the gold and ZnO:Al front contact will be directly in contact with the mesa, leading to possible shunts or parasitic cells. Given the small size A of the microcells compared to the 1 mm^2 mesa that surrounds them, we can detect the signal of the mesa when measuring the smallest microcells, as shown by the equivalent circuit of Figure IV-20.

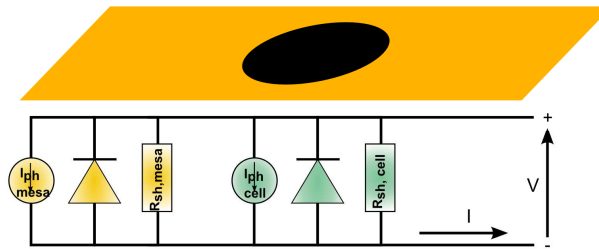


Figure IV-20 : Sketch of the two parallel diodes corresponding to the microcell and to the surrounding mesa.

In the case of a sample where the CdS layer is not properly cleaned from particles, parasitic cells can form on the mesa. The signal coming from parasitic cells situated in zones where SiO₂ was not deposited can be of the same magnitude as that coming from the desired microcell at low illumination intensity. The short-circuit current density is then apparently very high on the smallest devices (Figure IV-21 left), due to a mesa residual short-circuit current density of 1 μA (which corresponds to a surface coverage of 0.3%). These parasitic cells also lead to a residual dark saturation current J_{02} of 10⁻⁵-10⁻⁶ μA, and can easily be seen in electroluminescence images (Figure IV-21 right).

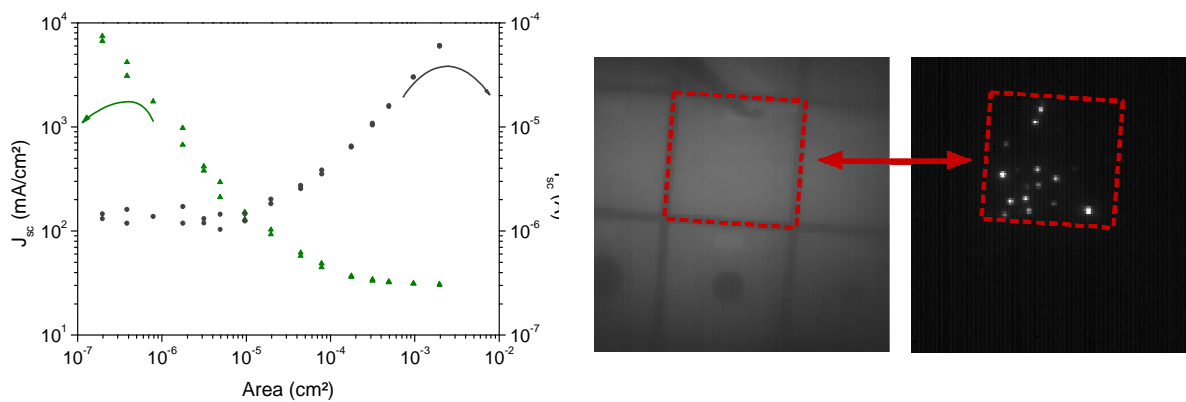


Figure IV-21 : (left) J_{sc} and I_{sc} under AM1.5G as a function of microcell size for a sample with particles deposited on CdS layer. (right) microscope and corresponding EL image for a 5 μm microcell under 1.1V applied bias.

When the process is well controlled, the short-circuit current density is found constant with size, showing the disappearance of parasitic cells (Figure IV-16). However one can see a clear decrease in open-circuit voltage for cells smaller than 10⁻⁵ cm², for industrial samples (Figure IV-16 right) as well as IRDEP samples (Figure IV-22 b). This decrease with size is not due to an increased saturation current. Indeed if illuminated saturation currents J_{02} are higher than in the dark, no size dependence appears (Figure IV-22 a). The decrease in V_{oc} of the smallest devices is due to an increased influence of the mesa on the shunt resistance. Indeed there are two components to determine the shunt resistance of a microcell: the shunt resistance of the mesa and that of the microcell (Figure IV-20).

When $1/R_{sh,mesa} \gg 1/R_{sh,cell}$, the mesa is the predominant shunt element. This can be seen by the constant value of the shunt resistance with cell size (Figure IV-22). Given that $R_{sh,mesa}$ is of the order of $2 \cdot 10^7$ ohm under illumination (Figure IV-22) and $R_{sh,cell} \times A$ of $1 \cdot 10^3$ ohm.cm², the mesa has a predominant influence for cells smaller than $5 \cdot 10^{-5}$ cm². This is indeed the threshold that can be seen on open-circuit voltage measurements. For the smallest devices, the open-circuit voltage drop is as high as 80 mV. This open-circuit voltage decrease is associated with the decrease in shunt resistance from 1000 ohm.cm² to 25 ohm.cm². For cells bigger than $5 \cdot 10^{-5}$ cm², the microcell is the predominant element and the shunt resistance becomes size dependent, and has a value of 1000 ohm.cm², which is what is observed on Figure IV-22 (b). One can also note that these illuminated shunt resistances are actually smaller than in the dark. The violation of shifting approximation has already been observed in Cu(In,Ga)Se₂, even if the exact origin is unclear [51], [101], [189].

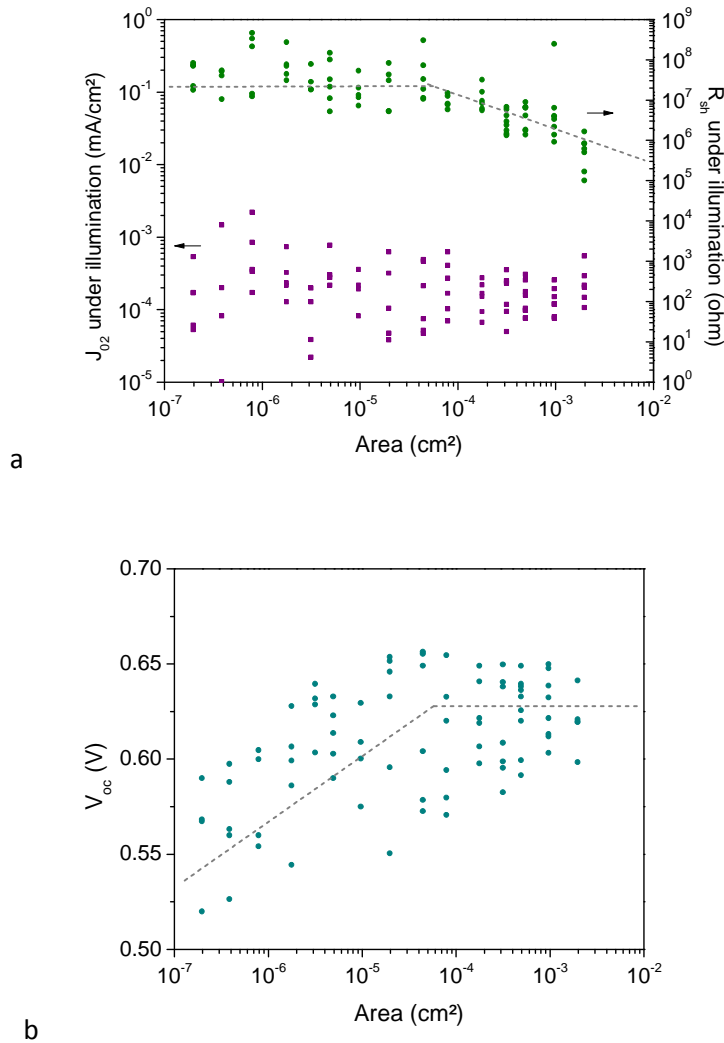


Figure IV-22 : (a) Illuminated saturation current J_{02} (mA/cm²) and shunt resistance (ohm) as a function of cell size. (b) V_{oc} as a function of cell size. Both graphs correspond to an IRDEP sample. Dotted lines are guides for the eye showing the threshold at $5 \cdot 10^{-5}$ cm².

5.3.2. Correlation of open circuit voltage to dark currents

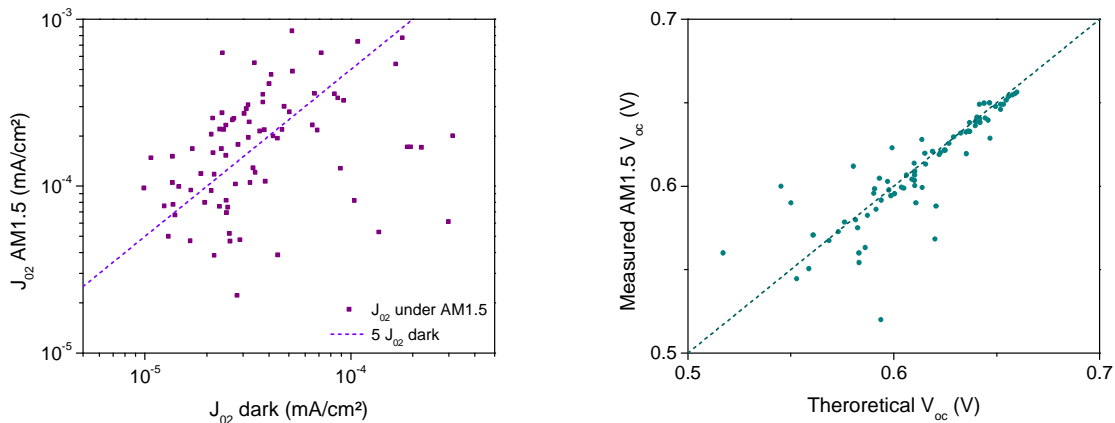


Figure IV-23 : (left) Illuminated saturation current J_{02} as a function the dark saturation current. The dotted line corresponds to a fivefold increase. (right) Measured AM1.5 V_{oc} as a function of theoretical V_{oc} calculated from illuminated saturation currents. The dotted line corresponds to $y=x$.

We study one of the homemade samples that were measured automatically in dark as well as under illumination. We fitted the dark as well as the illuminated J-V curves by a two-diode model. We found that the saturation current J_{02} is nearly five times higher under illumination than in the dark (Figure IV-23 (left)). The saturation current J_{01} was found nearly constant with illumination. This fivefold increase in J_{02} is also observed on industrial samples. It is traditionally explained in Cu(In,Ga)Se₂ by the modulation of electron barrier at the heterojunction under illumination [51]. This increase in saturation current is associated with important noise, and the coefficient of correlation between the saturation currents in the dark and under illumination of Figure IV-23 is 0.15. The coefficient of correlation is statistical tool to measure the degree of correlation of two variables. If its absolute value is close to 1, the data are strongly correlated, if it is close to 0, the data are more independent. It is calculated by the formula : $corr(X, Y) = (\sum(x - \bar{x})(y - \bar{y})) / (\sqrt{\sum(x - \bar{x})^2 \sum(y - \bar{y})^2})$.

We can then compare the measured V_{oc} to the theoretical value that can be estimated from the saturation currents in the absence of series resistance or shunts:

$$V_{oc, theo} = \frac{2kT}{q} \ln \left(\frac{-J_{02} + \sqrt{J_{02}^2 + 4J_{01}J_{sc}}}{2J_{01}} \right) \quad (IV-1)$$

Figure IV-23 (right) shows a very good correlation between the measured V_{oc} and the theoretical value (Equation (IV-1)) with a correlation coefficient of 0.85. One can see that the standard deviation increases with decreasing V_{oc} , indicating that poor device performances are linked with greater data

dispersion, and are also influenced by lower shunt resistances, which are not taken into account in equation (IV-1).

We saw that both saturation currents and open-circuit voltage data fluctuate. We can calculate the variation in V_{oc} that is the consequence of variations in J_{02} by derivation of equation (IV-1):

$$\Delta V_{oc} = \frac{2kT}{q} \frac{\Delta J_{02}}{\sqrt{J_{02}^2 + 4J_{01}J_{sc}}} \quad (IV-2)$$

With the data of one IRDEP sample (Figure IV-23 and Figure IV-22), we find for devices which diameters are superior or equal to 25 μm , ΔV_{oc} of 40 mV from the fitted J_{02} and J_{01} values. This is significantly larger than the standard deviation of the V_{oc} measurements under the solar simulator for this sample, which is 26 mV. This would suggest that dark saturation current data dispersion is not only due to physical differences between devices that are also reflected in the variations of V_{oc} , but also to fluctuations due to the non perfect numerical fitting of the dark current data (especially for the component J_{01}).

5.3.3. Analysis of samples homogeneity

Having numerous data on cells of sizes that are spread over six orders of magnitude also gives information on the homogeneity of our samples. Cu(In,Ga)Se₂ solar cells are known to be inhomogeneous at different lengths scales. First the Cu(In,Ga)Se₂ absorber is polycrystalline with grain sizes around 1 μm (see Chapter II). Then there are variations in the band-gap of the absorber due to variations in the stoichiometry at very short length scales, typically in the sub-100 nm range [205]. Measurements of the local open-circuit voltage were performed and variations as large as 100 meV on a length scale of 5 – 20 μm were reported [205]. These variations are explained by the inhomogeneous distribution of sodium that diffuses from the glass substrate into the absorber, which was detected by spatially resolved secondary ion mass spectroscopy (SIMS). As a consequence of these local variations, the macroscopic open-circuit voltage of a solar cell is reduced, and thus variations have to be limited as much as possible during fabrication. Theoretically, if the band-gap values are dispersed by a Gaussian law with standard deviation σ_g around the mean value, the actual V_{oc} is decreased from the ideal homogeneous case by $\sigma_g^2/2qkT$ [103].

Our smallest devices are 5 μm wide, therefore nano-scale variations of band-gap should be averaged on all microcell devices and are not expected to modify the coefficient of variation. The inhomogeneities in the absorber at the nm scale cannot be studied by microcell devices, but variations at the millimeter or micrometer scale should be visible.

In our samples we measured a rather constant coefficient of variation, i.e. inverse of signal-to-noise ratio of saturation current (Figure IV-22 a) and of V_{oc} (Figure IV-22 b) with size. This indicates fluctuations in solar cell properties that are independent of the device size. As a consequence we conclude that inhomogeneities in the mm range are seen in all our samples, as 1 mm is the distance between two microcells in our geometry. Large scale variations (mm or cm) have already been reported in the literature for similar devices [174], [204] and are detected in our electrical measurements. These variations are also seen in the X-ray fluorescence analysis of co-evaporated absorbers, routinely done at IRDEP (Figure IV-24). From these measurements we can estimate variations of the bandgap with a standard deviation of 3 meV.

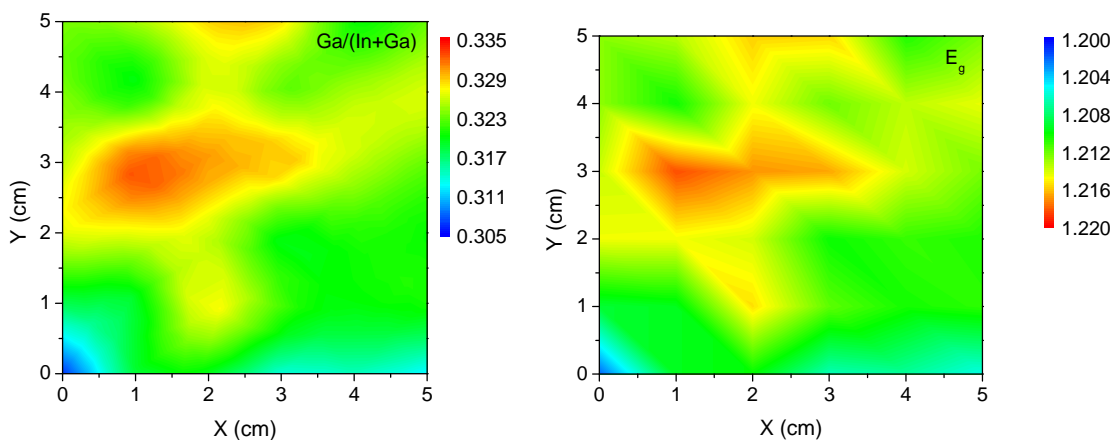


Figure IV-24 : (left) X-Ray fluorescence cartography of $x = \text{Ga}/(\text{Ga}+\text{In})$ ratio on the co-evaporated IRDEP sample shown on Figure IV-23 and Figure IV-22 (36 measurement points). (right) Calculated bandgap from $E_g(x) = 1.02 + 0.67x + 0.11x(x - 1)$ [54].

Micro-scale variations of $\text{Cu}(\text{In},\text{Ga})\text{Se}_2$ in the 5 - 20 μm range are commonly observed. Thus we could expect a decreasing coefficient of variation with increasing device surface, due to improved averaging on bigger devices. This is not directly observed as we have a constant signal to noise ratio. First, we have seen that the signal measured on the smallest devices ($<5 \cdot 10^{-5} \text{ cm}^2$) was greatly influenced by the surrounding mesa. Unfortunately these small microcells are crucial for an inhomogeneity analysis as they are the device on which the material inhomogeneity at the micro-scale will induce the stronger signal. As a consequence, samples with standalone microcells, which are electrically disconnected from the mesa, would be needed to get reliable variation coefficient from the smallest devices ($<5 \cdot 10^{-5} \text{ cm}^2$). Second, the surface coverage of our microcells on the substrate is very small (2.7%) as we have a single microcell per mm^2 . Therefore if micro-scale inhomogeneities are smaller than variations at the mm scale, they cannot be detected. To study these microscale variations we would need denser microcell arrays, in order to have microcells of different sizes in a region where the absorber can be considered homogeneous with respect to large

scale variations. More investigations on the material inhomogeneities, by electron beam induced voltage/current or localized secondary ion mass spectroscopy for example, are needed as a complement to our electrical measurements.

It is the first time that thin film devices are electrically measured on such a large size scale. Previous measurements were local measurements on a macroscopic device. Coupling the two approaches is now needed to investigate the impact of inhomogeneities at different scales on photovoltaic devices of different sizes more in details.

6. Conclusion

We have presented the fabrication of thin film Cu(In,Ga)Se₂ microcells. Structuring techniques from microelectronics were employed. Using polycrystalline materials requires much care in order to have functioning micro-devices. Indeed the signal to noise ratio on micro-devices can become very small if parasitic contributions are not properly eliminated. On our process a critical size of $5 \cdot 10^{-5} \text{ cm}^2$ is detected under which the electrical signal from the mesa becomes predominant compared to that of the microcell itself.

With a good control of the fabrication process and some optimizations, micro-photovoltaic devices are created. They have characteristics that are in-line with macro-devices fabricated with similar absorbers. Due to the reduced size, hundreds of devices can be created on a small surface. Microcells show reproducible statistical behavior. The high amount of data enables to study statistically the influence of the different diode parameters on the overall optoelectronic properties. Hints on the influence of material inhomogeneities on the device performances are drawn from our data. Coupling our electrical measurements to material cartographic methods is however required to get more insight in the impact of these homogeneities.

7. Memento

Cu(In,Ga)Se₂ microcells are fabricated for proof-of-concept, with diameter varying between 7 and 500 μm . Creation of microcells on a co-evaporated absorber is done with a photolithography technique. Optimization of the fabrication process, and adaptation to rough substrates, are described.

Microcells are good photovoltaic devices. Microcells larger than $5 \cdot 10^{-5} \text{ cm}^2$ have performances similar to that of macro-devices. The dark saturation current densities are of the order of $J_{01} = 10^{-10} \text{ mA/cm}^2$ and $J_{02} = 10^{-5} - 10^{-4} \text{ mA/cm}^2$.

The fabrication process is stable, giving reproducible results.

Statistical analysis of the data is possible due to the high number of microcell on each sample. Inhomogeneities at the millimeter-scale are evidenced.

CHAPTER V. CHARACTERISATION OF MICROCELLS UNDER INTENSE ILLUMINATION

1. Introduction	130
2. Characterization under concentrated monochromatic illumination	130
2.1. Experimental setup of the monochromatic concentration experiment	130
2.2. Results : Current-voltage Characteristics and comparison to simulation models	132
2.3. Discussion	136
2.4. Temperature of microcells under concentration	139
3. Characterization under concentrated polychromatic illumination	144
3.1. Influence of spectral variations on the behavior of a solar cell – consequences for monochromatic illumination.....	145
3.2. Concentration experiment with a 644 nm red laser	147
3.3. Experimental setup for sunlight concentration.....	152
4. Synthesis and Conclusion	156
5. Memento	157

1. Introduction

We have described the fabrication and low flux characterization of Cu(In,Ga)Se₂ microcells in the previous chapter. This chapter is focused on tests of Cu(In,Ga)Se₂ microcells under intense light fluxes, with emphasis on the effect of miniaturization.

Experiments of concentration on thin film solar cells are seldom and rely mainly on solar simulators [36], [37], [124]. With the help of concentrating optics, and neutral density filters, the intensity is varied and reached a maximum reported value of $\times 50$. The same solar concentrators enabled tests up to more than $\times 2000$ [143] on standard III-V concentrator cells due to efficient heat sinks and relatively small cells. It seems that the glass substrate of Cu(In,Ga)Se₂ solar cells prevented tests under more intense fluxes due to the difficulty to control temperature under large illuminations spots, even with flash tests. On thin films, a few experiments were also carried out with built-in concentrating optics, such as Fresnel lenses, but only at low concentration levels (< 10 suns) [38], [206].

In order to test our cells from low concentration to very intense fluxes we chose in a first part to use laser sources. With lasers, spot sizes can be controlled easily and matched to a variety of microcells areas. Laser tests of concentrator cells are common in research laboratories [207]. For thin film solar cell characterization, lasers are mostly employed for local LBIC or PL measurements [208–210]. They are not commonly employed for current-voltage characterization. We will therefore detail our testing methodology. In a second part of this chapter the choice of the laser wavelength and complementary sunlight illumination experiments will be presented.

2. Characterization under concentrated monochromatic illumination

2.1. Experimental setup of the monochromatic concentration experiment

2.1.1. *Sketch*

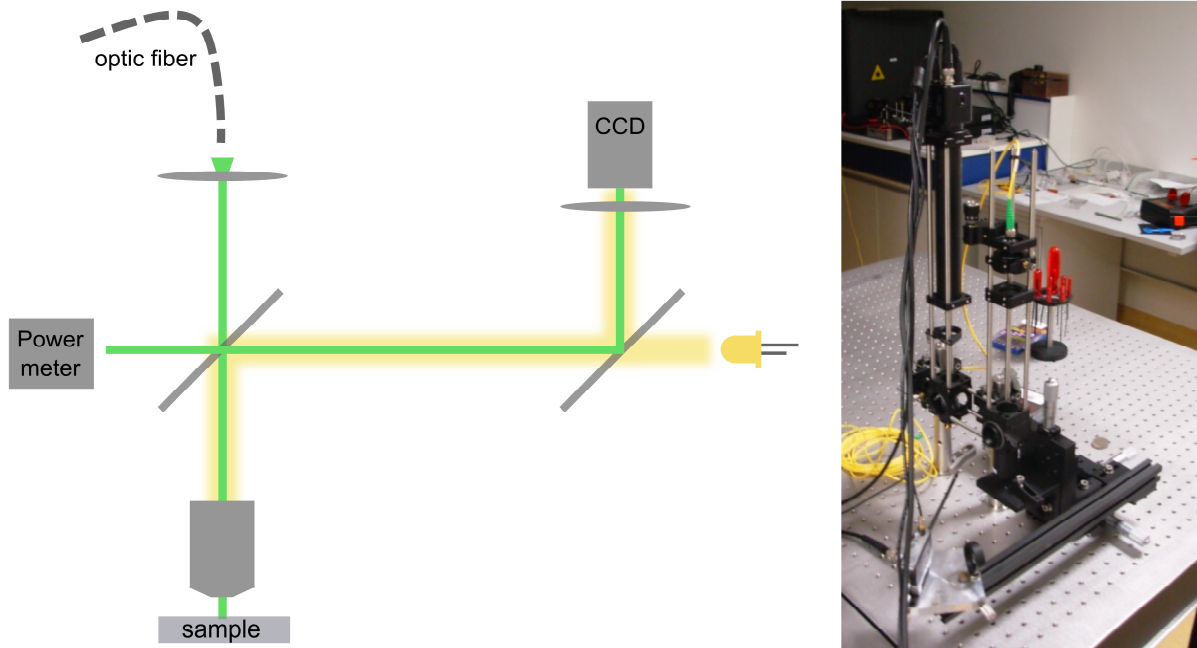


Figure V-1 : Sketch of the concentration setup at IRDEP

A homemade concentration setup has been created for this thesis. Continuous 532 nm laser (Opus, Laser Quantum) - 640 nm and 1062 nm lasers are coupled to optical fibers. For the experiments of paragraph 2, the laser wavelength employed is 532 nm. The laser light is then guided to a microscope, where a lens and a long working distance objective concentrate it on the surface. By displacing the lens in the z-direction closer (or further) from the objective object focal plane, the spot size is reduced (or enlarged). A beamsplitter reflects a part of the incident laser beam on a power-meter, for in-situ control of the incident power (note that calibration has to be performed for each position of the lens). The image of the sample can be done on a CCD camera with a second beamsplitter, that lets a LED light through to illuminate the sample surface and reflects the image of the sample to the camera. The LED-light is turned off during the measurements.

2.1.2. *Measurement process*

The electric measurements of our samples are done in a two terminal configuration with a Keithley 2635A. This configuration was chosen as the creation of the gold contacting pads drastically reduced contact resistance between the probe and the surface, thereby limiting the incentives for four terminal configuration. Then, even if the objective used has a long working distance (1 cm), it was difficult to place a four point terminal configuration setup. The laser spot size is controlled by the camera and adjusted to the cell area. No temperature control system was used, but temperature was evaluated from electrical measurements (see paragraph 2.4). The temperature elevation is localized around the illumination spot (See Chapter III), and no system can easily control the surface temperature of the device. Moreover we chose this configuration as it mimics that of standard use

under illumination without active cooling. The incident light power is varied with neutral density filters. With the minimum attenuation the incident power can reach illumination densities over 1000 W/cm² on the smallest microcells. The light power incident on the cell is monitored by the powermeter, after calibration.

2.1.3. Photoluminescence setup

This concentration setup can be used to detect photoluminescence (PL) by placing a spectrometer (BW Tek) after the beamsplitter, instead of the powermeter.

2.2. Results : Current-voltage Characteristics and comparison to simulation models

2.2.1. Evolution of short-circuit current density under concentration - J_{sc} (C)

The first measurement made is the evolution of short circuit current density with illumination. We are interested in evaluating if or when linearity applies. As long as linearity is valid, the measurement of the J_{sc} is a direct indication of the concentration factor, once J_{sc} (AM1.5) is determined with a calibrated solar simulator : $C = J_{sc}/J_{sc}(AM1.5)$ [124], [143]. Therefore the cell can be used as its own powermeter. For each incident light power P_{light} , we measure J_{sc} and compare this value to the theoretical one :

$$J_{sc,theo} = P_{light} \times EQE(\lambda) \times \frac{q}{h\nu} \quad (V-1)$$

where $EQE(\lambda)$ is the external quantum efficiency at the laser wavelength λ , q the elementary charge and $h\nu$ the energy of the incident photons of wavelength λ .

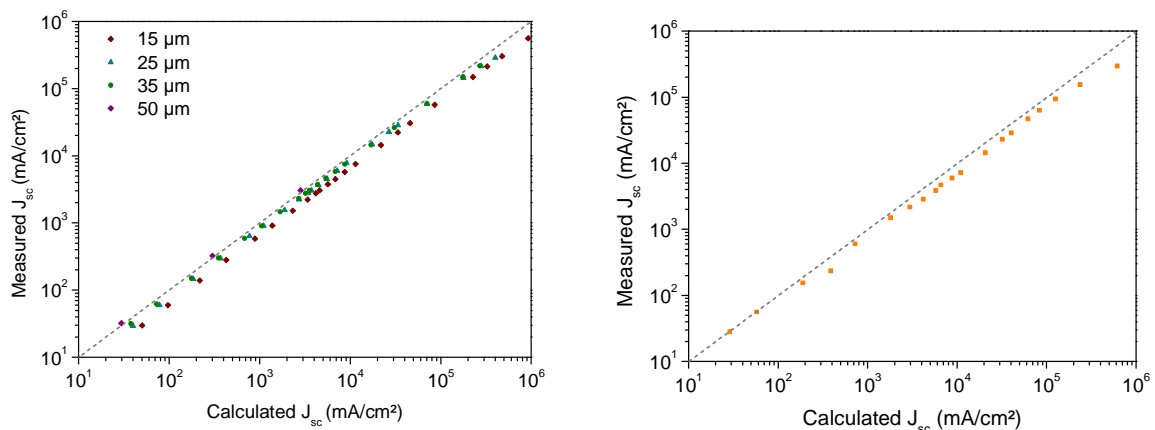


Figure V-2: (left) Measured J_{sc} as a function of the calculated J_{sc} (equation (V-1)) for four different cells (diameter indicated) on an IRDEP sample. (right) Measured J_{sc} as a function of the calculated J_{sc} (equation (V-1)) for a 7 μ m microcell from an industrial sample.

Figure V-2 (left) shows the behavior of four cells of an IRDEP sample. We found similar behavior for all tested samples (e.g. Figure V-2 right). One can see that linearity is valid up to 1000 A/cm^2 in the best cases. Linearity is a sign that resistive losses do not degrade short-circuit current, which therefore is nearly equal to the photocurrent. It also shows that in short-circuit conditions the photogenerated carrier collection efficiency does not vary with concentration up to very high illumination levels. The slight sub-linear behavior seen at very high intensities could be a resistive effect [211] or a decreased collection. For the smallest cells the measured J_{sc} tends to be smaller than the theoretical one, because the laser spot is larger than the cell. Now that linearity is proven, we can define the concentration ratio of an experiment as the ratio of its short-circuit current density to that of the short-circuit current density under AM1.5G, or 1 sun. Note that in this thesis, concentration ratios are defined relative to the AM1.5G and not the AM1.5D spectrum. Indeed, as no optical system dedicated to microcells is designed to date, we chose the broadest definition of concentration ratio. It is not clear yet, what the most appropriate concentrating optic for thin film microcells can be. It may be systems that collect a part of the indirect radiation, especially for relatively low concentration factors. This is why we did not define concentration with respect to AM1.5D.

2.2.2. *Evolution of open circuit voltage under concentration - V_{oc} (C)*

We measured the open-circuit voltage of different microcells under concentration (Figure V-3). We can see two regimes: for short-circuit current densities smaller than 10 A/cm^2 , the open-circuit voltage increases with the logarithm of concentration. In Figure V-3 (left) we can see that the slope of the increase is constant for the different cells of the same sample, except for the $25 \mu\text{m}$ one. Then at higher concentrations, V_{oc} reaches a maximum before decreasing. V_{oc} is maximum for the $15 \mu\text{m}$ microcell and reaches 859 mV at 2680 suns . The best sample tested in this thesis, made at IRDEP, shows a V_{oc} of 905 mV at 4750 suns (Figure V-3 (right)). This corresponds to less than 230 mV difference with the V_{oc} of an ideal cell of the same optical bandgap (1.16 eV) according to the Shockley-Queisser limit (Figure V-3 right). For the best solar cells to date, this difference under AM1.5 is around 200 mV [25], [55]. Details on the Shockley-Queisser limit can be found in Appendix D.

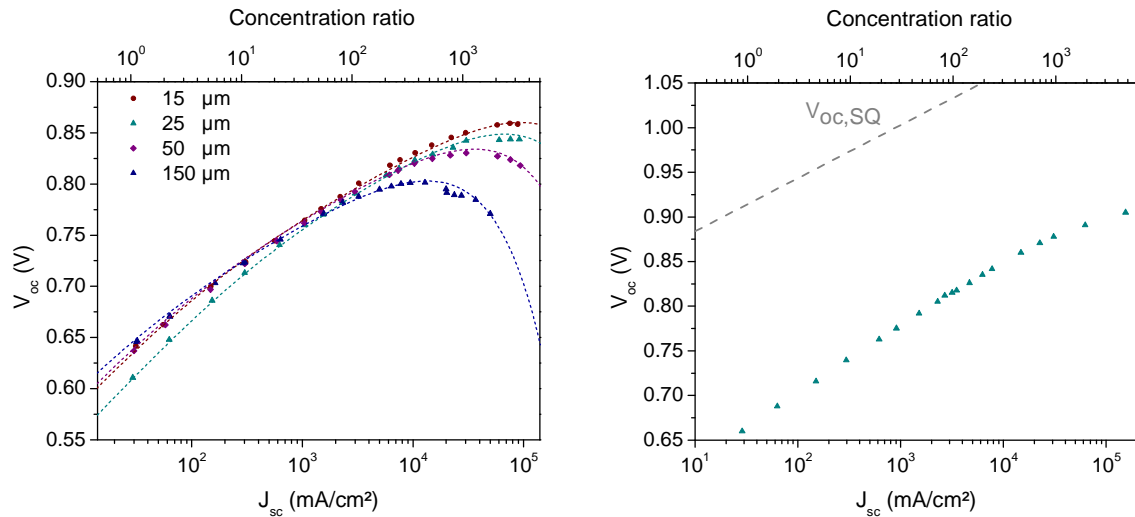


Figure V-3 : (left) Open-circuit voltage as a function of short-circuit current density for four cells (diameter indicated) of an industrial sample. The dotted lines correspond to fits described by equation (V-3). (right) Open-circuit voltage as a function of short-circuit current density for a 25 μm microcell of an IRDEP sample. This samples exhibits the highest V_{oc} measured in this thesis, i.e. 905 mV. The maximum theoretical V_{oc} in the Shockley-Queisser limit is displayed by a dashed grey line.

2.2.3. Evolution of current voltage characteristics

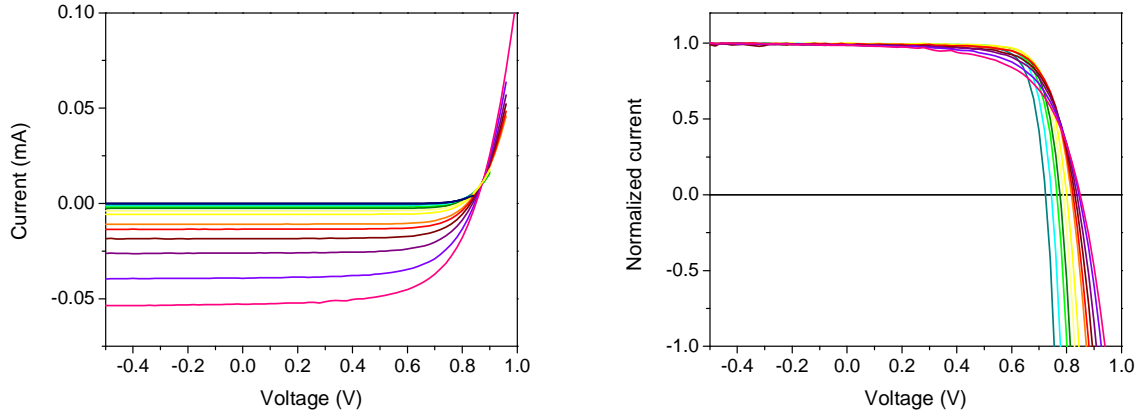


Figure V-4 : (left) Experimental current voltage curve of a 15 μm microcell of the reference sample of Figure V-3 (left) with concentration (from 1 to 1070 suns). (right) same curves normalized by short circuit current.

Open circuit and short circuit are two specific test conditions, but the entire current-voltage curve can be studied, with respect to the illumination intensity. On Figure V-4 we can see that up to middle concentration ($\approx \times 100$), the maximum power that can be extracted from the cell increases due to increased V_{oc} and constant fill factor. This stable fill factor means in particular that resistive losses on this cell stay limited even at high concentration. From this variation in maximum power and fill factor follows an increase in efficiency with concentration that is interesting to study. One can see that at

high concentrations (close to $\times 1000$) the fill factor degrades, and not only due to resistive losses. This degradation of fill factor will be carefully studied in Chapter VI of this thesis.

2.2.4. Microcell efficiency as a function of the illumination

We study the evolution of efficiency with concentration. The efficiency is not the monochromatic efficiency at 532 nm but an equivalent efficiency corrected from the spectral mismatch between the laser light and solar spectrum. The equivalent efficiency studied here is equal to $P_{max}/(P_{AM1.5} \times C)$, where P_{max} is the maximum power density output of the cell in the experiment, $P_{AM1.5}$ is the AM1.5G power density (100 mW/cm^2), and C the concentration factor.

On Figure V-5 (left) we plot the efficiency versus concentration for the cells shown on Figure V-3. We can see that the efficiency increases from 13.2% (average on the 0.1 cm^2 reference cells under AM1.5G) up to 17% for the $15 \mu\text{m}$ cell. This represents a 4% absolute efficiency increase. The maximum efficiency is reached at $\times 120$, which is well above previously reported values for Cu(In,Ga)Se_2 thin films [36]. On the Figure V-5 (right), the efficiency versus concentration for the cell fabricated at IRDEP is plotted, which presents the highest efficiency. An efficiency of 21.3% is recorded. This result was made possible by the low resistance of the sample that enabled a maximum efficiency at $\times 475$, which is a record for thin film solar cells.

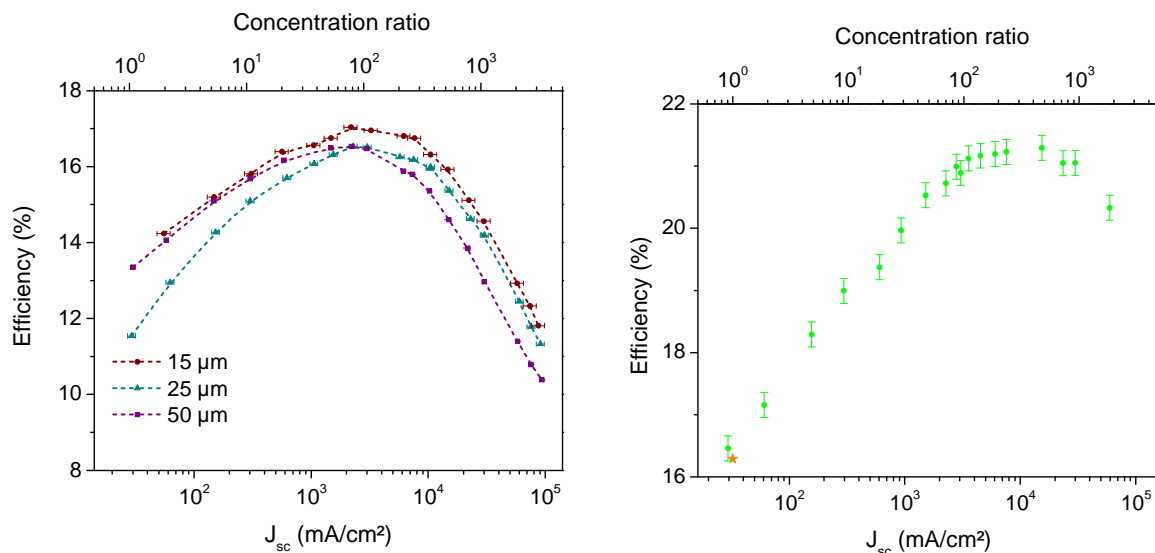


Figure V-5 : (left) Efficiency as a function of concentration for three cells of the industrial sample shown on Figure V-3. (right) Efficiency as a function of concentration for the record cell of IRDEP sample of diameter $50 \mu\text{m}$. The orange star corresponds to the measurement under AM1.5 spectrum with a solar simulator.

2.3. Discussion

2.3.1. Open circuit voltage V_{oc}

We have seen in Figure V-3 that the $V_{oc} - J_{sc}$ characteristics could be separated in two domains: low to middle concentration ($\times 1 - \times 100$) and high concentration ($> \times 100$).

Low concentration

In the low concentration part V_{oc} increases with the logarithm of concentration (see Chapter II, paragraph 4.5). As we have seen (equation (II-16)), the relation between V_{oc} and J_{sc} in the two-diodes model is :

$$V_{oc, 2\ diodes} = \frac{2kT}{q} \ln \left(\frac{-J_{02} + \sqrt{J_{02}^2 + 4J_{01}C \times J_{sc}(AM1.5)}}{2J_{01}} \right) \quad (V-2)$$

From the experimental $V_{oc} - J_{sc}$ characteristic we can thus fit the two saturation current densities J_{01} and J_{02} according to equation (V-2). The results of the fits for the low concentration range are the dotted lines on Figure V-3 (left), and the values are summarized in Table V-1. The two-diodes model is preferred in our study as it reflects more appropriately the experimental results and is more easily related to the physics. Indeed V_{oc} increases linearly with the logarithm of J_{sc} but two different slopes can actually be seen. These slopes are well fitted by the two-diode model, and correspond respectively at low concentration to an ideality factor close to 2 and at high concentration to an ideality factor close to 1. This is coherent with the fact that on current voltage curves, the diode of ideality 2 dominates at low voltage whereas at higher applied voltages the ideality 1 prevails. Indeed increasing concentration results in translating the current voltage curve of the solar cell due to increased photocurrent. Thus the open-circuit voltage increases, and the slope of this increase depends on the slope of the current voltage curve around V_{oc} . The change in the slope of $V_{oc} - J_{sc}$ curves has been analytically predicted for homojunctions under variable injection in the 1980s [212]. We can notice that J_{01} and J_{02} have values similar to what is observed under AM1.5. This trend is seen in all samples. Equation (V-2) relies on the assumption that each parameter is independent from the concentration ratio. Therefore J_{01} and J_{02} are to be understood as averages on the entire concentration range. In Figure V-3, we cannot detect a saturation of recombination mechanisms under increased concentration that would decrease saturation currents and thus increase open circuit voltage. Thus if such a saturation exists it is very limited, and the hypothesis of constant saturation currents on the whole concentration range is reasonable.

Table V-1 : Fitting parameters of the $V_{oc} - J_{sc}$ characteristics in the low to middle concentration range as seen in Figure V-3 (left), according to equation (V-2).

Area (cm ²)	J_{01} (mA/cm ²)	J_{02} (mA/cm ²)
$1.78 \cdot 10^{-4}$	$2.3 \cdot 10^{-10} \pm 1 \cdot 10^{-11}$	$1.2 \cdot 10^{-4} \pm 1 \cdot 10^{-5}$
$1.96 \cdot 10^{-5}$	$1.8 \cdot 10^{-10} \pm 1 \cdot 10^{-11}$	$1.6 \cdot 10^{-4} \pm 1 \cdot 10^{-5}$
$4.91 \cdot 10^{-6}$	$1.8 \cdot 10^{-10} \pm 1 \cdot 10^{-11}$	$3.1 \cdot 10^{-4} \pm 1 \cdot 10^{-5}$
$1.77 \cdot 10^{-6}$	$1.7 \cdot 10^{-10} \pm 1 \cdot 10^{-11}$	$1.8 \cdot 10^{-4} \pm 1 \cdot 10^{-5}$

High concentration

When the concentration ratio increases the $V_{oc} - J_{sc}$ characteristics deviate from the logarithmic behavior and a maximum and subsequent decrease in V_{oc} is seen. This decrease in open-circuit voltage is the evidence of the device's temperature increase. Indeed dark currents increase with temperature [213]. In a first order approximation, we will only consider the temperature dependence of the saturation currents in the form: $J_{01} = J_{001} \exp(-E_g/kT)$ and $J_{02} = J_{002} \exp(-E_g/2kT)$, which amounts to supposing that the activation energy of the dark current is the bandgap. If the Fermi level at the interface is pinned, this hypothesis is not true, and temperature dependence in the form $\exp(-E_a/kT)$ should be used [51]. We also make the hypothesis that the temperature increase is linear with concentration, which we found in our theoretical model of Chapter III. Thus we have $T = T_0 + \kappa \times J_{sc}$. The $V_{oc} - J_{sc}$ characteristic in the whole concentration range becomes:

$$V_{oc} = \frac{E_g}{q} + \frac{2kT_0}{q} \left(1 + \frac{\kappa J_{sc}}{T_0} \right) \ln \left(\frac{-J_{002} + \sqrt{J_{002}^2 + 4J_{001}J_{sc}}}{2J_{001}} \right) \quad (V-3)$$

We can adjust the values of the proportionality factor κ in our fits, the numerical values are given in Table V-1, and the corresponding fits are dotted lines in Figure V-3 (left). A study of this proportionality factor as a function of the microcell size will be described in paragraph 2.4.

Table V-2: Fitting parameters of the $V_{oc} - J_{sc}$ characteristics as seen in Figure V-3 (left), on the complete concentration range according to equation (V-3). We considered a bandgap value of 1.22 eV. J_{001} and J_{002} are correlated with the values of Table V-1 by a factor $\exp(-E_g/kT)$ and $\exp(-E_g/2kT)$. $T_0 = 300K$

Area (cm ²)	J_{001} (mA/cm ²)	J_{002} (mA/cm ²)	κ/T_0 (cm ² /A)
$1.78 \cdot 10^{-4}$	$7.3 \cdot 10^{10} \pm 1 \cdot 10^{10}$	$2.1 \cdot 10^6 \pm 1 \cdot 10^5$	$5.3 \cdot 10^{-3} \pm 2 \cdot 10^{-4}$
$1.96 \cdot 10^{-5}$	$5.6 \cdot 10^{10} \pm 1 \cdot 10^{10}$	$2.8 \cdot 10^6 \pm 1 \cdot 10^5$	$2.2 \cdot 10^{-3} \pm 1 \cdot 10^{-4}$
$4.91 \cdot 10^{-6}$	$5.6 \cdot 10^{10} \pm 1 \cdot 10^{10}$	$5.6 \cdot 10^6 \pm 1 \cdot 10^5$	$1.2 \cdot 10^{-3} \pm 1 \cdot 10^{-4}$
$1.77 \cdot 10^{-6}$	$5.3 \cdot 10^{10} \pm 1 \cdot 10^{10}$	$3.2 \cdot 10^6 \pm 1 \cdot 10^5$	$8.8 \cdot 10^{-4} \pm 2 \cdot 10^{-5}$

Shunt resistance

In the above analysis we neglected the influence of shunt resistances. Indeed our standard samples show high shunt resistances and their contributions can be neglected except for the smallest devices (Chapter IV). However, on samples that were obtained from a chemically etched absorber [32], [214], low shunt resistances could be observed for all microcell sizes (Figure V-6). This is for example due to pinholes in the etched absorber (800 nm thickness), usually associated with voids created between adjacent grains. The $V_{oc} - J_{sc}$ curve is modified by these low shunt resistances, but it can be seen that the influence of shunt resistance decreases with increasing concentration, and that V_{oc} goes back to a non-shunted value for a concentration above $\times 100$. This shows the favorable effect of concentration on shunted devices, which behaves as well as standard devices under sufficient concentration.

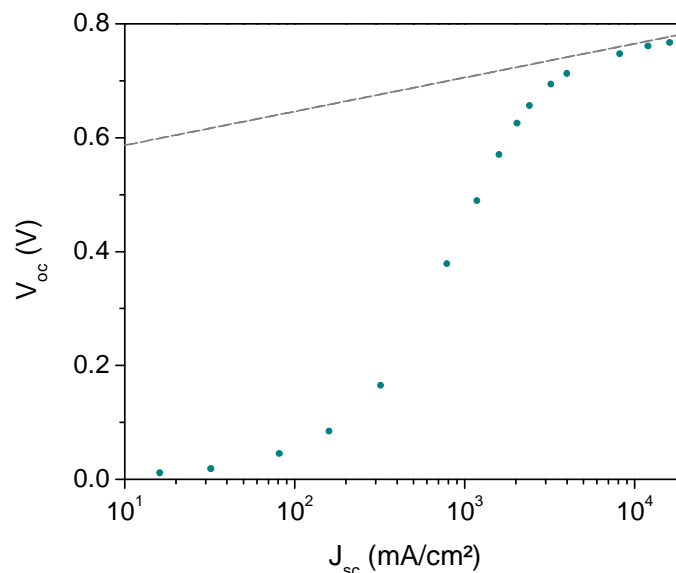


Figure V-6 : Open-circuit voltage as a function of short-circuit current density for a 50 μm microcell from a sample which absorber was etched to 800 nm thickness, causing shunts. A gray dotted line with slope kT/q is plotted as a guide to the eye.

2.3.2. Efficiency - Resistive scale effects with microcell size

We can see from Figure V-5 that the increase in efficiency with concentration can be important. The optimum concentration ratio on the industrial samples ($\times 120$) is nearly ten times higher than values previously reported in the literature [36], and reach values attained by the record GaAs concentrator cell of Franhofer ISE ($\times 117$) [22]. This shows that the decrease in size indeed resulted in a decrease in resistive losses. The optimum concentration on the IRDEP samples ($\times 475$) is a record for polycrystalline thin films solar cell and is in the high-end of what is found on single junction concentrator cells [143].

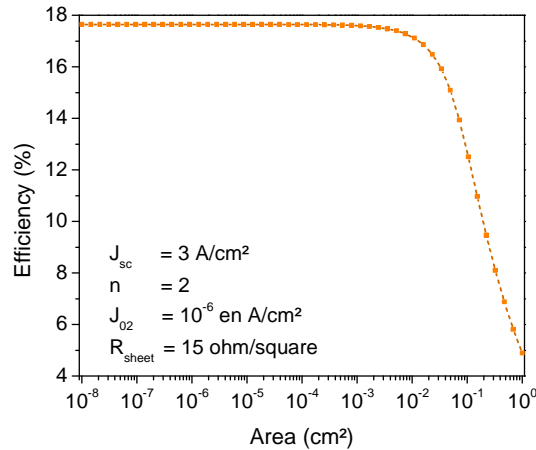


Figure V-7 : Efficiency as a function of microcell area by our spread resistance model. Parameters used are short-circuit current density of 3 A/cm², a sheet resistance of 15 ohm/square, an ideality factor equal to 2 with corresponding saturation current density 10⁻⁶ A/cm².

In Figure V-5 (left) the maximum in efficiency appears at roughly the same concentration ratio ($\times 120$) for the three cells, despite their different sizes. This means that the size effect is saturated. This is what is expected from our sheet resistance model (Figure V-7), where parameters close to that observed on our samples were chosen. We can see from our calculation that the efficiency at $\times 100$ of a microcell is maximum, i.e. negligible spreading resistive losses, for area smaller than 10^{-3} cm^2 . Therefore it is logical that no size effect can be detected for microcells of diameter inferior to $50 \mu\text{m}$ up to $\times 100$. The fact that the maximum efficiency appears at the same concentration ratio also means that the resistance causing the saturation is not that of the window layer, or any spreading resistance, but that of a parasitic series resistance in the device. From a mathematical analysis [121], it was determined that the maximum efficiency is obtained when the product of the cell's series resistance by the photocurrent density equals the product of thermal voltage by ideality factor (for a one-diode model). We can thus estimate for the cells of Figure V-5 (left) that the series resistance limiting concentration is $\sim 2kT / (q \times 100 \times J_{sc}(AM1.5)) \sim 0.02 \text{ ohm.cm}^2$. It can be noted that this value is well below that measured on our device under AM1.5. An entire section of the next chapter will therefore be dedicated in the detailed study of the resistive sources in our $\text{Cu}(\text{In,Ga})\text{Se}_2$ solar cells.

As seen in the paragraph 2.3.1, in our measurements we can detect the signal coming from the temperature elevation of the devices. In the next section, we will study more in detail the temperature effect in our microcells.

2.4. Temperature of microcells under concentration

2.4.1. Extraction of temperature from $V_{oc} - J_{sc}$ curves

We have seen in the paragraph 2.3.1 that we can fit $V_{oc} - J_{sc}$ curves to extract the coefficient of proportionality between the temperature elevation and the short-circuit current density (proportional to the incident power). We can thus determine the temperature of the cell relative to the concentration ratio, and analyze the influence of the device size (Figure V-8).

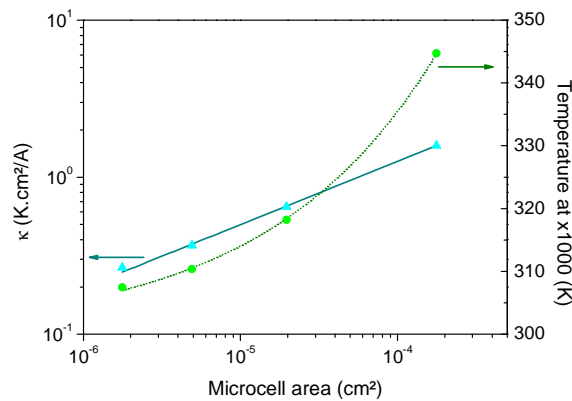


Figure V-8 : Proportionality factor κ and temperature at $\times 1000$ as a function of microcell area (dots are the experimental data, the lines are least square regressions).

We find that the factor κ , and thus the temperature elevation, is proportional to the radius of the cell to the power 0.8. This is close to what is predicted in the case of a semi-infinite medium under localized irradiation (see Chapter III), where the maximum temperature elevation, found at the beam center, is proportional to illumination and heat source radius, and inversely proportional to the thermal conductivity of the medium. However there is a discrepancy that will be discussed in the paragraph 2.4.3.

If we consider that the device temperature in the dark is 300K, we find that the temperature elevation at $\times 1000$ is as small as 7K for the 15 μm sample. It is very interesting to note that thin film solar cells grown on a glass substrate so efficiently can dissipate heat under high fluxes due to the beneficial scale effect.

2.4.2. Estimation of temperature from photoluminescence

In order to complete the study of the temperature of $\text{Cu}(\text{In,Ga})\text{Se}_2$ microcells, we used photoluminescence spectra to estimate carrier temperatures under intense fluxes.

Photoluminescence (PL) is a luminescence process provoked by light excitation. Light emission is due to the transition of electrons from high energy states to lower energy states by the emission of photons. The luminescence spectra of a semiconductor under light excitation is described by the generalized Planck's law [215]:

$$PL(E) = \frac{1}{4\pi\bar{h}^3c^2} \frac{a(E)E^2}{\exp((E - \Delta\mu)/kT) - 1} \quad (V-4)$$

Where \bar{h} is the reduced Planck's constant, c the light velocity, E the photon energy, $a(E)$ the absorptivity and $\Delta\mu$ the quasi-Fermi level splitting. At room temperature several processes can lead to photoluminescence emission [210]. First band-to-band transitions can occur between free carriers of the valence and conduction bands, and lead to a maximum intensity at $E_g + 0.5kT$. The dependence of band-to-band recombination on excitation power is super-linear. Free-to-bound transitions are also possible, and are related to the transition between free carrier in a band and localized states in the bandgap. The peak in emission is situated at $E_g + 0.5kT - E_t$, where E_t is the ionization energy of the defect state, and the dependence with excitation power is linear. Donor-acceptor transitions if both donor and acceptor states are present are also possible, and the transition probability increases as the logarithm of the excitation power. At room temperature excitons are not observable, thus signals from free or bound excitons cannot be studied. Spatial inhomogeneities in the material can lead to band fluctuations and deform the PL spectra. In Cu(In,Ga)Se₂ both band-to-band and free-to-bound signatures can be observed on PL spectra [208]. We measured a peak energy of our PL spectra of 1.12 eV (Figure V-9), which is associated with band-to-band transitions. This value is smaller than the band-gap extracted from EQE measurements. This can be due to bandgap grading as the emission from the low bandgap region will be predominant, or to potential fluctuations due to spatial Cu(In,Ga)Se₂ inhomogeneities. We can also see in Figure V-9 that the low energy part of the spectrum proportionally decreases with increasing power. This is related to the lower dependence of free-to-bound or donor-acceptor transitions on excitation power compared to band-to-band transitions.

The temperature is extracted from PL spectra by normalizing each spectrum with a reference spectrum, measured at a given incident power. Thus, from equation (VI-2), the normalized PL intensity in the high energy domain is proportional to an energy-dependent term as [215] :

$$\frac{PL(E)}{PL_{ref}(E)} \propto \exp\left(\frac{-E}{k} \left(\frac{1}{T_{ref}} - \frac{1}{T}\right)\right) \quad (V-5)$$

where $PL(E)$ and $PL_{ref}(E)$ are respectively the studied and reference PL spectra, E the energy of emitted photons, T the average temperature of the carriers, and T_{ref} a reference temperature. We assume that the carrier temperature is the same as the lattice temperature in the injection range studied. Normalizing PL spectra is done as we do not precisely know the variations of the absorption $a(E)$ with wavelength. As a consequence these PL measurements will not give absolute temperature

but relative increase in temperature with respect to the reference. The temperature increase is extracted by fitting the normalized curves between 1.15 and 1.22 eV. Linearity of the temperature with incident power is verified, and by extrapolation the reference temperature is chosen so that the temperature in the dark is 300K. We can see that at $\times 1000$ the temperature elevation on the 25 μm microcell is around 10K.

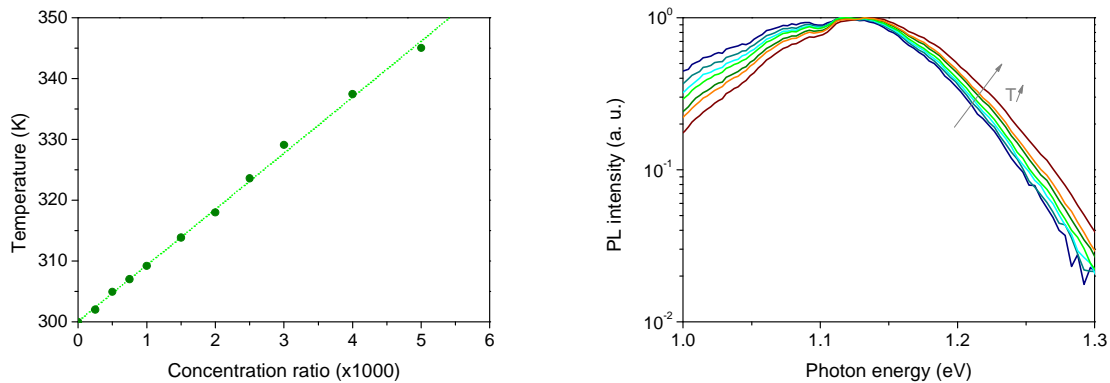


Figure V-9 : (left) Temperature of a 25 μm diameter microcell from industrial sample as a function of concentration measured from PL (green dots). The line is a least square fit. (right) Normalized PL spectra.

2.4.3. Discussion

For our PL measurements we can deduce the proportionality factor κ_{PL} linking the temperature increase to the short-circuit current density, on a 25 μm microcell of an industrial sample. We found that κ_{PL} is $3.3 \cdot 10^{-1} \text{ K.cm}^2/\text{A}$, which is very close to the value extracted from the $V_{\text{oc}} - J_{\text{sc}}$ analysis on the same cell ($\kappa = 3.7 \cdot 10^{-1} \text{ K.cm}^2/\text{A}$). The PL experiment thus confirms that the microcell temperature stays close to the ambient temperature even under highly concentrated fluxes.

For the PL measurements, tests were limited to small devices. Indeed on our setup, given the fixed value of the laser power available and limited collecting angle of the objective, we did not have sufficient sensitivity to keep good signal-to-noise ratio for large cells that have lower illumination densities. Tests on larger cells would however be beneficial to confirm the size effect detected with the analysis of $V_{\text{oc}} - J_{\text{sc}}$ curves and would have to be performed on a more sensitive setup.

In the analysis of $V_{\text{oc}} - J_{\text{sc}}$ curves, a simple expression of open-circuit voltage as a function of temperature was taken. Indeed the components J_{001} and J_{002} , as well as the gap energy, should also be slightly temperature dependent. These dependences should be taken into account for better precision but the data that we have do not permit to fit these additional parameters with sufficient accuracy. Temperature dependent current-voltage curves, at different illumination levels, would be a way to gain more details on the exact temperature dependence of the diode parameters.

We have seen that the proportionality factor κ deduced from $V_{oc} - J_{sc}$ curves, and thus average temperature elevation, is proportional to the radius of the cell to the power 0.8. It can be interesting to see why we do not have perfect linearity, as the exponent 0.8 is a clear signal that is not in the error margin. According to the theory the maximum temperature increase on a semi-infinite medium in the absence of convection is strictly proportional to the heat source's radius. When we consider a slab, or take into account convection, slight departures from linearity of the maximum temperature are expected (See appendix A). Deviation from linearity can also come from the fact that the temperature measured by $V_{oc} - J_{sc}$ curve analysis, or by PL, is an averaged temperature on the microcell. If the device temperature is a function of the position, as we have shown in Chapter III, then the averaged temperature T_{av} given by the analysis of the dark current variations is the solution of the following equation $J_0 \exp(qV/AkT_{av}(R)) = \frac{2J_0}{R^2} \int_0^R \exp(qV/AkT(r))rdr$. The dependence of the average temperature on the heat source radius is intricate and depends on the form of the temperature field on the device. Dependence weaker than linearity can be observed and may explain our experimental results (See Appendix A). However we could not explain exactly the exponent 0.8. A complete 3D thermal simulation of our microcells (including the gold and SiO₂ layers) may be necessary to thoroughly understand our results.

It should be noted that these experiments are done with laser illumination and not concentrated sunlight. We have to verify if the temperature increase of a microcell under laser illumination is over- or underestimated compared to natural sunlight. No electric power is generated at V_{oc} , the incident light is therefore entirely converted to heat. For a solar illumination, the absorbed photon have an energy that is superior or equal to the absorber band gap E_g . For the industrial Cu(In,Ga)Se₂ microcells, $E_g=1.22$ eV, one can calculate that the average energy per absorbed photons of the solar spectrum AM1.5G is 1.73 eV. For the 532 nm laser illumination, the average energy per absorbed photons is the laser energy (2.33 eV) as each photon entering the cell is absorbed. As the average energy per absorbed photon is higher, the absorbed thermal power for a constant electric current density will be higher for the laser than for the solar illumination. As a consequence, our experiments with a laser tend to overestimate by ~25% the temperature increase on the microcell, compared to what can be expected with a solar irradiation giving the same photocurrent. The values given in this section are therefore the maximum values that would be observed under a broadband solar illumination.

2.4.4. Influence of molybdenum thickness

In the samples studied in this thesis, two molybdenum thicknesses were used: 500 nm and 1 μ m. Indeed the IRDEP samples are grown on a thick Mo layer whereas Würth samples use a thinner back

contact. We have seen in Chapter III that the Mo layer plays an important role in the heat dissipation in $\text{Cu}(\text{In,Ga})\text{Se}_2$ microcells. We can verify it by looking at $V_{oc} - J_{sc}$ curves of the different samples (Figure V-10). It is clear that V_{oc} saturates at higher concentration on samples with thicker molybdenum layers. It becomes difficult to extract the factor κ with good precision, and experiments at higher concentration ratio would be needed.

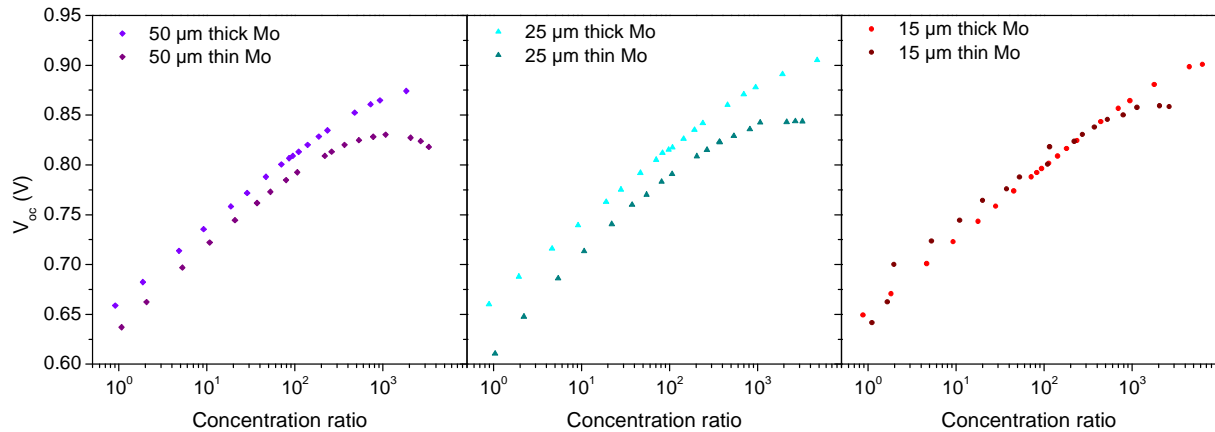


Figure V-10 : V_{oc} vs concentration ratio for the industrial cells shown on Figure V-3 (thin Mo), and comparison to IRDEP cells of the same size (thick Mo). The samples have the same glass thickness (3 mm).

2.4.5. Conclusion

We find that the microcell temperature is proportional to the device radius to the power of 0.8, which is close to analytical results. For small devices ($< 25 \mu\text{m}$), the temperature elevation stays smaller than 10 K, which is compatible with a long term operation of the device. We can also remark that by using thicker back contact metallic layers, the thermal management of the microcells is enhanced. Our measurements are done on a sample with a single microcell illuminated. If an array of microcells was illuminated simultaneously, the average temperature would increase. As discussed in Chapter III, the upper boundary of the local temperature elevation in this case has to be understood as the temperature difference with respect to the temperature of a flat-plate panel under AM1.5.

We can thus conclude from our measurements and thermal analysis that $\text{Cu}(\text{In,Ga})\text{Se}_2$ thin film microcells grown on glass are not limited by the temperature elevation under concentration.

3. Characterization under concentrated polychromatic illumination

We performed our tests with a laser of wavelength 532 nm, which energy is close to or above the absorber and buffer layer bandgaps. The question raised is the representativeness of laser results for solar cells aimed at functioning under the broadband sun spectrum [216], [217]. We will review the

different spectral dependences of Cu(In,Ga)Se_2 solar cells and evaluate the need for a broadband test of our devices.

3.1. Influence of spectral variations on the behavior of a solar cell – consequences for monochromatic illumination

3.1.1. Temperature

Depending on the energy of the incident photons, a varying part of the incident light power is lost as heat. Indeed in standard monojunction devices the excess energy between incident light and bandgap, $h\nu - E_g$, is lost by the thermalization of carriers, and all the incident energy $h\nu$ is lost at open-circuit voltage [218]. As seen in paragraph 2.4.3, the 532 nm laser light is more energetic than the average AM1.5 sunlight absorbed in Cu(In,Ga)Se_2 . Thermalization is more important in our laser experiment than for sunlight. Therefore laser tests will overestimate the temperature elevation under concentration by nearly 25%.

3.1.2. Absorption depth

The absorption coefficient of a semiconductor is highly dependent on wavelength [213]. Therefore when sunlight arrives on a solar cell, its different spectral components will not be absorbed at the same depth (Figure V-11). For example, green light will be strongly absorbed in the Cu(In,Ga)Se_2 layer, and therefore carriers will be generated in the space charge-region and efficiently collected. Conversely red or infrared light will be weakly absorbed and carriers will be generated throughout the absorber. Consequently an important proportion will be generated near the back contact, where recombination probability is high. Thus collection of carriers for infrared light is expected to be less efficient than for green light.

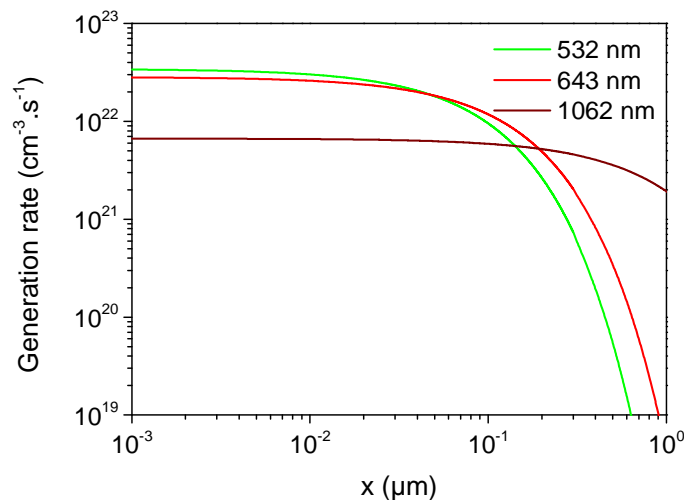


Figure V-11 : Generation rate as a function of depth in Cu(In,Ga)Se_2 for three incident wavelength under incident light flux of 100mW/cm^2 . Absorption coefficient according to [62].

We try to account for this effect by calibrating our measurements with respect to AM1.5G spectrum. Indeed we define short-circuit current density under one sun as that measured from our solar simulator. Then we adjust the laser power so that the short-circuit current density in our experiments are multiples of this reference. We then calculated the efficiency as $= P_{max}/(P_{AM1.5} \times C)$, and not as $\eta = P_{max}/P_{laser}$ to account for the higher collection factor at 532 nm as compared to averaged over the AM1.5G spectrum. Our calibration thus adjusts the photocurrent level, but does not take into account possible changes in the recombination mechanisms. Cu(In,Ga)Se₂ solar cells under sunlight are mainly limited by recombination in the space-charge region or at the heterointerface [51]. 532 nm light is absorbed in these regions and is thus expected to behave similar to sunlight.

3.1.3. Photoconductivity

The Cu(In,Ga)Se₂ solar cells have several photoconductive layers. The photoconductivity effect, i.e. increased conductivity under illumination, is highly dependent on spectral content of the incident light [51].

Persistent photoconductivity of Cu(In,Ga)Se₂, for example, is known for years now [219]. Compensating donors in the absorber, due to large lattice defects, may be ionized when illuminated with sufficient energy. Thus they can cause persistent changes in the net doping of the Cu(In,Ga)Se₂ absorber layer after illumination. The V_{Cu}-V_{Se} complex is the candidate for this defect as signaled by ab-initio predictions or experimental evidence [220], [221]. The carrier mobility in Cu(In,Ga)Se₂ increases under illumination too, and thus participates in the increased conductivity. (However mobility transients are very short and this effect is not accountable for persistent photoconductivity. The increased mobility may be due to the passivation of grain boundary defects by capture of photogenerated carriers). The persistent photoconductivity phenomena is detected even with subband gap energy (0.6 eV), indicating the presence of a defect level at 0.6 eV above the valence band [219]. For lights with energies higher than 0.6 eV, persistent photoconductivity in Cu(In,Ga)Se₂ cannot be neglected.

The CdS is also assumed to have deep acceptor states, in a quantity similar to that of donors, which compensate CdS in the dark [222], [223]. If CdS is illuminated with light, which energy is higher than its band-gap, the occupancy of the deep states in CdS is decreased [224]. Consequently, the net electron concentration increases upon illumination in CdS, if these deep traps are long-lived (which is experimentally observed with long-time relaxation). This effect in CdS is partly responsible for the non-superposition of dark and light current-voltage curves of Cu(In,Ga)Se₂ solar cells. The compensation of CdS increases the resistivity of the layer in the dark but also results in higher

secondary barriers. Indeed for Cu(In,Ga)Se_2 absorbers with relatively low Ga content ($Ga/(In + Ga) < \sim 0.5$), there is a positive band offset at the Cu(In,Ga)Se_2 /CdS interface. Upon illumination, the increased net doping in CdS leads to a downward shift of the conduction band and thus the energy of the barrier decreases (Figure V-14) [222], [223]. As a consequence the illumination of CdS with light of energy superior to its bandgap results in both a resistivity modulation and a change of secondary barriers in the Cu(In,Ga)Se_2 solar cell.

3.1.4. Conclusions

We have seen that the spectral content of the illumination has potentially an important role in the physics of Cu(In,Ga)Se_2 solar cells. We will therefore present some results recorded with lasers of different wavelengths. And then we conclude on the necessity or not of tests under concentrated sunlight.

3.2. Concentration experiment with a 644 nm red laser

3.2.1. Results of concentration with laser of different wavelengths

In order to check if the results we found with the 532 nm laser are representative of sunlight illumination, we performed tests with lower energy lasers, respectively 643 nm and 1062 nm. We found different behaviors depending on the samples. Samples with Würth Solar absorbers (industrial) behave differently than those fabricated with IRDEP absorbers.

The industrial samples show a distortion of the current-voltage characteristic upon red illumination, that tends to disappear with increasing white light bias (Figure V-12 (left)). Our white source is a 150 W halogen cold light source (KL 1500 LCD, Schott). If we illuminate the cell with a very intense laser beam, the white bias is not sufficient to recover a good fill factor. At important flux the red illumination gives a characteristic “double-diode” like behavior. The distortion is significant at any electric forward bias (Figure V-12 right).

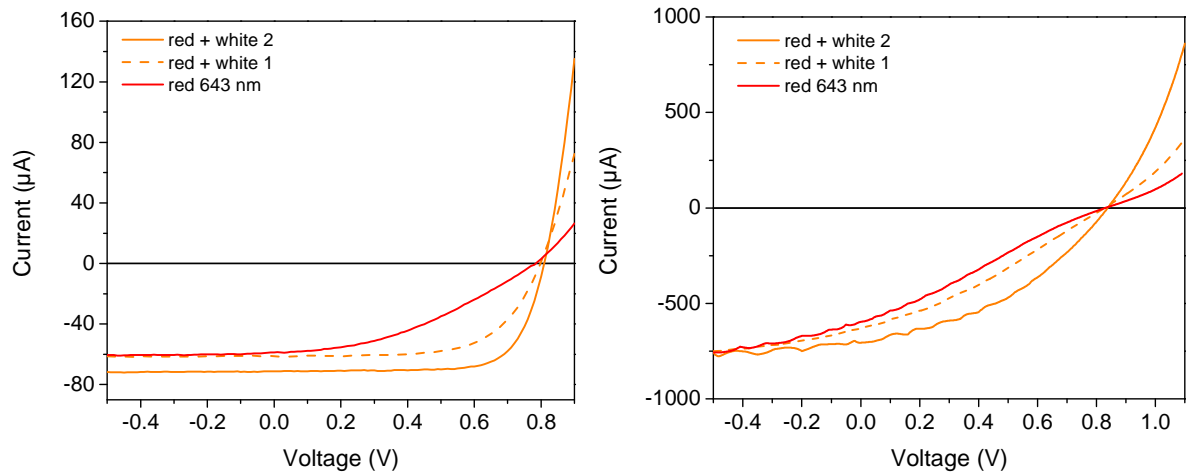


Figure V-12 : (left) Current-voltage curve of a 50 μm microcell of an industrial sample under 643 nm laser alone ($J_{sc} = 3.00 \text{ A/cm}^2$) or with two different white light biases (white 1 alone corresponds to a short-circuit current density of 42.3 mA/cm^2 , and white 2 to 487 mA/cm^2). (right) Current-voltage curve of the same 50 μm microcell under more intense flux. The 643 nm laser alone leads to $J_{sc} = 30.2 \text{ A/cm}^2$.

Conversely, samples fabricated at IRDEP do not show significant distortion upon red illumination (Figure V-13 (left)). We also tested the IRDEP cells with an infrared laser (1062 nm). We found a distortion around the maximum power point, but the diode characteristic goes back to the green one at higher voltages (Figure V-13 (right)). Therefore, red and infrared illumination does not give “double-diode” behavior, even under concentrated illumination.

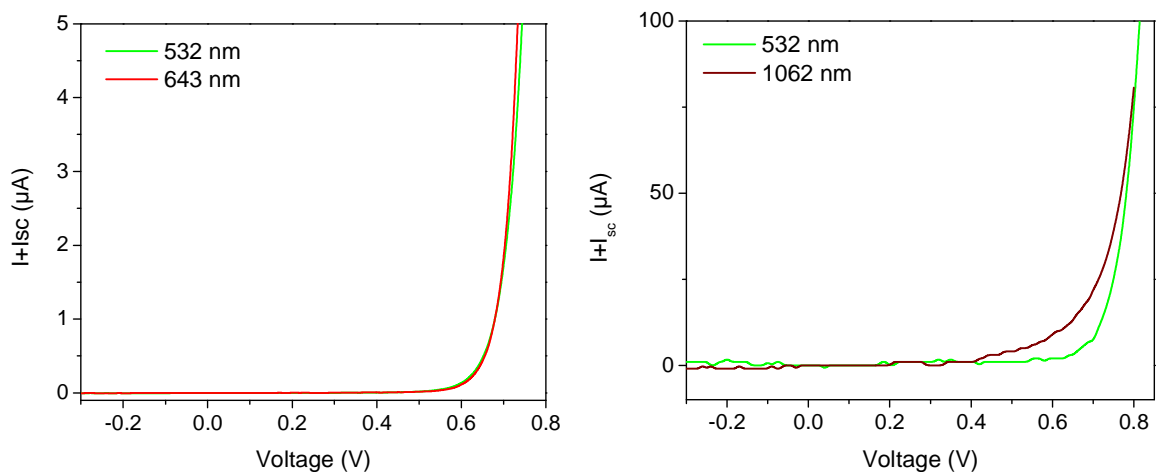


Figure V-13 : (left) Current-voltage curve of a 50 μm microcell of an IRDEP sample under 532 nm or 643 nm lasers without light bias ($J_{sc,532 \text{ nm}} = 29.5 \text{ mA/cm}^2$, $J_{sc,643 \text{ nm}} = 33.5 \text{ mA/cm}^2$). Curves have been translated of their respective J_{sc} for better visualization. (right) Current-voltage curve the same microcell under 532 nm or 1062 nm lasers without light bias ($J_{sc,532 \text{ nm}} = 7.59 \text{ A/cm}^2$, $J_{sc,1062 \text{ nm}} = 6.57 \text{ A/cm}^2$). Curves have been translated of their respective J_{sc} for better visualization.

3.2.2. Discussion

The distortion of current-voltage curve under infrared illumination in the IRDEP samples (Figure V-13 (right)) is likely due to a decreased collection efficiency. Indeed infrared light is absorbed throughout the Cu(In,Ga)Se₂ layer, and thus an important part is generated near the back contact (Figure V-11). When the cell is forward biased, the back surface field, caused by a Ga gradient [225], is not sufficient to repel the electron from the recombining back contact. Therefore the photogenerated electrons recombine, and the collection factor drops (equation (VI-12)). This increased influence of the back contact under infrared illumination is similar to what happens in thinner devices under standard illumination [32].

Samples, which absorbers come from Würth solar, exhibit a strong distortion of the current-voltage curve under red-light illumination, whereas red-light does not affect IRDEP samples. The behavior of the Würth sample is commonly referred to as the “red kink” effect [222], [223], [226]. However, to the best of our knowledge, there is no data in the literature on the absence of red-kink effect on Cu(In,Ga)Se₂ of bandgaps smaller than 1.3 eV, and we propose possible explanations.

The model proposed for the red-kink effect is based on the photoconductive characteristics of the CdS layer, described in paragraph 3.1.3. Upon illumination with light more energetic than the CdS band gap (2.42 eV), the net electron concentration increases. As a consequence, the maximum of the conduction band at the interface decreases (Figure V-14 left). Thus the thermionic current over the barrier is increased, due to the smaller energy distance between the maximum of the barrier and the Fermi level. Indeed the thermionic current over the positive conduction band offset barrier is $j_{thermo} = -A'T^2 \exp(-q\phi/kT) \exp(-\Delta E_c/kT)$, where ϕ is the potential difference between the conduction band minimum and the Fermi level at the interface, A' is the Richardson constant multiplied by the ratio of the electron effective masses of the two semiconductors [227]. However low energy photons cannot de-trap electrons from the deep states, and thus the thermionic current is reduced. Under red-illumination a double diode behavior appears due to this secondary barrier. At important forward bias the current-voltage curve is thus similar to that in the dark, as the collection of photocarriers is made impossible. This double diode disappears progressively with white light exposure [112].

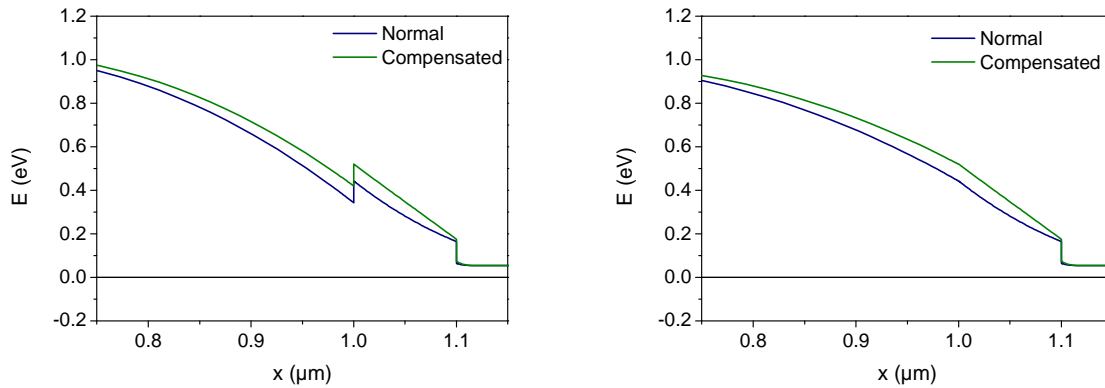


Figure V-14 : Numerical simulation with SCAPS (see box n°2 p 150) . Conduction bands at the Cu(In,Ga)Se₂ /CdS interface are displayed. The blue line corresponds to a ‘normal’ CdS with a doping density of 10^{16} cm⁻³, and the green line to a compensated CdS with an effective doping level of 10^{14} cm⁻³. (left) Simulation of a uniform Cu(In,Ga)Se₂ absorber with band gap 1.20 eV and a CdS buffer of bandgap 2.45 eV, with electron affinity 4.55 and 4.45 eV. (right) Simulation of a graded Cu(In,Ga)Se₂ absorber with band gap 1.20 eV at the back, 1.30 at the front and a minimum bandgap of 1.15 eV. A constant valence band offset is implemented by the introduction of a graded electron affinity of 4.55 at the back and 4.45 at the front. CdS has the same characteristic as for the previous simulations: bandgap 2.45 eV, with 4.45 eV electron affinity. The other parameters are that of the definition file ‘Example CIGS SCAPS28.def’.

In order to detect a red-kink effect, a secondary barrier has to be present. In other terms there must be a positive conduction band offset at the Cu(In,Ga)Se₂/CdS interface. It was shown that increased Ga content in Cu(In,Ga)Se₂ increased the bandgap, and that the conduction band was the only affected [228]. The electronic affinity of Cu(In,Ga)Se₂ is a function of Ga content and thus of bandgap. For bandgaps higher than 1.3, the conduction band offset is negative and no secondary barrier is present [112] (Figure V-14 right). We measured the optical bandgap of the Würth and IRDEP absorbers by wavelength dependent external quantum efficiency, measured with a spectral response setup. We found bandgap values of Würth absorbers between 1.22 - 1.24 eV and bandgap values of IRDEP absorbers between 1.15 – 1.17 eV. The samples we fabricated at IRDEP are double-graded samples, due to the three-stage process. They present a front surface grading, due to a richer Ga

Box 2 :

SCAPS (Solar Cell Capacitance Simulator) is a simulation software developed at the Department of Electronics and Information Systems (ELIS) of the University of Gent, Belgium [15]. SCAPS performs 1D simulations, and was originally developed for the study of chalcopyrite solar cells. Recent versions can take into account graded layers, interface states or metastabilities for example. It is based on the resolution of continuity and Poisson equations by Gummel’s algorithm [16].

content, as confirmed by SIMS measurements (Figure V-15). As a control procedure, we measured dark current activation energy of the industrial and IRDEP samples from temperature dependent open-circuit voltage and we found a value close to 1.23 ± 0.03 eV for industrial sample and around 1.34 ± 0.02 eV for IRDEP samples (Figure V-15). The activation energy of industrial sample is equal to the average bandgap, which is logical for linearly-graded samples. On the contrary for IRDEP double-graded samples, the activation energy of the dark current is significantly higher than the optical band gap extracted from EQE measurements. This is in coherence with a predominant recombination mechanism that is space-charge region recombination, which activation energy is the average bandgap energy in the SCR, close to that at the heterointerface, and thus higher than the average bandgap that is seen in EQE (minimum bandgap) [54].

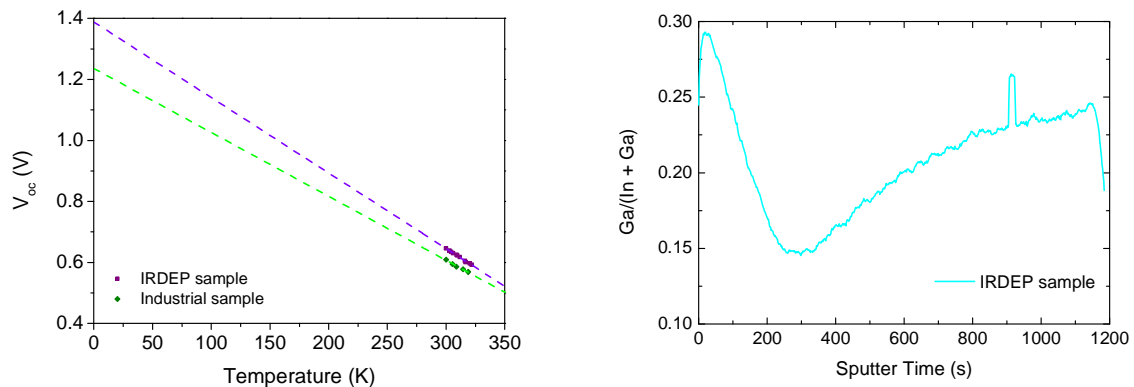


Figure V-15: (left) Open circuit voltage as a function of sample temperature for an IRDEP and an industrial sample. Dots are measurements points and dotted lines are least-square regressions. The temperature is measured with a thermocouple placed on the microcell's surface. (right) Measurement of the Ga/(In+Ga) ratio by secondary Ion mass spectrometry on the IRDEP sample. Variations in the Ga/(In+Ga) ratio induce variation of the bandgap, calibration of the signal by comparison with the mean composition measured in X-Ray fluorescence spectroscopy. The sputter time is proportional to the depth of the sample etching.

The increase in bandgap in the vicinity of the heterointerface that leads to the increase in the absorber conduction band minimum, could lead to the suppression of the secondary barrier and the formation of an interface without, or with very small, conduction band discontinuity, as proposed by Chirila [19]. We simulated with SCAPS the band diagram of a $\text{Cu}(\text{In,Ga})\text{Se}_2$ solar cell with a double-graded absorber (Figure V-14 right). We can see that for a well chosen grading profile, the conduction band offset can be suppressed even with a minimum bandgap of 1.15 eV. Thus we propose that a front bandgap grading in the $\text{Cu}(\text{In,Ga})\text{Se}_2$ that can suppress the positive conduction band offset at the heterointerface, may be the reason for the good collection efficiency of IRDEP solar cell under red and infra-red illumination.

Another explanation for the presence/absence of the secondary barrier can be the presence of a defect layer at the heterointerface. If the defects are sufficiently charged, the quasi Fermi level at the interface can be pinned [71]. Thus the thermionic current would be less sensitive to the compensation level of the CdS layer, and thus the carrier collection efficiency should not be sensitive to the illumination wavelength.

3.2.3. Conclusions

The red kink effect we detected in industrial samples is related to low energy illumination. If the incident spectrum contents short wavelengths, the red-kink effect disappears. Therefore tests under 532 nm, or real sunlight should be very similar. On the IRDEP sample no red kink effect was visible, and we expect green laser illumination to be very representative of real sunlight conditions.

We have seen that infrared light leads to lower collection efficiency at forward bias superior to 0.4 V. Laser illumination at 532 nm should therefore lead to a slightly improved fill factor compared to sunlight illumination, due to the minimization of back surface recombination, and therefore a more constant collection factor with respect to applied voltage.

In view of these results, concentration experiments under real sunlight illumination are desirable to check the behavior of our Cu(In,Ga)Se₂ microcells. Indeed the multiplicity of spectral effects in Cu(In,Ga)Se₂ solar cells may bias pure monochromatic tests. Low energy lasers lead to important bias due to photoconductivity and secondary barriers modulation effects. Conversely, green laser tests are expected to give results very close to that under real conditions.

3.3. Experimental setup for sunlight concentration

As discussed above it is important to proof the results obtained with laser light, with a broadband solar source. To perform this experiment, we tested our microcell at the PROMES-Odeillo facility. In this center we had access to a concentrating setup composed of a 1 m large parabolic mirror coupled to a heliostat. At the parabola focus, a solar spot is created that is approximately 1 cm large and can reach a concentration of $\times 12\,000$. We modified the setup to enable the test of our Cu(In,Ga)Se₂ microcells. The microcells tested are industrial cells, from Würth solar absorbers. No tests on the IRDEP samples were performed during this thesis.

3.3.1. Sketch

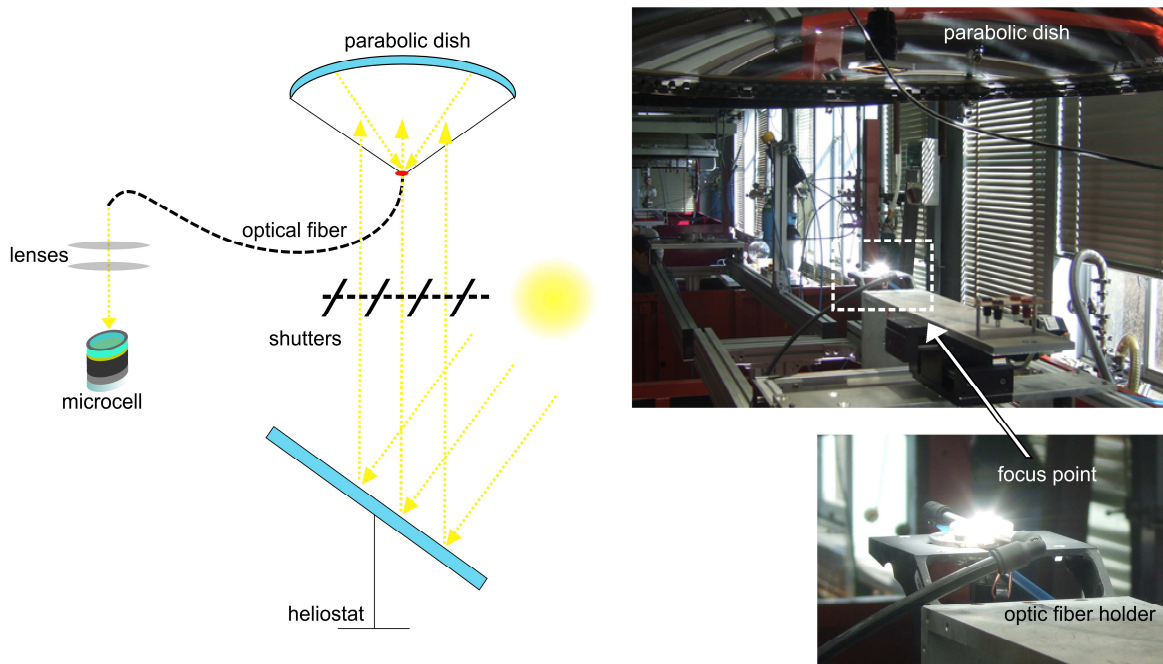


Figure V-16 : (left) Sketch of the experimental setup at the Odeillo facility. (right) photographs of the heliostats, shutters, parabola and zoom on the optical fiber holder at the focus point.

A heliostat directs the sunlight on a parabolic dish. Between these two elements mechanical shutters are placed to vary the intensity of illumination. At the parabola focus point an optical fiber is placed, that is maintained by a holder linked to a water cooling system (Figure V-16). The optical fiber used is a high damage threshold optical fiber (M200L2 Thorlabs, 200 μm core, 0.22 numeric aperture, attenuation <100 dB/km between 300 and 2100 nm). The sunlight is directed to our microscope for the test of microcells. Spot sizes as small as 30 μm were achieved.

3.3.2. Description of the measurement process

Testing microcells under real sunlight required an adapted methodology. The microscope and measurement setup are similar to that used with laser sources. The main difference comes from incident light management. Due to the bright environment, no powermeter could be placed to in situ control the incident light power by deviation of a part of the beam. On this concentration system the sunlight intensity is thus controlled by shutters, placed between the heliostat and the parabola. In order to determine the incident power two parameters have to be recorded simultaneously: the direct normal irradiance (DNI) at the time of the measurement (that is dependent on meteorological conditions) and the shutter opening. With these and a proper calibration, we know for each IV measurement the sunlight power at the optical fiber tip, and thus we can control short-circuit current linearity with concentration. However, we did not have a pyrometer capable of measuring the flux after the microscope objective. Therefore calibration is done omitting the transmission of

our microscope. The power that can be monitored is thus not that impinging on the microcell, but only proportional to it. Thus, after verification of linearity of short-circuit current with incident power, we controlled the incident power by the measurement of short-circuit current density.

The measurements under real sunlight are associated with more noise than the laser tests (Figure V-17 (right)). Indeed the incident power may vary during current-voltage curve recording, thus leading to an uncertainty in the efficiency. In case of partly cloudy sky for example the DNI varies very abruptly. In case of windy conditions, as the shutters are flexible they oscillate and the incident power varies. Despite our best efforts to limit these effects, exclude badly recorded curves, these conditions lead to an increase in the uncertainty of the measurements (estimated to 10% for J_{sc} and efficiency).

The concentration setup at Odeillo is designed to obtain ultrahigh concentrations on relatively large spot sizes (1-2 cm²). As we collect the sunlight at the focus point by an optical fiber of numerical aperture 0.22 and core diameter of 200 μm, a small portion of the flux impinging at the focus point is in fact collected in the optical fiber. Indeed the numeric aperture (NA) is $NA = \sin(\theta)$, where θ is the half-angle of the maximum light cone that can enter the optical fiber. Therefore a NA of 0.22 defines an angle θ of 13°. Additionally there are losses in the microscope as the sunlight beam is not collimated. Therefore despite the small spots needed for our microcells we did not reach concentration level much higher than $\times 100$.

3.3.3. Experimental results

We tested several industrial samples. We verified the linearity of J_{sc} with incident power, in order to determine the concentration as the ratio of $J_{sc}/J_{sc}(AM1.5G)$, as we did in laser experiments in paragraph 2.2.1.

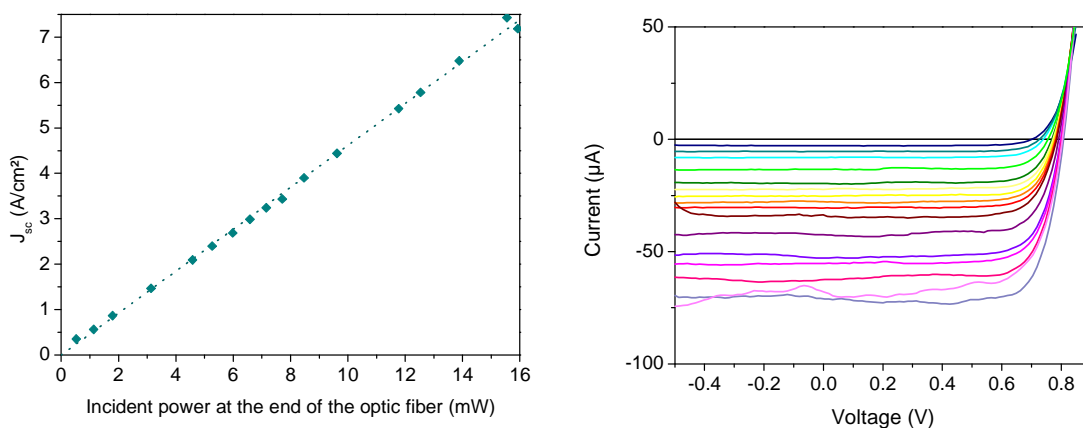


Figure V-17 : (left) J_{sc} as a function of the power at the fiber tip for a industrial sample and a microcell of diameter 35 μm. (right) current-voltage curves under real sunlight for the same industrial 35 μm microcell.

Current-voltage curves are acquired (Figure V-17 (right)) and analyzed. Due to the noise that is present on solar current-voltage curves, the short circuit current density was evaluated by a least square regression between the minimum applied voltage and 0.1 V. Short-circuit current linearity was observed for all tested devices (Figure V-17 (left)). Given the relatively low concentration reached ($\sim \times 100$), no sub-linearity was detected, which is coherent with results from paragraph 2.2.1.

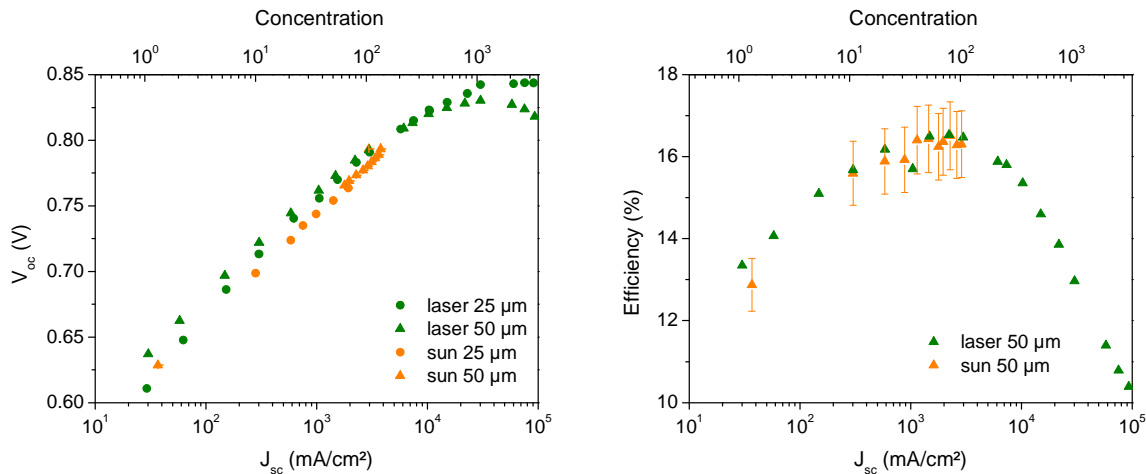


Figure V-18 : (left) V_{oc} vs. J_{sc} of microcells under laser and solar concentrated illumination. (right) Efficiency vs. J_{sc} of a microcell under laser and concentrated solar radiation. Both graphs correspond to industrial samples.

One can see that the measurements under sunlight are very similar to previous laser tests. V_{oc} increases with the logarithm of concentration ratio. As a result of the increase in V_{oc} , the efficiencies of the cells increase (Figure V-18). On the 50 μm microcell tested here, a 3% absolute increase in efficiency is measured.

3.3.4. Discussion

The measurements of the microcell current-voltage characteristics show that V_{oc} increases as the logarithm of J_{sc} (Figure V-18) as in the laser tests. One can see in Figure V-18 that the variations of V_{oc} and efficiency are very similar for the experiments performed under laser or concentrated sunlight. This clearly indicates that in $\text{Cu}(\text{In,Ga})\text{Se}_2$ industrial microcells, the quasi Fermi level splitting does not depend strongly on the wavelength of the incident photons but mainly on the number of generated electron-hole pairs, or photocurrent if the exciting wavelength is superior to 532 nm. The small discrepancies between solar and laser tests can arise from the different measurement setups, in particular from the difference in the homogeneity of illumination, or from the aging of the non-encapsulated microcells that were tested under sunlight illumination more than six months after fabrication. Besides, it can be noted that measurements under solar radiation were only performed

up to a concentration of around $\times 100$, due to the strong optical losses encountered. The saturation of open-circuit voltage due to temperature increase was therefore not detected.

4. Synthesis and Conclusion

For the first time current-voltage curves of polycrystalline thin film solar cells were measured under high fluxes ($> \times 100$). Concentrated illumination was obtained with lasers and sunlight, and good agreement between the different sources was found. Due to the miniaturization of the cells, the spreading resistance losses are negligible. V_{oc} increases up to $\times 1000$ suns, with maximum improvement of nearly 250 mV, leading to a V_{oc} above 900 mV. Cu(In,Ga)Se₂ microcells show an improvement in efficiency up to $\times 100$ on industrial samples and up to $\times 475$ on IRDEP samples. A 3% to 5% absolute efficiency increase is therefore measured. A record 21.3% efficient solar cell at $\times 475$ was measured.

The limiting parameter on microcells is series resistance, which is not size dependent, stemming from the absorber and/or the contacts. This situation is remarkably different from standard thin film solar cells. In the next chapter, light will be shed on the resistive sources limiting microcells and on the specific physics of Cu(In,Ga)Se₂ solar cells under intense light fluxes.

The analysis of the temperature elevation of microcells under high fluxes, confirmed the scale effect studied in Chapter III. Temperature elevations as small as 10 K on microcells of diameters smaller than 25 μm were measured at $\times 1000$. The influence of the back contact thickness is also highlighted. The temperature increase does not appear as a strong obstacle to the implementation of microscale thin film concentrator cells.

5. Memento

Cu(In,Ga)Se₂ microcells are tested under concentrated light, with laser (532 nm – 644 nm – 1062 nm) or sunlight.

For devices smaller than 50 μm, it was assessed that spreading resistance losses are negligible up to more than ×100.

V_{oc} increases up to ×1000 suns, with a maximum measured V_{oc} of 905 mV.

Cu(In,Ga)Se₂ microcells show an improvement in efficiency up to ×100 on industrial samples and up to ×475 on IRDEP samples. A record 21.3% efficient solar cell at ×475 was measured, and compared to a 16% efficiency at ×1.

Temperature increase on the microcell under concentrated sunlight is proportional to the radius of the cell to the power 0.8. Devices with diameters smaller than 25 μm have temperature increases at ×1000 below 10 K, which permits a good functioning of the solar cell.

CHAPTER VI. ANALYSIS AND MODELING OF THE PHYSICS OF CU(IN,GA)SE₂ MICROCELLS UNDER HIGH CONCENTRATION, OPTIMIZATION

1. Introduction	160
1.1. Analysis of concentration dependent $I-V$ curves on Cu(In,Ga)Se ₂ solar cells.	160
1.2. Physics of solar cells under concentrated illumination.....	161
2. Series resistance modulation under illumination	163
2.1. Experimental results.....	163
2.2. Modeling of series resistance modulation.	165
3. Collection factor variations	171
3.1. Experimental measurements	171
3.2. Apparent shunt resistance analysis and modeling.....	174
3.3. General 1D model of collection in a semiconductor	179
3.4. Conclusions.....	189
4. Very high concentration experiments	189
5. Conclusions	191
6. Memento	193

1. Introduction

Concentrated photovoltaics is a domain that has been developed industrially for more than a decade now [29], [30], [229]. Concentrator cells are made of crystalline material. They can be a mono-junction either in Si, GaAs or a multijunction (two to four junctions) made of III-V semiconductors grown by epitaxy on Ge substrates. Due to the intense illumination, concentrator cells are functioning in an electrical regime that is not that of standard flat panels. Surprisingly, the studies of the specifics of the physics of those devices under intense illumination have been scarce. Almost all work on the physics of solar cells under high illumination, and thus possible high injection, dates from the 1970s to early 1990s [212], [230], [231].

This chapter will be dedicated to the study of specific features of the high concentration on $\text{Cu}(\text{In,Ga})\text{Se}_2$, seen experimentally during this thesis. In this introduction we will briefly review possible effects arising under high illumination, and show how it can impact $\text{Cu}(\text{In,Ga})\text{Se}_2$ microcells.

1.1. Analysis of concentration dependent I - V curves on $\text{Cu}(\text{In,Ga})\text{Se}_2$ solar cells.

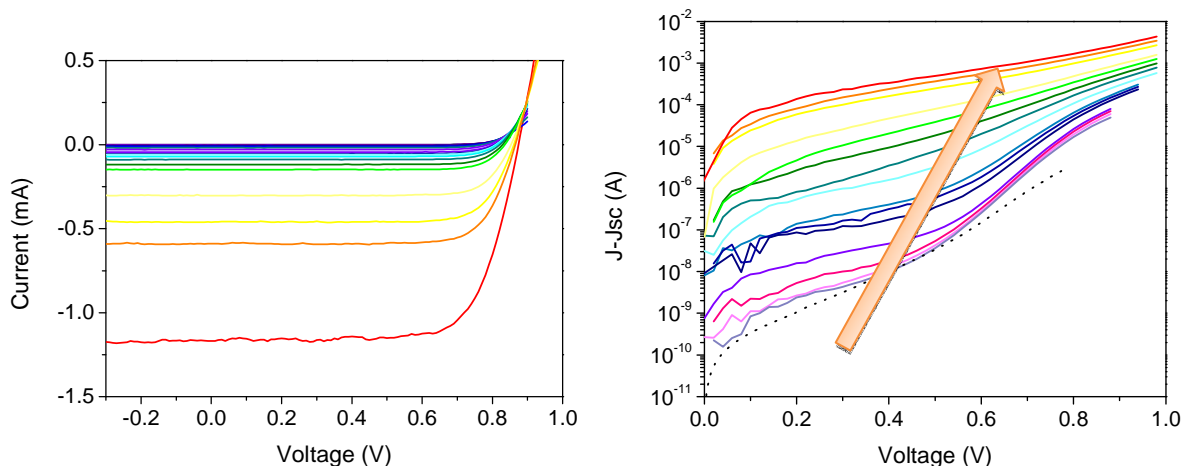


Figure VI-1 : (left) Current-voltage curves measured on a 50 μm microcell of an industrial sample under increasing illumination with 532 nm laser (right) I_{sc} - shifted current - voltage curves of the same cell. The dotted line corresponds to the dark current voltage curve. The arrow indicates increasing incident power.

Figure VI-1 shows current-voltage characteristics of a Cu(In,Ga)Se₂ microcell under increasing laser power. We can see that current-voltage curves at different light intensities on Cu(In,Ga)Se₂ microcells are not simply translated by a constant photocurrent term. The shifting approximation is not respected. Indeed by looking at the J_{sc} - shifted current voltage curves (Figure VI-1 right) we can observe that J_{sc} - shifted current voltage curves are not superimposed. Two interesting features can be seen in Figure VI-1 and will be studied in this chapter. First, series resistance is not constant with concentration, and this dependency will be reviewed. Second, the increase in J_{sc} - shifted current voltage curves will be studied to determine which mechanism is responsible. Beforehand, some of the physics of solar cells under high illumination will be reviewed to put the results of Figure VI-1 in perspective.

1.2. Physics of solar cells under concentrated illumination

Ambipolar diffusion

Usually, the analyses of the physics of solar cells rely on the assumption that the photogenerated carriers have a concentration much smaller than the doping of the semiconductor. Minority and majority carriers are thus defined. As a consequence, the space charge associated with minority carriers is supposed to be completely negligible, due to the relaxation of majority carriers. However the assumption of minority carrier is valid only when incident light intensity is sufficiently low. For high light intensities and moderate doping, the photogenerated electron and hole concentrations can become large compared to that of the dark state. (For example if we consider a carrier lifetime of 10 ns, the photogenerated carrier concentration under AM1.5 in a 1 μm thick absorber is $2 \cdot 10^{13} \text{ cm}^{-3}$. At $\times 500$ the photogenerated carriers concentration is 10^{16} cm^{-3} , which is a level comparable to doping in Cu(In,Ga)Se₂ [166]). In the case of photogenerated carriers in concentration close to the doping, no carrier type can be neglected and space charge effects have to be taken into account. The electric field induced by the difference in the mobility of holes and electrons tends to accelerate the slowest carrier and slow the fastest (this phenomenon is called ambipolar diffusion) (Figure VI-2 left). The electric field that can be calculated from continuity equations is [212]:

$$E = \frac{J}{q(n\mu_n + p\mu_p)} - \frac{kT}{q} \frac{1}{n\mu_n + p\mu_p} \left(\mu_n \frac{d(\Delta n)}{dx} - \mu_p \frac{d(\Delta p)}{dx} \right) + \frac{n_0\mu_n + p_0\mu_p}{n\mu_n + p\mu_p} E_0 \quad (\text{VI-1})$$

Subscript 0 correspond to quantities at thermal equilibrium without injection. The electric field is the sum of three components: an ohmic term (left) (depending on injection level and current density), a 'Dember' term (middle), depending on injection level and its derivatives, and a term reflecting the modification of the original electric field (right). Note that the Dember term is zero when the two

types of carriers have the same mobility or when excess carrier concentration shows no gradients. The third term is the modification of the original electric field (at thermal equilibrium) due to injected carriers, which may not be neglected under high illumination. Thus the superposition principle can become invalid.

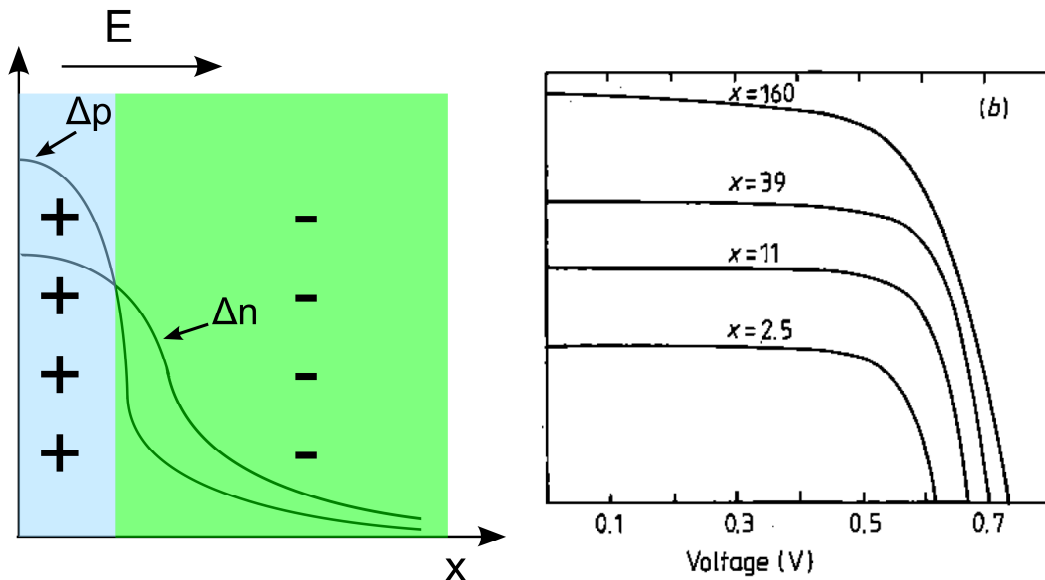


Figure VI-2 : (left) Ambipolar diffusion : photogenerated carriers as a function of position in an illuminated semiconductor. Due to their different mobilities, photogenerated holes and electrons diffuse at different speed after illumination and create an internal electric field. (right) Current-voltage curves at different concentration ratio for a n^+pp^+ Si solar cell with a base resistivity of 50 ohm.cm. Graph reproduced from [232]

Short-circuit current density non-linearity

Due to the influence of high concentration of photogenerated carriers, non-linear effects can arise. Short circuit current can become non-linear with incident power for example [211]. Sub-linearity is often seen and usually due to resistive losses. For a photocurrent density that is linear with incident power, short-circuit current can be decreased by a substantial resistive loss term. In the extreme cases a saturation of the short-circuit current can thus be seen. The short-circuit current can also become non-linear due to the non-linear behavior of some recombination mechanisms (such as radiative or Auger recombination) [233]. But the photocurrent density itself can become non-linear with incident power at high intensity, as observed in silicon concentrator cells [233–235]. Indeed due to increased current density, an ohmic electric field in the lightly-doped quasi-neutral region is created. This leads to the enhancement of minority carrier collection, along with inevitable majority carriers slowing down, and decreases recombination, leading to a higher photocurrent [232], [234], [235]. This explains the slight superlinearity of short-circuit current density observed experimentally.

Non linearity at high concentration can also stem from conductivity demodulation [232], [236], [237]. In thick solar cells such as crystalline silicon solar cells, the base conductivity can be enhanced by electron or hole injection. Under concentration the modulation of resistance with bias becomes non negligible as the modulation range is wide and can spread from negative bias to around maximum power point. Therefore an apparent shunt resistance can be detected on current-voltage curves (Figure VI-2 right) [232].

Defect saturation

High injection in solar cells may also result in the saturation of some recombination paths. For example, if one assumes that Shockley-Read-Hall recombination (SRH) has a finite rate, the limited number of defects can result in the saturation of this recombination mechanism if the photogenerated carriers are sufficiently numerous [238]. Thus the diode current component under illumination will tend to be smaller than in the dark due to the increased carrier lifetime [239]. As a consequence the shifting approximation is no longer valid [51].

We can see that high illumination effects lead to modifications of the classic solar cell description (Chapter II). In order to understand the signals detected in Figure VI-1, we will in a first part study the evolution of series resistance with concentration.

2. Series resistance modulation under illumination

We have seen in the preceding chapter that $\text{Cu}(\text{In,Ga})\text{Se}_2$ microcells present size-independent sources of resistance. Figure VI-1 (left) suggests that these resistance sources are not constant over the wide concentration range studied. We will thus determine experimentally the resistance as a function of illumination, and present a model to explain the observed behavior.

2.1. Experimental results

2.1.1. *Methodology of the determination of the series resistance at a given illumination intensity*

In order to determine the series resistance at different concentration ratios we follow a precise methodology. First $V_{OC} - J_{SC}$ and efficiency - J_{SC} curves are fitted in order to determine saturation currents and temperature dependence, as seen in the previous chapter. With these values of saturation currents, that are supposed to be constant over the whole concentration range, series resistance at each incident power is determined in order to fit the corresponding current-voltage curve, especially in the bias range above the maximum power point. The hypothesis of constant saturation current may not be perfectly true and the variation of the slope at high forward bias that we attribute here solely to series resistance may be slightly modulated.

2.1.2. Variation of series resistance with concentration

We study the variation of series resistance as a function of light concentration for industrial microcells. We observe a clear variation of series resistance with light intensity (Figure VI-3). Series resistance drops by a factor of nearly ten between 1 and 1000 suns. One can observe that at $\times 100$, near the optimum concentration ratio, the series resistance is about 0.02 ohm.cm^2 . This value corresponds to what we predicted from the appearance of the maximum in efficiency (Figure V-5) [121]. Thus the decrease in series resistance with light intensity explains that the optimum concentration is around $\times 100$, whereas the values of dark series resistance between 0.1 and 1 ohm.cm^2 would have led to much smaller optimum concentration ratio.

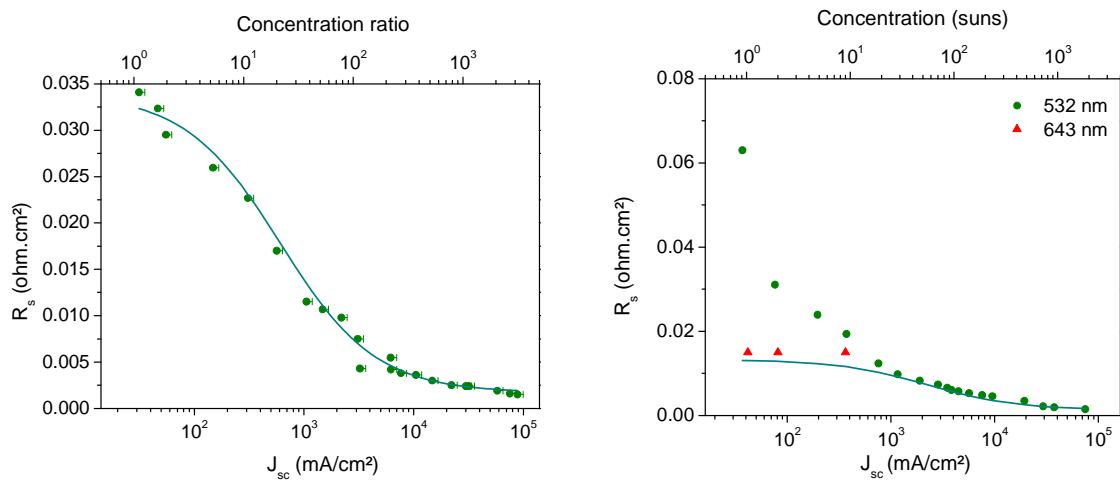


Figure VI-3 : (left) Series resistance vs. J_{sc} for a cell of $15 \mu\text{m}$ of industrial sample. (right) Series resistance vs. J_{sc} for a cell of $50 \mu\text{m}$ of IRDEP sample. Green points correspond to concentration experiments with a 532 nm laser source. Red triangles correspond to 643 nm laser illumination with preliminary cell forward biasing. Solid line to our fit.

We also analyzed IRDEP samples (Figure VI-3 right). We found similarly a decrease in series resistance with incident intensity. However the form of the $R_s - J_{sc}$ curve is considerably different in the two samples. Even if the series resistance evolution at $\times 100$ and higher concentrations is similar, the series resistance under low concentration ratio differs significantly. It should be noted that the series resistance values in the IRDEP sample are dependent on the measurement method (i.e. in the presence or absence of preliminary forward biasing) as they present a slight metastability. However both the industrial and IRDEP samples show a one sun series resistance that is much smaller than that in the dark.

2.2. Modeling of series resistance modulation.

2.2.1. Photoconductivity effect on semiconductors

We have seen in the previous chapter that several layers in the Cu(In,Ga)Se₂ solar cells are known to be compensated. An increase in their conductivity under illumination is thus expected through the detrapping of carriers from deep defect states. However this effect will only lead to the recovery of the net doping density that would be present without deep defects. The increase in conductivity at values greater than that of the non-compensated material relies on the increase in carrier concentration due to photogeneration. Two photoconductive effects have therefore to be distinguished: decompensation of the semiconductor under illumination and “pure” photoconduction.

The number of deep-defects that are the source of compensation are of the order of 10¹⁷ cm⁻³ in CdS [224], and smaller than 10¹⁶ cm⁻³ in Cu(In,Ga)Se₂. The compensation effect is thus expected to be much more important in CdS than in Cu(In,Ga)Se₂. Under large incident light power, the occupancy factor of the deep defects is expected to be small, and the semiconductor should not be compensated. Indeed the occupation of defects states under illumination [110] is :

$$f = (C_n n + C_p p_1) / (C_p (p + p_1) + C_n (n + n_1)) \quad (\text{VI-2})$$

where $n_1 = n_i \exp((E_d - E_i)/kT)$ and $p_1 = p_i \exp((E_i - E_d)/kT)$ with n_i and p_i the intrinsic concentrations, E_i the intrinsic Fermi level, and E_d the energy level of the defects. If we suppose the energy of the defects to be above the intrinsic Fermi level ($E_d > E_i$), then $n_1 > n_i > p_1$, and we suppose a photogeneration high enough so that n_1 is small compared to the total electron concentration n , the occupancy factor becomes $f \cong C_n / C_p (1 + C_p n_i^2 / C_n n_1 n)$. If the capture cross sections of these defects are highly asymmetric [224], i.e. much higher for holes than for electrons ($C_p \gg C_n$), the occupancy of these defects stays very small as long as $n_i^2 / n_1 n \ll 1$. Therefore depending on the position of the defects with respect to the intrinsic Fermi level, the generation level needed to empty the deep defect states can vary. However it is clear that the occupancy factor will decrease with increasing incident light power. The effect of compensation can therefore be neglected at very high concentration levels.

In the high concentration range, the characteristics of the different samples are similar and are due to photoconduction. Given the doping levels and thicknesses of the different layers, the photoconduction will mainly occur in the Cu(In,Ga)Se₂ absorber. The increase in photogenerated carrier density is proportional to the incident light power density P_{light} , $\Delta n = \Delta p = \beta P_{light}$, where Δn and Δp are respectively the increase in electron and hole average concentrations and β a

proportionality factor. Cu(In,Ga)Se₂ is a p-type semiconductor, so that we can neglect the dark electron concentration (n_0) compared to both the dark hole (p_0) and photogenerated carrier concentration (Δn). Therefore the conductivity of the absorber σ is expressed as :

$$\sigma = q(\mu_n n + \mu_p p) = q \left(\mu_n \beta P_{light} + \mu_p (p_0 + \beta P_{light}) \right) \quad (VI-3)$$

where q is the elementary charge and μ_n (μ_p) is the electron (hole) mobility in the absorber. We can thus determine the series resistance associated with the absorber layer :

$$R_{s,CIGS} = \frac{R_{s0}}{\left(1 + \left(1 + \frac{\mu_n}{\mu_p} \right) \frac{\beta P_{light}}{p_0} \right)} \quad (VI-4)$$

where R_{s0} is the absorber resistance in dark condition, $R_{s0} = t/q\mu_p p_0$, with t the absorber thickness. β can be evaluated around open-circuit voltage, where the series resistance is fitted from current-voltage measurements, and where the recombination rate equals the generation rate. Expressing the recombination rate U in terms of photogenerated carriers and lifetime, and the generation rate G as a function of the incident laser power density gives :

$$U = \frac{\Delta n}{\tau_n} = G = \frac{P_{light} \times EQE}{h\nu \times t} \quad (VI-5)$$

where τ_n is the minority carrier lifetime, EQE is the external quantum efficiency at the incident wavelength (532 nm), and $h\nu$ the energy of the incident photons. Equation (VI-5) is based on the assumption of carrier lifetime independent of the concentration. This is reasonable in low injection when Shockley-Read-Hall recombination is dominant. In high injection, radiative recombination can become important and the radiative lifetime τ_{rad} decreases with increasing photogenerated carriers concentration Δn , which in a p-type material gives $\tau_{rad,high} = \tau_{rad,low}/(1 + \Delta n/N_A)$ [213]. However the radiative lifetime in low injection in Cu(In,Ga)Se₂ is around 1 μ s for samples with a doping density of 10^{16} cm⁻³ [115], which is also the doping level of our samples. This value is nearly a thousand times more important than the low injection effective lifetime, dominated by Shockley-Read-Hall recombination. Thus considering a constant lifetime should be a valid assumption as long as $\Delta n < 1000 \times N_A$, which is true in the entire concentration range studied in this thesis [115]. Auger recombination can also decrease the effective carrier lifetime. Unfortunately we have no data concerning Auger recombination on Cu(In,Ga)Se₂. As shown in Chapter II, the Auger recombination coefficient of Cu(In,Ga)Se₂ (1.1-1.2 eV in our samples) can reasonably be estimated around 10^{-30} cm⁶s⁻¹ from the Auger coefficients of various direct bandgap III-V semiconductors [116]. The Auger

lifetime under illumination is $\tau_{Auger} = \left(C_p N_A^2 (1 + \Delta n/N_A)^2 + C_n N_A^2 \Delta n/N_A (1 + \Delta n/N_A) \right)^{-1}$, where C_p and C_n are Auger recombination coefficients. Thus Auger recombination is not expected to be limiting our devices, i.e. leading to carrier lifetimes of the order of 1 ns, up to $\Delta n \approx 3000 \times N_A$, which is well above the concentration range studied in this work. However given the absence of experimental values for Cu(In,Ga)Se₂ Auger coefficients, caution is required. As a conclusion, the hypothesis of constant lifetime is reasonable in the concentration range studied here.

We can thus deduce that $\beta P_{light} = \tau_n P_{light} EQE / (t \times hv)$. Equation (VI-4) thus becomes:

$$R_{s,CIGS} = \frac{R_{s0}}{\left(1 + \left(1 + \frac{\mu_p}{\mu_n} \right) \frac{\mu_n \tau_n EQE \times P_{light}}{\mu_p p_0 \times t \times hv} \right)} \quad (VI-6)$$

We can express the product $\mu_n \tau_n$ as a function of the minority carrier diffusion length in the absorber L_n , $\mu_n \tau_n = q/kT \times L_n^2$. Replacing $\mu_p p_0$ by its expression as a function of R_{s0} , we find :

$$R_{s,CIGS} = \frac{R_{s0}}{\left(1 + \left(1 + \frac{\mu_p}{\mu_n} \right) \frac{q^2 L_n^2 EQE \times R_{s0} \times P_{light}}{kT \times hv \times t^2} \right)} \quad (VI-7)$$

Therefore the series resistance of a microcell, for which we can neglect the compensation of CdS, is composed of a light independent series resistance R_c , stemming from the contacts, and a light modulated series resistance originating from the absorber :

$$R_{s,microcell} = R_c + \frac{R_{s0}}{\left(1 + \left(1 + \frac{\mu_p}{\mu_n} \right) \frac{q^2 L_n^2 EQE \times R_{s0} \times P_{light}}{kT \times hv \times t^2} \right)} \quad (VI-8)$$

Equation (VI-8) can be rewritten as:

$$R_{s,microcell} = R_c + \frac{R_{s0}}{\left(1 + \left(1 + \frac{\mu_p}{\mu_n} \right) \left(\frac{L_n}{t} \right)^2 \frac{q R_{s0} J_{sc}}{kT} \right)} \quad (VI-9)$$

The ohmic drop related to the absorber, normalized by kT/q , $q R_{CIGS} J_{sc} / kT$ leads at high current densities to a maximum value of $(t/L_n)^2 / (1 + \mu_p/\mu_n) \sim (t/L_n)^2$, as $\mu_p \ll \mu_n$. Therefore we can see that Cu(In,Ga)Se₂ microcells for ultrahigh fluxes should be designed so that the ratio t/L_n is minimum. However practical limitations can arise for such devices, as the back contact recombination will become increasingly detrimental as diffusion length increases or thickness

decreases. Equation (VI-9) is adequate when the influence of CdS compensation can be neglected, i.e. when the light concentration is sufficient.

2.2.2. Comparison with experimental results.

We use the model developed above to fit our experimental results. On industrial samples (Figure VI-3 (left)) only one effect is visible, the photoconduction. Thus we can use equation (VI-4), or equivalently (VI-8). The fit is represented by the solid curve. From this fit we can extract an estimation of the diffusion length of electrons in $\text{Cu}(\text{In,Ga})\text{Se}_2$ (equation (VI-8)). We find $R_c = 1.8 \cdot 10^{-3}$ ohm.cm², $R_{s0} = 3.1 \cdot 10^{-2}$ ohm.cm². Given that the external quantum efficiency of our device at 532 nm is 84%, and the absorber thickness is 2.5 μm , we evaluate L_n to 3 μm (assuming $\mu_p \ll \mu_n$). This value is in the high-end of reported values for $\text{Cu}(\text{In,Ga})\text{Se}_2$. However in graded samples, the back-surface field enhances the collection efficiency and diffusion lengths between 1 μm to absorber thickness have been measured [240]. It should also be noted that the analysis of both electron beam induced current and external quantum efficiency experiments rely on a guess of back surface recombination velocity which results in a large uncertainty on the determination of diffusion lengths when they are in the order of the film thickness. Keeping also in mind that our estimation of diffusion length relies also on strong hypothesis, e.g. constant Δn , we consider $L_n = 3 \mu\text{m}$ as a good estimate compared to published results.

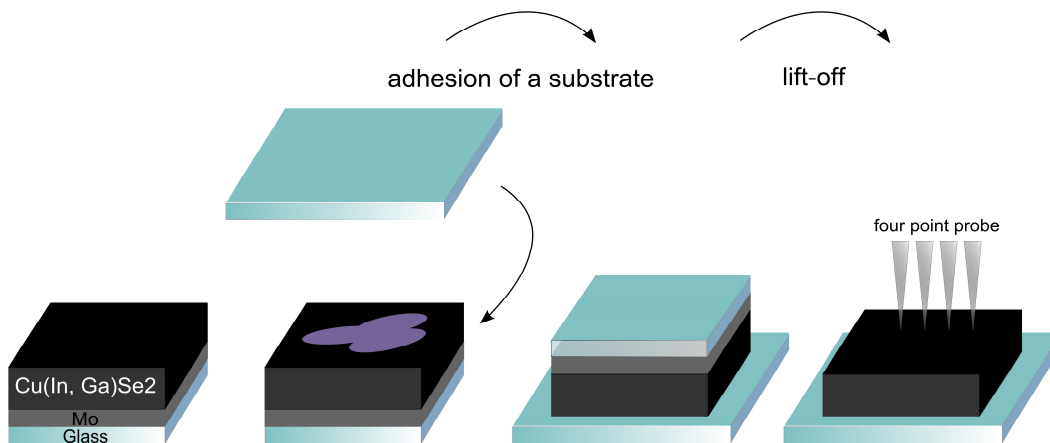


Figure VI-4 : Sketch of the lift-off procedure

On the IRDEP absorber (Figure VI-3 (right)), one can see that the previous model cannot apply at low concentration ratio. If the current-voltage curves are taken without preliminary biasing of the cell, high series resistance at low illumination are measured (532 nm measurements), whereas if we polarize the cell for 1 min at 0.8V before measuring the current voltage curve, the series resistance is smaller (643 nm illumination measurements). At high concentration we have a modulation of series resistance with concentration similar to that of industrial samples. In order to have a measurement of the resistance induced by the $\text{Cu}(\text{In,Ga})\text{Se}_2$ layer in the dark R_{s0} , we performed four point probe

measurements on the bare absorber. The measurement of the resistivity of the absorber was performed as follows. A lift-off procedure reports the Cu(In,Ga)Se₂ layer from the Mo substrate to a glass host substrate (Figure VI-4). This enables us to do a measure on the absorber layer alone, without the influence of the conductive back contact. Four point probe measurement is performed, which gives us an information on the sheet resistance of the sample. In order to determine the resistivity of the sample, we measure its thickness using a profilometer, and found 2.9 μm +/- 5%. (The thickness found is in good agreement with that extracted from the interference fringes seen on reflectance spectra, 3 μm +/- 0.2 μm). We found lateral resistivity of 40 ohm.cm² (+/- 5%). Then the resistance due to the Cu(In,Ga)Se₂ layer, R_{s0} , is calculated supposing equal lateral and vertical conductivity, and we found $1.2 \cdot 10^{-2}$ ohm.cm². This value is in coherence with the measurements with preliminary biasing of the cell. Then we can fit the only free parameters that are R_c and β . The fitted results are represented in Figure VI-3 (right) by the solid blue curve. We found $R_c = 1.3 \cdot 10^{-3}$ ohm.cm², β/p_0 of $1.8 \cdot 10^{-1} \text{ W}^{-1}\text{cm}^{-1}$. We can thus determine the diffusion length in the Cu(In,Ga)Se₂ as done previously and we found a value of 3 μm on the IRDEP sample. This value, which is the same as in the industrial samples, has to be understood as a rough estimate, due to the numerous hypotheses done in the model.

Our measurements of series resistance as a function of concentration are done with at least one sun illumination. The value of the series resistance for all our samples at this illumination level is found significantly smaller than that in the dark. For example the IRDEP sample shows on average a series resistance of 0.27 ohm.cm² in the dark. This difference can be attributed to the CdS compensation.

2.2.3. Discussion

We have seen that the series resistance of Cu(In,Ga)Se₂ devices is highly modulated under incident light. A nearly tenfold decrease between low and high concentration value is seen. At high concentration the source of resistance that is modulated is the Cu(In,Ga)Se₂ absorber. The modulation enables the estimation of the minority carrier diffusion length, and a value of 3 μm that is high but still comparable to published results is found.

At low concentration ratio, differences between the different samples are seen. However both samples show a 1 sun series resistance that is much smaller than the dark value ($\approx 0.3 \text{ ohm.cm}^2$). The compensated character of the CdS layer is likely involved. We have seen from a simple analysis that a high density of compensating acceptor defects leads to a high dark resistivity. However upon illumination with light more energetic than the compensation defect ionization energy, higher conductivity can be reached. In the absence of complementary measurements, our interpretation stays simple. We have not determined the ionization energy of the defects, and we can only say that

it is smaller than 1.16 eV, because our 1064 nm laser provokes a decrease in series resistance. This is a small value, as the defect acceptor level in CdS ($E_g = 2.4$ eV) is usually supposed to be situated around 1eV above valence band or mid-gap [224]. Moreover we cannot discriminate between an effect that would be a CdS bulk property, a grain boundary effect or the influence of defect layer at the heterointerface.

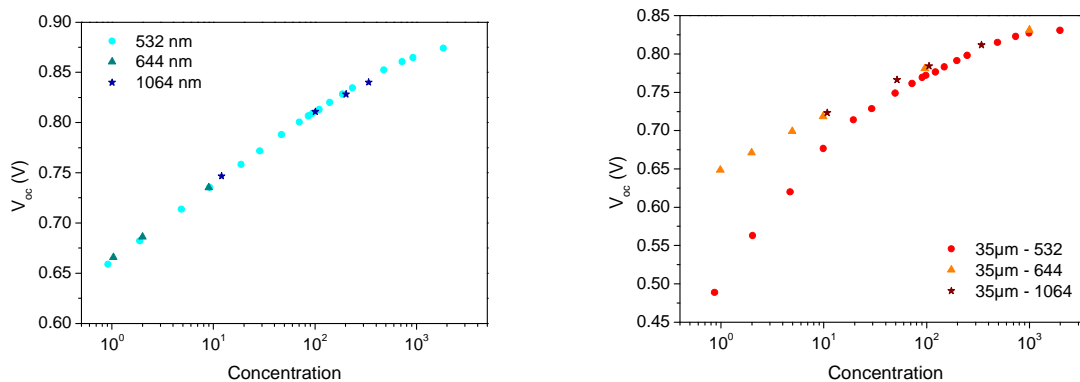


Figure VI-5 : Open-circuit voltage as a function of concentration for two IRDEP samples. Measurement with 532 nm is done without preliminary biasing of the cell, whereas for red and infrared illumination the cell is forward biased for 1 min at 0.8V before measurement. (left) IRDEP sample studied in this thesis. No dependence on the measurement method seen. (right) Strongly metastable IRDEP sample. At high concentration the measurements are similar but strong difference is seen at low illumination levels.

For the low illumination range, the IRDEP sample presents a clear metastability. Depending on whether it is forward biased or not before the current-voltage measurements, the series resistance values change. However this metastability does not affect open-circuit voltage measurements (Figure VI-5 left). However, on other IRDEP samples, not described in this thesis, a stronger metastability was detected. Open-circuit voltage values in the low concentration range were strongly dependent on measurement procedure (Figure VI-5 right). For concentration ratio over $\times 100$ however, the results converge. We can correlate this result as a quicker steady state appearance with more intense illumination, which has already been seen in $\text{Cu}(\text{In,Ga})\text{Se}_2$ [221]. Thus we are confident that the results at high concentration factor on the slightly metastable samples are not modified by this effect, and that the decrease in series resistance is not an artifact.

The value of the light independent resistance that we attribute mainly to the contacts is very small, of the order of $1-2 \cdot 10^{-3} \text{ ohm.cm}^2$, which is below reported values for the $\text{Mo}/\text{Cu}(\text{In,Ga})\text{Se}_2$ interface that tends to be an order of magnitude higher [41], [46]. However measurements of the $\text{Mo}/\text{Cu}(\text{In,Ga})\text{Se}_2$ interface, where a MoSe_2 layer is formed, is always done with an additional metallic contact deposited after the growth of $\text{Cu}(\text{In,Ga})\text{Se}_2$ (either Au or Mo). Thus the measurements can be

biased by the contribution of the Au/Cu(In,Ga)Se₂ or MoSe₂-free Mo/Cu(In,Ga)Se₂ interfaces, and this can explain the discrepancies between our value and that reported in the literature. The value of the front contact resistance that we determined in Chapter IV by TLM was well below 10⁻³ ohm.cm², showing that optimization of the back contact is more crucial than that of front contact.

2.2.4. Conclusions on the limit concentration intensity on microcells

Our results show that the resistance modulation is substantial enough to decrease the series resistance by more than one order of magnitude in the concentration range explored. Maximum efficiencies at concentrations around ×1000 would require improved contact resistance, but also increased diffusion lengths or reduced Cu(In,Ga)Se₂ thickness. However a use up to ×475 is already possible with absorber materials, where the ratio of diffusion length over thickness is close to 1.

The value of the light independent resistance that we attribute mainly to the contacts is in the order of 1-2 10⁻³ ohm.cm², and sufficiently low to enable the operation of devices up to ×1000. To decrease this resistance further, optimization of the back contact is needed.

We have seen in Figure VI-1 that the series resistance was modulated with illumination level, and we studied this modulation. We also saw that there was an increase in J_{sc} - shifted current voltage curves. The next section is dedicated to the study of that effect.

3. Collection factor variations

3.1. Experimental measurements

3.1.1. I-V curves with apparent shunt resistance

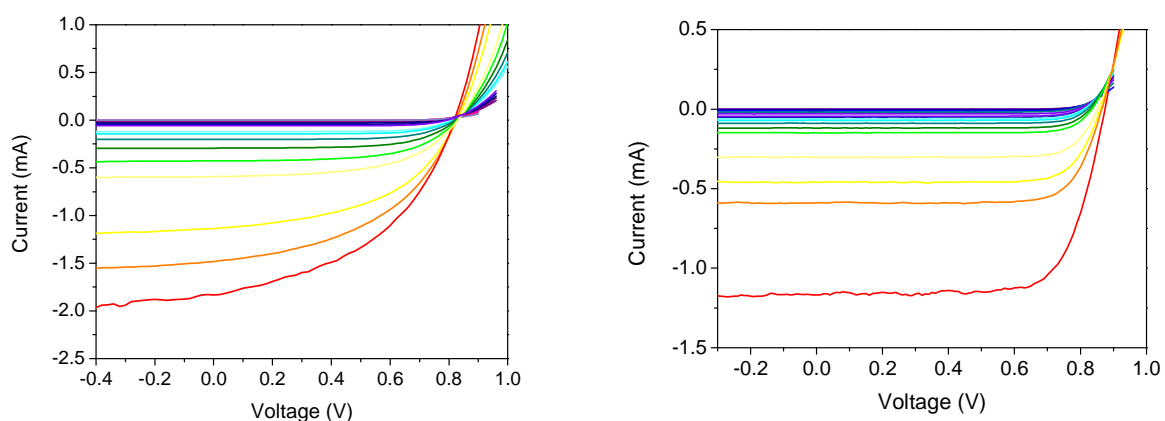


Figure VI-6 : Current-voltage curves measured on a 50 μm microcell under increasing illumination with a 532 nm laser. (left) industrial sample (right) IRDEP sample.

We have seen in paragraph 1.1, that there was an increase in the I_{sc} -shifted current - voltage curves with concentration. On Figure VI-6 (left) we can see a strong decrease in the fill factor with concentration, due to the appearance of a slope of the current-voltage curve at small applied bias. It seems that there is a shunt conductance that increases with illumination intensity. A classic leakage current, defined by a shunt resistance R_{sh} , has an influence that weakens under concentration. Moreover under reverse bias a shunt resistance does not result in a plateau as observed on Figure VI-6 (left). Therefore we have to determine the origin of this behavior, which will be called “apparent shunt resistance”, as a reference to what is seen on Si solar cells (Figure VI-2 right). This trend is seen in all industrial samples. This behavior is hardly seen on IRDEP samples and the fill factor losses are less important (Figure VI-6 (right)).

Several sources can explain such a behavior, and we will review them in the next paragraphs. In order to get more insight in the phenomena under study, we performed modulated photocurrent experiments.

3.1.2. Principals of the modulated photocurrent experiment

The modulated photocurrent experiment relies on the modulation of the light intensity. The photocurrent J_{ph} is directly proportional to illumination intensity, and will be modulated. If the modulation is small, the other parameters of the cell should stay rather constant. Thus by recording the signal that is in phase with the light excitation with a lock-in analyzer, at different applied voltages, we can have a direct measure of the photocurrent as a function of voltage. We would therefore be able to detect if the apparent shunt resistance is a diode current or a photocurrent term.

The experimental setup for the modulated photocurrent experiment consists of an acousto-optic modulator (AOM, AA optoelectronic) that modulates the light beam of a 532 nm laser. The AOM is composed of a crystal attached to a piezoelectric device that vibrates under an oscillating voltage signal. The vibrations in the crystal can change the refractive index of the crystal, through variation of its strain field. A beam incident on the AOM will be diffracted in several orders that are controlled by the voltage modulation of the piezoelectric device. A signal generator (Tektronik AFG3102) produced a sinusoidal signal that is the input of the AOM and that is the reference for the lock-in detection. The lock-in detection (EG&G 5206 2 phase lock-in analyzer) extracts the electric signal coming from the solar cell that is in phase with the light sinusoidal signal.

3.1.3. Results of modulated photocurrent

We performed different tests on industrial samples. We determine that the signal was independent of the modulating frequency, at least between 70 and 420 Hz, and we chose 420 Hz as the modulation frequency. For very high frequency, detection becomes difficult.

We first modulate the incident light in “on-off” configuration: the voltage signal that feeds the AOM is a sinusoid with peak-to-peak value twice the average value (Figure VI-7 left). We observed that the modulated photocurrent curves superimposed with dark current shifted current-voltage curves. Thus on-off modulation does not give supplementary information from the comparison of dark and illuminated current-voltage curves. A second order signal, detected at a frequency double than that applied to the AOM, was also detected by our lock-in analyzer. This means that non-linear effects affect on-off modulation. This configuration is not precise enough to conclude the origin of the apparent shunt.

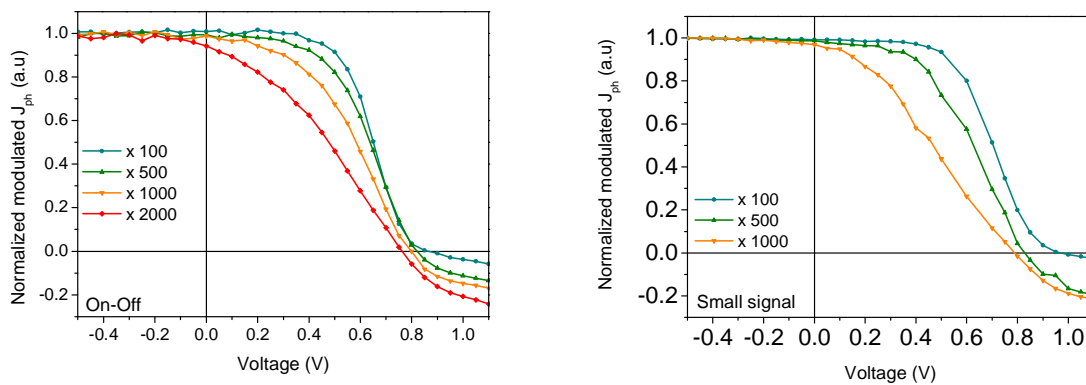


Figure VI-7 : Normalized modulated photocurrent as a function of applied voltage. (left) On-Off modulation, at a frequency of 420 Hz. (right) in a small signal configuration at 420 Hz.

In order to minimize non-linear effects, we place ourselves in small signal configuration. The amplitude of voltage modulation is 100 mV for an average offset of 4V. We measure the modulated photocurrent for different values of the average concentration ratio at different applied voltages (Figure VI-7 right). It is clear that the apparent shunt resistance effect is visible on small signal curves, which are different from the on-off signals. No second order signal is detected, which means that non-linear effects are negligible. The apparent shunt resistance effect may originate from voltage dependent collection efficiency. The collection efficiency η in a solar cell is the ratio of the collected over photogenerated carriers, i.e. $I_{ph} = \eta(V)I_{ph,max}$. Another source of signal can be the photoconductivity effects that modulate CdS or Cu(In,Ga)Se₂ conductivity with illumination. Indeed as series resistance depends on the illumination, as seen previously, the diode current depends on illumination through a voltage term $V - R_s I$. We exclude the increase in saturation current as a

significant source of the apparent shunt resistance. If the saturation current were dependent on illumination at small signals, we would detect a second order signal. Indeed as series resistance is dependent on illumination, the combined dependence of saturation current and series resistance would lead to second order signals that are not detected.

In the high voltage range, we can see that both on-off and small modulation signals show a negative photocurrent term. This is mainly a photoconductive effect. Indeed if we zoom on the high forward bias range of Figure VI-1, we can see that the current-voltage curve cross over each other, which explains the negative photocurrent term even in small signal (Figure VI-8). However it is clear that our small signal measurements, and especially the one recorded under the lowest light intensity, are more difficult to detect than on-off measurements, which leads to experimental curves with more noise.

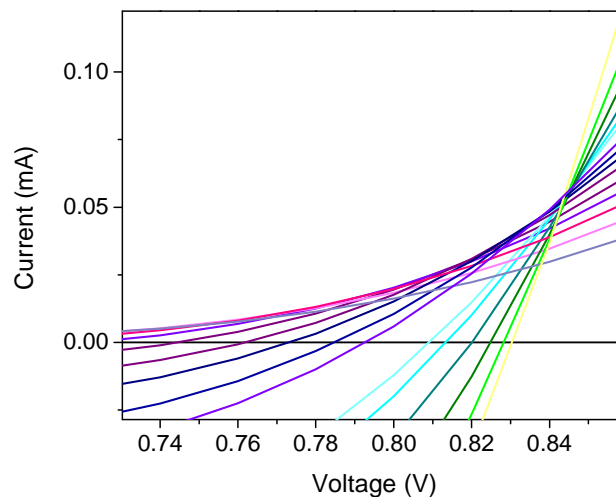


Figure VI-8 : Current voltage characteristic of a 50 μm microcell of an industrial sample. Zoom of Figure VI-1.

We found that the apparent shunt resistance visible on the current-voltage curve can be seen on modulated photocurrent experiments. The origin of this behavior is not clear yet, but we can exclude an increase in saturation current. We will therefore review the other possible causes of this apparent shunt resistance effects for $\text{Cu}(\text{In,Ga})\text{Se}_2$ solar cells under concentration. We will study the different explanations that can be found in the literature, and see to what extent they can explain our experimental observations.

3.2. Apparent shunt resistance analysis and modeling

3.2.1. Modulation of series resistance with bias

A model that can explain the emergence of apparent shunt resistance is modulation of series resistance with bias [237], as mentioned in the introduction of this chapter. In silicon solar cells for

example, the base resistivity can be enhanced by electric injection. The base resistivity is smaller in high injection due to increased carriers. Under low optical concentration, the voltage range over which the injected carriers modulate the resistivity is limited in a small voltage range around the maximum power point, and is not really detectable on the current-voltage curve. Under intense illumination however, the increased current density enlarges this voltage range. Therefore series resistance modulation with bias can take place between negative voltages and voltages higher than the maximum power point, which results in an apparent shunt resistance [232], [236]. In order to diminish this effect, the reduction of the cell thickness and thus of the influence of the base resistivity is proposed.

This apparent shunt resistance due to the modulation of series resistance with electric bias has been seen in thick solar cells, with moderately or highly resistive bases. We shall study if this effect can explain the apparent shunt resistance of thin samples which base doping is in the order of 10^{16} cm^{-3} . In order to do so we follow a methodology close to that of paragraph 2.2.1, without neglecting the electric injection. Indeed we consider that when charge extraction is present, equation (VI-5) becomes $\Delta n \times t / \tau_n = G - I$, where I represent carrier extraction. Thus series resistance as a function of voltage and concentration ratio can be determined as the solution of a system of three equations.

$$R_s(C, V) = R_c + \frac{R_{s0}}{\left(1 + \left(1 + \frac{\mu_n}{\mu_p}\right) \frac{\Delta n(C, V)}{p_0}\right)}$$

$$\Delta n(C, V) = \frac{P_{light}(AM1.5) \times \tau_n}{t \times h\nu} \times C - \frac{\tau_n}{q \times t} J(C, V) \quad (VI-10)$$

$$J(C, V) = C \times J_{ph}(AM1.5) - J_0 \left(\exp\left(q \frac{V - R_s(C, V)J}{AkT}\right) - 1 \right)$$

Where $P_{light}(AM1.5)$ and $J_{ph}(AM1.5)$ are respectively the power density and photocurrent density under AM1.5G illumination, τ_n minority carrier lifetime, $h\nu$ energy of the incident photons, C the concentration ratio, q the elementary charge, t the absorber thickness, A the ideality factor and $J(V)$ the current density at a certain voltage V . The first equation is the adaptation of equation (VI-4), the second equation represents the balance between generation, recombination and electric extraction, and the third equation is the expression of a diode current under optical generation in the presence of series resistance. A one-diode model was chosen for simplicity. We solve the system in MATLAB, and we can analyze the variation of series resistance with bias and concentration. The

parameters are set as follows: $J_{ph} = 30 \text{ mA/cm}^2$, $J_0 = 10^{-4} \text{ mA/cm}^2$, $A=2$, $R_c = 10^{-3} \text{ ohm.cm}^2$, $R_{s0} = 3 \cdot 10^{-2} \text{ ohm.cm}^2$, $\mu_n/\mu_p = 10$, $\tau_n = 10 \text{ ns}$, $p_0 = 10^{16} \text{ cm}^{-3}$, $t = 10^{-4} \text{ cm}$, $h\nu = 2.3 \text{ eV}$.

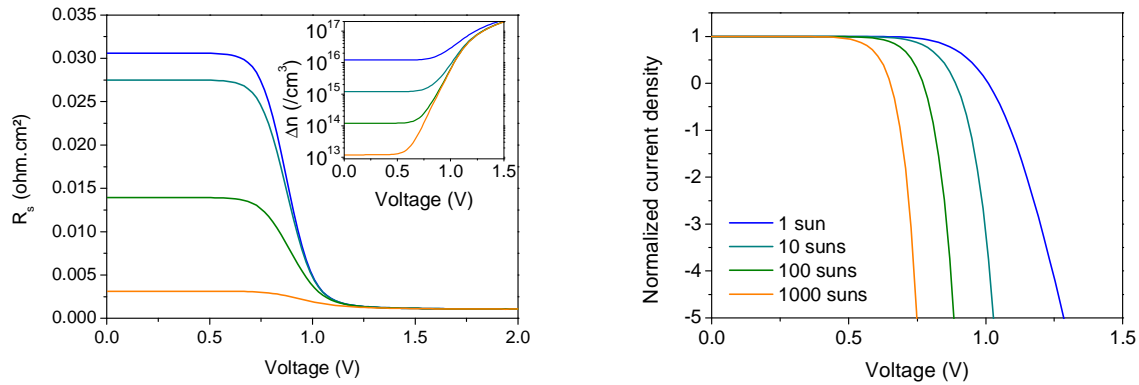


Figure VI-9 : (left) Series resistance as a function of applied voltage for four concentration ratio $\times 1$, $\times 10$, $\times 100$ and $\times 1000$. (Inset: corresponding Δn). (right) Current voltage curves, normalized by short circuit current value at the four illumination intensities. Other parameter values : $J_{ph} = 30 \text{ mA/cm}^2$, $J_0 = 10^{-4} \text{ mA/cm}^2$, $A=2$, $R_c = 10^{-3} \text{ ohm.cm}^2$, $R_{s0} = 3 \cdot 10^{-2} \text{ ohm.cm}^2$, $\mu_n/\mu_p = 10$, $\tau_n = 10 \text{ ns}$, $p_0 = 10^{16} \text{ cm}^{-3}$, $t = 10^{-4} \text{ cm}$, $h\nu = 2.3 \text{ eV}$.

We find that with numerical values close to our experimental observations, the modulation of series resistance with applied bias is low in the voltage range, where we see the apparent shunt resistance (Figure VI-9 left). Indeed on the simulated current-voltage curves no slope can be seen (Figure VI-9 right).

However the modulation of series resistance with bias cannot entirely be excluded for Cu(In,Ga)Se₂ solar cells under concentration in general, as the appearance of a modulation highly depends on the parameter input in the model. In Cu(In,Ga)Se₂ solar cell with different characteristics, this series resistance modulation could have an effect on current-voltage curve fill factor, and modulated photocurrent curves.

As in our samples the voltage modulated R_s does not seem to be the source of the apparent shunt resistance, we suppose that the apparent shunt resistance is due to the variation of collection efficiency.

3.2.2. Standard models of collection in thin film solar cells

A perfect device should have a constant collection factor equal to 1. The hypothesis of constant collection factor is that done in the so called one-diode or two-diodes model, where the photocurrent term has no dependence with bias. Unfortunately, in real devices, the collection factor is lower and depends on applied voltage. A few models are available in the literature that explains this variation.

Gärtner model

The Gärtner model [119] supposes a perfect collection for the carriers photogenerated in the depletion region and neglects photogeneration in the window layers. In addition to this “drift” current, “diffusion” current from the carriers photogenerated in the neutral region is taken into account. The diffusion current is determined by supposing that there are no minority carriers at the boundary of the depletion region and that the back surface of the semi-infinite sample is perfectly recombining. This model is therefore especially suited for thick samples, which are not influenced by the back contact. The external collection efficiency in a Cu(In,Ga)Se₂ solar cell, with p-type absorber, according to the Gärtner model is (see equation (II-14)):

$$\eta(V) = 1 - \frac{\exp(-\alpha_a w_a(V))}{1 + \alpha_a L_n} \quad (\text{VI-11})$$

Where α_a is the absorption coefficient, $w_a(V)$ the width of the space charge region in the absorber, t the thickness of the absorber, L_n the diffusion length of minority carriers.

If we do not want to neglect the influence of the recombining back surface, an extension of equation (VI-11) is necessary. The collection efficiency, when the back surface recombination is taken infinite in a sample of finite thickness t , can be written in the form [241], [242]:

$$\eta(V) = 1 - \frac{\exp(-\alpha_a w_a)}{1 + \alpha_a L_n} \left(1 + \frac{\alpha_a L_n}{\alpha_a L_n - 1} \frac{\exp(-\alpha_a(t - w_a)) - \exp(-(t - w_a)/L_n)}{\sinh((t - w_a)/L_n)} \right) \quad (\text{VI-12})$$

As a consequence, thinner samples will experience lower collection efficiencies. Depending on the diffusion length and space-charge width, the collection efficiency can be decreased by a small space-charge width (but relatively low back contact recombination), or by a high back contact recombination (but large space-charge width).

The space charge region width is dependent on voltage, and if we consider the model of an abrupt n-p junction we have $w_a(V) = \sqrt{2\varepsilon/qN_A(V_{bi} - V)}$. This model explains the variation of collection efficiency with applied bias in an ideal cell, via the variation of the space-charge region width. However this model does not account for illumination intensity dependence, and is limited to low injection due to the assumption of quasi neutral region. Moreover, if the space-charge width becomes negligible, the Gärtner model and its extensions do not account for voltage dependence of the collection factor.

Interface recombination

Another model explains the varying collection efficiency with applied bias. It was developed for early chalcogenide solar cells, where the heterointerface was highly defective [120], [243], [244]. The collection factor is set as the balance between the electric field at the interface that help the collection of photogenerated carriers and the recombination velocity that prevents it. The interface collection efficiency is (equation (II-15)):

$$\eta(V) = \frac{\mu F_0(V)}{S + \mu F_0(V)} \quad (\text{VI-13})$$

where μ is the mobility of minority carrier, $F_0(V)$ the voltage dependent electric field at the heterointerface and S the recombination velocity. The determination of the exact form of $F_0(V)$ is not trivial in the heterojunction, but a good approximation is that of the abrupt p-n junction, $F_0(V) = \sqrt{2qN_a/\epsilon(V_{bi} - V)}$. However this model is not adapted to high illumination as the possible variation of the electric field with illumination is neglected.

Space charge region recombination

The Gärtner model supposes a perfect collection within the space-charge region but this approximation can be too limiting. We have seen in Chapter II, that the space-charge recombination current could be written in the form (equation (II-11)) :

$$J_{diode,SCR} = \frac{C_1}{F_m} \exp\left(\frac{qV}{2kT}\right) \quad (\text{VI-14})$$

where C_1 is a term independent of potential or electric field, and F_m the electric field at the position of the maximum recombination (within the space-charge region). This current is mainly generated in the vicinity of the position where electrons and holes have equal concentrations. The effective width of recombination is thus $\pi kT/qF_m$. If the maximum of the electric field in the space-charge region decreases, or if the carrier concentration profile is changed so that the width of the region where electron and holes are in similar concentrations is large, this term can become very important.

3.2.3. *Parameters influencing the collection efficiency at high concentration*

We have seen the principal models that can explain the variation of collection efficiency in a solar cell, and we have seen that the collection efficiency can vary with applied voltage, electric field strength or space-charge width. In order to take into account the variation of the collection efficiency

with illumination intensity, the impact of the concentration on the electric field or space-charge width should be elucidated.

Under illumination the carriers generated in the space charge or neutral regions will impact the charge distribution. When the photogenerated carriers are in concentrations higher than the doping, a space-charge effect occurs [213]. The photogenerated carriers set the space charge width and electric field that in turn influence the carrier concentrations. The carrier concentration and electric field are thus the solution of a self-consistent problem. In order to grasp the origin and extent of the influence of illumination level, we decided to have a numerical resolution of the problem.

3.3. General 1D model of collection in a semiconductor

3.3.1. Introduction

Solving the system of continuity and Poisson equations ((VI-15), (VI-16) and (VI-18)) by self-consistency can be difficult, as the convergence is not obtained easily [245]. There are several algorithms that are designed to solve the continuity and Poisson equations. One of the most famous methods is the Gummel's algorithm [246]. However, it is based on a linearization scheme and is not appropriate when the equations are strongly coupled, which is the case under high illuminations. This scheme is however often used in simulation softwares, such a SCAPS [108] (see box n°2 page 150), and it explains the lack of convergence of this software in the high illumination regimes. Thus we use a classic Finite Element Method with a relaxation scheme to solve these equations in 1D. This technique is working but more complex algorithms can help increase the speed of convergence. The complete resolution of the problem is described in Appendix E, we present here the hypotheses and main results.

3.3.2. Hypotheses

We want to determine the carrier concentrations n and p , and electric field E in a semiconductor, or a junction, as a function of position. Thus we have to solve the continuity equations :

$$-\frac{1}{q} \operatorname{div}(j_n) = g_n(x) - r_n(x) = g(x) - r(x) = \mu_n \frac{d}{dx} \left(n \frac{dv}{dx} \right) - D_n \frac{d^2 n}{dx^2} \quad (\text{VI-15})$$

$$\frac{1}{q} \operatorname{div}(j_p) = g_p(x) - r_p(x) = g(x) - r(x) = -\mu_p \frac{d}{dx} \left(p \frac{dv}{dx} \right) - D_p \frac{d^2 p}{dx^2} \quad (\text{VI-16})$$

where g is the generation rate and r the recombination rate that are equal for holes and electrons, q is the elementary charge, $\mu_{n/p}$ the mobility, v the electrostatic potential, E the electric field

($E = -\frac{dv}{dx}$). We choose a simple source of recombination that is the radiative recombination, or more generally a bi-molecular recombination:

$$r(x) = b(np - n_i^2) \quad (\text{VI-17})$$

where b is the radiative recombination coefficient, and n_i^2 the value of $n \times p$ at equilibrium. Other recombination mechanisms, such as Shockley-Read, could be employed as well. It should be noted that here b is supposed to be independent on the carrier concentration, i.e. on the illumination intensity. This hypothesis will not be valid under ultra-high illumination, where Auger recombination is non-negligible, leading to a coefficient b that is dependent on illumination. The generation is taken constant over the homojunction thickness. Indeed as we are simulating a symmetric homojunction, the constant generation is a mean to ensure that the carrier concentration at the junction is high. In next versions of this program, we should implement asymmetric junctions, with a thin window, and a thick absorber, where the generation would be of the form $g(x) = a \exp(-\alpha x) I_0$, where α is the absorption coefficient and I_0 the number of incident photons. As we are not yet able to simulate important asymmetry in a reasonable time, the constant generation rate appeared as a good working hypothesis.

The electric potential v is linked to the carrier concentrations through Poisson's equation:

$$-\frac{d^2v}{dx^2} = \frac{q}{\epsilon} (p - n + \rho) \quad (\text{VI-18})$$

It is important to note that no simplifications are made concerning majority or minority carrier. Indeed our aim is to study a regime where the incident light flux generates carriers in a quantity close to or superior to the doping. In this regime no carrier type can be considered in majority (or minority) and the complete form of equations (VI-15) and (VI-16) has to be kept.

In order to solve equations (VI-15), (VI-16) and (VI-18), proper boundary conditions have to be determined. At the surface the bulk current have to be equal to the surface current:

$$j_n(0) = q\mu_n nE(0) + qD_n \frac{dn}{dx}(0) = q(n(0) - n_{eq})S_{nf} \quad (\text{VI-19})$$

$$j_p(0) = q\mu_p pE(0) - qD_p \frac{dp}{dx}(0) = -q(p(0) - p_{eq})S_{pf} \quad (\text{VI-20})$$

where n_{eq} and p_{eq} are the electron and hole concentrations at equilibrium, without illumination.

We considered in equations (VI-19) and (VI-20) that the electric fields can be neglected at the surface, which represents a situation where the surfaces are ideal in the sense that no defect can induce a charging of the interface. The only source of electric field considered here is the charge carriers and doping of the bulk semiconductor.

For $x = 0$, that will be called “front” position, the boundary conditions are:

$$\begin{aligned} v(0) &= 0 \\ j_n(0) &= q(n(0) - n_{eq})s_{nf} \\ j_p(0) &= -q(p(0) - p_{eq})s_{pf} \end{aligned} \quad (\text{VI-21})$$

For $x = L$, that is called “back” position, the boundary conditions are :

$$\begin{aligned} v(L) &= v_0 \\ j_n(L) &= -q(n(L) - n_{eq})s_{nb} \\ j_p(L) &= q(p(L) - p_{eq})s_{pb} \end{aligned} \quad (\text{VI-22})$$

3.3.3. Modeling

In order to solve these equations, we write the dimensionless equivalent problem and solve it by finite Element Method (See Appendix E).

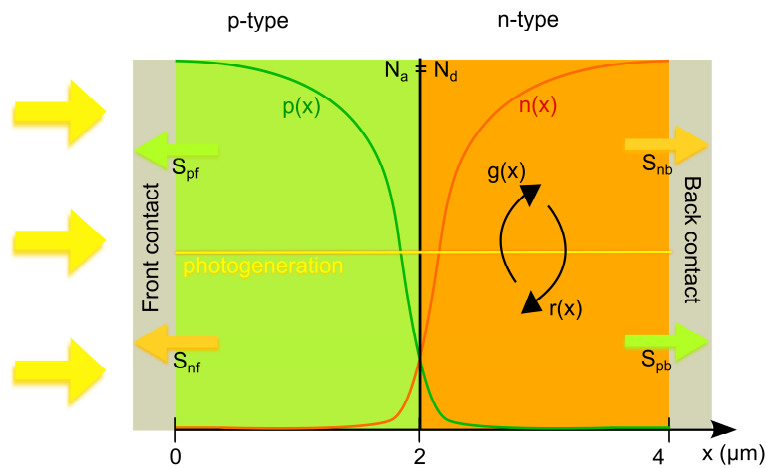


Figure VI-10 : Sketch of an abrupt p-n homojunction, as simulated in our program

In order to study high illumination effects, we study a simple geometry (Figure VI-10). We consider a symmetric abrupt homojunction of 4 μm thickness, with symmetric p-type doping on the first 2 μm and n-type doping for the last 2 μm , that are set to 10^{15} or 10^{16} cm^{-3} respectively. The semiconductor

bandgap energy is 1.22 eV. Electron mobility is fixed to 100 cm²/(V.s) and hole mobility to 25 cm²/(V.s). (We did not set a limit to the mobility value to ensure that the carrier velocity was always smaller than 10⁷ cm/s, however we never encountered electric fields higher than 10⁵ V/cm, thus this simplification is justified). The density of states in the conduction and valence bands are set to 6.8 10¹⁷ cm⁻³ and 1.1 10¹⁹ cm⁻³ respectively. The intrinsic carrier concentration n_i is thus 1.8 10⁸ cm⁻³. The coefficient of radiative recombination is set to between 10⁻⁵ and 10⁻⁷ cm³.s⁻¹. The surface transfer velocities are 10⁷ cm/s for the “majority” carriers and 10² cm/s for the “minority” carriers. “Majority” (“minority”) carriers refers to electrons (holes) in the n-type doped part of the homojunction and vice-versa in the p-type part, independently of the injection level. The minority carrier transfer velocity can be understood as a recombination current, if we suppose that the semiconductor is in ohmic contact with a metal at the front and back. The generation rate was taken constant over the homojunction thickness and varied to simulate various injection levels.

The applied potential is set by the value of the electrostatic potential at $x = L$. Indeed we consider that $v(L) = v_0 = v_{bi} - v_{appl}$, where v_{bi} is the dimensionless built-in voltage and v_{appl} the dimensionless applied voltage. This applied voltage has to be understood as the band-bending in the dark, and may not be the band bending under illumination [247].

The simulation is stopped when two consecutive steps, k and $k + 1$, are sufficiently close, i.e. if $\left\| \left(n^{k+1}(x) - n^k(x) \right) / n^{k+1}(x) \right\| + \left\| \left(p^{k+1}(x) - p^k(x) \right) / p^{k+1}(x) \right\| \ll 10^{-6}$.

Our simulations are done in a rather simple configuration, the homojunction. This structure differs from that of Cu(In,Ga)Se₂ solar cells. This simulation is still a first step in the study of a thin film device under high illumination. The homojunction is thus a tool to get physical insight in the phenomena seen in our experimental data. Numerical values of doping, bandgap, mobilities are taken close to that of Cu(In,Ga)Se₂ in order to be as representative as possible. Generation was set constant and not exponentially decreasing, as discussed before. Our results should thus be interpreted with care, as the simulations are not done on a structure strictly equivalent to the one measured experimentally.

3.3.4. Results

We first assessed the validity of our model by comparison with SCAPS at low fluxes. The results are described in details in the Appendix E. We can say that our convergence criterion for the carrier concentration is more restrictive than that of SCAPS, and thus we obtain carrier concentrations with more precision.

The resolution of the continuity and Poisson's equations gives access to carrier concentration and electric field through the homojunction. For example Figure VI-11 shows carrier concentration as well as electric field and electrostatic potential in a p-n junction with symmetric doping of 10^{16} cm^{-3} under increasing illumination. The reference illumination I_0 corresponds to a generation rate of $6.8 \cdot 10^{20} \text{ cm}^{-3} \text{ s}^{-1}$ (i.e. a photocurrent of 43.6 mA/cm^2 in the case of perfect collection).

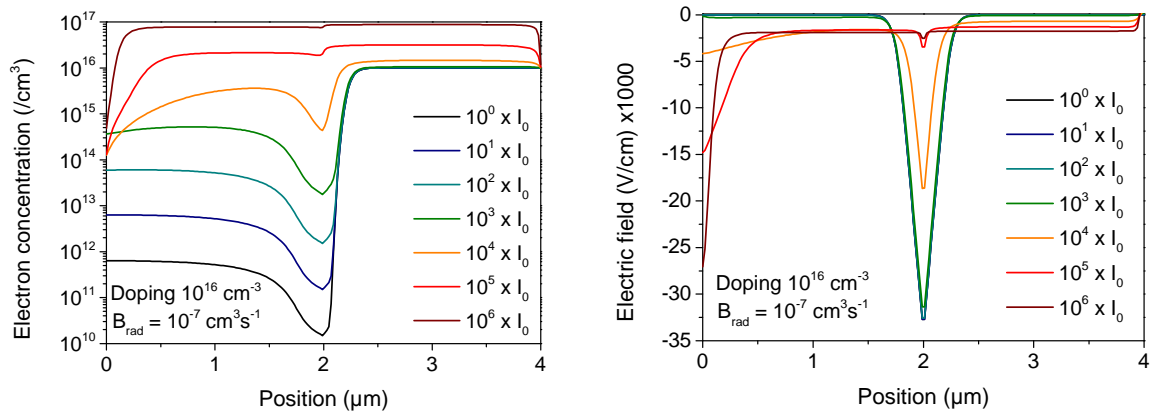


Figure VI-11 : Simulation of a homojunction between p and n-type semiconductors of 10^{16} cm^{-3} doping and a recombination coefficient b of $10^{-7} \text{ cm}^3 \text{ s}^{-1}$ at a zero applied voltage under various illumination. (left) Electron concentrations as a function of position. (right) Electric field as a function of position.

We have a complete description of the homojunction at a certain generation level (Figure VI-11). Thus we can study the influence of increasing illumination of the homojunction with various doping level or recombination coefficients. In Figure VI-11 one can see the electron concentration under increasing illumination. On the n-type side of the junction the influence of photogenerated carriers is seen when the photogenerated carriers are in a concentration similar to the doping. On the p-type side of the junction however, the photogenerated carriers fix the electron carrier concentration. When the photogenerated carriers concentration is of the order of the doping level, one can see that the electric field at the junction and the space-charge region width decrease.

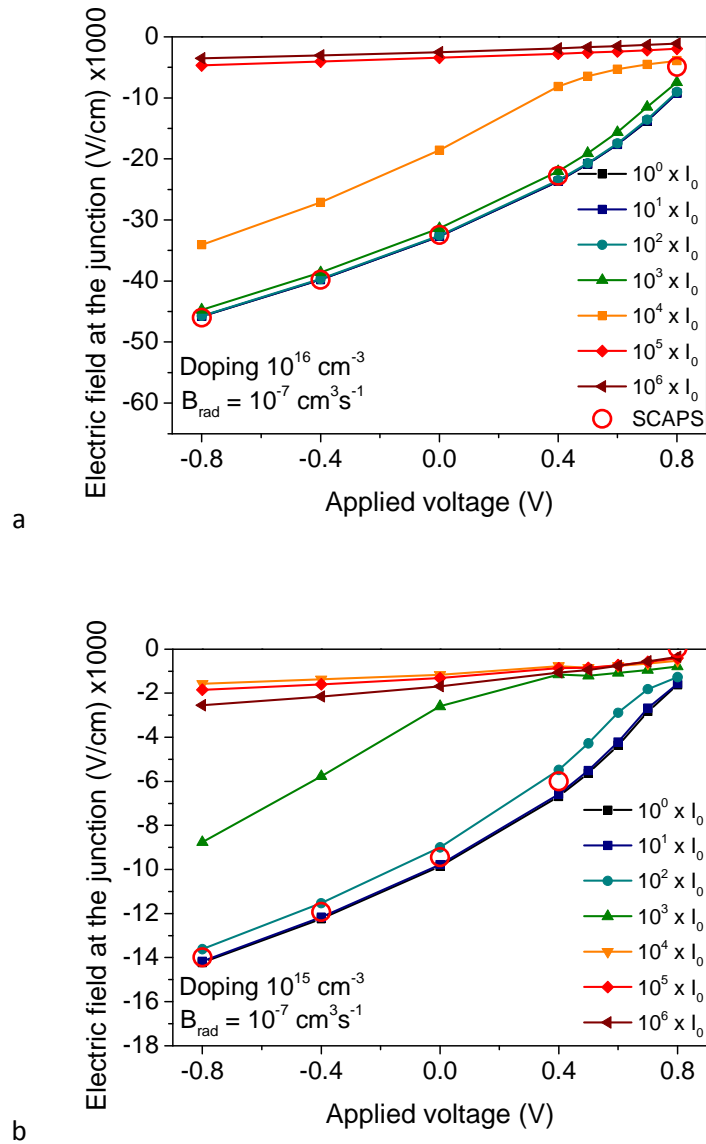


Figure VI-12 : (a) Electric field at the homojunction as a function of applied voltage and illumination intensity, for a homojunction between semiconductors of 10^{16} cm^{-3} doping and a recombination coefficient b of $10^{-7} \text{ cm}^3 \text{ s}^{-1}$. Values given by SCAPS for the same structure in the dark are displayed for reference. Note that at 0.8V SCAPS has a lack of convergence that explains the discrepancies with our results. (b) Corresponding data for a homojunction with doping level 10^{15} cm^{-3} .

We first study the electric field strength at the homojunction ($x = 2 \mu\text{m}$), for doping levels of 10^{16} and 10^{15} cm^{-3} , and a recombination coefficient of $10^{-7} \text{ cm}^3 \cdot \text{s}^{-1}$. It can be seen that at a given applied voltage, the field at the junction decreases with incident light intensity (Figure VI-11 and Figure VI-12). This phenomenon is referred to as a screening effect. The decrease in the electric field strength at the homojunction leads to a decreased collection. This can be seen on the normalized current-voltage curves of Figure VI-13 where the fill factor and ultimately the short-circuit current

densities are affected by the increasing illumination. On Figure VI-13a a superlinearity is observed at moderate concentrations, and will be discussed hereafter.

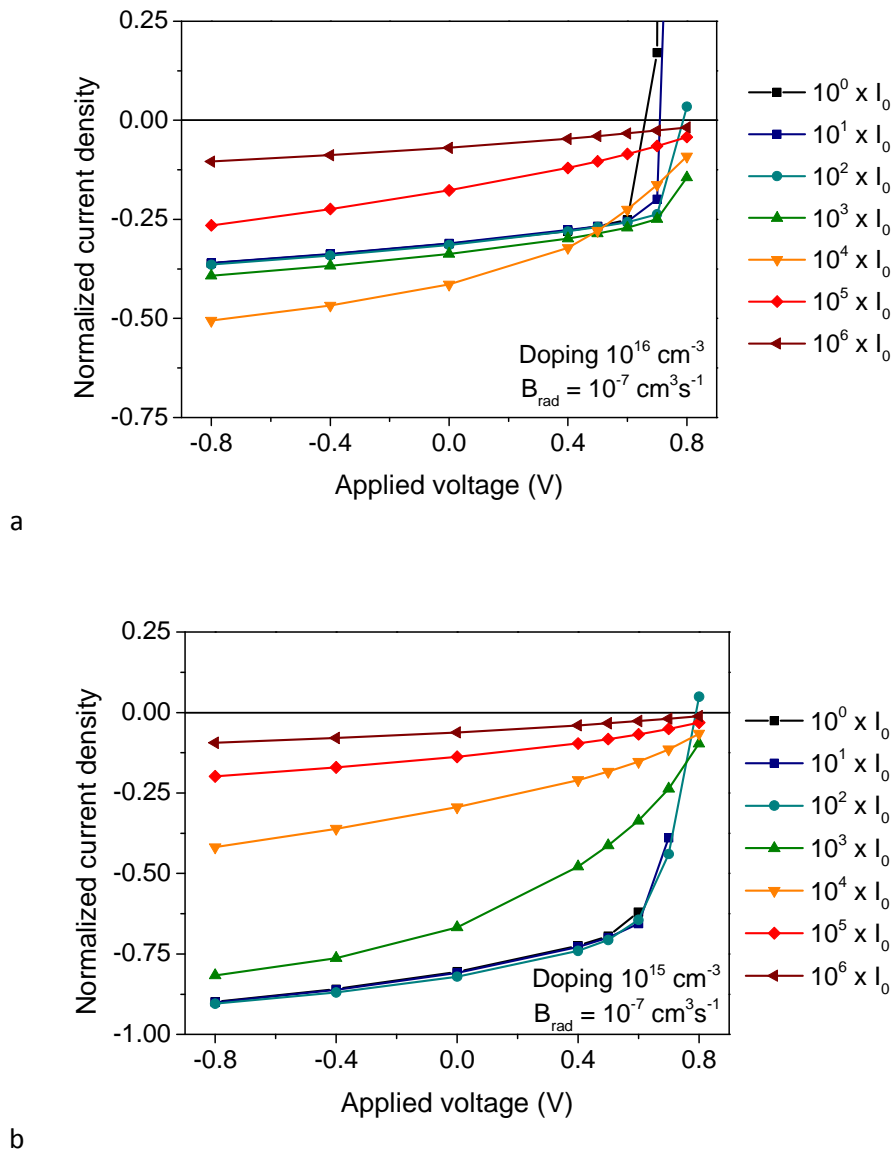


Figure VI-13: (above) Normalized current-voltage characteristic of a homojunction as a function of applied voltage and illumination intensity, for a homojunction between semiconductors of 10^{16} cm^{-3} doping and a recombination coefficient b of $10^{-7} \text{ cm}^3 \text{ s}^{-1}$. Normalization is done by dividing the current density by the value of the maximum photocurrent (deduced from the generation rate) (below) Corresponding data for a homojunction with doping level 10^{15} cm^{-3} .

The intensity of the electric field screening is dependent on the homojunction parameters. We can see that the screening effect decreases with increasing doping densities. Indeed at a given illumination intensity, the photogenerated carriers have less impact on the highly doped junction, as they represent a smaller proportion of the intrinsic charge distribution.

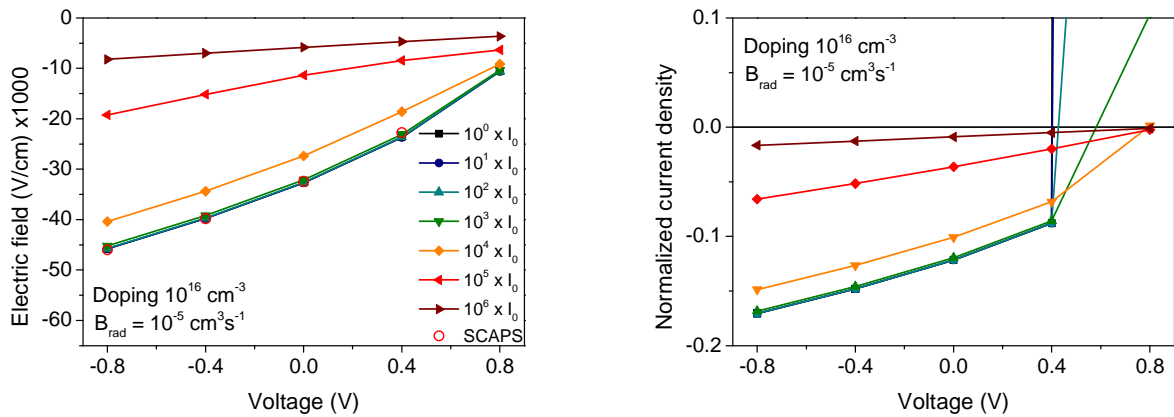


Figure VI-14 : (left) Electric field at the homojunction as a function of applied voltage and illumination intensity, for a homojunction between semiconductors of 10^{16} cm^{-3} doping and a recombination coefficient b of $10^{-5} \text{ cm}^3 \text{ s}^{-1}$. Values given by SCAPS for the same structure in the dark are displayed for reference. (right) Normalized current-voltage characteristic of a homojunction as a function of applied voltage and illumination intensity, for the same structure.

Furthermore, the screening effect decreases with increasing recombination (Figure VI-14). This can be understood as a decrease in the amount of photogenerated carriers due to increased recombination. Thus the screening effect, due to free charges, is reduced.

More details can be found in the Appendix. Notably, we showed that the surface carrier transfer velocity values only have an influence at the edges, and do not affect bulk behavior. We also simulated a junction with equal electron and hole mobility. The screening effect was still visible, and cannot therefore be attributed to a Demer term, which originated in the asymmetry of the carrier mobilities. When we tested a non-uniform generation profile, the photogenerated carrier concentration gradients created modify the electric field, but the screening effect was still visible.

3.3.5. Discussion

Our simulations show that under concentration the photogenerated carriers impact the charge distribution and may thus affect collection.

Our simulations are done in a rather simple configuration, the homojunction. A direct and precise simulation of a Cu(In,Ga)Se₂ solar cell cannot be implemented in our algorithm capacity at the time of this study. Cu(In,Ga)Se₂ solar cells are not homojunctions. They are highly non-symmetric abrupt heterojunctions between a highly doped n-type semiconductor and a lightly p-type absorber (N_A comprised between $10^{15} - 10^{16} \text{ cm}^{-3}$). Due to the high absorption coefficient of Cu(In,Ga)Se₂ most light is absorbed within the first 20 nm (see Figure V-11), and thus carrier concentrations are very important close to the heterojunction. If we consider a lifetime of 1 ns, we can estimate the photogenerated carriers near the heterointerface at $\times 100$ to be 10^{17} cm^{-3} , which is far more

important than the absorber doping level. Our simulations did not take into account this abrupt generation on one side of the junction. We chose a constant generation configuration throughout the homojunction, and we run simulations up to very high concentrations. Accordingly we simulated those very high photogeneration rates, but we do not have data on the effect of the localization of photogeneration close to the homojunction. From preliminary tests shown in Appendix E, we can see that a non-uniform generation profile results in carrier concentration gradients, which can affect the electric field. More generally, we content ourselves to highlight general physical phenomena in order to interpret our experimental data.

We have seen that the space charge width and maximum electric field at the junction tend to decrease with increasing illumination due to the screening effect caused by photogenerated carriers. This effect is already known in photodetectors, where high illumination can screen the intrinsic and bias electric field under sufficient incident light power, and thus change the dominant transport mechanisms [247–249]. This effect was also detected recently in Cu(In,Ga)Se₂ solar cells by time-dependent photoluminescence measurements. Indeed under increased laser power, the initial part of the photoluminescence decay is governed by recombination and not charge separation. It was interpreted as a sign of a smaller electric field, which no longer separates charges efficiently [250], [251].

The decrease in space-charge width and maximum electric field may impact several of the collection models we presented in paragraph 3.2.2. At moderate illumination intensity the Gärtner model could apply, and the decrease in the space-charge width would result in lower collection. The Gärtner model cannot however be applied in high injection, as the discrimination between a perfectly collecting space-charge region and quasi-neutral region is no longer valid. Moreover, when the space-charge width becomes negligible, no bias dependent collection can be accounted for by a Gärtner model. This is opposite to our experimental evidences, where the decrease of collection with voltage becomes increasingly important under high fluxes. The decrease in the maximum electric field in the space-charge region can drastically increase recombination via Shockley-Read-Hall mechanisms. Indeed we have seen that the effective volume of recombination is inversely proportional to the value of the electric field at the position where electron and holes are present in similar concentrations. Thus the space-charge region recombination is roughly scaled with the inverse of the maximum electric field. The electric field screening can also enhance the influence of heterointerface recombination. Indeed recombination at the heterointerface is given by the balance of the recombination velocity and the strength of the electric field at the interface (equation (VI-13)). If the interface collection probability for a given value of the electric field is 90%, the collection

probability becomes 82% when the electric field strength is divided by 2 and 64% if the electric field is divided by 5, for a constant recombination velocity. Thus interface recombination that is no longer limiting for state-of-the-art devices in standard conditions may become increasingly important under concentration.

The role of interface recombination in the variation of collection efficiency under illumination is corroborated by experimental evidence. The data of Figure VI-1 correspond to an industrial sample. We have seen in the last chapter that these samples present a distinct red-kink effect, which can be associated with a positive conduction band offset at the interface that impedes collection if the CdS is strongly compensated. On IRDEP samples, this effect did not appear and we postulated a negligible conduction band offset, due to adapted front bandgap grading. On IRDEP samples the decrease in collection efficiency under concentration is much less apparent than for industrial samples (Figure VI-6), whereas the two samples are close from a material point of view (doping levels or recombination level). We thus make the assumption that the better interface of IRDEP samples, in terms of band alignment, decreases the interface recombination velocity. Thus the modulation of the electric field in the space-charge region has less influence on the collection efficiency than on the industrial samples. These observations are however not sufficient to exclude other phenomena, and further numerical simulations, closer to the $\text{Cu}(\text{In,Ga})\text{Se}_2$ structure, coupled with the test of specific samples (with different buffer layer or bandgap for example), would be needed to validate the exact mechanisms involved in the collection reduction.

We have seen in our simulations that the screening effect may be sufficiently high to directly impede charge collection in the homojunction. This can be seen by the slope of the current-voltage curve at low forward or even reverse bias in a homojunction under high illumination. This decrease in collection is due to the simultaneous decrease in the electric field strength at the junction and of the space-charge width, which both increase recombination in high field and low field region (Figure VI-11 and Appendix E (figure E-6)). In our simulations, the recombination term was bi-molecular, and therefore increased when the product of electron and hole concentrations is high. For some simulation parameters, a superlinearity of the current was even found (seen for example in Figure VI-13 a), due to the positive effect of the ohmic electric field on minority carrier collection. This superlinearity is comparable to that seen on silicon solar cells (see paragraph 1.2). In $\text{Cu}(\text{In,Ga})\text{Se}_2$ solar cell the main recombination mechanism is via defects. At low illumination intensities the collection in $\text{Cu}(\text{In,Ga})\text{Se}_2$ solar cell is high, as seen in EQE measurements (see Figure IV-18). The appearance of a superlinearity, which is the sign of an imperfect collection at low intensity, is thus improbable on $\text{Cu}(\text{In,Ga})\text{Se}_2$.

3.4. Conclusions

We have measured a decrease in collection efficiency in Cu(In,Ga)Se₂ solar cells under highly concentrated sunlight especially important on industrial samples.

We associated this variation of collection efficiency to the screening of the heterojunction electric field by photogenerated carriers. The evidence of the screening effect is the decrease in electric field strength and space-charge region width, as modeled in a homemade Finite-Element-Method program.

In Cu(In,Ga)Se₂ solar cells, the phenomena at stake may be the increased influence of the interface recombination when the electric field is weakened. Indeed we observed differences in the collection efficiency between industrial and IRDEP samples, which differ by the presence or absence of conduction band offset at the heterointerface. The presence of a conduction band offset increases the heterointerface recombination velocity, and thus enhances the importance of an intense electric field for good collection. However, we cannot exclude other phenomena such as an increase of space-charge region recombination or increased of the influence of the back contact.

We have seen by simulation that the screening effect was more apparent in lightly doped samples. Thus Cu(In,Ga)Se₂ solar cells designed for concentration should have a relatively high doping level. This may also be beneficial in terms of absorber conductivity, as long as the carrier mobility is not affected. Most importantly the heterointerface should be carefully designed so that the recombination velocity is as low as possible, and adequate bandgap engineering is of prime importance.

4. Very high concentration experiments

We tested microcells up to ultrahigh concentration ratios (> ×1000). We detected a saturation of the open-circuit voltage with incident light power before a decrease due to excessive heating (Figure VI-15) on two samples.

Saturation of the open-circuit voltage of p-n junction under ultrahigh fluxes was observed on Si diodes [231] or GaAs diodes [252] in the 1960s. This saturation was reached with a laser source when the photogenerated carrier concentration is higher than the doping of the heavily doped side of the junction. It was found that the saturated open circuit voltage could be smaller or higher than the built-in voltage depending on the n⁺-p or n-p⁺ type of the junction. Indeed the saturated open circuit voltage is set by the built-in voltage and a Dember term that can add or subtract to the diffusion potential depending on the junction type. The Dember effect is related to the creation of an electric

field between photogenerated electrons and holes when they have different mobilities (as mentioned in paragraph 1.1). This field accelerates the slowest carrier and slows down the fastest. The Dember term depends thus on the ratio of mobility of electron and holes. The maximum open-circuit voltage obtainable from a n⁺-p homojunction with acceptor and donor densities, N_A and N_D is [212], [230]:

$$V_{oc,max} = \frac{kT}{q} \ln\left(\frac{N_A N_D}{n_i^2}\right) + \frac{mkT}{q} \ln\left(\frac{N_A}{b N_D}\right) \quad (VI-23)$$

Where $b = \mu_n/\mu_p$ and $m = (b - 1)/(b + 1)$.

One of the samples, on which we observed saturation, was an industrial sample from Würth. The cell where the saturation is visible is a 7 μm diameter microcell (Figure VI-15 left). The saturation of open circuit voltage can be seen as this cell is small enough so that the temperature elevation is limited up to × 10 000, and does not provoke a significant voltage drop. The saturation of the open circuit voltage can be seen between ×3 000 and ×10 000. It is however a small signal. On Figure VI-15 (left) the dots correspond to experimental data and the solid line to the fit of $V_{oc} - J_{sc}$ characteristic according to equation (V-2). The temperature coefficient κ is set so that the fit goes perfectly through the highest illumination measurement point. This value of κ, $4.7 \cdot 10^{-4} \text{ cm}^2/\text{A}$, corresponds to the scale effect that we detected on this sample, i.e. a temperature elevation proportional to the radius of the device at the power 0.8. It should be noted that if we chose a least-square-distance fit of the $V_{oc} - J_{sc}$ curve, it would not account for saturation and would overestimate heating, leading to smaller open-circuit voltages at ultrahigh intensities than the experimental data. The saturated open-circuit voltage reached on this sample is 862 mV +/- 2 mV. The built-in voltage in a Cu(In,Ga)Se₂ solar cells is around 1.05 V ($N_A = 10^{16} \text{ cm}^{-3}$ and $N_D = 10^{18} \text{ cm}^{-3}$, $n_i^2 = 3.2 \cdot 10^{16} \text{ cm}^{-6}$). If we consider a mobility ratio b of 4, the Dember term of equation (VI-23) is 93 mV. This Dember term can thus explain the saturation of the voltage at roughly 100 mV below the built-in voltage. It should be noted however that equation (VI-23) was derived from a n⁺-p homojunction and that adaptations may be necessary for heterojunctions, such as Cu(In,Ga)Se₂ solar cells, for a precise quantitative analysis. Moreover we do not have direct measurements of the doping levels or intrinsic carrier densities for this sample, thus the values of the built-in voltage and Dember terms are to be understood as rough estimates.

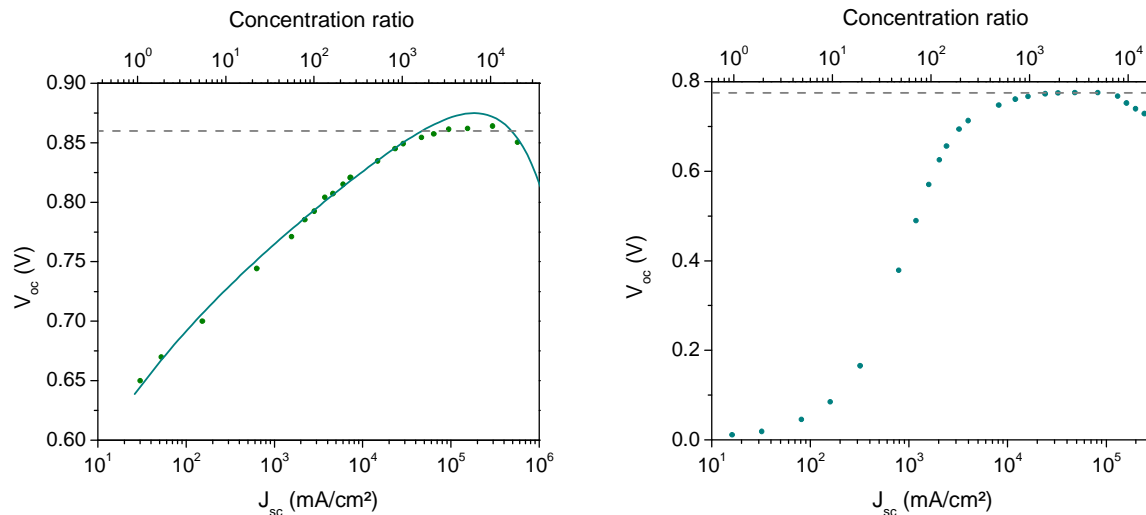


Figure VI-15 : (left) $V_{oc} - J_{sc}$ curve for a 7 μm microcell of an industrial sample. Dots correspond to experimental data and the line to our model's fit (temperature coefficient is set as to respect the scale effect $r^{0.8}$ seen in the previous chapter for this sample. A guide for the eye at 0.86 V is plotted in the grey dashed line (right) $V_{oc} - J_{sc}$ curve for a 15 μm microcell. This is an extended graph from Figure V-6. A guide for the eye at 0.775 V is plotted in the grey dashed line. Both curves correspond to illumination with the 532 nm laser.

The other sample on which saturation was evident was an industrial sample with chemically etched absorber (the absorber was thinned to 800 nm with help of a bromine solution) (Figure VI-15 right). This behavior is seen on each tested microcell of the sample, independent of the cell size. At low concentration the open-circuit voltage is dramatically low due to high shunt conductance. Then open-circuit voltage recovers a standard value above $\times 100$. For concentration ratios between $\times 1000$ and $\times 10\ 000$ the open-circuit voltage saturates at 776 mV. This value is smaller than for non-etched samples, which is logical as thin samples present enhanced back surface recombination.

This is the first time that saturation of open-circuit voltage is observed on $\text{Cu}(\text{In,Ga})\text{Se}_2/\text{CdS}$ diodes, to the best of the author knowledge. This saturation arises at ultrahigh fluxes, and as such may not be detrimental for the use of $\text{Cu}(\text{In,Ga})\text{Se}_2$ under concentration. From a fundamental point of view however, this saturation phenomena is interesting and may be used to get an evaluation of the mobility ratio b under high illumination.

5. Conclusions

In this chapter we focused on high concentration experiments on $\text{Cu}(\text{In,Ga})\text{Se}_2$ microcells. Due to the microcell architecture, current-voltage curves under very high concentrations could be measured for the first time.

We observed a decrease in series resistance with concentration. We attributed that effect to the photodoping of the $\text{Cu}(\text{In,Ga})\text{Se}_2$ absorber. Thus the series resistance can present a tenfold decrease from AM1.5 values to concentrations of $\times 500$ or higher. This observation is very important as it confirms that $\text{Cu}(\text{In,Ga})\text{Se}_2$ can be used under very high concentration ratio without detrimental resistive losses.

In our measurements we observed a decrease in the collection efficiency under high illumination fluxes. We attribute this to the screening of the electric field at the junction under increasing illumination. This decrease in electric field strength that we simulated in the simplified case of a homojunction, can have several consequences. First the increase in recombination in the high field region, and decrease in the space charge width both impede collection. Second if the heterointerface is defective, the collection efficiency of the interface is a balance between recombination velocity and electric field strength. Thus a reduced electric field at the junction will result in a smaller interface collection efficiency. This second mechanism is highly probable in $\text{Cu}(\text{In,Ga})\text{Se}_2$ solar cell, where the $\text{Cu}(\text{In,Ga})\text{Se}_2/\text{CdS}$ interface is known to impede collection, especially when conduction band offsets are present. Indeed on IRDEP samples the decrease in collection efficiency under concentration is found to be smaller than on the industrial samples, due to a smaller conduction band offset, that results also in the absence of a red kink effect.

Finally we observed the saturation of open-circuit voltage below the built-in voltage. This fact can be attributed to the Dember effect, which limits the possible attainable voltage in a n^+p junction. This fact is observed for the first time on $\text{Cu}(\text{In,Ga})\text{Se}_2$ solar cells, and complementary experiments could be interesting to have a better quantification of the phenomenon.

6. Memento

Series resistance is modulated under concentration. The decrease of series resistance with increasing flux is a consequence of Cu(In,Ga)Se₂ photodoping.

The collection efficiency of Cu(In,Ga)Se₂ solar cells is dependent on the illumination level. By numerical simulations, we showed that the electric field and space-charge width of a homojunction are screened at high illumination intensities. A similar phenomena in the Cu(In,Ga)Se₂ heterojunction explains the decreased collection efficiency, via the increase of bulk or interface recombination.

We observed the saturation of open-circuit voltage under very high illumination, below built-in voltage values. The influence of Dember field is likely involved.

CHAPTER VII. TOWARDS INDUSTRIAL APPLICATIONS: MICROCELLS WITH LOCALIZED ABSORBER

1. Introduction: localized depositions techniques.....	196
2. A top down fabrication process: study of mesa delineated microcells on co-evaporated Cu(In, Ga)Se₂ absorbers	198
2.1. The need for a model architecture.....	198
2.2. Fabrication process from a standard Cu(In, Ga)Se ₂ solar cell	198
2.3. Results : electrical characterization.....	200
2.4. Discussion	203
2.5. Conclusions.....	205
3. A bottom-up process: electrodeposition	205
3.1. State-of-the art electrodeposition	205
3.2. Fabrication of electrodeposited CuInSe ₂ microcells.....	208
3.3. Results	210
3.4. Discussion	213
4. Synthesis and discussion on industrial relevance.....	214
5. Memento.....	216

1. Introduction: localized depositions techniques

In this thesis we focused on prototype microcell devices for a proof of concept. We presented in the previous chapters a fabrication process that was not selective. The absorber layer was deposited on the whole substrate. From an industrial application point of view, this fabrication process is far from ideal. Indeed on a concentration module, the proportion of the surface covered by solar cells is small and roughly equal to the inverse of the concentration ratio. Thus it is a waste to have absorber material covering the entire substrate. Indeed elements used in the $\text{Cu}(\text{In,Ga})\text{Se}_2$ absorber synthesis, such as In and Ga, are expensive and have limited availability [16], [253], [254]. They should thus be used with parsimony. In this sense selective deposition techniques that enable the deposition of thin films at defined places are highly desirable. With such methods solar cells could be grown directly on a substrate at spots where the concentrating optics directs sunlight. Non selective deposition techniques associated with etching can also be a way of creating localized solar cells. However without proper material recycling, this solution has no interest from raw material economy point of view. The association of the etching and recycling steps make these types of solutions less attractive than direct selective growth, due to a cumbersome process. We will thus focus on thin film localized deposition techniques that can permit the deposition of microcells.

There are several types of selective deposition techniques. Some are based on the deposition of a patterned template through which the selective growth is carried out. This is the case of electrodeposition, which enables the deposition of numerous thin films from a solution onto conductive substrates. If an insulating template is deposited on the electrode, the electrodeposition reaction will occur only on the conductive areas of the substrate. This enables the deposition of patterned thin films or high aspect ratio structures as shown for example in Figure VII-1 (left) [255]. Atomic layer deposition on a substrate covered by a compound on which the growth is inhibited, such as a self assembled monolayer of octadecyltrichlorosilane [256], or microprinted polymethacrylamide layers [257] can also give selective growth.

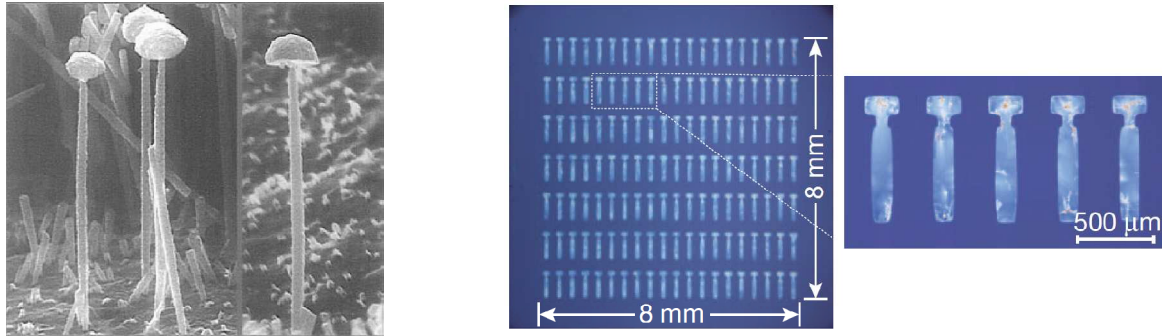


Figure VII-1 : (left) SEM images of Ni wires grown by electrodeposition after dissolution of the polycarbonate track-etched template. The wires have a length of 6 μm and an apparent diameter of 100-280 nm [255]. (right) Micrographs of a 20 \times 7 array of inkjet-printed organic semiconductor 2,7-dioctyl[1]benzothieno[3,2-b][1] benzothiophene single-crystal thin films transistors.

The second type of techniques enables the localized deposition without a preliminary structuring of the substrate. This can be interesting for example to form the templates needed for the localized deposition methods presented above. Among these techniques, we can cite the self-assembled techniques, where non-covalent interactions permit the formation of ordered structures [258]. Printing techniques, such as inkjet printing, are selective deposition techniques widely employed. It permits the local deposition of semiconducting polymers [259] (Figure VII-2 right). Printing also has applications to large area deposition of $\text{Cu}(\text{In,Ga})\text{Se}_2$ solar cells [260]. Localized depositions are not limited to wet processes. Laser assisted chemical vapor deposition, where the laser creates a localized hot spot at which the reaction takes place, enables the selective deposition of various materials on an absorbing substrate [261]. Micro-Knudsen effusion cells are also used to have localized depositions by evaporation [262]. Vapor-liquid-solid growth is widely used to create nanowires and nanowhiskers [263].

In this thesis we deal with the problem of selective deposition for $\text{Cu}(\text{In,Ga})\text{Se}_2$ microcells. The goal is to develop a process in which the absorber is deposited at the microcell location solely. There are many aspects to this work: to limit the use of absorber materials, to see how such devices work, especially to determine the role of the microcell edges, and to open perspectives for an industrial application.

In order to study all of these aspects we follow two distinct routes: a top-down approach to pattern $\text{Cu}(\text{In,Ga})\text{Se}_2$ layers co-evaporated on a substrate, and a bottom-up approach with selective absorber growth. The first approach is intended to show prototype devices with high quality materials to study in particular edge effects. The second axis aimed at fabricating devices on a process transferable to industrial production lines.

2. A top down fabrication process: study of mesa delineated microcells on co-evaporated Cu(In, Ga)Se₂ absorbers

2.1. The need for a model architecture

We decided to fabricate Cu(In,Ga)Se₂ microcells from co-evaporated substrates by post-deposition patterning. Indeed some aspects were not tackled with our previous devices. In particular recombination at the edges that is known to limit the miniaturization of III-V concentrator cells [159] was absent from the previous device generation, as the absorber was not patterned. Thus we decided to make these top-down structures before implementing bottom-up approaches. This enables us to have microcells with localized, “state-of-the-art”, absorbers and features comparable to our previous generation of microcells.

2.2. Fabrication process from a standard Cu(In, Ga)Se₂ solar cell

2.2.1. Principle

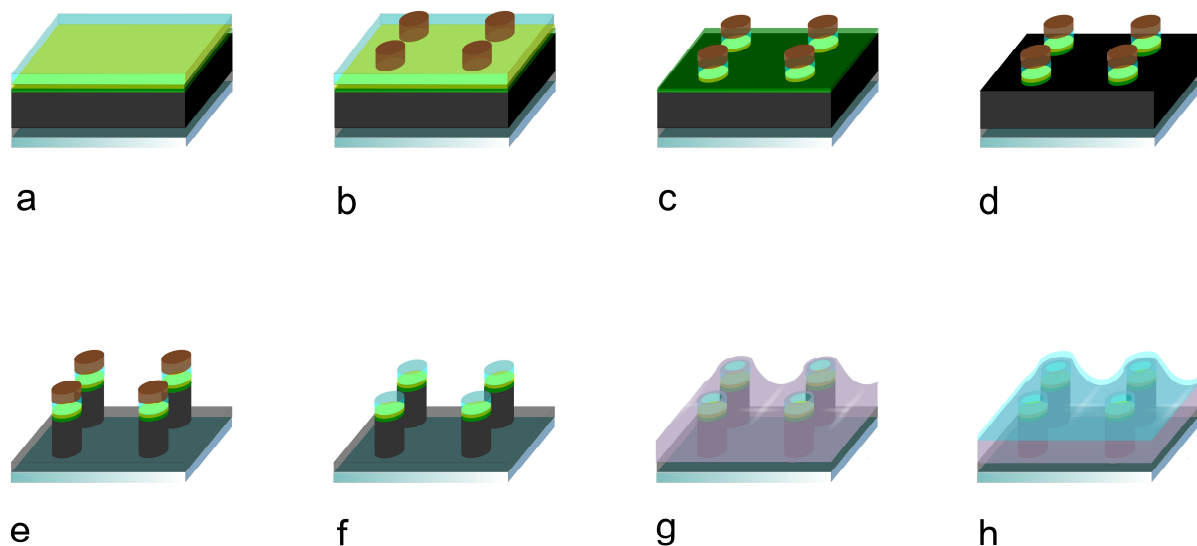


Figure VII-2 : Sketch of the top-down Cu(In,Ga)Se₂ microcell process. (a) Complete Cu(In,Ga)Se₂ solar cell (b) Creation of photoresist microblocks (c) ZnO etching (d) CdS etching (e) Cu(In,Ga)Se₂ etching (f) Resist removal (g) Polymer insulation (h) ZnO:Al sputtering for electric contact.

In order to create these “micro-blocks” solar cells, we use etching through a photomask of a complete Cu(In,Ga)Se₂ solar cell (Figure VII-2). The details of the process are given in Appendix F. We chose to start from complete solar cells in order to avoid degradation of the Cu(In,Ga)Se₂ surface before buffer deposition. For this study we use solely co-evaporated substrates coming from Würth Solar.

2.2.2. Etching of Cu(In,Ga)Se₂

Etching of Cu(In,Ga)Se₂ was performed by two different techniques : Ion beam etching and chemical etching.

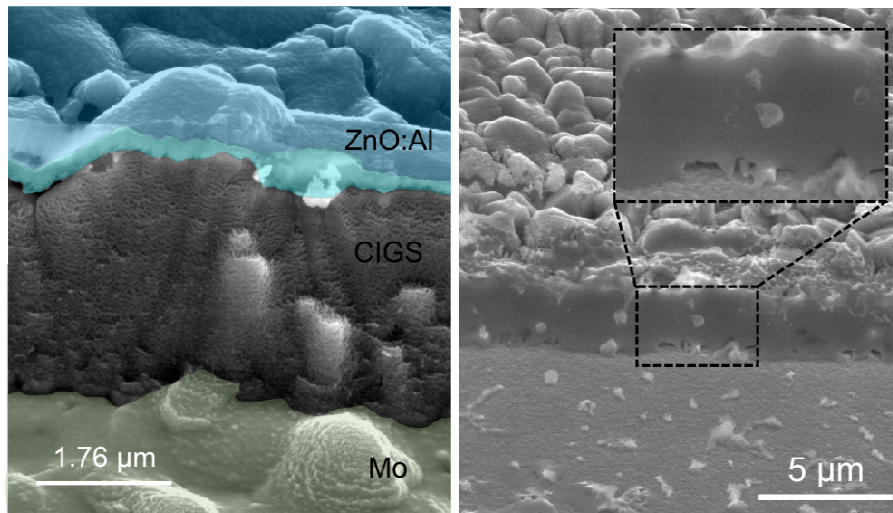


Figure VII-3 : (left) Colorized SEM image of a Cu(In,Ga)Se₂ micro-block solar cell after IBE etching of 98'. Highly structured Cu(In,Ga)Se₂ edge is visible. (right) SEM image of a microcell where ZnO has been sufficiently etched to observe the Cu(In,Ga)Se₂ edge. On the inset one can see that the edge surface is smooth.

Ion beam etching

Ion beam etching was used to pattern Cu(In,Ga)Se₂ through a patterned photoresist layer. The ion beam etching is based on the bombardment of the sample by Ar⁺ ions generated in a Ar plasma. The etch rate in our experimental conditions, described in Appendix F, is found to be 40 nm/mn.

Ion beam etching was successful in creating Cu(In,Ga)Se₂ micro-blocks (Figure VII-3 left). The edges of the Cu(In,Ga)Se₂ layer present a specific texture. This texture is found on all etched samples, and is resistant to acetone cleaning, and thus is unlikely due to photoresist residuals. It may come from the rotation of the sample, inclined with respect to the plasma direction, which exposed periodically the edges to the ion bombardment and thus create trenches.

Chemical etching of Cu(In,Ga)Se₂

Table VII-1 : Properties of the two bromide solutions used for chemical patterning of Cu(In,Ga)Se₂ micro-blocks solar cells.

	Br ₂ (mol.L ⁻¹)	KBr (mol.L ⁻¹)	KOH (mol.L ⁻¹)	pH	Etch rate (μm/mn)
Solution 1	4 10 ⁻²	1	9.5 10 ⁻⁴	7.1	1
Solution 2	8 10 ⁻²	2	9.5 10 ⁻⁴	7.2	4

In order to pattern Cu(In,Ga)Se₂ micro-blocks by a wet chemical process we chose to use a solution of the bromide family [201], [264]. As we are processing on complete solar cells, the pH of the solution has to be quasi-neutral to prevent the etch of both ZnO and CdS layers, during the etch of the 2 to 3 μm Cu(In,Ga)Se₂ layer. Thus we prepared solutions of bromine and potassium bromide, and adjusted the pH with potassium hydroxide (Table VII-1). The solution preparation was done in collaboration with Isabelle Gerard of the Institut Lavoisier de Versailles, who has a strong know-how on bromide etching.

We proceed by successive etching steps. The etching rate is dependent on the solution concentration and trenching occurs, i.e. etching is faster close to the patterns. Moreover etching is not unidirectional. Thus there is under-etching of the patterns, i.e. Cu(In,Ga)Se₂ is etched under the ZnO and photoresist layer. The under-etched length is of the order of the Cu(In,Ga)Se₂ layer thickness. More details on chemical etch can be found in Appendix F.

2.2.3. *Contacting microcells*

With the etching procedure we create micro-block solar cells (Figure VII-2 f) that we can measure by contacting the Mo back contact and ZnO:Al window layers with micro-probes. Even if this technique is satisfactory for dark characterization, we need to have a better contacting method if we want to measure the devices under illumination. Thus we developed a contacting procedure. A polymer is deposited around the microblocks (Figure VII-2 g) before the sputtering of a ZnO:Al layer that contacts the microblocks upper surfaces, and connects the devices in parallel (Figure VII-2 h). Details on the contacting procedure can be found in Appendix F.

In order to evaluate the impact of the different fabrication processes, we test the current-voltage characteristic of micro-block solar cells in the dark and under AM1.5 illumination.

2.3. Results : electrical characterization

2.3.1. *Dark current voltage characterization of micro-block solar cells*

We tested the samples done in IBE etching. Unfortunately the results in terms of saturation currents are dispersed on more than six orders of magnitude. Some devices have good characteristics, but a majority has poor performances (See appendix F).

Then we tested samples realized by chemical etching. No difference was found between samples etched in solution 1 or 2, thus we presented samples etched in solution 1 that have about 5 μm under-etching. As both J_{01} and J_{02} signals can be detected, we analyze our devices using the two-diodes model (See Chapter II).

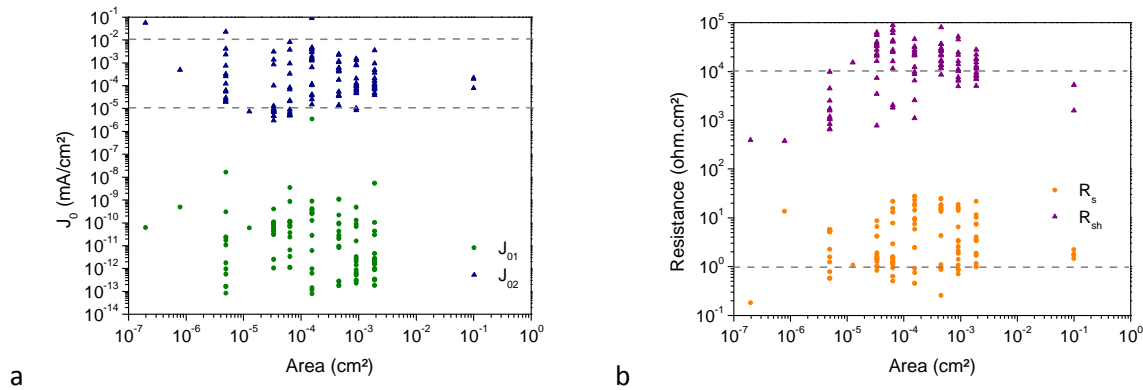


Figure VII-4 : (a) Saturation currents J_{01} and J_{02} as a function of size for a micro-blocks sample patterned by chemical etching after contacting with procedure a→b→c. (b) Shunt and series resistance as a function of micro-blocks size after contacting with procedure a→b→c. Samples are etched in solution 1. Samples with shunt resistance smaller than 100 ohm.cm² are not displayed. Dotted lines are guides for the eye.

We can see that, as for microcells presented in the last chapters, the saturation current J_{02} of ideality 2 is predominant. It is comprised between 10⁻⁵ and 10⁻² mA/cm². The saturation current J_{01} is comprised between 10⁻¹³ and 10⁻⁹ mA/cm² (Figure VII-4 a). These values are comparable to that of unpatterned microcells even if the dispersion of the data is higher. This increase in dispersion is not an artifact of numerical fitting, but reveals a higher spread of solar cell performance on a single sample. The series resistances are roughly proportional to the cell surface, i.e. the value in ohm.cm² is roughly constant. The values of series resistance are higher compared to previous microcell devices (Figure VII-4 b). This is probably due to a bad contact between the probe tip and the ZnO surface. It is comprised between 1 and 10 ohm.cm². The shunt resistance is roughly proportional to the cell surface. Thus the area around the micro-blocks seems correctly isolated. We can see however that for small devices the shunt resistance is low, due to shunts between the ZnO and Mo layers. This is due to misalignment in the process that makes shunts between ZnO:Al and Mo more probable for the smallest devices.

2.3.2. Current voltage characterization of contacted microcells under illumination

AM1.5 illumination

For the chemically etched sample that we contacted with procedure a→b→c, as described in the Appendix F, we can measure AM1.5 current-voltage characteristics as the probe, positioned outside the micro-blocks, does not provoke shading. The average short circuit current density J_{sc} for cells larger than 1 10⁻⁵ cm² is 27.7 +/- 0.3 mA/cm² and the V_{oc} is 620 +/- 11 mV.

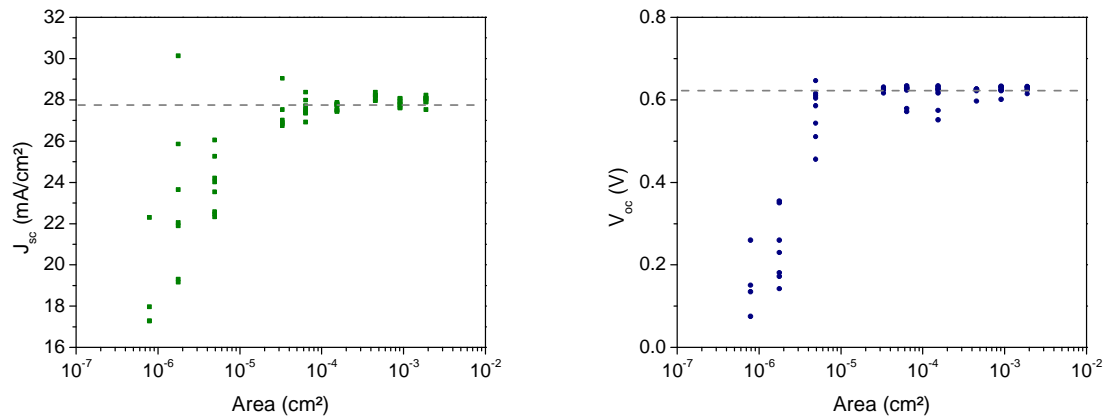


Figure VII-5 : (left) Short circuit current density as a function of cell size for micro-blocks solar cell under AM1.5. (right) Open-circuit voltage as a function of micro-blocks solar cell size. In both graphs, the micro-block size accounts for a 5 μm under-etch. The lines are guides for the eye to situate the average over the devices larger than 10^{-5} cm^2

The short-circuit current and open-circuit voltage are stable for devices larger than 10^{-5} cm^2 . For smaller devices, J_{sc} and V_{oc} drop. The decrease in V_{oc} comes partly from increased shunts for smaller devices as explained in paragraph 2.3.1. The decrease in J_{sc} may be due to different sources. In our analysis, we consider that the devices have on average 5 μm under-etch as observed by optical microscopy. However the under-etch is found slightly higher for smaller devices as the etch is not perfectly homogeneous, which results in an underestimation of the J_{sc} of the smallest micro-blocks.

Laser illumination

Unfortunately we did not have the time in this study to fabricate chemically etched samples with a contacting procedure $a \rightarrow b \rightarrow d \rightarrow e \rightarrow f$. Thus we tested devices without the gold peripheral contact. A 532nm laser was used, in the configuration described in the previous chapters. Due to increased resistive losses in these devices, especially due to the bad electrical contact between our test probe and the ZnO:Al surface, the series resistance is large (as seen in dark measurements Figure VII-4 c and d). The improvement of efficiency with concentration ratio is limited to the low concentration range ($C < 10$). However the open-circuit voltage is less affected by this series resistance and a 154 mV increase is observed between $\times 0.84$ and $\times 220$. At a concentration ratio above $\times 220$, the short-circuit current density becomes non-linear with incident power due to the resistive losses, and the calibration of our setup is no longer valid.

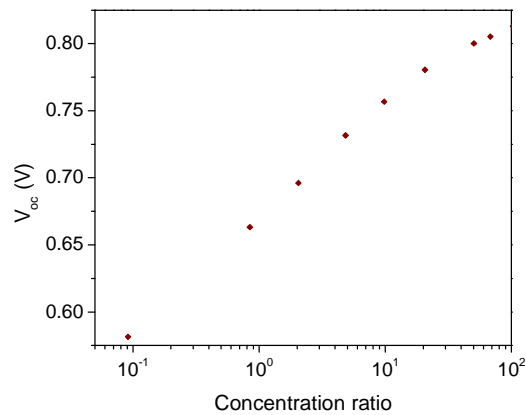


Figure VII-6 : Open-circuit voltage as a function of concentration ratio for a 75 μm micro-block solar cell. Test with 532 nm laser.

2.4. Discussion

2.4.1. Comparison of the different etching processes.

Chemical etch is the process that yields the smallest dispersion of the results. Ion beam-etching is probably deteriorating the performances due to the high surface temperature induced on the sample by the ion bombardment. This is a critical point for physical etch. The $\text{Cu}(\text{In}, \text{Ga})\text{Se}_2$ is 2 to 3 μm thick thus the etching time (> 1 hour) is sufficient to provoke an important sample heating under ion bombardment. Reducing the surface temperature can be done by changing the substrate from glass to a substrate with higher thermal conductivity. Thus the thermal connection between the sample-holder, that is cooled, and the sample surface could be improved. The surface temperature can also be reduced by shortening the duration of the etching steps. However this second solution is impractical as it will result in hours-long etches. We have developed a few chemical treatments of the $\text{Cu}(\text{In}, \text{Ga})\text{Se}_2$ micro-blocks edge surfaces after IBE etching. No drastic differences were found on IBE-etched samples. The dispersion of data was not reduced by treatment in bromine solution or cyanide solution. The damage caused by IBE etching could not be recovered with surface treatments.

Chemical etch results in micro-block devices, which characteristics are reasonably dispersed compared to what was observed on microcells. The chemical etch is selective and the window and buffer layers are not etched. The back contact is etched in the solution but slowly, thus the complete removal of $\text{Cu}(\text{In}, \text{Ga})\text{Se}_2$ is possible. The chemical etch is fast and the edges of the micro-blocks are sharp and smooth. Storage in atmospheric condition was quickly studied. After storage the devices have slightly higher averaged saturations currents, even if for a major part of the samples the saturation currents are stable. The resulting micro-block solar cells show good photovoltaic

performance with an average 10% conversion efficiency for devices larger than 10^{-5} cm², an average J_{sc} is 27.7 +/- 0.3 mA/cm² and a mean V_{oc} of 620 +/- 11 mV. Thus in this study, the most favorable patterning process is wet chemical etching.

In the literature photodetectors were fabricated by means of an inductively coupled-plasma reactive ion etching technique of a Cu(In,Ga)Se₂ layer with HBr and Ar gases, the residues being removed in hydrochloric acidic solution [190]. We did not study inductively coupled-plasma reactive ion etching during this thesis but this technique also gives good results and may be interesting in the future. Indeed leakage currents of 10^{-7} A/cm² for an i-ZnO of 50 nm thickness were obtained on 10 μm × 10 μm pixels. However the use of HBr and subsequent HCl residue removal may be difficult to achieve on a complete solar cell as it may deteriorate the front contact layers.

2.4.2. Comparison of localized and non-localized Cu(In, Ga)Se₂ microcells

We can see that micro-blocks solar cells created by chemical etching are good photovoltaic devices. Saturation currents J_{02} as low as 10^{-5} mA/cm² are obtained. These values are comparable to what was observed on microscale solar cells with non-localized absorbers (see Chapter IV). This value of saturation current is also coherent with the leakage current at -1V measured on image sensor Cu(In,Ga)Se₂ pixels. For these sensors, with a i-ZnO layer of 50 nm thickness, the leakage current is 10^{-4} mA/cm² on 10 × 10 μm pixels [190]. This suggests that the edges are not detrimental to these micro-devices.

We cannot in our measurements see a dependence of saturation current with micro-block perimeter. Thus edge recombination velocities are small, and the dark current due to the edge surface of micro-blocks only have a minor influence on the device performance. As seen in Chapter III, the saturation current of ideality factor 2, can be written in the form :

$$J_{02} = J_{02,bulk} + J_{02,P} = J_{02,bulk} + P/S \times J_{02,P}' \quad (VII-1)$$

where P/S is the ratio of the cell perimeter over area. As we do not detect the component $J_{02,P}'$, we can write that $J_{02,P}' \ll J_{02,bulk} \times S/P$. Thus as we have values of $J_{02,bulk}$ as low as 10^{-8} A/cm² for cells of area 5×10^{-6} cm² and perimeter 8×10^{-3} cm, $J_{02,P}' \ll 6 \times 10^{-12}$ A/cm. This upper limit for edge recombination in Cu(In,Ga)Se₂ device has to be compared to the 10^{-13} A/cm value for GaAs devices. The saturation current component $J_{02,P}$ can be related to a surface recombination velocity [265]. Namely it was shown that $J_{02,P} = qn_i L_n s_0$, where n_i is the intrinsic carrier density, L_n the diffusion length, s_0 the recombination velocity. If we consider $n_i = 10^8$ cm⁻³, $L_n = 1$ μm, the upper boundary of the dark current $J_{02,P}' \ll 6 \times 10^{-12}$ A/cm is equivalent to $s_0 \ll 4 \times 10^3$ cm/s. This low recombination velocity is coherent with values of grain boundary recombination velocity that are known to be less

than 10^4 cm/s[66] or even less than 10^3 cm/s [266]. Thus our measurements confirm that Cu(In,Ga)Se₂ surfaces have a low recombination velocity, and do not impede the device performance even for microscale devices. This is very different from what is observed on GaAs solar cells where the edge recombination current can be the predominant recombination path [159], [161], [265].

2.5. Conclusions

Prototype Cu(In,Ga)Se₂ micro-block solar cells were created. Wet chemical etching was found preferable to physical IBE etching. With dark current-voltage characteristics, it was possible to estimate an upper boundary for edge recombination velocity of $4 \cdot 10^3$ cm/s, which is coherent with previous results for grain-boundary recombination velocity. However the precise estimation of the edge saturation current was impossible due to its negligible impact on our micro-blocks solar cells. The performances of micro-blocks under concentration are promising, even if the work done during this thesis is preliminary.

As a conclusion we can say that these prototypes showed that the edges do not hinder micro-block solar cell performances. Thus selectively deposited microcells can be considered as a promising option for an industrial fabrication of Cu(In,Ga)Se₂ microcells.

In the next paragraph a preliminary study of electrodeposition of Cu(In,Ga)Se₂ micro-block solar cells is presented. Electrodeposition was chosen for this study because of its capability to selectively deposit thin films on conductive surfaces. Among the multitude of selective deposition techniques that can be applied to Cu(In,Ga)Se₂ synthesis, electrodeposition was chosen due to the strong knowledge and know-how of IRDEP laboratory in this technique [60], [80], [267], [268]. Other approaches, such as printing, seem also very promising, but we did not have the time in the course of this thesis to tackle them.

3. A bottom-up process: electrodeposition

We decided to study the electrodeposition of Cu(In,Ga)Se₂ microcells. This study is preliminary and is intended to show the potential of electrodeposition for localized deposition of Cu(In,Ga)Se₂ absorbers. However the study was too short to provide a complete understanding of the deposition process for micro-devices. Thus a detailed electrochemical analysis will be needed in the future. Our work however highlights the promises and possible obstacles to the implementation of Cu(In,Ga)Se₂ electrodeposition for microcells.

3.1. State-of-the art electrodeposition

3.1.1. Principle of electrodeposition

Electrodeposition is the reaction of reduction of metal ions from a solution in which a power supply provides the necessary electrons:



The Nernst equation gives the potential of the equilibrium potential M^{+z}/M at an electrode as a function of the ion concentration:

$$E = E^0 + \frac{RT}{zF} \ln([M^{+z}]) \quad (\text{VII-3})$$

where E^0 is the standard electrochemical potential of the M^{+z}/M electrode, F the Faraday number, $[M^{+z}]$ the concentration of the M^{+z} ions. When two electrodes are electrically connected, an electrochemical cell is created. The equilibrium potential difference across a cell is the difference between the two electrode potentials. Reference electrodes are used such as the normal hydrogen electrode (NHE) H^+/H_2 , which standard potential is set to zero at 25°C by convention. The standard potentials of the other electrodes are thus determined with reference to the normal hydrogen electrode.

Table VII-2 : Standard potential with respect to the normal hydrogen electrode reference of various reactions.

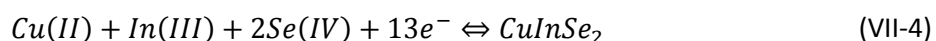
Electrode name	M^{+z}/M couple	Electrode reaction	Standard potential (V) vs. NHE
	Se^{4+}/Se	$Se^{4+} + 4e^{-} \rightleftharpoons Se$	0.75
	Cu^{2+}/Cu	$Cu^{2+} + 2e^{-} \rightleftharpoons Cu$	0.34
	In^{3+}/In	$In^{3+} + 3e^{-} \rightleftharpoons In$	-0.34
	Ga^{3+}/Ga	$Ga^{3+} + 3e^{-} \rightleftharpoons Ga$	-0.53
Mercury mercurous sulfate $Hg Hg_2SO_4 SO_4^{2-}$		$Hg_2SO_4 + 2e^{-} \rightleftharpoons SO_4^{2-} + 2Hg$	0.66
Normal hydrogen electrode (NHE) $Pt H^+ H_2$		$2H^+ + 2e^{-} \rightleftharpoons H_2$	0

When an external supply enables a current flow through the electrochemical cell, the potential at the electrode $E(I)$ is modified from equilibrium E and an overpotential is created, $\Delta\psi = E(I) - E$. This overpotential enables charge-transfer, diffusion, chemical reaction or crystallization [269].

3.1.2. *CuInSe₂ electrodeposition*

The electrodeposition of CuInSe₂ was first studied in 1983 [270]. Since then it has become the most studied non-vacuum fabrication process for Cu(In,Ga)(S,Se)₂ solar cells [80]. Electrodeposition is a solution based process in which a substrate is immersed in a chemical bath. As the baths can be kept at constant composition by adding the consumed elements frequently, electrodeposition can reach

nearly 100% material utilization efficiencies, compared to at most 75-80% for the most advanced physical processes. Thus material consumption and consequently material costs can be greatly diminished. There are several processes to fabricate Cu(In,Ga)(S,Se)₂ cells by electrodeposition. One can proceed to a one step co-electrodeposition where a precursor layer having a desirable stoichiometry is deposited and then annealed. Codeposition is difficult due to the difference in electrode potential of the different elements (Table VII-2). Incorporating Ga in the electrodeposited layer is the most difficult task, owing to its highly negative potential (Table VII-2), and many electrodeposited cells are in fact CuInSe₂ solar cells. In our group one-step codeposition of CuInSe₂ led to a record of 11.3% [268]. The global reaction of CuInSe₂ formation is [271]:



However this global reaction is not the exact description of the electrochemical process, as intermediary reactions involving binaries or metal complexes take place [271]. One-step codeposition is also a promising way of introducing Ga in electrodeposited cells, via the formation of Ga-Se bonds [268]. One can also deposit a stack of metallic layers that is annealed afterwards in a chalcogen atmosphere. The electrodeposition process is simpler but a succession of chemical baths to deposit sequentially each element is needed. The method is used industrially by Nexcis or Solopower for example and led to a record efficiency of 13.76% of a 0.5 cm² solar cell [88]. Annealing is up to now a mandatory step in all electrochemical processes as the precursor layers, electrodeposited at low temperature, are amorphous and highly defective. The annealing step can be done by a rapid thermal treatment (flash), or longer processes, and in a Se containing atmosphere.

3.1.3. Electrodeposition: a tool for micro-structuring

As already mentioned, electrodeposition is a selective deposition technique. Deposition occurs at the electrode, i.e. on a conductive surface. Partially covering an electrode by an insulator results in the inhibition of growth on the insulated areas. Thus micro-structuring is easily done with electrodeposition.

In fact electrodeposition on microelectrodes is a vast field of study [272–274]. Indeed electrodeposition on microelectrodes present numerous advantages compared to large area deposition. On microelectrodes the currents are small, thus low conductive media can be used, and electrodeposition is not limited to concentrated aqueous solutions. Then diffusion mass transport is highly efficient on microelectrodes, as the diffusion field is spherical instead of planar (Figure VII-7). Mass transport rates on microelectrodes are equivalent to that on microelectrodes rotated at several

thousand r.p.m [272]. Microelectrodes have fast response and can be used for highly accurate time-resolved voltammetric measurements.

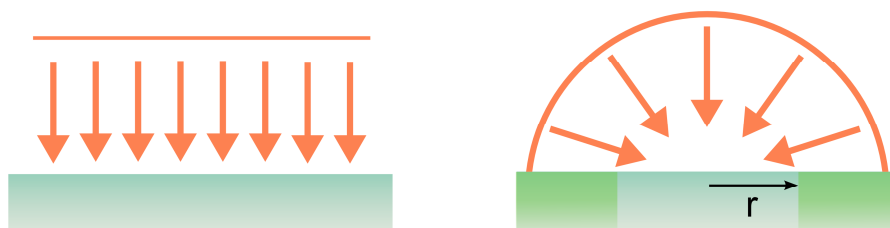


Figure VII-7 : Sketch of a linear diffusion field on a macroelectrode (left) and spherical diffusion field at a microelectrode of radius r (right).

Due to the spherical diffusion field (Figure VII-7), the current density at a micro-disk electrode is the sum of a transient and a steady-state current density that can be calculated from Fick's second law [272], [273]:

$$J = \frac{4nFDc_{\infty}}{\pi r} + \frac{nF\sqrt{D}c_{\infty}}{\sqrt{\pi t}} \quad (\text{VII-5})$$

where r is the micro-disk radius, c_{∞} the concentration of the solution far from the electrode, D the diffusion coefficient of the electrodeposited species in solution, F the Faraday constant (electric charge per mole of electrons) and t the time. For microelectrodes the transient current is rapidly becoming small compared to the steady-state current, and equilibrium is reached fast (for a species with a diffusion coefficient of $10^{-5} \text{ cm}^2 \cdot \text{s}^{-1}$ the steady state is reached in 0.5 s for a microelectrode of diameter 100 μm). Moreover due to the small microelectrode radius, the current density can be large and the electrodeposition fast. However due to the spherical diffusion field the deposition cannot be homogeneous, as the diffusion rate will be higher at the edge than at the center of the microdisk.

3.2. Fabrication of electrodeposited CuInSe_2 microcells

3.2.1. Principle

The fabrication of electrodeposited microcells consists in different steps, described in details in Appendix F, and shown in Figure VII-8.

One of the most important steps in the realization of electrodeposited microcells is the fabrication of an adapted structured substrate. We chose Al_2O_3 as the insulating layer due to its high thermal and chemical stability. The temperature of the Al_2O_3 synthesis was adapted to ensure thermal stability of

the glass/Mo/Al₂O₃ stack during precursor layer annealing. The Al₂O₃ is etched in an orthophosphoric solution that does not attack the Mo layer (see Appendix F for more details).

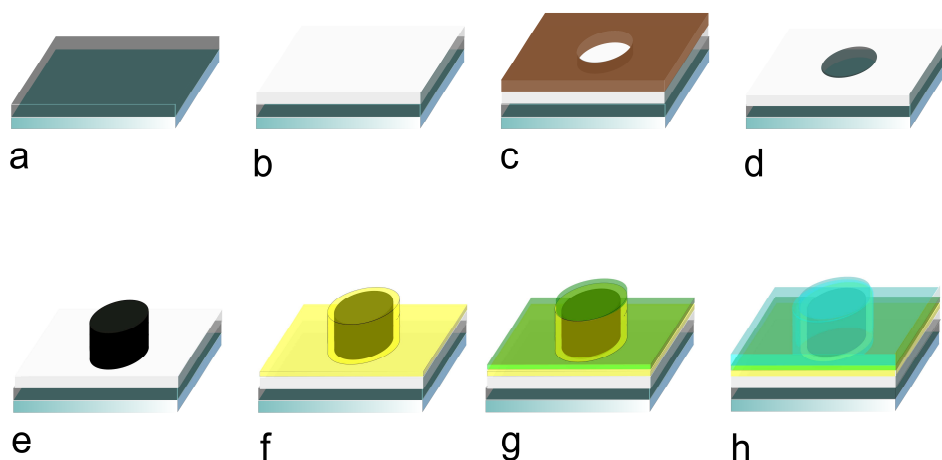


Figure VII-8 : Micro-block solar cell electrodeposition process.(a) Mo layer sputtering on soda-lime glass (b) Al₂O₃ Atomic Layer deposition (c) Photolithography (d) Mo etch and resist removal. (e) CuInSe₂ electrodeposition (f) CdS chemical bath deposition (g) intrinsic ZnO sputtering (h) ZnO:Al sputtering.

3.2.2. *Role of microcells area homogeneity and design*

In order to proceed to an electrodeposition through a pattern, two approaches can prevail. One can study the influence of the microelectrode size on the electrodeposited layer characteristics. Thus a pattern with multiple electrodes of various sizes can be desirable. However in this configuration it is not possible to determine the current flowing through each electrode and only the total current on the sample is controlled. One can choose on the contrary to study deposition on electrodes of a fixed size. Thus the current flowing through an electrode can be deduced from the total current and the number of electrodes, as the deposition should be homogeneous. More details on the electrodeposition mechanism can thus be exploited.

The two approaches were followed in this preliminary work. One pattern contains microelectrodes with diameter varying from 3570 μm to 5 μm . The other pattern is made of microelectrodes of 25 μm of diameter.

3.2.3. *Electrodeposition processes*

The bath is an aqueous solution containing Na₂SO₄ as supporting electrolyte, CuSO₄, In₂(SO₄)₃ and SeO₂. The pH is fixed at 2.2 by addition of hydrochloric acid. The electrodeposition is carried out with an applied potential at the working electrode of -0.9V (or -1V) with respect to mercury/mercurous sulfate reference electrode (potentiostatic control). The duration of electrodeposition is fixed by the charge exchanged, in order to attain a precursor layer thickness between 1 and 3 μm .

3.2.4. Annealing

As-deposited films are microcrystalline. The deposits are referred to as precursor layers. In order to have crystalline films, an annealing step is mandatory. Annealing is done either by rapid thermal annealing in a flash system, or longer processes in a tubular heater. Different maximum temperatures were tested, as well as annealing time. Thermal annealing treatments are done in a selenium overpressure atmosphere.

3.3. Results

3.3.1. Deposition and composition of the electrodeposited layer

Electrodeposition is done in a potentiostatic mode, with imposed potential versus the mercury/mercurous sulfate electrode (MSE). The current is recorded as a function of time. If we know the proportion of parasitic reactions, such as hydrogen creation reaction, the charge exchanged at the working electrode, deduced from the cumulative current, is related to the amount of deposited material via Faraday's law.

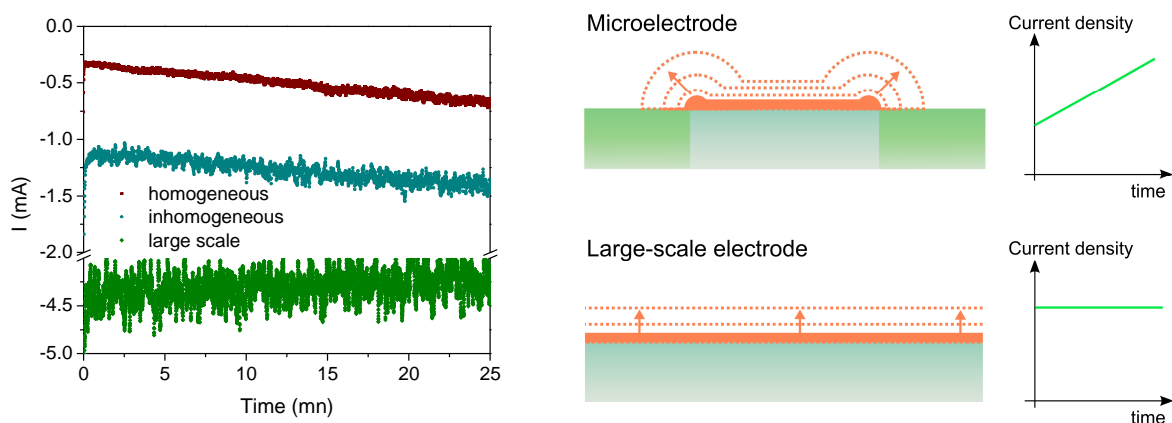


Figure VII-9 : (left) Current vs. time during three electrodeposition processes, on a sample with microelectrodes of the same size (red) on a sample with microelectrode sizes varying between 3570 and 5 μm (blue) on a large scale sample 2.5 \times 2.5 cm^2 (green). Deposition at -0.9V vs. MSE under 500 rpm. (right) Sketch of the deposition processes : electrodeposition on microelectrodes, with increasing current density with deposition time, electrodeposition on large scale electrode with constant current density with deposition time.

In our experiments we can see that the current tends to increase with deposition time (Figure VII-9). This is due to the lateral overgrowth of deposits, due to the edge effects. This phenomenon is more pronounced on the sample with 25 μm microelectrodes, where a 50% current increase is observed. On the sample with electrodes inhomogeneous in size, the phenomenon is proportionally less important, as the current is dominated by the signal of the largest electrodes (0.1 cm^2), on which the current is constant as observed on large scale samples (Figure VII-9).

3.3.2. Crystallographic characterization of electrodeposited absorbers before and after annealing

Before annealing

The electrodeposition on microelectrodes was performed. Before annealing, the deposits are mainly amorphous and secondary phases (Cu_xSe) may be present (Figure VII-10 b).

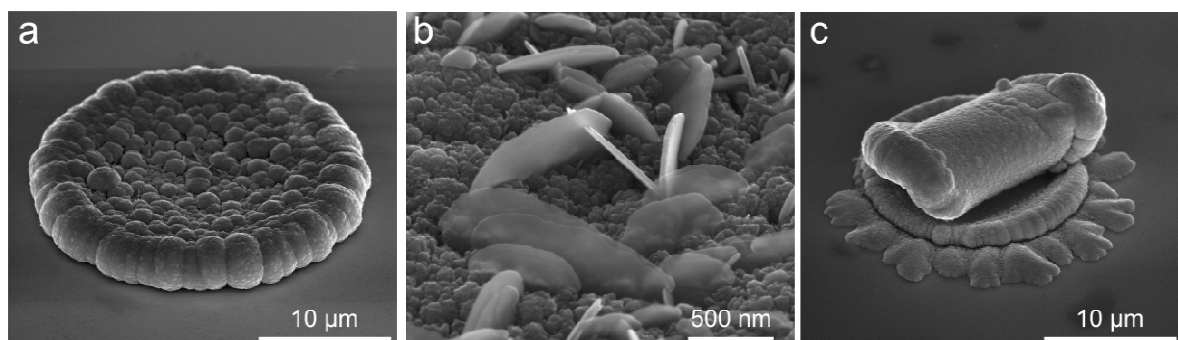


Figure VII-10 : Scanning electron microscope image of an electrodeposited sample before annealing . Electrodeposition at -0.9V at ambient temperature during 30 min on a substrate with $25\ \mu\text{m}$ holes patterned in the Al_2O_3 layer. (a) As deposited sample. (b) Zoom on binary phases. (c) Adherence problem. The deposit should be under compressive strain and peel-off occurs. Deposit roll up on themselves, and deposition starts again on the substrate.

The increased thickness of the deposits at the edges of the microelectrode is clearly visible on all samples (Figure VII-10 a). When the microelectrodes are small enough the deposition is controlled by the edges (Figure VII-11 a and b). The thickness of the precursor layer increases with decreasing electrode size and increasing applied potential (Figure VII-11). One problem encountered in this work is the poor adhesion of the electrodeposited films on the substrate (Figure VII-10 c). This problem is classic in electrodeposition. It seems that the precursor layers are under stress during deposition. Thus peel-off can occur during deposition and the electrodeposition starts again on the microelectrodes (Figure VII-10 c).

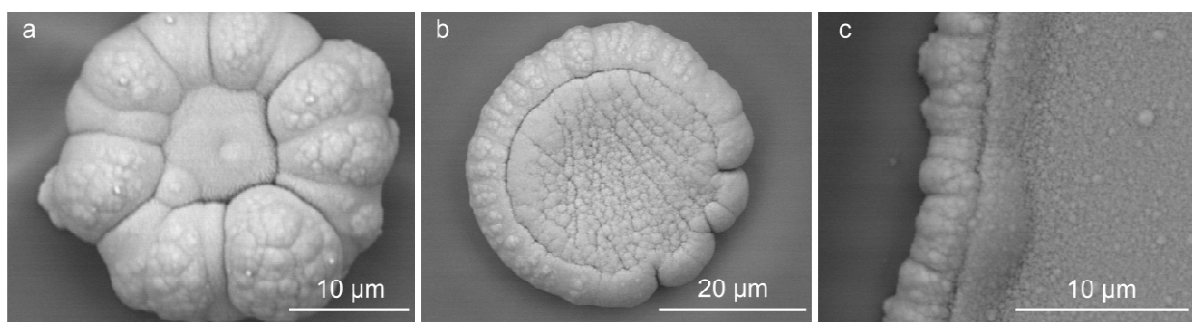


Figure VII-11 : Scanning electron microscope image of an electrodeposited sample before annealing . Electrodeposition at ambient temperature during 25 min on a substrate with holes of different sizes patterned in the Al_2O_3 layer. (a)

Deposition at -1V stirring at 500 rpm at a 20 μm microelectrode (b) Deposition at -0.9V, stirring at 350 rpm at a 25 μm microelectrode. (c) Deposition at -0.9 V stirring at 500 rpm at a 3570 μm microelectrode.

After annealing

After annealing, the crystallinity of the electrodeposited layer improves. Depending on the sample, its composition and the annealing process, large crystallites ($\approx 1 \mu\text{m}$) can be observed or not.

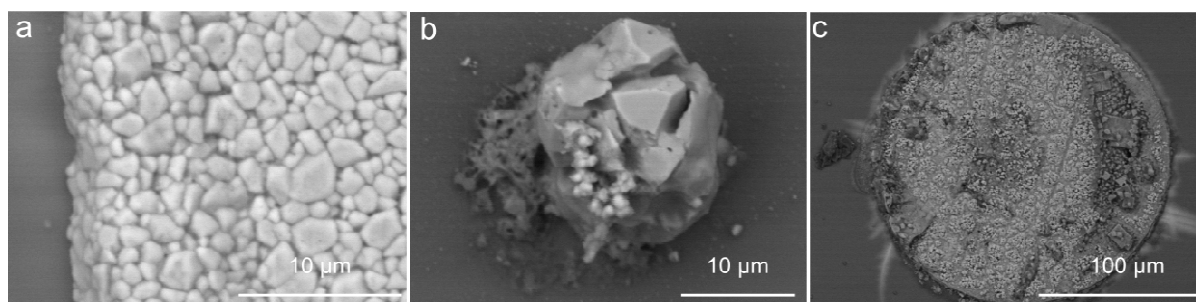


Figure VII-12 : Scanning electron microscope image of an electrodeposited sample after annealing. Electrodeposition at ambient temperature during 25 min on a substrate with holes of different sizes patterned in the Al_2O_3 layer. (a) Deposition at -0.9V stirring at 500 rpm at a 0.1 cm^2 electrode, annealing with flash process with maximum temperature of 435 $^\circ\text{C}$ (b) Deposition at -1V, stirring at 300 rpm at a microelectrode of nominal size 50 μm , annealing with a 450 $^\circ\text{C}$ plateau of 5 min (c) Deposition at -1 V stirring at 500 rpm, annealing with flash process with maximum temperature of 505 $^\circ\text{C}$

3.3.3. Composition

The composition of the samples is evaluated by X-ray fluorescence. The probed area is of the order of 0.1 cm^2 . Thus the composition is evaluated on the 0.1 cm^2 cells when they are present on the sample, or is an average over several 25 μm microdeposits, on the equi-sized samples.

Sample	E(i) (V)	Stirring (rpm)	Annealing		Before annealing			After annealing		
			Temp. ($^\circ\text{C}$)	Plateau Time (mn)	Cu (% atm)	In (% atm)	Se (% atm)	Cu (% atm)	In (% atm)	Se (% atm)
Figure VII-12 a	-0.9	500	450	0	23.7	22.5	53.8	16.8	17.4	65.9
Figure VII-12 b	-1	300	465	5	23.2	23.8	52.9	9	12.8	78.2
Figure VII-12 c	-1	500	505	0	23.2	24.4	52.4	14.4	17.2	68.5

The In/Cu ratio on the well crystallized sample is 0.97 (Figure VII-12 a) and tends to 1.2 for the badly crystalline samples (Figure VII-12 b). This is coherent with the fact that Cu-rich chalcopyrites generally present better crystallinity, as crystal growth in CuInSe_2 is mediated by copper binaries such as Cu_xSe [51]. It should be noted that very high selenium contents after thermal annealing are related

to a measurement error. Indeed if the deposit is not adhering during thermal treatment, the Mo surface is exposed, and MoSe_2 is formed. As the X-ray fluorescence spectroscopy probe is 0.1 cm^2 , the average content seems to be a Se-rich CuInSe_2 whereas it is just the addition of a regular CuInSe_2 phase with a MoSe_2 phase.

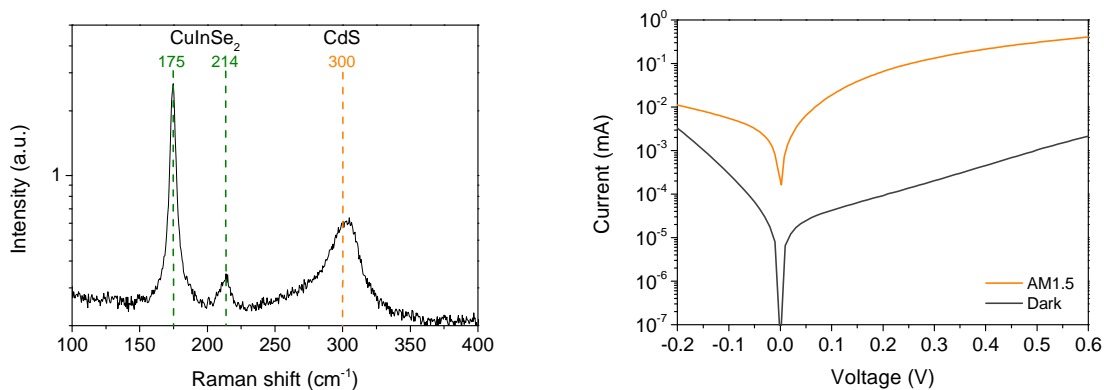


Figure VII-13 : (left) Raman spectra of the cell of Figure VII-12 a. The presence of a CuInSe_2 phase is confirmed. No binary can be detected. (right) Dark and AM1.5 current voltage characteristics. For reverse bias the absolute value of the current is displayed.

Raman study was carried out to verify the formation of a CuInSe_2 phase in the electrodeposits (Figure VII-13 left). For the cell of Figure VII-12 a, two peaks at 175 cm^{-1} and 214 cm^{-1} are seen and are characteristic of CuInSe_2 [275]. The signature of the CdS buffer layer is also visible.

We also examined the samples by energy-dispersive X-ray analysis (EDX) to have a smaller probed volume ($\approx 1 \mu\text{m}^3$) and get an estimation of the composition on micro-deposits, and see if the composition is homogeneous over the sample area. We found no significant differences between the centre and edge composition on the sample of Figure VII-10. Thus the edges of the micro-deposits are thicker but tend to be of the same composition as the center.

3.3.4. Characterization of photovoltaic performances

We tested the finished cells by measuring dark, as well as AM1.5, current-voltage characteristics. The devices are diodes, but no photo-response (open-circuit voltage or short-circuit current density) was measured (Figure VII-13 right). However the dark and AM1.5 characteristics do not superimpose perfectly, indicating a photoconductivity.

3.4. Discussion

The results presented in this study are preliminary. Several electrodeposited samples were fabricated but the results are not perfectly reproducible. This is not particularly surprising for a preliminary

electrochemical study [276]. More knowledge on the parameters that should be controlled with particular attention would come from further studies. In this work, we draw general conclusions but precise results would only be deduced from a more extensive work.

We can see from our study that the size of the microelectrode is important for the deposition. Important edge effect is seen on our sample. Due to the change of linear to spherical diffusion field, from center to periphery of a sample, the edges are prone to a higher diffusion current, and the deposits are thicker there (Figure VII-10 and Figure VII-11). This edge zone is around 5-10 μm large. Thus the importance of edge effect varies with the electrode size. The smaller the microelectrode the higher in proportion is the influence of the edges. If the microelectrode diameter is of the order of a few micrometers then the deposition is entirely under spherical diffusion control. If we want to have uniform deposition for all microelectrode sizes, a deposition in a high aspect ratio pattern mask will be required (recessed microdisk electrode configuration) [277]. Indeed a deposition in the bottom of a well will come closer to the linear diffusion geometry. However the thickness nonuniformity might not be detrimental to the device performances, and standard deposition could be satisfactory.

Our deposits have compositions that are in the range of what can be expected for CuInSe_2 , showing that CuInSe_2 one step codeposition is possible on microelectrodes. However our devices have no photovoltaic performances in spite of a photoconductivity. A study of the annealing process and a better control of the precursor composition is necessary.

4. Synthesis and discussion on industrial relevance

We have shown that Cu(In,Ga)Se_2 microcells with localized absorbers can be developed. Our top-down approach shows that the micro-block edge surfaces have a low recombination velocity ($s_0 \ll 4 \cdot 10^3 \text{ cm/s}$), comparable to that reported for twin grain boundaries [65]. Thus microcells with localized absorber do not have increased saturation current density due to the contribution of the edges. In fact no dark current signal proportional to the perimeter length of the microcells could be detected for devices down to 10^{-5} cm^2 . These microcells have good photovoltaic behavior: under concentrated illumination an open-circuit voltage above 817 mV at $\times 220$ was measured.

We look at a localized deposition method, electrodeposition. Co-deposition of CuInSe_2 on microelectrodes was performed. The influence of the microelectrode geometry on the deposit was studied. However this study is very preliminary and no working electrodeposited microcell was synthesized.

From an industrial point of view the localized microcell geometry can present several advantages. The low material consumption will reduce material costs in the cell, and lift material shortages threats on Cu(In,Ga)Se₂ technology [254]. Important efficiency increases under concentrated sunlight are expected, as already assessed by microcells with non-localized absorber and the top-down prototypes presented in this chapter. The possible economical relevance of a microcell concentrating module would have to be determined by further studies. The elaboration of a relatively low-cost deposition process that maintains good device performances is needed. The recent advances in solution-based Cu(In,Ga)Se₂ processes, such as electrodeposition and printing, prove that these techniques can lead to high efficiency for large areas devices [20], [26]. Even if these techniques have not reached record efficiencies yet, one advantage when working with concentrated illumination, is that lower performance devices have more important efficiency increase under concentration than their high performance counterparts [37], [124]. This fact may help solution-based processes to be competitive on microcell concentrating modules. Though, in order to have a commercial module, a concentrating optics has to be developed. This point was not tackled in this thesis. Given the size of our microcell devices, microlense arrays is an obvious solution [278–282]. Optical design has to be carried out to assess the optical efficiency of these optics, the concentration ratio that can be obtained as well as their sensitivity to misalignments and tracking precision. In conclusion, we can expect microcell concentrating modules to have a market application in the near future. The economic feasibility of such an application relies on whether the balance between higher efficiency and lower material consumption versus localized deposition process and complex optical system is positive or not.

5. Memento

Cu(In,Ga)Se₂ microcells with localized absorber have been created. These devices have a geometry closer to what would be needed for industrial applications, compared to the previous generation of prototypes.

A top-down approach by etching of co-evaporated absorber permits the fabrication of efficient proof-of concept devices. The edges of the microcells have low recombination velocity ($s_0 \ll 4 \cdot 10^3$ cm/s), allowing fabrication of devices as small as 10^{-5} cm² without measurable edge dark current. Open-circuit voltage above 817 mV at $\times 220$ concentration was measured on a 75 μ m diameter micro-block Cu(In,Ga)Se₂ solar cell.

Electrodeposition was studied as a localized deposition technique, in order to directly fabricate microcells with localized absorber by a bottom up approach. The CuInSe₂ ternary was deposited on microelectrodes. Influence of the microelectrode size on the electrodeposition regime was studied. No photovoltaic device was created by this technique yet.

GENERAL CONCLUSIONS AND PERSPECTIVES

Main results of this thesis

Within the course of this PhD thesis we studied the potential of concentrator thin film solar cells. The incentives to pursue this research are manifolds. In the first place, it is based on the assumption and belief that future photovoltaic technologies will rely on high throughput, large-surface-area processes. This requirement, which emanates from the necessity of terawatt development of photovoltaics in the coming decades, favors coating technologies such as thin films. Second, it proceeds from the need of highly efficient, material thrifty, photovoltaic technologies, which are best represented by the concentrating community. The material consumption of c-Si technology is indeed around 5g/W[2], that of standard thin films 0.1 g/Wp, when concentrated applications uses $5 \cdot 10^{-4}$ g/W. After the brief overview of the energy sector and different photovoltaic technologies given in Chapter I, the idea of coupling thin film technologies to the concentrating photovoltaic approach is only logical.

If the possibility of a concentrating thin film technology was only seldom studied before this thesis, it is because thin film solar cells in their standard large area architecture present excessive resistive losses that impede efficiency, when current densities are high. We have shown in Chapter III by analytical and numerical work that decreasing the area of the solar cell was a way of making the window layer resistive contribution negligible, without shadowing the solar cell. Precisely, the dimensionless factor controlling the scale effect is $\alpha = R_{\square} a^2 C J_{ph}(1 \text{ sun}) q / AkT$, where a^2 is the square of the solar cell radius, R_{\square} the window layer sheet resistance and C the concentration ratio. As a consequence, we showed that for solar cells with a window layer sheet resistance of 10 ohm/square, efficiency gains can be expected up to concentrations of $\times 100$ for solar cells smaller than 200 μm in diameter. If scaling down thin film solar cells is essential for controlling resistive losses, the miniaturization is also a substantial leverage to ease solar cells thermal management. By solving heat equations analytically, we could observe that the maximum temperature increase on a solar cell varies proportionally to the illumination source radius, at the first order. We also highlighted the role of the Mo layer thickness on its heat sink properties. In the case of a concentrating module, where solar cells are illuminated simultaneously, we found that the maximum local temperature increase compared to a flat plate is 45°C at $\times 1000$ for microcells of 100 μm diameter with a 1 μm thick Mo back contact. This value can be decreased by scaling down the solar

cells or thickening the back contact. These results show that microscale solar cells are an innovative design that overcomes classic obstacles of the concentrating community.

Given the incentives for miniaturizing solar cells, we fabricated Cu(In,Ga)Se₂ microcells in order to have an experimental proof of concept. If the miniaturization can impact several thin film technologies, we chose to focus on Cu(In,Ga)Se₂, since it is the efficiency record holder technology and because the scarcity of In makes it important for the Cu(In,Ga)Se₂ branch to develop In-thrifty designs. With help of photolithography we designed prototype Cu(In,Ga)Se₂ microcells with diameters varying between 7 and 500 μm. In the first prototype generation, described in Chapter IV, the Cu(In,Ga)Se₂ layer is co-evaporated on the whole substrate without subsequent patterning. The microcells are delineated by the insertion of a 300 nm thick insulating SiO₂ patterned layer between the intrinsic ZnO and Al-doped ZnO layers. The devices show good photovoltaic properties. The dark saturation currents are of the order of $J_{01} = 10^{-10}$ mA/cm² and $J_{02} = 10^{-5} - 10^{-4}$ mA/cm². These results are reproducible, which shows the good stability of the fabrication process. Devices of 7 μm of diameter were fabricated, which are the smallest Cu(In,Ga)Se₂ solar cells to date. At this scale only a few Cu(In,Ga)Se₂ grains are active, and discrete effect may happen. Due to the fact that the Cu(In,Ga)Se₂ layer was not patterned, the performance of the smallest devices (<5 × 10⁻⁵ cm²) is reduced. A statistical analysis of the device performance highlighted material inhomogeneities at the mm scale that are confirmed by cartographic measurements such as X-Ray fluorescence spectroscopy.

These microcells were then tested under concentrated illumination with both laser sources and sunlight, and the results presented in Chapter V. We assessed that for devices of 50 μm or smaller spreading resistance losses are negligible up to more than ×100. Due to this low resistive design, microcells present a significant efficiency increase under concentration with a record 21.3% conversion efficiency on a 50 μm device at ×475. These high efficiencies are due to improved open-circuit voltages that can reach up to 905 mV on a graded sample with 1.15 eV optical bandgap. These values of V_{oc} , optimum concentration ratio or absolute efficiency gain under concentration are records in the Cu(In,Ga)Se₂ community. From the $V_{oc} - J_{sc}$ curves we extracted the device temperature under illumination, and we found that the temperature elevation is proportional to the radius of the microcell to the power of 0.8. This result is close to theoretical predictions. Non-linear behavior may come from the role of convection that theoretically causes a deviation from linearity and/or from the fact that the temperature extracted from $V_{oc} - J_{sc}$ curves or PL analysis is an average of the temperature field over the whole device area. The spectrum of the concentrated light incident on the cell is found crucial in the analysis of the devices performance. The industrial samples

present a characteristic red-kink effect that results in a poor fill factor under red-illumination, contrary to the samples fabricated at IRDEP. The reason seems to be a better band alignment in the IRDEP sample due to adequate front bandgap grading.

We took advantage of the microcell geometry to study more in details the physics of Cu(In,Ga)Se₂ under high illumination intensities in Chapter VI. Series resistance is found to be decreasing under increasing incident power. This modulation is due to the photoconductivity of the Cu(In,Ga)Se₂ layer. From the form of the series resistance variation, we derived a characteristic diffusion length of 3 μm in our samples, which is in the high-end of published results, and corresponds to a high injection value. We found that the constant part of the series resistance, essentially due to contact resistances, was of the order of 1-2 10⁻³ ohm.cm², which is below reported values of the Cu(In,Ga)Se₂/MoSe₂/Mo contact resistance for example. We also evidenced that the collection efficiency of the Cu(In,Ga)Se₂ solar cell was a function of both voltage and light intensity. On the industrial samples, a strong decrease in the collection efficiency is measured under concentration, whereas this phenomenon is considerably less on homemade samples. In order to study those very high illumination regimes that are out of reach of common solar cell simulation software we built a finite element simulation code to solve self-consistently the continuity and Poisson's equations. We could simulate the electric field screening at a symmetric homojunction when the photogenerated carrier concentration is close to the junction doping level. This effect can explain the collection efficiency decrease in our devices, via an increase in recombination paths, either in the bulk or at the interface. Thus the importance of careful interface engineering, via appropriate bandgap gradients, correct band alignments and efficient passivation, is highlighted.

In the Chapter VII of this thesis we looked more closely to the possible industrial application of a thin film concentrator microcell. In a first part we fabricated and tested micro-blocks solar cells. This second generation of prototypes is created by etching the Cu(In,Ga)Se₂ layer after co-evaporation, in order to have microcell devices with localized absorbers. These devices have good performance and confirm the low impact of edge recombination of Cu(In,Ga)Se₂ solar cells. We evaluated that the edge surface recombination velocity is less than 4 10³ cm/s, as we did not detect an edge dark current signal for devices as small as 10⁻⁵ cm². High open-circuit voltages are measured on micro-block devices and we reached 817 mV at ×220 on a 75 μm microcell. As micro-blocks solar cells performance is not hindered by edge effects and because the succession of co-evaporation and etching steps is cumbersome in the perspective of industrial application, we began the creation of a third generation of prototypes: electrodeposited microcells. Electrodeposition is a solution-based coating process by which a conductive substrate is covered by a deposit under an applied bias. This

technique is intrinsically localized, and microdeposits were fabricated. In the microelectrode configuration, edge effects are significant due to a spherical diffusion field, which provides a high amount of material to the microelectrode perimeter. We could assess the formation of a CuInSe_2 phase on the microelectrodes that can be well crystallized. However our study is preliminary and solar cells have still poor photovoltaic performances.

Perspectives

As often in scientific research, this thesis explored different options, but the work ahead is very substantial. From these three years of research, several options emerge as the most promising perspectives.

Before being a possible new architecture of commercial solar cells, thin film microcells are an auspicious design as research and development tool. With dense arrays of microcells of various sizes it should be possible to study the effect of material inhomogeneities on electric performances of the solar cell, a study we have only begun in this thesis due to a millimeter-spaced pattern. This study could be very helpful to understand how microscale inhomogeneities impact parameters such as shunt resistance or open-circuit voltage. Microcells are also an opportunity to study specific pixels on large scale solar cells with both optical (PL, EQE, Raman ...) and electrical (EL, IV, C-V) characterization techniques. Coupling these approaches at a small scale would make it possible to determine which material parameters are leading to the highest efficiencies. Finally with the microcell design we accessed for the first time the very high illumination regime on Cu(In,Ga)Se_2 solar cells, without detrimental resistive losses. We initiated studies on this physical regime, but there is still much work ahead. In particular we showed that physical parameters such as diffusion lengths could be extracted from the photoconductive behavior of Cu(In,Ga)Se_2 . A more detailed analysis of the photoconductivity signal, associated with light-beam induced current measurements for example, would be needed to determine the extent and applicability of this characterization technique. We have also evidenced electric field screening effects, which increase the weight of interface recombination on devices performance. Hence, high illumination current-voltage characteristics could be a helpful complement to low temperature measurements to characterize the Cu(In,Ga)Se_2 /buffer heterointerface, and its impact on complete devices.

Aside from these applications as a research and development characterization tool, thin film microscale concentrator solar cells may play a role in industrial applications. Like each concentrating application, Cu(In,Ga)Se_2 concentrator microcells consume a very low amount of material. Namely,

12.8 grams of $\text{Cu}_1\text{In}_{0.6}\text{Ga}_{0.4}\text{Se}_2$ are needed to cover 1m^2 panel with $2.5\ \mu\text{m}$ thickness, among which 21.6% of Indium (in mass). As a consequence if we consider a microcell module under a concentration of $\times 100$, with an absorber thickness of $2.5\ \mu\text{m}$ and an efficiency of 24% (a 4% absolute efficiency increase from the current AM1.5 record efficiency), the indium consumption can be estimated as low as 115 kg/GW. Thus restraints to the up-scaling of $\text{Cu}(\text{In,Ga})\text{Se}_2$ capacity regarding material availability can be alleviated. Selective processes appear as the most promising absorber deposition techniques. Even if much progress has been made in the past years, these techniques are still lagging behind state-of-the-art devices in terms of efficiency. As the concentration efficiency gains are more important on poorly performing devices, either shunted or with higher dark currents, concentration could be a way for these techniques to bridge the efficiency gap. The development of robust localized deposition processes will be a short term challenge for thin film microcells. From a balance of system cost perspective, the possibility of a viable thin film micro-concentrator technology is dependent on the development of appropriate concentrating and tracking systems. If there are a lot of studies on micro-optics, and their replication on large-areas, the concentration system adapted to microcells is an aspect that we did not tackle in this thesis. Miniaturization, which brought advances in terms of resistive and thermal management of the thin film solar cell, may as well impact the optical system with more compact designs, and lighter modules. Tracking could also be impacted, as proposed by [283], with tracking implemented at the module level by the translation of the solar cells array, instead of the motion of the whole panel.

As a conclusion this thesis was an opportunity to initiate studies on microscale thin film solar cells, and the coupling with concentrated illumination. Promising results were found in terms of conversion efficiency and the low concentration as well as high concentration ranges are now open for thin films. Mesa-delineated solar cells showed that miniaturization is not hindered by edge recombination, and direct deposition of CuInSe_2 on microelectrodes was performed. Microscale solar cells are thus an auspicious design for thin films. In the future, would micro-structuring processes more largely impact photovoltaic technologies as they have transformed electronics?

RESUME EN FRANCAIS

Introduction

L'effet photovoltaïque a été découvert en 1839 par Alexandre Edmond Becquerel. Depuis ce travail avant-gardiste, le domaine de connaissances lié au photovoltaïque s'est fortement étendu et de nombreuses applications pratiques ont vues le jour. Si l'idée d'utiliser l'énergie solaire pour fournir de l'énergie en grande quantité n'est pas nouvelle, "Nous sommes comme des fermiers abatant la clôture autour de notre maison pour disposer de carburant alors que nous devrions être en train d'utiliser les sources naturelles inépuisables d'énergie - le soleil, le vent et la marée. ... J'investirais mon argent sur le soleil et l'énergie solaire. Quelle source d'énergie! J'espère que nous n'aurons pas à attendre que le pétrole et le charbon s'épuisent pour nous y mettre » (Thomas Edison, 1931), aucune application à grande échelle n'a fait son apparition jusqu'à la fin du XXe siècle. Par contre, de 2000 à 2010, le taux de croissance de l'industrie photovoltaïque a atteint 40% [2]. En 2011, la puissance installée cumulée s'élevait à près de 70 GW [3], [4]. Dans certains pays, le photovoltaïque est devenu au cours des dernières années une source à grande échelle de production d'électricité. Actuellement en Allemagne, par exemple, plus de 10% de la consommation quotidienne d'électricité est fournie par l'énergie photovoltaïque les jours ensoleillés.

Les panneaux solaires actuels atteignent des rendements record de 33% [5]. Les technologies de revêtement telles que les films minces permettent des rendements élevés et de faibles coûts de fabrication. Les défis auxquels la communauté scientifique est dorénavant confrontée sont ceux du développement du photovoltaïque à l'échelle du térawatt, tant du point de vue de la disponibilité des matières premières que des moyens de productions, dans un monde où les ressources aussi bien naturelles que financières sont limitées et où la concurrence avec les sources d'énergie fossiles bon marché est rude. Cette thèse étudie la possibilité de coupler deux domaines du photovoltaïque afin de relever ces défis: les couches minces et le photovoltaïque à concentration. Les couches minces permettent une fabrication facile et des flux de production élevés, tandis que le photovoltaïque à concentration est peu consommateur de matière première et permet d'atteindre des haut rendements. Cet axe de recherche n'a pas été exploré en détails jusqu'à présent, en raison des limites résistives dans les cellules solaires en couches minces. L'originalité de ce travail réside dans la conception d'une architecture innovante de cellule solaire. Afin de construire des prototypes, nous nous sommes concentrés sur le composé $\text{Cu}(\text{In,Ga})\text{Se}_2$. Cependant, les conclusions du travail sont générales et peuvent s'appliquer à d'autres familles de matériaux. Cette thèse est organisée en sept chapitres. Dans le chapitre I, nous replaçons l'étude dans le

contexte général des défis énergétiques actuels et expliquons nos motivations pour associer couches minces et concentration lumineuse. Dans le chapitre II, la physique des cellules solaires en général, et celle des cellules Cu(In,Ga)Se_2 en particulier, est décrite. Dans le chapitre III, les effets des échelles qui régissent les sources de résistance et la gestion thermique des cellules solaires en couches minces sous concentration sont étudiés. Des simulations numériques étayent la compréhension des phénomènes en jeu. Grâce aux lignes directrices mises en évidence dans le chapitre III, le processus de fabrication d'un prototype de microcellules Cu(In,Ga)Se_2 et les propriétés de base des dispositifs photovoltaïques sont décrits dans le chapitre IV. Dans le chapitre V, les prototypes sont testés sous un flux lumineux concentré et l'influence du spectre incident est analysée. Dans le chapitre VI la physique des dispositifs Cu(In,Ga)Se_2 sous forte concentration est étudiée, et une attention particulière est attirée sur les caractéristiques spécifiques de ce régime de forte concentration. Enfin, au chapitre VII, les perspectives sur d'éventuelles applications industrielles sont décrites et la possibilité de dépôts localisés est abordée.

Nous présentons ici un résumé des résultats marquants du travail, l'ensemble des éléments pouvant être trouvés dans la version anglaise du manuscrit.

Panorama des technologies photovoltaïques et motivation de l'étude

Le défi énergétique actuel est multiforme. Une forte augmentation de la demande énergétique est prévue dans les années à venir. La consommation mondiale pourrait passer de 140 000 TWh en 2009 à 200 000 TWh en 2030 [1]. En plus de fournir cette énergie supplémentaire nous devons veiller à lutter contre le changement climatique. En ce sens, la moitié des nouvelles sources d'énergie développées dans le monde d'ici 2035 seront renouvelables [2]. C'est dans ce contexte que le photovoltaïque, qui permet la conversion directe de l'énergie lumineuse en énergie électrique, a un rôle à jouer.

La ressource solaire est gigantesque. A la surface de la Terre, nous recevons une puissance moyenne de 198 W.m^{-2} . Au total nous recevons du soleil chaque année une énergie 6400 fois plus importante que celle que nous consommons [3]. En comparaison des énergies fossiles, dont les ressources représentent entre 50 et 150 ans de consommation, le photovoltaïque a une ressource abondante et renouvelable. Ce domaine a d'ailleurs connu un très fort développement depuis le début du XXIème siècle. La capacité totale connectée au réseau à la fin 2011 s'élevait à 70 GWc [4], et un pays comme l'Allemagne est aujourd'hui capable de produire 14% de son électricité à partir de photovoltaïque les

jours ensoleillés[5]. Le principal challenge du photovoltaïque est la capacité à se développer rapidement à très grande échelle, pour pouvoir répondre aux défis énergétiques de façon globale. Pour cela les technologies doivent avoir des flux de production élevés, une empreinte écologique faible, notamment une consommation limitée en matière première, de façon à se prémunir de problèmes de disponibilité de certains éléments. Les rendements doivent être élevés pour économiser les matières premières, l'empreinte au sol et baisser les prix.

Le développement du photovoltaïque est porté par une multitude de filières (Figure I-4 gauche). A côté de la filière silicium qui représentait 85% du marché en 2010 [6], ce développent deux filières intéressantes pour notre étude. La filière couche minces (Cu(In,Ga)Se_2 , CdTe ou silicium amorphe) et le photovoltaïque à concentration. Les couches minces ont permis d'atteindre de très bas cout de production (0.75\$/W en 2011 sur CdTe [7]) , d'important flux de production, tout en atteignant des rendements rivalisant avec la filière silicium (20.3% de rendement sur cellule de laboratoire en Cu(In,Ga)Se_2 [8]). Néanmoins dans les années à venir la production pourrait être limitée par la disponibilité des matières premières, si l'architecture des cellules n'est pas modifiée [9]. Le photovoltaïque à concentration, qui permet des rendements record, est basé sur une géométrie où un système optique concentre la lumière solaire incidente sur une cellule solaire, reliée si besoin à un dissipateur thermique (Figure 1 droite).

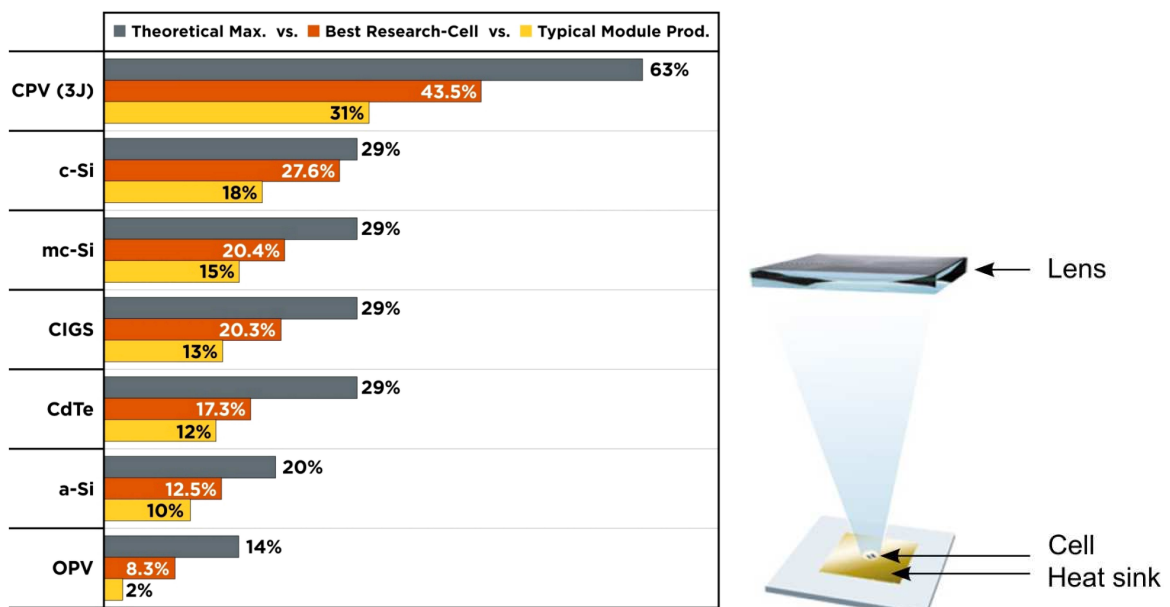


Figure 1 : (gauche) Technologies photovoltaïques, leur rendement maximum, les performances des cellules de laboratoire, et valeur typique de rendement de cellules commerciales. CPV (3J) est l'acronyme de photovoltaïque à concentration à base de cellules triple jonction. c-Si signifie silicium cristallin, mc- Si silicium multicristallin, CIGS se réfère aux composés de la famille Cu(In,Ga)Se_2 , a-Si silicium amorphe et OPV photovoltaïque organique. [10] (droite) Photovoltaïque à concentration, schéma de principe. : une lentille concentre la lumière sur une petite cellule

photovoltaïque. La cellule est relié à un dissipateur thermique pour favoriser son refroidissement. (Extrait du site web de Soitec).

L'idée de coupler les approches couches minces et concentration découle du besoin de hautes performances, d'économie de matériau et de facilité de fabrication. Une concentration optique de $\times 50$, tout à fait réalisable en pratique, permet un gain de matière première bien plus important que celui offert par les approches d'affinage [11]. L'idée d'utiliser la concentration sur des couches minces avait été évoquée à la fin des années 90, pour de très faibles niveaux de concentration ($\times 1 - \times 20$). Les contraintes thermiques et résistives sur des cellules en couches mince classiques ne permettent pas l'utilisation de lumière plus intense, et les avantages de ces systèmes étaient limités, ce qui a conduit à l'arrêt de ces recherches au début des années 2000. Notre approche est de développer une nouvelle architecture de cellule en couches minces, adaptée au fonctionnement sous flux lumineux intense, d'un point de vue résistif et thermique.

Physique des cellules solaires à base de Cu(In,Ga)Se_2

Nous nous concentrons dans cette thèse sur la filière Cu(In,Ga)Se_2 , et nous faisons ici très une brève revue des propriétés physiques de ce type de cellule photovoltaïque.

Les cellules Cu(In,Ga)Se_2 sont composées d'un empilement de couches minces sur un substrat de verre ou de métal : Mo (contact arrière) / Cu(In,Ga)Se_2 (absorbeur) / CdS (couche tampon et partenaire de l'hétérojonction) / ZnO (contact avant) / Mg F_2 (antireflet) (Figure II-1 gauche). Le semiconducteur Cu(In,Ga)Se_2 peut être synthétisé par une multitude de techniques. Celle qui donne les meilleures performances est la coévaporation qui forme un composé multi-cristallin dont les grains sont de l'ordre du micron [8]. Elle est réalisée dans une enceinte sous-vide à partir de quatre cellules à effusion : Cu, In, Ga et Se. Les flux de ces éléments sont variés durant le dépôt (Figure 2 droite), pour donner des gradients de composition qui résultent en des gradients de bande interdite. Le Cu(In,Ga)Se_2 a un très fort coefficient d'absorption, supérieur à 10^4 cm^{-1} dans tout le visible.

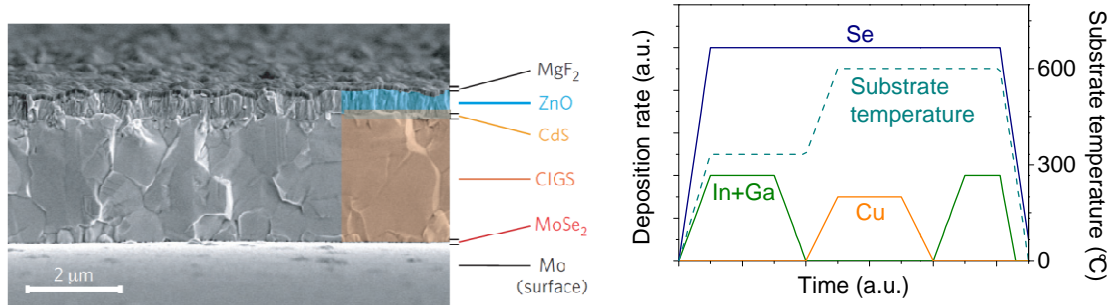


Figure 2: (gauche) Vue en coupe d'une cellule Cu(In,Ga)Se₂ coévaporée au microscope électronique à balayage. Image extraite de la référence [12]. (droite) Schéma d'un procédé trois étapes.

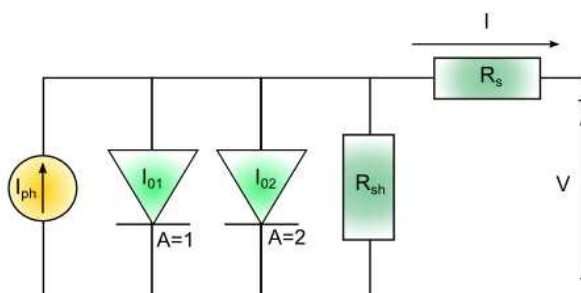


Figure 3 : Circuit équivalent d'un modèle à deux diodes avec facteurs d'idéalité fixés A=1 et A=2. Les résistances parasites série et parallèle sont représentées.

Le comportement d'une cellule solaire est décrit de manière générale par une courbe courant-tension. Dans cette thèse nous choisissons la description dite à deux diodes (Figure 3), et le courant d'une cellule solaire J_{light} à une tension V s'écrit :

$$\begin{aligned}
 J_{light}(V) = & J_{ph,max} \times \eta(V) - J_{01} \left(\exp \left(\frac{q(V + J_{light}R_s)}{kT} \right) - 1 \right) \\
 & - J_{02} \left(\exp \left(\frac{q(V + J_{light}R_s)}{2kT} \right) - 1 \right) - \frac{(V + J_{light}R_s)}{R_{sh}}
 \end{aligned} \tag{1}$$

où $J_{ph,max}$ est le photocourant maximum qui peut être collecté, $\eta(V)$ le facteur de collecte, R_s la résistance série, R_{sh} la résistance parallèle, J_{01} et J_{02} les densités de courant de saturation des diodes d'idéalité respectives 1 et 2.

Le photocourant est proportionnel au flux lumineux incident. Si l'intensité lumineuse est multipliée par un facteur C , on dit qu'on utilise une concentration de C , aussi notée $\times C$. La tension de circuit ouvert est dépendante du facteur de concentration :

$$V_{oc} = \frac{2kT}{q} \ln \left(\frac{-J_{02} + \sqrt{J_{02}^2 + 4J_{01}C \times J_{ph,1sun}}}{2J_{01}} \right) \quad (2)$$

Ainsi, la tension de circuit ouvert augmente avec le logarithme du facteur de concentration. En conséquence, le rendement de conversion de la cellule, ratio de la puissance maximale fournie par la cellule et de la puissance lumineuse incidente, augmente avec la concentration, et ceci tant que les effets résistifs et thermiques peuvent être négligés.

Quelques travaux ont essayé de tirer parti de cette augmentation de rendement sous concentration pour des cellules $\text{Cu}(\text{In,Ga})\text{Se}_2$. Une augmentation de la tension de circuit ouvert est observable et les rendements augmentent jusqu'à une concentration lumineuse entre $\times 10$ et $\times 14$ (Figure II-14). Malheureusement les rendements saturent ensuite à cause de la température trop importante atteinte sur ces cellules, ainsi que de problèmes de résistance.

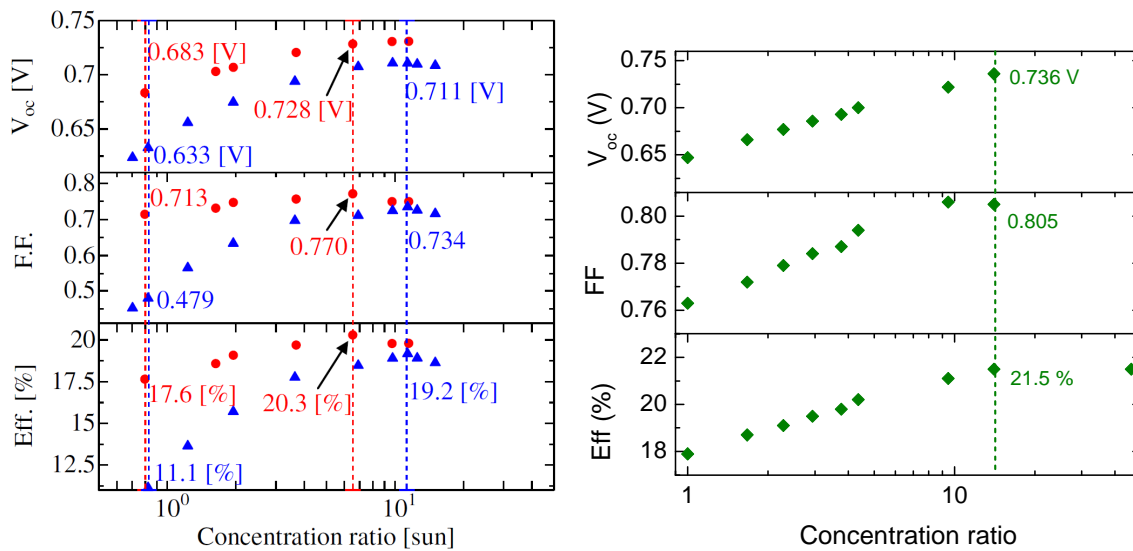


Figure 4 : (gauche) Evolution de la tension de circuit ouvert, du rendement et du facteur de forme avec la concentration de cellules solaires $\text{Cu}(\text{In,Ga})\text{Se}_2$ de plus ou moins fortes performances . Tiré de la référence [13]. (droite) Evolution de la tension de circuit ouvert, du rendement et du facteur de forme avec la concentration de la cellule solaire record $\text{Cu}(\text{In,Ga})\text{Se}_2$ (0.1 cm²). Données extraites de la référence [14].

Effets d'échelle sur les cellules solaires en couches minces

Nous nous intéressons au rôle porté par la taille des dispositifs électroniques sur leurs propriétés électriques et thermiques. En effet, dans le domaine des diodes électroluminescentes, proche physiquement de celui du photovoltaïque [15], la diminution de la taille des dispositifs a entraîné des gains dans la gestion thermique mais aussi dans la répartition des densités de courant [16–18].

D'un point de vue électrique, la résistivité de la couche fenêtre des cellules en couches minces provoque une chute de potentiel à la surface de la cellule solaire. Ainsi le potentiel à la surface de la cellule varie avec la position. Dans le cas d'une géométrie cylindrique, le potentiel $\psi(r)$ est régi par l'équation :

$$\frac{\partial^2 \psi}{\partial r^2} + \frac{1}{r} \frac{\partial \psi}{\partial r} + R_{\square} \left(J_{ph} - J_0 \left(\exp \left(\frac{q\psi}{AkT} \right) - 1 \right) - \frac{\psi}{R_{sh}} \right) = 0 \quad (3)$$

Une analyse dimensionnelle a montré que le facteur adimensionnel principal de ce problème est $\alpha = R_{\square} a^2 C J_{ph} (1 \text{ sun}) q / AkT$. Ainsi la réduction de la taille des cellules, de rayon a , peut compenser une augmentation de la concentration lumineuse C , ou de la résistance répartie de la couche fenêtre R_{\square} .

En résolvant l'équation (3), nous pouvons prédire le comportement de cellules solaires en fonction de leur taille et de la concentration lumineuse. La miniaturisation semble permettre de forts gains de rendement, en permettant de rendre la contribution résistive de la couche fenêtre négligeable (Figure 5).

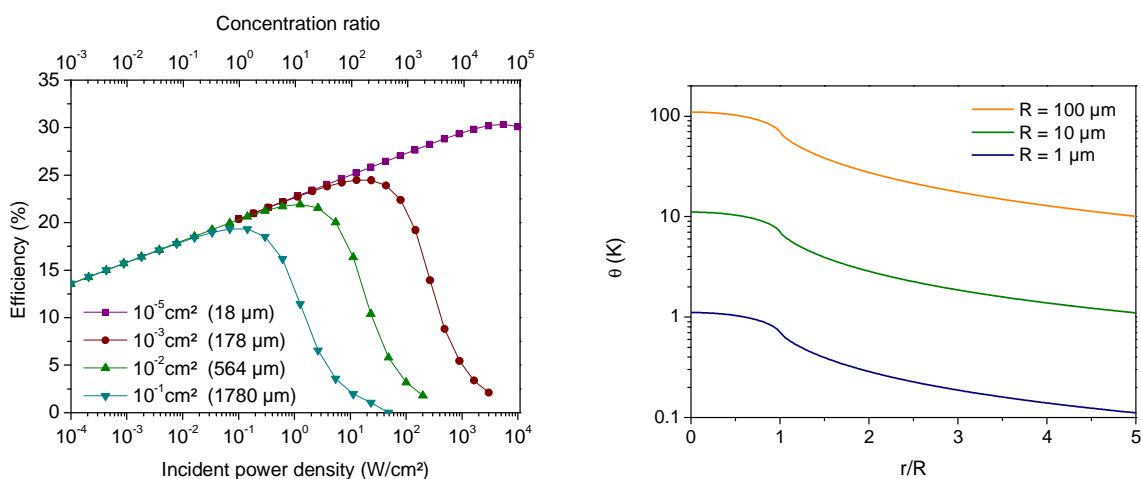


Figure 5 : Rendement vs. (gauche) densité de puissance incidente pour quatre cellules de rayon 1780 μm (10⁻¹ cm²), 564 μm (10⁻² cm²), 178 μm (10⁻³ cm²), 18 μm (10⁻⁵ cm²) dans une géométrie de contact central. (droite) Elévation de température à la surface d'un milieu semi-infini pour des sources d'échauffement de différents rayons (1 μm -10 μm -100 μm) en fonction de la variable adimensionnelle r/R.

Nous regardons également le rôle de la taille du dispositif sur la température atteinte par la cellule solaire. Dans le cas simple, où la cellule est considérée comme un milieu uniforme semi-infini de conductivité thermique k_{th} chauffé localement avec une densité de puissance Q , l'élévation de température atteinte au centre de la zone chauffée de rayon R est :

$$\theta(0,0) = \frac{QR}{k_{th}} \quad (0-4)$$

Le maximum d'élévation de température est donc proportionnel au rayon de l'éclairement.

Un comportement très similaire est trouvé lorsqu'on considère un empilement de couches minces sur un substrat, avec de la convection en face avant et arrière. La réduction de taille des cellules devrait donc permettre un fonctionnement des cellules sous concentration sans refroidissement actif.

La fabrication et la caractérisation de microcellules Cu(In,Ga)Se₂

Nous avons fabriqué des microcellules Cu(In,Ga)Se₂ à partir des procédés de dépôt de couches minces et de procédés de photolithographie UV, selon le schéma de la Figure 6. Les cellules ont des rayons variant de 5 à 500 μm.

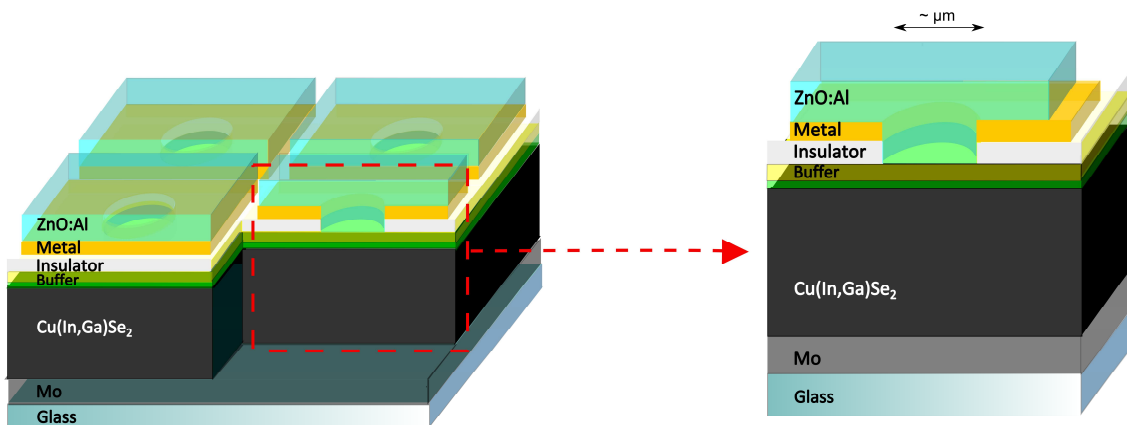


Figure 6 : Schéma de la coupe d'une microcellule solaire Cu(In,Ga)Se₂.

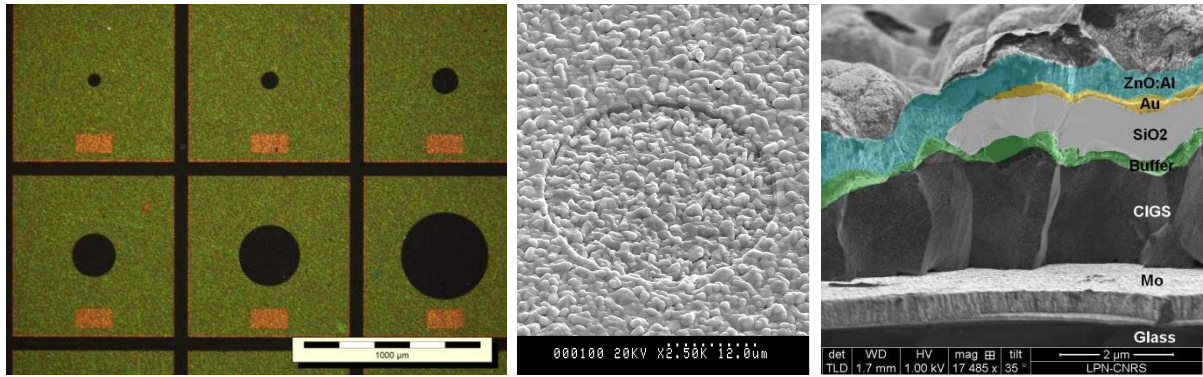


Figure 7 : (gauche) Image au microscope optique d'un échantillon à la fin du procédé de fabrication. (milieu) Image au microscope électronique à balayage. (droite) Image en coupe colorisée au microscope électronique à balayage du bord d'une micro-cellule.

Les cellules solaires sont ensuite testées électriquement au noir et sous éclairage. Nous trouvons que le procédé de microcellules permet de fabriquer des dispositifs ayant de bonnes caractéristiques photovoltaïques. Les densités de courant de saturation au noir sont de l'ordre de $J_{01} = 10^{-10}$ mA/cm² et $J_{02} = 10^{-5} - 10^{-4}$ mA/cm².

Le procédé de fabrication donne des résultats reproductibles. Les tensions de circuit-ouvert sont stables jusqu'à des tailles de $5 \cdot 10^{-5}$ cm², ensuite elles chutent, ce qui est notamment causé par l'influence croissante sur les petits dispositifs des courant de fuite sur le méso (Figure 8).

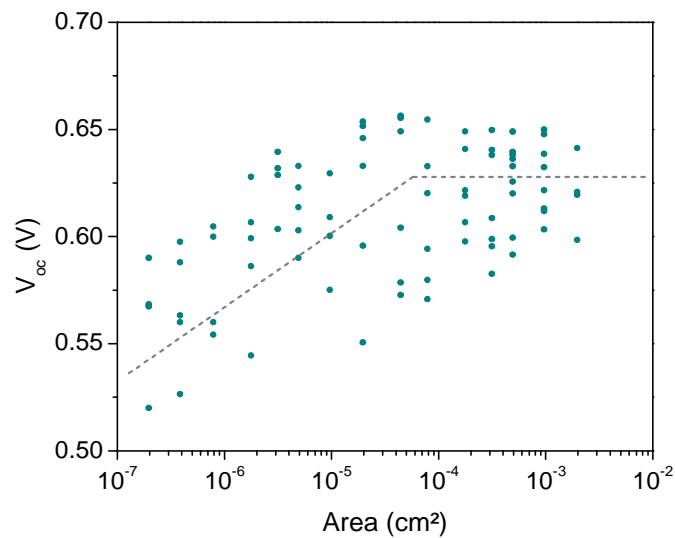


Figure 8 : V_{oc} en fonction de la taille de la microcellule. La ligne pointillée est tracée pour favoriser la visualisation du seuil à $5 \cdot 10^{-5}$ cm².

Une analyse statistique des résultats est possible grâce au grand nombre de cellules fabriquées sur un même substrat. Les inhomogénéités de composition à l'échelle du millimètre, mesurables par des techniques de cartographie, sont ici mises en évidence.

Caractérisation de microcellule sous flux lumineux intense

Nous testons les microcellules sous des flux lumineux intenses. Nous utilisons des lasers (532 nm – 644 nm – 1062 nm) ou de la lumière solaire. Nous observons une augmentation de la tension de circuit ouvert avec la puissance incidente, qui correspond à la loi théorique. Nous avons mesuré un V_{oc} de 905 mV. En conséquence une augmentation des rendements de conversion se produit. Un rendement équivalent record de 21.3% sous un flux de $\times 475$ a été mesuré, alors que le rendement était de 16% sous $\times 1$.

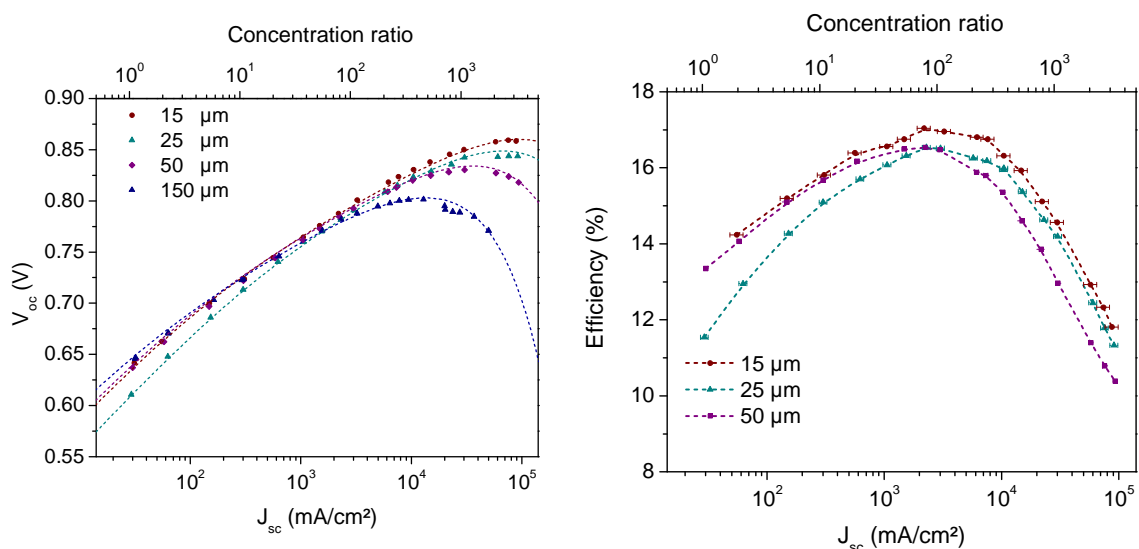


Figure 9: (gauche) Tension de circuit ouvert en fonction de la densité de courant de court-circuit pour quatre cellules de différent diamètres. (droite) Rendement en fonction de la densité de courant de court-circuit pour trois cellules. Tests à 532 nm.

Nous observons une diminution de la pente de V_{oc} - J_{sc} puis une diminution du V_{oc} sous très fort flux. Ceci peut être attribué à l'augmentation de la température du dispositif. Nous voyons que cet effet est d'autant plus fort que la cellule est grande (Figure 9 gauche) et nous en déduisons donc une loi d'échelle (Figure 10 gauche) . Le facteur κ régissant l'augmentation de température en fonction du flux suit une loi $r^{0.8}$, proche de la linéarité décrite au chapitre III.

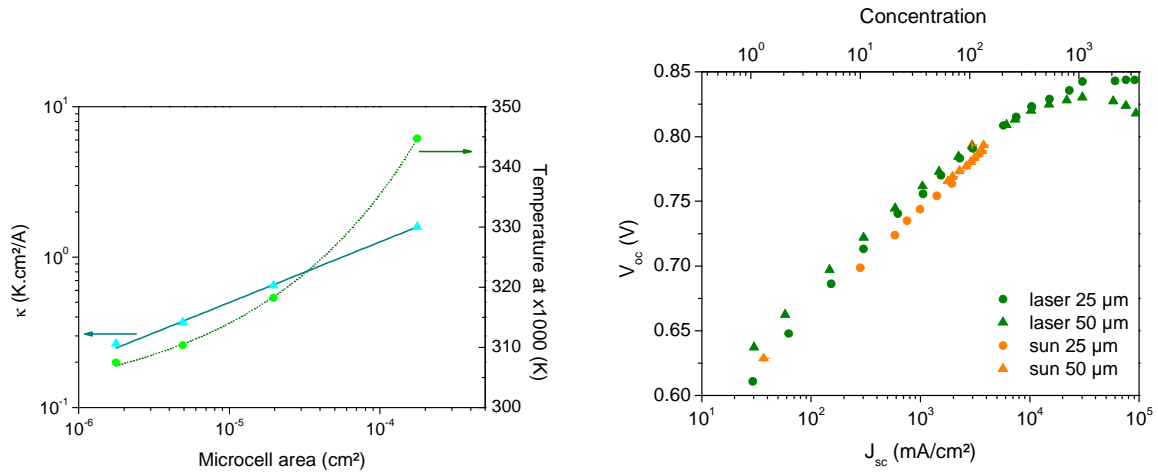


Figure 10 : (gauche) κ et élévation de température à $\times 1000$ en fonction de l'aire de la microcellule. (droite) Tension de ouvert en fonction de la densité de courant de court-circuit pour des illuminations laser ou lumière naturelle.

Lors de ces caractérisations nous nous sommes servis en grande partie de lasers. Pour les cellules solaires en général, et les cellules $\text{Cu}(\text{In,Ga})\text{Se}_2$, la longueur d'onde de la lumière incidente peut avoir des conséquences importantes sur la réponse physique de la cellule. Nous avons observé sur certains échantillons le phénomène dit de « red-kink » [19]. Soumise à une lumière rouge, les cellules $\text{Cu}(\text{In,Ga})\text{Se}_2$ présentent une barrière secondaire qui diminue la collecte. Celle-ci a été attribuée à l'interface $\text{Cu}(\text{In,Ga})\text{Se}_2/\text{CdS}$. Suivant que l'illumination contient ou non de la lumière de courte longueur d'onde, le CdS, matériau très fortement compensé, présente un taux de dopage effectif plus ou moins élevé, ce qui impacte le diagramme de bande de la cellule. Cet effet n'a pas été observé dans toutes les cellules testées. Celles qui présentent un gradient de composition à l'interface, et donc présentent une grande bande interdite en face avant, ne sont pas touchées. Nous supposons que l'absence de l'effet « red-kink » est dû à la disparition de la barrière secondaire, grâce à un meilleur alignement des bandes. Cet alignement de bande a pu être montré dans la littérature pour des cellules $\text{Cu}(\text{In,Ga})\text{Se}_2$ de très haut rendement, présentant des gradients de composition similaires [12].

Nous avons donc voulu savoir si les caractérisations lasers effectués aux courtes longueurs d'ondes (532 nm) pouvaient être représentatives. Nous avons effectué des tests sous lumière solaire sur le site du PROMES à Odeillo. Il en ressort que les résultats sont très proches, ce qui valide nos tests lasers à 532 nm (Figure 10 droite).

Analyse et modélisation de la physique des microcellules Cu(In,Ga)Se₂ sous forte concentration, optimization

Nos mesures de microcellules Cu(In,Ga)Se₂ sous concentration nous ont permis de mettre à jour des phénomènes physiques nouveaux.

Nous avons tout d'abord observé une diminution de la résistance série sous fort flux (Figure 11). Nous attribuons cela à un photodopage des couches semiconductrices de la cellule. De la forme de la variation nous pouvons donner une estimation grossière de la longueur de diffusion, environ 3 μm dans les échantillons que nous avons étudiés.

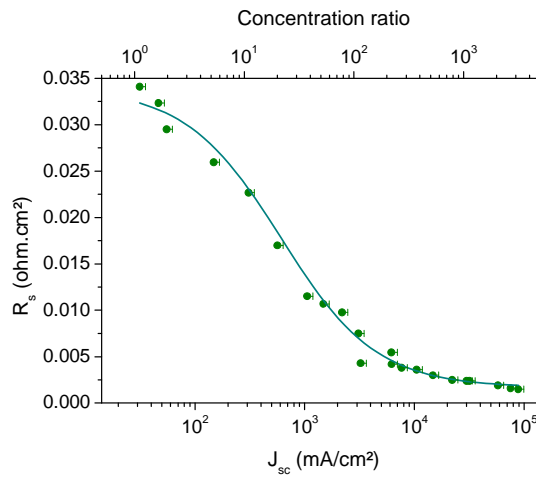


Figure 11 : Résistance série en fonction de la densité de courant de court-circuit.

Nous observons également une baisse du facteur de collecte lorsque la densité de puissance lumineuse augmente, sur certains échantillons (Figure 11). Nous avons mis au point un code d'éléments finis, pour simuler une homojonction sous flux lumineux variable (

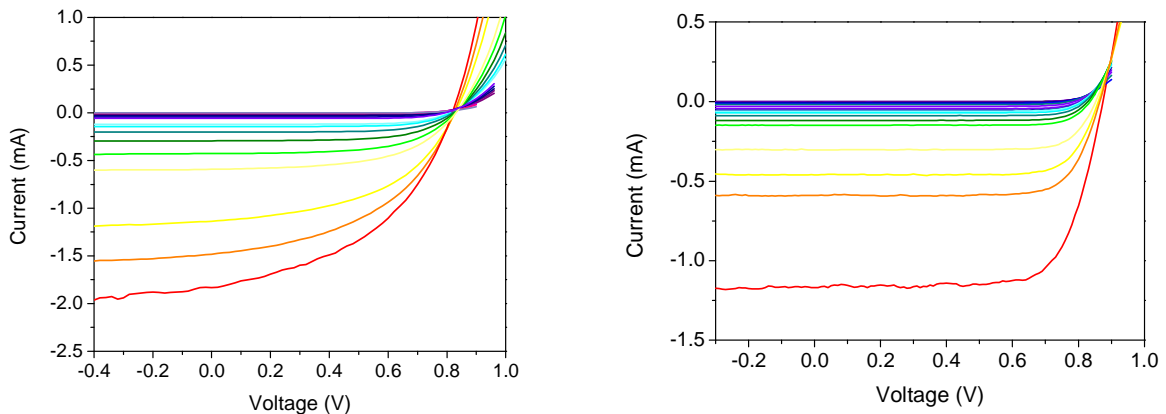


Figure 12). Nous mettons en évidence un écrantage du champ électrique de la jonction. Dans une cellule Cu(In,Ga)Se₂, système plus complexe, ceci pourrait avoir diverses conséquences. En particulier la baisse du champ à l'hétérointerface Cu(In,Ga)Se₂/CdS peut favoriser les recombinaisons. Suivant que l'interface présente plus ou moins de défauts, l'effet de l'écrantage du champ électrique sur la collecte se fait plus ou moins sentir, expliquant les variations entre échantillons observées sur la Figure VI-6.

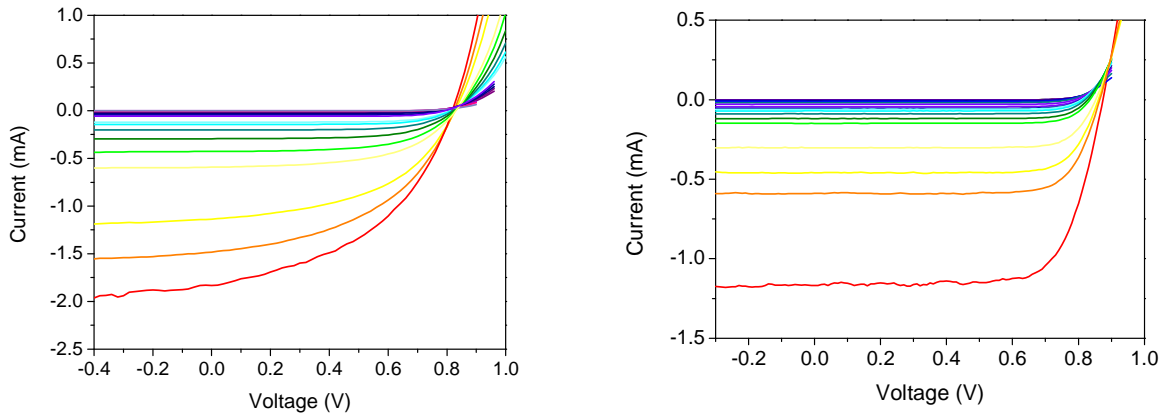


Figure 12 : Courbes courant-tension mesurées sur une microcellules de 50 μm de diamètre sous lumière laser 532 nm dont la densité de puissance est augmentée progressivement. (gauche) échantillon industriel (droite) échantillon IRDEP.

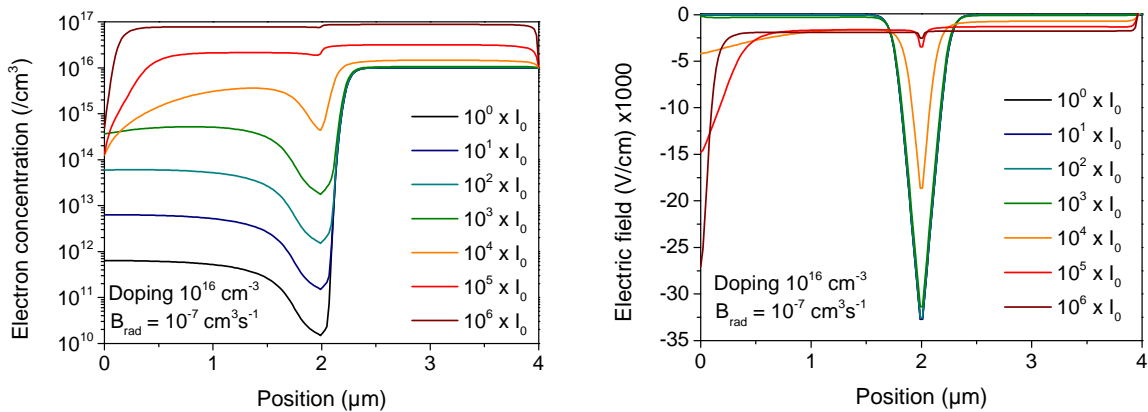


Figure 13 : Simulation numérique d'une homojonction entre deux semi-conducteurs p et n de dopage 10^{16} cm^{-3} avec un coefficient de recombinaison b de $10^{-7} \text{ cm}^3 \text{ s}^{-1}$ pour une tension appliquée nulle sous diverses intensité d'illumination (gauche) Concentration d'électrons en fonction de la position dans la jonction. (droite) Champ électrique en fonction de la position.

Nous avons également observé une saturation de la tension de circuit ouvert sous flux très intense. Ce phénomène a déjà été reporté sur des diodes électroluminescentes. La saturation du V_{oc} à une valeur plus faible que celle de la tension de diffusion, serait le signe de l'effet Dember. Des

RESUME EN FRANCAIS

paramètres physiques tels que la mobilité des porteurs pourraient être étudiés dans ce régime de saturation du V_{oc} .

Vers l'application industrielle : des microcellules à absorbeur localisé

Notre étude nous a poussé jusqu'à utiliser des échantillons, dont la fabrication ne pourrait pas être transférée directement à l'échelle industrielle. En effet garder l'absorbeur sur toute la surface de l'échantillon ne permet pas d'économie de matière première. Nous regardons dans ce dernier chapitre la possibilité de fabriquer des échantillons à absorbeur localisé.

Nous commençons par des échantillons obtenus par gravure de l'absorbeur pour voir si les flancs du dispositif ne sont pas sources de défauts. Nous utilisons une gravure physique par IBE, et une gravure chimique en solution bromée. L'approche chimique donne de meilleurs résultats.

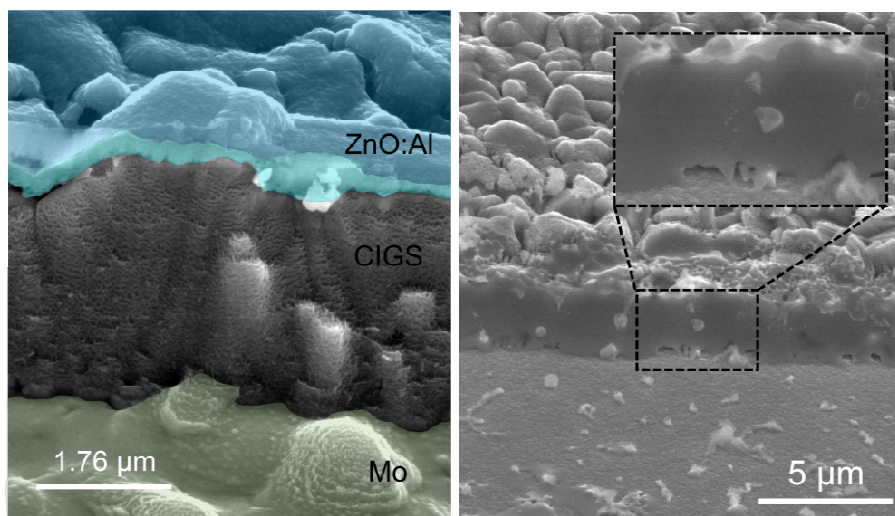


Figure 14 : (gauche) Image MEB colorisée d'une microcellule solaire $\text{Cu}(\text{In,Ga})\text{Se}_2$ à absorbeur localisé, après gravure IBE. On voit une structure sur les flancs de gravure. (droite) Image MEB colorisée d'une microcellule solaire $\text{Cu}(\text{In,Ga})\text{Se}_2$ à absorbeur localisé, après gravure chimique, où le ZnO a été suffisamment sous-gravé pour rendre visible le $\text{Cu}(\text{In,Ga})\text{Se}_2$. L'insert montre le flanc lisse de gravure.

Electriquement, les échantillons gravés chimiquement ont des caractéristiques stables jusqu'à des tailles de 10^{-5} cm^2 . Ceci montre que les flancs de gravure n'ont que très peu d'influence sur les caractéristiques électriques. Nous pouvons estimer que la vitesse de recombinaison en surface est inférieure à $4 \cdot 10^3 \text{ cm/s}$, ce qui vient confirmer les résultats des études des vitesses de recombinaison aux joints de grains.

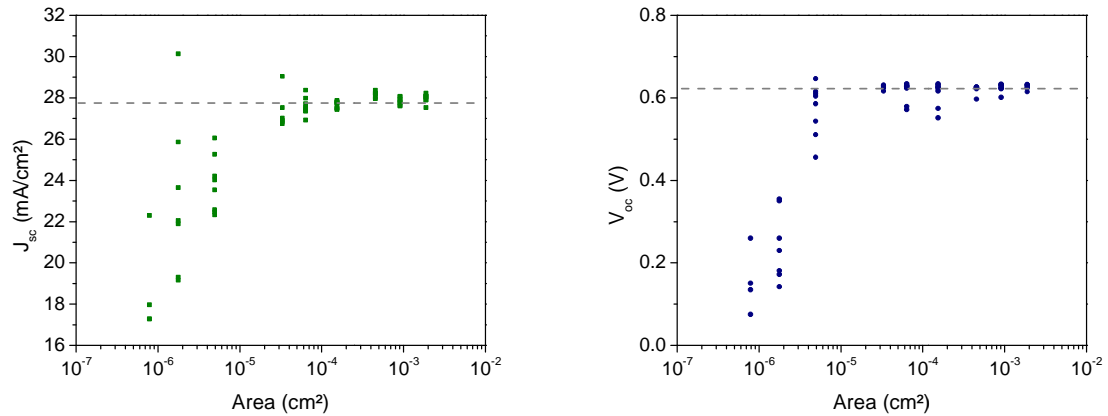


Figure 15 : (gauche) Densité de courant de court-circuit en fonction de la taille des microcellules, à absorbeur localisé fabriquées par gravure chimique, sous flux AM1.5. (right) Tension de circuit ouvert en fonction de la taille des microcellules . Pour les deux graphiques, nous avons pris en compte une sous-gravure de 5 μm . Les lignes pointillées représentent les moyennes sur les dispositifs de taille supérieure à 10^{-5} cm^2 .

Afin d'envisager des procédés plus réalistes industriellement que l'enchaînement dépôt/gravure, nous regardons les méthodes de dépôts sélectifs. Parmi elles nous choisissons de faire de premiers essais en électrodépôts, méthode reconnue du dépôt de cellules $\text{Cu}(\text{In,Ga})\text{Se}_2$ [20].

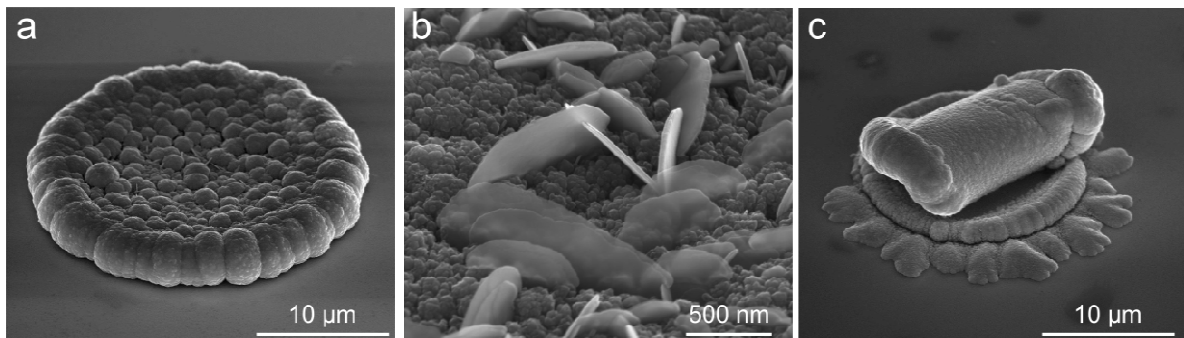


Figure 16 : (a) Image MEB d'échantillons électrodépôts avant recuit. (b) Des binaires sont visibles sur la surface sous forme de plaquettes. (c) Nous observons un problème d'adhérence des dépôts à cause de contraintes mécaniques lors du dépôt.

Nous arrivons à déposer du CuInSe_2 sur des microélectrodes. Nous voyons une influence de la taille des dépôts sur leur morphologie. En effet pour les plus petites microélectrodes le régime de diffusion est en trois dimensions. C'est aussi le cas sur les bords de grands échantillons. Pour le centre des grands échantillons la diffusion est seulement 2D. Ainsi les bords et les petites microélectrodes ont des densités de courant plus fortes, ce qui augmente la vitesse de dépôt. Ceci peut poser des problèmes de contraintes mécaniques lors du dépôt et provoquer une perte d'adhérence. Pour l'instant aucun rendement photovoltaïque n'a été mesuré sur ce type de d'échantillons.

Conclusions générales, perspectives de l'étude

Ce travail a permis de mieux cerner les possibilités offertes par l'usage de la concentration sur les cellules en couches minces. Plusieurs voies sont encore à explorer, et certaines options paraissent les plus prometteuses.

Avant d'être une architecture avantageuse de cellules solaires, les microcellules sont un outil de recherche et développement très intéressant. Avec des réseaux denses de microcellules solaires les inhomogénéités des matériaux et leur influence sur les caractéristiques des cellules solaires pourraient être étudiées. On pourrait également coupler des études optiques (PL, EQE, Raman ...) et électriques (EL, IV, C-V) sur des pixels fixés, et déterminer ce qui caractérise à l'échelle micrométrique les meilleurs rendements de conversion. Enfin les microcellules, qui supportent de forts flux lumineux sans dommage, sont un outil essentiel de l'étude de la forte injection. Nous avons commencé à aborder la physique des cellules $\text{Cu}(\text{In,Ga})\text{Se}_2$ sous fort flux mais beaucoup reste à éclaircir et consolider, pour comprendre, entre autre, le rôle de l'interface $\text{Cu}(\text{In,Ga})\text{Se}_2/\text{CdS}$

En parallèle de ces études amont, une application industrielle des microcellules semble possible. Comme toute application sous concentration, la consommation de matière première est réduite. 12.8 grammes de $\text{Cu}_1\text{In}_{0.6}\text{Ga}_{0.4}\text{Se}_2$ sont nécessaires pour couvrir un mètre carré de panneau avec une épaisseur de 2.5 μm , dont 21.6% massiques d'indium. Si on considère une application à une concentration de $\times 100$, et un absorbeur de 2.5 μm d'épais avec des cellules de 24% de rendement, la consommation d'indium peut être réduite à 115 kg/GW. Les contraintes au développement à grande échelle de la filière $\text{Cu}(\text{In,Ga})\text{Se}_2$, et CdTe, peuvent être ainsi surmontées.

Les méthodes de dépôt sélectives apparaissent comme les plus prometteuses pour la fabrication de microcellules en couches minces. Ces méthodes sont actuellement un peu en retrait au niveau des rendements de conversion, malgré de grands progrès. Comme les gains de rendement en concentration sont les plus forts sur les dispositifs les moins efficaces (faibles résistances parallèles ou courant noirs), la concentration pourrait leur permettre de rattraper une partie de leur retard. Le développement de méthodes de dépôt localisées adaptées aux microcellules est un challenge à court terme. D'un point de vue économique la viabilité de la filière dépendra des performances des méthodes de dépôts et des systèmes de concentration, et éventuellement de suivi du soleil. Ces aspects n'ont pas été abordés dans cette thèse, mais une optique dédiée aux microcellules doit être mise au point. Des gains de matière première sur les optiques peuvent être envisagés avec la miniaturisation des cellules.

Cette thèse aura été l'occasion de démarrer les études sur les microcellules solaires en couches minces et le couplage avec la concentration. Des résultats prometteurs en termes de rendement de conversion ont été trouvés, et l'étude la concentration sur ces cellules est maintenant ouverte sur une grande gamme d'intensités lumineuses. Les cellules à absorbeur localisé nous permettent de dire que les surfaces périphériques ne sont pas un problème pour la miniaturisation. Les microcellules solaires sont donc une architecture prometteuse pour les couches minces. Dans le futur, est-ce que les techniques de micro-structuration utilisés ici pourraient impacter plus largement le photovoltaïque comme elles ont déjà transformé l'électronique ?

BIBLIOGRAPHY

- [1] A. E. Becquerel, "Mémoire sur les effets électriques produits sous l'influence des rayons solaires," *Comptes Rendus de L'Academie des Sciences*, vol. 9, pp. 561–567, 1839.
- [2] JRC Scientific and Technical reports, "PV status report 2011." 2011.
- [3] IEA, "Renewable energy technologies, Solar Energy Perspectives." 2012.
- [4] EPIA, "Global market outlook for photovoltaics until 2016." 2012.
- [5] Semprius Press release, "Semprius sets world record for solar module efficiency," http://www.semprius.com/pdf/press_releases/press_release_19.pdf. 2012.
- [6] S. G. Benka, "Special Issue The Energy Challenge," *Physics Today*, vol. 55, no. 4, p. 38, 2002.
- [7] IEA, "World Energy Outlook 2011, Executive summary." 2011.
- [8] IEA, "Key world energy Statistics." 2009.
- [9] IEA, "IEA Energy Technology Essentials, Nuclear Power." 2007.
- [10] Newsletter of the International Energy Agency Solar Heating and Cooling Programme, "the world's energy reserves, a fundamental look." 2009.
- [11] PV magazine, "Germany : Record 40 percent solar weekend." 2012.
- [12] EPIA, "Solar photovoltaics competing in the energy sector, on the road to competitiveness." 2011.
- [13] K. Branker, M. J. M. Pathak, and J. M. Pearce, "A review of solar photovoltaic levelized cost of electricity," *Renewable and Sustainable Energy Reviews*, 2011.
- [14] E. Yang, "Reconsidering solar grid parity," *Energy Policy*, vol. 38, pp. 3270–3273, 2010.
- [15] C. A. Wolden, J. Kurtin, J. B. Baxter, I. Repins, S. E. Shaheen, J. T. Torvik, A. A. Rockett, V. M. Fthenakis, and E. S. Aydil, "Photovoltaic manufacturing: Present status, future prospects, and research needs," *J. Vac. Sci. Technol. A*, vol. 29, no. 3, p. 030801, 2011.
- [16] V. Fthenakis, "Sustainability of photovoltaics: The case for thin-film solar cells," *Renewable and Sustainable Energy Reviews*, vol. 13, no. 9, pp. 2746–2750, 2009.
- [17] V. Fthenakis and H. C. Kim, "Land use and electricity generation: A life-cycle analysis," *Renewable and Sustainable Energy Reviews*, vol. 13, no. 6–7, pp. 1465–1474, 2009.
- [18] SunShot US Department of Energy, "Photovoltaics: Technologies, Cost, and Performance," in *SunShot Vision Study*, vol. 4, 2012.
- [19] A. Chirilă, S. Buecheler, F. Pianezzi, P. Bloesch, C. Gretener, A. R. Uhl, C. Fella, L. Kranz, J. Perrenoud, S. Seyrling, R. Verma, S. Nishiwaki, Y. E. Romanyuk, G. Bilger, and A. N. Tiwari, "Highly efficient Cu(In,Ga)Se₂ solar cells grown on flexible polymer films," *Nat Mater*, vol. 10, no. 11, pp. 857–861, 2011.

BIBLIOGRAPHY

- [20] SoloPower Press release, "SoloPower sets record for flexible CIGS solar panel efficiency," <http://solopower.com/2012/03/solopower-sets-record-for-flexible-cigs-solar-panel-efficiency/>. 2012.
- [21] Greentech Solar, "Thin Film Manufacturing in the Sub-Dollar-Per-Watt Market: Part II," <http://www.greentechmedia.com/articles/read/thin-film-manufacturing-in-a-sub-dollar-the-watt-market-ii/>. .
- [22] M. A. Green, K. Emery, Y. Hishikawa, W. Warta, and E. D. Dunlop, "Solar cell efficiency tables (version 39)," *Progress in Photovoltaics: Research and Applications*, vol. 20, no. 1, pp. 12–20, 2012.
- [23] First Solar Press Release, "First Solar Sets World Record for CdTe Solar PV Efficiency." 2011.
- [24] First Solar, "Annual Report," http://files.shareholder.com/downloads/FSLR/1912986479x0x559533/4bf0e522-1f34-489c-921d-6c77bf43de01/Final_11_Annual_Report.pdf. 2011.
- [25] P. Jackson, D. Hariskos, E. Lotter, S. Paetel, R. Wuerz, R. Menner, W. Wischmann, and M. Powalla, "New world record efficiency for Cu(In,Ga)Se₂ thin-film solar cells beyond 20%," *Prog. Photovolt: Res. Appl.*, vol. 19, pp. 894–897, 2011.
- [26] Nanosolar Press release, "Nanosolar Secures \$20 Million in New Funds," <http://www.nanosolar.com/company/blog>. 2012.
- [27] T. K. Todorov, K. B. Reuter, and D. B. Mitzi, "High-Efficiency Solar Cell with Earth-Abundant Liquid-Processed Absorber," *Adv. Mater.*, vol. 22, no. 20, pp. E156–E159, 2010.
- [28] A. Luque, *Handbook of photovoltaic science and engineering*. John Wiley and Sons, 2003.
- [29] Anton, I. and G. Sala, "The EUCLIDES Concentrator," in *Concentrator Photovoltaics*, vol. 130, Springer-Verlag Berlin Heidelberg, 2007, pp. 279–299.
- [30] A. W. Bett and Lerchenmüller, H., "The FLATCON System from Concentrix Solar," in *Concentrator Photovoltaics*, vol. 130, Springer-Verlag Berlin Heidelberg, 2007, pp. 301–319.
- [31] A. Feltrin and A. Freundlich, "Material considerations for terawatt level deployment of photovoltaics," *Renewable Energy*, vol. 33, no. 2, pp. 180–185, 2008.
- [32] Z. Jehl Li Kao, N. Naghavi, F. Erfurth, J. F. Guillemoles, I. Gérard, A. Etcheberry, J. L. Pelouard, S. Collin, G. Voorwinden, and D. Lincot, "Towards ultrathin copper indium gallium diselenide solar cells: proof of concept study by chemical etching and gold back contact engineering," *Progress in Photovoltaics: Research and Applications*, p. n/a–n/a, 2012.
- [33] A. Gupta, V. Parikh, and A. D. Compaan, "High efficiency ultra-thin sputtered CdTe solar cells," *Solar Energy Materials and Solar Cells*, vol. 90, no. 15, pp. 2263–2271, Sep. 2006.
- [34] B. Furman, E. Menard, A. Gray, M. Meitl, S. Bonafede, D. Kneeburg, K. Ghosal, R. Bukovnik, W. Wagner, J. Gabriel, S. Seel, and S. Burroughs, "A high concentration photovoltaic module utilizing micro-transfer printing and surface mount technology," in *Proceedings of the 35th IEEE Photovoltaic Specialists Conference (PVSC)*, 2010, pp. 000475–000480.
- [35] C. Algora, I. Rey-Stolle, B. Galiana, J. R. Gonzalez, M. Baudrit, and I. Garcia, "Strategic options for a led-like approach in III-V concentrator photovoltaics," in *Conference Record of the 2006 IEEE 4th World Conference on Photovoltaic Energy Conversion, Vols 1 and 2*, New York, 2006, pp. 741–744.

- [36] J. S. Ward, K. Ramanathan, F. S. Hasoon, T. J. Coutts, J. Keane, M. A. Contreras, T. Moriarty, and R. Noufi, "A 21.5% efficient Cu(In,Ga)Se₂ thin-film concentrator solar cell," *Prog. Photovolt: Res. Appl.*, vol. 10, no. 1, pp. 41–46, 2002.
- [37] J. R. Tuttle, "The Performance of Cu(In,Ga)Se₂-Based Solar Cells in Conventional and Concentrator Applications," in *Material Research Society Proceedings*, San Francisco, CA, USA, 1996, vol. 426, pp. 143–151.
- [38] J. Wennerberg, J. Kessler, J. Hedstrom, L. Stolt, B. Karlsson, and M. Ronnelid, "Thin film PV modules for low-concentrating systems," *Solar Energy*, vol. 69, no. 1–6, pp. 243–255, 2000.
- [39] J. L. Shay, S. Wagner, and H. M. Kasper, "Efficient CuInSe₂/CdS solar cells," *Applied Physics Letters*, vol. 27, no. 2, p. 89, 1975.
- [40] F. Pianezzi, A. Chirilă, P. Blösch, S. Seyrling, S. Buecheler, L. Kranz, C. Fella, and A. N. Tiwari, "Electronic properties of Cu(In,Ga)Se₂ solar cells on stainless steel foils without diffusion barrier," *Progress in Photovoltaics: Research and Applications*, p. n/a–n/a, 2012.
- [41] G. Gordillo, M. Grizález, and L. C. Hernandez, "Structural and electrical properties of DC sputtered molybdenum films," *Solar Energy Materials and Solar Cells*, vol. 51, no. 3–4, pp. 327–337, 1998.
- [42] J. H. Yoon, K. H. Yoon, W. M. Kim, J. K. Park, Y. J. Baik, T. Y. Seong, and J. Jeong, "High-temperature stability of molybdenum (Mo) back contacts for CIGS solar cells: a route towards more robust back contacts," *Journal of Physics D: Applied Physics*, vol. 44, p. 425302, 2011.
- [43] P. Salomé, J. Malaquias, P. Fernandes, and A. F. Cunha, "Mo bilayer for thin film photovoltaics revisited," *Journal of Physics D: Applied Physics*, vol. 43, p. 345501, 2010.
- [44] K. Orgassa, H. W. Schock, and J. H. Werner, "Alternative back contact materials for thin film Cu (In, Ga) Se₂ solar cells," *Thin Solid Films*, vol. 431, pp. 387–391, 2003.
- [45] T. Nakada, Y. Hirabayashi, T. Tokado, D. Ohmori, and T. Mise, "Novel device structure for Cu(In,Ga)Se₂ thin film solar cells using transparent conducting oxide back and front contacts," *Solar Energy*, vol. 77, no. 6, pp. 739–747, 2004.
- [46] L. Assmann, J. C. Bernède, A. Drici, C. Amory, E. Halgand, and M. Morsli, "Study of the Mo thin films and Mo/CIGS interface properties," *Applied Surface Science*, vol. 246, no. 1–3, pp. 159–166, 2005.
- [47] X. Zhu, Z. Zhou, Y. Wang, L. Zhang, A. Li, and F. Huang, "Determining factor of MoSe₂ formation in Cu(In,Ga)Se₂ solar Cells," *Solar Energy Materials and Solar Cells*, vol. 101, pp. 57–61, 2012.
- [48] T. Wada, N. Kohara, T. Negami, and M. Nishitani, "Chemical and Structural Characterization of Cu(In,Ga)Se₂/Mo Interface in Cu(In,Ga)Se₂ Solar Cells," *Jpn. J. Appl. Phys.*, vol. 35, no. 10A, p. L1253, 1996.
- [49] P. Bommersbach, L. Arzel, M. Tomassini, E. Gautron, C. Leyder, M. Urien, D. Dupuy, and N. Barreau, "Influence of Mo back contact porosity on co-evaporated Cu(In,Ga)Se₂ thin film properties and related solar cell," *Progress in Photovoltaics: Research and Applications*, p. n/a–n/a, 2011.

BIBLIOGRAPHY

- [50] L. Kronik, D. Cahen, and H. W. Schock, "Effects of Sodium on Polycrystalline Cu(In,Ga)Se₂ and Its Solar Cell Performance," *Adv. Mater.*, vol. 10, no. 1, pp. 31–36, 1998.
- [51] R. Scheer and H. W. Schock, *Chalcogenide Photovoltaics : Physics, Technologies, and Thin Film Devices*. Weinheim, Germany: Wiley-VCH Verlag & Co, 2011.
- [52] A. O. Pudov, "Impact of secondary barrier on CuInGaSe₂ solar cell operation," Colorado State University, Fort Collins, Colorado, 2005.
- [53] M. A. Contreras, L. M. Mansfield, B. Egaas, J. Li, M. Romero, R. Noufi, E. Rudiger-Voigt, and W. Mannstadt, "Wide bandgap Cu(In,Ga)Se₂ solar cells with improved energy conversion efficiency," *Prog. Photovolt: Res. Appl.*, p. n/a, 2012.
- [54] T. Dullweber, U. Rau, M. A. Contreras, R. Noufi, and H.-W. Schock, "Photogeneration and carrier recombination in graded gap Cu(In, Ga)Se₂ solar cells," *Electron Devices, IEEE Transactions on DOI - 10.1109/16.887004*, vol. 47, no. 12, pp. 2249–2254, 2000.
- [55] I. Repins, M. A. Contreras, B. Egaas, C. DeHart, J. Scharf, C. L. Perkins, B. To, and R. Noufi, "19.9% efficient ZnO/CdS/CuInGaSe₂ solar cell with 81.2% fill factor," *Prog. Photovolt: Res. Appl.*, vol. 16, no. 3, pp. 235–239, 2008.
- [56] M. Igalson and P. Zabierowski, "Electron traps in Cu(In, Ga)Se₂ absorbers of thin film solar cells studied by junction capacitance techniques," *Opto-Electronics Review*, no. 4, pp. 261–268, 2003.
- [57] S. B. Zhang, S. H. Wei, A. Zunger, and H. Katayama-Yoshida, "Defect physics of the CuInSe₂ chalcopyrite semiconductor," *Physical Review B*, vol. 57, no. 16, pp. 9642–9656, 1998.
- [58] J. Pettersson, C. Platzer-Björkman, U. Zimmermann, and M. Edoff, "Baseline model of graded-absorber Cu(In,Ga)Se₂ solar cells applied to cells with Zn(1-x)MgxO buffer layers," *Thin Solid Films*, vol. 519, no. 21, pp. 7476–7480, 2011.
- [59] Z. Djebbour, A. Darga, A. Migan Dubois, D. Mencaraglia, N. Naghavi, J. F. Guillemoles, and D. Lincot, "Admittance spectroscopy of cadmium free CIGS solar cells heterointerfaces," *Thin solid films*, vol. 511, pp. 320–324, 2006.
- [60] Z. Djebbour, A. M. Dubois, A. Darga, D. Mencaraglia, C. Bazin, J. P. Connolly, J. F. Guillemoles, D. Lincot, B. Canava, and A. Etcheberry, "Comparison of optical and electrical gap of electrodeposited CuIn(S,Se)₂ determined by spectral photo response and I–V–T measurements," *Thin solid films*, vol. 515, no. 15, pp. 6233–6237, 2007.
- [61] J. Serhan, Z. Djebbour, D. Mencaraglia, F. Couzinié-Devy, N. Barreau, and J. Kessler, "Influence of Ga content on defects in CuIn_xGa_{1-x}Se₂ based solar cell absorbers investigated by sub gap modulated photocurrent and admittance spectroscopy," *Thin Solid Films*, vol. 519, no. 21, pp. 7312–7316, Aug. 2011.
- [62] M. Gloeckler, "Device physics of Cu(In,Ga)Se₂ thin film solar cells," PhD dissertation, Colorado State University, Fort Collins, Colorado, 2005.
- [63] D. Abou-Ras, S. Schorr, and H. W. Schock, "Grain-size distributions and grain boundaries of chalcopyrite-type thin films," *Journal of Applied Crystallography*, vol. 40, no. 5, pp. 841–848, 2007.

- [64] H. Du, I. Shih, and C. H. Champness, "Monocrystalline CuInSe₂ photovoltaic cell of superior performance," *Journal of Vacuum Science & Technology A: Vacuum, Surfaces, and Films*, vol. 22, no. 3, pp. 1023–1026, 2004.
- [65] D. Abou-Ras, C. T. Koch, V. Küstner, P. A. van Aken, U. Jahn, M. A. Contreras, R. Caballero, C. A. Kaufmann, R. Scheer, T. Unold, and H.-W. Schock, "Grain-boundary types in chalcopyrite-type thin films and their correlations with film texture and electrical properties," *Thin Solid Films*, vol. 517, no. 7, pp. 2545–2549, 2009.
- [66] M. Gloeckler, J. R. Sites, and W. K. Metzger, "Grain-boundary recombination in Cu(In,Ga)Se₂ solar cells," *Journal of Applied Physics*, vol. 98, no. 11, 2005.
- [67] U. Rau, K. Taretto, and S. Siebentritt, "Grain boundaries in Cu(In, Ga)(Se, S)₂ thin-film solar cells," *Applied Physics A: Materials Science & Processing*, vol. 96, no. 1, pp. 221–234, Jul. 2009.
- [68] M. Nichterwitz, D. Abou-Ras, K. Sakurai, J. Bundesmann, T. Unold, R. Scheer, and H. W. Schock, "Influence of grain boundaries on current collection in Cu(In,Ga)Se₂ thin-film solar cells," *Thin Solid Films*, vol. 517, no. 7, pp. 2554–2557, 2009.
- [69] A. Rockett, "Surface analysis of chalcopyrite materials for photovoltaics," *Progress in Photovoltaics: Research and Applications*, p. n/a–n/a, 2012.
- [70] D. Cahen and R. Noufi, "Defect chemical explanation for the effect of air anneal on CdS/CuInSe₂ solar cell performance," *Applied Physics Letters*, vol. 54, no. 6, p. 558, 1989.
- [71] U. Rau, D. Braunger, R. Herberholz, H. W. Schock, J.-F. Guillemoles, L. Kronik, and D. Cahen, "Oxygenation and air-annealing effects on the electronic properties of Cu(In,Ga)Se₂ films and devices," *J. Appl. Phys.*, vol. 86, no. 1, pp. 497–505, 1999.
- [72] M. J. Hetzer, Y. M. Strzhemechny, M. Gao, M. A. Contreras, A. Zunger, and L. J. Brillson, "Direct observation of copper depletion and potential changes at copper indium gallium diselenide grain boundaries," *Applied Physics Letters*, vol. 86, no. 16, 2005.
- [73] A. M. Gabor, J. R. Tuttle, D. S. Albin, M. A. Contreras, R. Noufi, and A. M. Hermann, "High-efficiency CuIn_xGa_{1-x}Se₂ solar cells made from (In_xGa_{1-x})₂Se₃ precursor films," *Applied Physics Letters*, vol. 65, no. 2, p. 198, 1994.
- [74] R. A. Mickelsen and W. S. Chen, "High photocurrent polycrystalline thin-film CdS/CuInSe₂ solar cell," *Applied Physics Letters*, vol. 36, no. 5, p. 371, 1980.
- [75] G. Voorwinden, R. Kniese, and M. Powalla, "In-line Cu(In,Ga)Se₂ co-evaporation processes with graded band gaps on large substrates," *Thin Solid Films*, vol. 431–432, no. 0, pp. 538–542, 2003.
- [76] S. Niki, M. Contreras, I. Repins, M. Powalla, K. Kushiya, S. Ishizuka, and K. Matsubara, "CIGS absorbers and processes," *Progress in Photovoltaics: Research and Applications*, vol. 18, no. 6, pp. 453–466, 2010.
- [77] E. Wallin, T. Jarmar, U. Malm, M. Edoff, and L. Stolt, "Influence of the average Se-to-metal overpressure during co-evaporation of Cu(In_xGa_{1-x})Se₂," *Thin Solid Films*, vol. 519, no. 21, pp. 7237–7240, 2011.

BIBLIOGRAPHY

- [78] A. M. Gabor, J. R. Tuttle, M. H. Bode, A. Franz, A. L. Tennant, M. A. Contreras, R. Noufi, D. G. Jensen, and A. M. Hermann, "Band-gap engineering in Cu (In, Ga) Se₂ thin films grown from (In, Ga) 2Se₃ precursors," *Solar energy materials and solar cells*, vol. 41, pp. 247–260, 1996.
- [79] S. M. Schleussner, T. Törndahl, M. Linnarsson, U. Zimmermann, T. Wätjen, and M. Edoff, "Development of gallium gradients in three-stage Cu(In,Ga)Se₂ co-evaporation processes," *Progress in Photovoltaics: Research and Applications*, vol. 20, no. 3, pp. 284–293, 2012.
- [80] C. J. Hibberd, E. Chassaing, W. Liu, D. B. Mitzi, D. Lincot, and A. N. Tiwari, "Non-vacuum methods for formation of Cu(In, Ga)(Se, S)₂ thin film photovoltaic absorbers," *Progress in Photovoltaics: Research and Applications*, vol. 18, no. 6, pp. 434–452, 2010.
- [81] T. K. Todorov, O. Gunawan, T. Gokmen, and D. B. Mitzi, "Solution-processed Cu(In,Ga)(S,Se)₂ absorber yielding a 15.2% efficient solar cell," *Progress in Photovoltaics: Research and Applications*, p. n/a–n/a, 2012.
- [82] EMPA, "Record efficiency of 18.7% for flexible CIGS solar cells on plastics," http://www.empa.ch/plugin/template/empa/3/107447/---/l=2/changeLang=true/lartid=107447/orga=/type=/theme=/bestellbar=/new_abt=/uacc=. 2011.
- [83] Press release Q-Cells SE, "CIGS thin-film technology reaches world-record efficiency of 17.4%," <http://www.q-cells.com/en/press/article//CIGS-thin-film-technology-reaches-world-record-efficiency-of-174.html>. 2011.
- [84] Press release Q-Cells SE, "Q-Cells achieves with 13.4% new efficiency world record for CIGS thin film solar module out of mass production," <http://www.q-cells.com/en/press/article//Q-Cells-achieves-with-134-new-efficiency-world-record-for-CIGS-thin-film-solar-module-out-of-mass.html>. 2011.
- [85] E. Wallin, U. Malm, T. Jarmar, O. L. M. Edoff, and L. Stolt, "World-record Cu(In,Ga)Se₂-based thin-film sub-module with 17.4% efficiency," *Progress in Photovoltaics: Research and Applications*, p. n/a–n/a, May 2012.
- [86] Manz Press Release, "Manz plans to acquire CIGS modules innovation line from Würth Solar." 2011.
- [87] V. Bermudez, "Développements industriels du CIGS électrodéposé," presented at the Journées nationales du photovoltaïque, Dourdan, France, 2011.
- [88] B. Basol, "Commercialization of High Efficiency Low Cost CIGS Technology Based on Electroplating, Final Technical Progress Report," National Renewable Energy Laboratory, 2009.
- [89] Avancis GmbH & Co. KG,, "PowerMax Strong Datasheet," http://www.avancis.de/fileadmin/media/portal/produkt/Data_sheet_PowerMax_STRONG_2012_03_EN.pdf. 2012.
- [90] Avancis Press Release, "World record in efficiency: AVANCIS again achieves best value for thin-film modules," <http://www.avancis.de/en/press/press-releases/view/meldung/wirkungsgrad-weltrekord-avancis-erzielt-erneut-bestwert-fuer-duennschichtmodule/>. 2011.
- [91] D. Lu, B. Sang, Y. Deng, B. J. Stanbery, and L. Eldada, "Copper Indium Gallium Selenide photovoltaic modules manufactured by reactive transfer," in *Proceedings of the 35th IEEE Photovoltaic Specialists Conference*, Honolulu, HI, 2010, pp. 000175–000178.

- [92] MiaSolé, "MiaSolé Achieves 15.7% Efficiency with Commercial-Scale CIGS Thin Film Solar Modules," http://www.miasole.com/sites/default/files/MiaSole_release_Dec_02_2010.pdf. 2010.
- [93] Solar Frontier, "Solar Frontier Sets New Efficiency World Record," <http://www.solar-frontier.com/news/179>. 2012.
- [94] A. Neisser, "Manufacturing of Large-Area Cu(In,Ga)Se₂ Solar Modules Fast Ramp Up to More than 12% Module Efficiency in Mass Production – Road Map to 14%," presented at the European Photovoltaic Solar Energy Conference and Exhibition, Hambourg, 2011.
- [95] D. Lincot and R. O. Borges, "Chemical Bath Deposition of Cadmium Sulfide Thin Films. In Situ Growth and Structural Studies by Combined Quartz Crystal Microbalance and Electrochemical Impedance Techniques," *Journal of The Electrochemical Society*, vol. 139, no. 7, pp. 1880–1889, 1992.
- [96] R. Ortega-Borges and D. Lincot, "Mechanism of Chemical Bath Deposition of Cadmium Sulfide Thin Films in the Ammonia-Thiourea System," *Journal of The Electrochemical Society*, vol. 140, no. 12, pp. 3464–3473, 1993.
- [97] K. Orgassa, U. Rau, Q. Nguyen, H. W. Schock, and J. H. Werner, "Role of the CdS buffer layer as an active optical element in Cu(In,Ga)Se₂ thin-film solar cells," *Progress in Photovoltaics*, vol. 10, no. 7, pp. 457–463, 2002.
- [98] N. Naghavi, D. Abou-Ras, N. Allsop, N. Barreau, S. Bücheler, A. Ennaoui, C.-H. Fischer, C. Guillen, D. Hariskos, J. Herrero, R. Klenk, K. Kushiya, D. Lincot, R. Menner, T. Nakada, C. Platzer-Björkman, S. Spiering, A. N. Tiwari, and T. Törndahl, "Buffer layers and transparent conducting oxides for chalcopyrite Cu(In,Ga)(S,Se)₂ based thin film photovoltaics: present status and current developments," *Progress in Photovoltaics: Research and Applications*, vol. 18, no. 6, pp. 411–433, 2010.
- [99] M. Edoff, L. Malmberg, U. Malm, and L. Stolt, "Influence of Cbd-Deposited CdS on the Carrier Collection in Cigs-Based Solar Cells," in *Records of the 4th IEEE World Conference on Photovoltaic Energy Conversion*, Waikoloa, HI, USA, 2006, vol. 1, pp. 396–399.
- [100] K. Hiepkö, J. Bastek, R. Schlesiger, G. Schmitz, R. Wuerz, and N. A. Stolwijk, "Diffusion and incorporation of Cd in solar-grade Cu(In,Ga)Se₂ layers," *Applied Physics Letters*, vol. 99, no. 23, p. 234101, 2011.
- [101] K. Ottosson, "The role of i-ZnO for shunt prevention in Cu(In,Ga)Se₂-based solar cells," Upsalla University, 2006.
- [102] R. Scheer, L. Messmann-Vera, R. Klenk, and H.-W. Schock, "On the role of non-doped ZnO in CIGSe solar cells," *Prog. Photovolt: Res. Appl.*, p. n/a–n/a, 2011.
- [103] U. Rau, P. O. Grabitz, and J. H. Werner, "Resistive limitations to spatially inhomogeneous electronic losses in solar cells," *Applied Physics Letters*, vol. 85, no. 24, p. 6010, 2004.
- [104] N. F. Cooray, K. Kushiya, A. Fujimaki, D. Okumura, M. Sato, M. Ooshita, and O. Yamase, "Optimization of Al-doped ZnO Window Layers for Large-Area Cu(InGa)Se₂-Based Modules by RF/DC/DC Multiple Magnetron Sputtering," *Jpn. J. Appl. Phys.*, vol. 38, no. 11, p. 6213, 1999.
- [105] R. L. Anderson, "Experiments on Ge-GaAs heterojunctions," *Solid-State Electronics*, vol. 5, no. 5, pp. 341–351, 1962.

BIBLIOGRAPHY

- [106] L. J. Brillson, *Surfaces and Interfaces of Electronic Materials*. John Wiley & Sons, 2010.
- [107] J. Tersoff, "Theory of semiconductor heterojunctions: The role of quantum dipoles," *Physical Review B*, vol. 30, no. 8, p. 4874, 1984.
- [108] M. Burgelman, P. Nollet, and S. Degrave, "Modelling polycrystalline semiconductor solar cells," *Thin Solid Films*, vol. 361, pp. 527–532, 2000.
- [109] M. Troviano and K. Taretto, "Analysis of internal quantum efficiency in double-graded bandgap solar cells including sub-bandgap absorption," *Solar Energy Materials and Solar Cells*, vol. 95, no. 3, pp. 821–828, 2011.
- [110] W. Shockley and W. T. Read Jr, "Statistics of the recombinations of holes and electrons," *Physical Review*, vol. 87, no. 5, p. 835, 1952.
- [111] H. Wilhelm, H.-W. Schock, and R. Scheer, "Interface recombination in heterojunction solar cells: Influence of buffer layer thickness," *Journal of Applied Physics*, vol. 109, no. 8, p. 084514, 2011.
- [112] A. O. Pudov, A. Kanevce, H. A. Al-Thani, J. R. Sites, and F. S. Hasoon, "Secondary barriers in CdS–CuIn(1–x)Ga_xSe₂ solar cells," *Journal of Applied Physics*, vol. 97, no. 6, p. 064901, 2005.
- [113] G. Brown, A. Pudov, B. Cardozo, V. Faifer, E. Bykov, and M. Contreras, "Quantitative imaging of electronic nonuniformities in Cu(In,Ga)Se₂ solar cells," *J. Appl. Phys.*, vol. 108, no. 7, p. 074516, 2010.
- [114] O. Lundberg, M. Edoff, and L. Stolt, "The effect of Ga-grading in CIGS thin film solar cells," *Thin Solid Films*, vol. 480–481, no. 0, pp. 520–525, 2005.
- [115] J. H. Werner, J. Mattheis, and U. Rau, "Efficiency limitations of polycrystalline thin film solar cells: case of Cu(In,Ga)Se₂," *Thin Solid Films*, vol. 480–481, no. 0, pp. 399–409, 2005.
- [116] K. A. Bulashevich and S. Y. Karpov, "Is Auger recombination responsible for the efficiency rollover in III-nitride light-emitting diodes?," *physica status solidi (c)*, vol. 5, no. 6, pp. 2066–2069, 2008.
- [117] U. Rau, A. Jasenek, H. W. Schock, F. Engelhardt, and T. Meyer, "Electronic loss mechanisms in chalcopyrite based heterojunction solar cells," *Thin Solid Films*, vol. 361, pp. 298–302, 2000.
- [118] R. Scheer, "Activation energy of heterojunction diode currents in the limit of interface recombination," *Journal of Applied Physics*, vol. 105, no. 10, p. 104505, 2009.
- [119] W. W. Gärtner, "Depletion-Layer Photoeffects in Semiconductors," *Phys. Rev.*, vol. 116, no. 1, p. 84, 1959.
- [120] A. Rothwarf, "CuInSe₂/Cd(Zn)S solar cell modeling and analysis," *Solar Cells*, vol. 16, pp. 567–590, 1986.
- [121] E. Sanchez and G. L. Araujo, "Mathematical analysis of the efficiency-concentration characteristic of a solar cell," *Solar Cells*, vol. 12, no. 3, pp. 263–276, 1984.
- [122] J. Ward, "Cu(In,Ga)Se₂ Thin-Film Concentrator Solar Cells," *NCPV Program Review Meeting Lakewood, Colorado*, 2001.

- [123] M. Brogren, J. Wennerberg, R. Kapper, and B. Karlsson, "Design of concentrating elements with CIS thin-film solar cells for facade integration," *Solar Energy Materials and Solar Cells*, vol. 75, no. 3–4, pp. 567–575, 2003.
- [124] Y. Hirai, H. Nagashima, Y. Kurokawa, and A. Yamada, "Experimental and Theoretical Evaluation of Cu(In,Ga)Se₂ Concentrator Solar Cells," *Japanese Journal of Applied Physics*, vol. 51, no. 1, p. 014101, 2012.
- [125] S. M. Sze and K. K. Ng, "LEDs and lasers," in *Physics of semiconductor devices*, Wiley-Interscience., John Wiley and Sons, 2007, pp. 601–662.
- [126] A. V. Zinovchuk, O. Y. Malyutenko, V. K. Malyutenko, A. D. Podoltsev, and A. A. Vilisov, "The effect of current crowding on the heat and light pattern in high-power AlGaAs light emitting diodes," *Journal of Applied Physics*, vol. 104, no. 3, p. 033115, 2008.
- [127] F. A. Kish and R. M. Fletcher, "AlGaInP Light-Emitting Diodes," in *High Brightness Light Emitting Diodes*, Academic press., vol. 48, San Diego, CA, USA: Stringfellow, G.B. and George Carford,M., 1997, p. 469.
- [128] A. Khan, K. Balakrishnan, and T. Katona, "Ultraviolet light-emitting diodes based on group three nitrides," *Nat Photonics*, vol. 2, no. 2, pp. 77–84, 2008.
- [129] H. Kim, E. Brueckner, J. Song, Y. Li, S. Kim, C. Lu, J. Sulkin, K. Choquette, Y. Huang, R. G. Nuzzo, and others, "Unusual strategies for using indium gallium nitride grown on silicon (111) for solid-state lighting," *Proceedings of the National Academy of Sciences*, vol. 108, no. 25, p. 10072, 2011.
- [130] H. Kim, S.-J. Park, H. Hwang, and N.-M. Park, "Lateral current transport path, a model for GaN-based light-emitting diodes: Applications to practical device designs," *Applied Physics Letters*, vol. 81, no. 7, p. 1326, 2002.
- [131] H. Morkoç, *Handbook of Nitride Semiconductors and Devices: GaN-based Optical and Electronic Devices*, vol. GaN-Based optical and Electronic Devices, 3 vols. Wiley-VCH, 2008.
- [132] H. Kim and S.-N. Lee, "Theoretical Considerations on Current Spreading in GaN-Based Light Emitting Diodes Fabricated with Top-Emission Geometry," *Journal of The Electrochemical Society*, vol. 157, no. 5, p. H562, 2010.
- [133] V. Adivarahan, S. Wu, W. H. Sun, V. Mandavilli, M. S. Shatalov, G. Simin, J. W. Yang, H. P. Maruska, and M. A. Khan, "High-power deep ultraviolet light-emitting diodes based on a micro-pixel design," *Applied Physics Letters*, vol. 85, no. 10, p. 1838, 2004.
- [134] M. A. Khan, S. Wu, W. Sun, A. Chitnis, V. Adivarahan, M. Shatalov, and J. Yang, "255 nm interconnected micro-pixel deep ultraviolet light emitting diodes," in *Electron Devices Meeting, 2004. IEDM Technical Digest. IEEE International*, 2004, pp. 347–350.
- [135] Q. Shan, Q. Dai, S. Chhajed, J. Cho, and E. F. Schubert, "Analysis of thermal properties of GaInN light-emitting diodes and laser diodes," *Journal of Applied Physics*, vol. 108, p. 084504, 2010.
- [136] T. Weber, "Dark IV curve analysis of single solar cells in photovoltaic modules using electroluminescence imaging," in *Proceedings of the 24th European Photovoltaic Solar Energy Conference*, Hamburg, Germany, 2009, pp. 477–479.

BIBLIOGRAPHY

- [137] H. Sugimoto, "Impact of Cu(In,Ga)Se₂ absorber quality and circuit uniformity on improved efficiency; application of photoluminescence and electroluminescence techniques," in *Proceedings of the 24th European Photovoltaic Solar Energy Conference*, Hamburg, Germany, 2009, pp. 2465–2468.
- [138] A. Helbig, T. Kirchartz, R. Schaeffler, J. H. Werner, and U. Rau, "Quantitative electroluminescence analysis of resistive losses in Cu(In, Ga)Se₂ thin-film modules," *Solar Energy Materials and Solar Cells*, vol. 94, no. 6, pp. 979–984, 2010.
- [139] K. Xiong, W. He, S. Lu, T. Zhou, D. Jiang, R. Wang, K. Qiu, J. Dong, and H. Yang, "Analysis of lateral current spreading in solar cell devices by spatially-resolved electroluminescence," *Journal of Applied Physics*, vol. 107, no. 12, p. 124501, 2010.
- [140] V. D. Rumyantsev, "Solar concentrator modules with silicone-on-glass Fresnel lens panels and multijunction cells," *Optics express*, vol. 18, no. S1, pp. A17–A24, 2010.
- [141] U. Rau, "Reciprocity relation between photovoltaic quantum efficiency and electroluminescent emission of solar cells," *Physical Review B*, vol. 76, no. 8, 2007.
- [142] S. Kurtz, "Synergies connecting the photovoltaics solid-state lighting industries," *National Center for Photovoltaics and Solar Program Review Meeting*, 2003.
- [143] C. Algora, E. Ortiz, I. Rey-Stolle, V. Diaz, R. Pena, V. M. Andreev, V. P. Khvostikov, and V. D. Rumyantsev, "A GaAs solar cell with an efficiency of 26.2% at 1000 suns and 25.0% at 2000 suns," *IEEE Transactions on Electron Devices*, vol. 48, no. 5, pp. 840–844, 2001.
- [144] B. Galiana, C. Algora, and I. Rey-Stolle, "Comparison of 1D and 3D analysis of the front contact influence on GaAs concentrator solar cell performance," *Solar Energy Materials and Solar Cells*, vol. 90, no. 16, pp. 2589–2604, 2006.
- [145] J. Wennerberg, J. Kessler, and L. Stolt, "Design of grided Cu(In,Ga)Se₂ thin-film PV modules," *Solar Energy Materials and Solar Cells*, vol. 67, no. 1–4, pp. 59–65, 2001.
- [146] C. Algora and V. Diaz, "Influence of series resistance on guidelines for manufacture of concentrator p-on-n GaAs solar cells," *Progress in Photovoltaics: Research and Applications*, vol. 8, no. 2, pp. 211–225, 2000.
- [147] K. Nishioka, T. Takamoto, T. Agui, M. Kaneiwa, Y. Uraoka, and T. Fuyuki, "Evaluation of InGaP/InGaAs/Ge triple-junction solar cell and optimization of solar cell's structure focusing on series resistance for high-efficiency concentrator photovoltaic systems," *Solar Energy Materials and Solar Cells*, vol. 90, no. 9, pp. 1308–1321, 2006.
- [148] L. D. Nielsen, "Distributed Series Resistance Effects in Solar-Cells," *IEEE Transactions on Electron Devices*, vol. 29, no. 5, pp. 821–827, 1982.
- [149] G. T. Koishiyev and J. R. Sites, "Impact of sheet resistance on 2-D modeling of thin-film solar cells," *Solar Energy Materials and Solar Cells*, vol. 93, no. 3, pp. 350–354, 2009.
- [150] D. Lincot, M. Barbe, G. Cohensolal, and F. Bailly, "Analysis of the Effects of the Lateral Resistivity of the Superficial Zone on the Current-Voltage Characteristics of Linear-Gridded Solar-Cells," *Solar Cells*, vol. 8, no. 4, pp. 361–369, 1983.
- [151] G. M. Smirnov and J. E. Mahan, "Distributed Series Resistance in Photo-Voltaic Devices - Intensity and Loading Effects," *Solid-State Electronics*, vol. 23, no. 10, pp. 1055–1058, 1980.

- [152] J. L. Boone and T. P. Vandoren, "Solar-Cell Design Based on a Distributed Diode Analysis," *IEEE Transactions on Electron Devices*, vol. 25, no. 7, pp. 767–771, 1978.
- [153] O. Korech, J. M. Gordon, E. A. Katz, D. Feuermann, and N. Eisenberg, "Dielectric microconcentrators for efficiency enhancement in concentrator solar cells," *Opt. Lett.*, vol. 32, no. 19, pp. 2789–2791, 2007.
- [154] J. Yoon, A. J. Baca, S. I. Park, P. Elvikis, J. B. Geddes, L. F. Li, R. H. Kim, J. L. Xiao, S. D. Wang, T. H. Kim, M. J. Motala, B. Y. Ahn, E. B. Duoss, J. A. Lewis, R. G. Nuzzo, P. M. Ferreira, Y. G. Huang, A. Rockett, and J. A. Rogers, "Ultrathin silicon solar microcells for semitransparent, mechanically flexible and microconcentrator module designs," *Nature Materials*, vol. 7, no. 11, pp. 907–915, 2008.
- [155] NREL Newsroom, "Tiny Solar Cell Could Make a Big Difference," http://www.nrel.gov/news/features/feature_detail.cfm/feature_id=1668. 2011.
- [156] O. Korech, B. Hirsch, E. A. Katz, and J. M. Gordon, "High-flux characterization of ultras-small multijunction concentrator solar cells," *Applied Physics Letters*, vol. 91, no. 6, 2007.
- [157] G. N. Nielsen, "Microscale PV cells for concentrated PV applications," in *Proceedings of the 24th European Photovoltaic Solar Energy Conference*, Hamburg, Germany, 2009, pp. 170–174.
- [158] Nielson, Gregory N., Okandan, Murat, Resnick, Paul, Cruz-Campa, Jose Luis, Clews, Peggy J., Steebergen, Elizabeth, and Gupta, Vipin P., "Microscale c-Si (C)PV Cells for Low-Cost Power," in *Proceedings of the 34th IEEE Photovoltaic Specialists Conference (PVSC)*, Philadelphia, 2009, pp. 001816–001821.
- [159] C. Algora, V. Diaz, J. C. Minano, and A. Luque, "Cost reduction in concentrator GaAs solar cells based PV plants: going from photovoltaics to optoelectronic processing," in *Proceedings of the 2nd World conference on Photovoltaic Solar Energy Conversion*, Vienna, Austria, 1998, pp. 2225–2228.
- [160] A. Luque, G. Sala, and I. Luque-Heredia, "Photovoltaic concentration at the onset of its commercial deployment," *Progress in Photovoltaics: Research and Applications*, vol. 14, no. 5, pp. 413–428, 2006.
- [161] M. S. Carpenter, M. R. Melloch, M. S. Lundstrom, and S. P. Tobin, "Effects of Na₂S and (NH₄)₂S edge passivation treatments on the dark current-voltage characteristics of GaAs pn diodes," *Applied Physics Letters*, vol. 52, no. 25, p. 2157, 1988.
- [162] A. Vossier, B. Hirsch, E. A. Katz, and J. M. Gordon, "On the ultra-miniaturization of concentrator solar cells," *Solar Energy Materials and Solar Cells*, 2011.
- [163] R. J. Handy, "Theoretical analysis of the series resistance of a solar cell," *Solid-State Electronics*, vol. 10, no. 8, pp. 765–775, 1967.
- [164] V. G. Karpov, M. L. C. Cooray, and D. Shvydka, "Physics of ultrathin photovoltaics," *Appl. Phys. Lett.*, vol. 89, no. 16, p. 163518, 2006.
- [165] A. Virtuani, E. Lotter, M. Powalla, U. Rau, J. H. Werner, and M. Acciarri, "Influence of Cu content on electronic transport and shunting behavior of Cu(In,Ga)Se₂ solar cells," *Journal of Applied Physics*, vol. 99, no. 1, p. 014906, 2006.

BIBLIOGRAPHY

- [166] I. L. Repins, B. J. Stanbery, D. L. Young, S. S. Li, W. K. Metzger, C. L. Perkins, W. N. Shafarman, M. E. Beck, L. Chen, V. K. Kapur, D. Tarrant, M. D. Gonzalez, D. G. Jensen, T. J. Anderson, X. Wang, L. L. Kerr, B. Keyes, S. Asher, A. Delahoy, and B. Von Roedern, "Comparison of device performance and measured transport parameters in widely-varying Cu(In,Ga)(Se,S) solar cells," *Progress in Photovoltaics*, vol. 14, no. 1, pp. 25–43, 2006.
- [167] H. Khallaf, I. O. Oladeji, G. Chai, and L. Chow, "Characterization of CdS thin films grown by chemical bath deposition using four different cadmium sources," *Thin Solid Films*, vol. 516, no. 21, pp. 7306–7312, 2008.
- [168] D. Petre, I. Pintilie, E. Pentia, I. Pintilie, and T. Botila, "The influence of Cu doping on optoelectronic properties of chemically deposited CdS," *Materials Science and Engineering: B*, vol. 58, no. 3, pp. 238–243, 1999.
- [169] Z. A. Wang, J. B. Chu, H. B. Zhu, Z. Sun, Y. W. Chen, and S. M. Huang, "Growth of ZnO:Al films by RF sputtering at room temperature for solar cell applications," *Solid-State Electronics*, vol. 53, no. 11, pp. 1149–1153, 2009.
- [170] M. Paire, L. Lombez, J.-F. Guillemoles, and D. Lincot, "Toward microscale Cu(In,Ga)Se₂ solar cells for efficient conversion and optimized material usage: Theoretical evaluation," *J. Appl. Phys.*, vol. 108, no. 3, p. 034907, 2010.
- [171] N. C. Wyeth, "Sheet Resistance Component of Series Resistance in a Solar-Cell as a Function of Grid Geometry," *Solid-State Electronics*, vol. 20, no. 7, pp. 629–634, 1977.
- [172] A. S. H. van der Heide, A. Schonecker, J. H. Bultman, and W. C. Sinke, "Explanation of high solar cell diode factors by nonuniform contact resistance," *Prog. Photovolt: Res. Appl.*, vol. 13, no. 1, pp. 3–16, 2005.
- [173] I. Repins, "Characterization of 19.9% efficient CIGS absorbers," in *Proceedings of the 33rd IEEE Photovoltaic Specialists Conference*, San Diego, CA, USA, 2008, pp. 1 – 6.
- [174] V. G. Karpov, A. D. Compaan, and D. Shvydka, "Random diode arrays and mesoscale physics of large-area semiconductor devices," *Phys. Rev. B*, vol. 69, no. 4, p. 045325, 2004.
- [175] M. Paire, L. Lombez, J. F. Guillemoles, and D. Lincot, "Measuring sheet resistance of CIGS solar cell's window layer by spatially resolved electroluminescence imaging," *Thin Solid Films*, no. 519, pp. 7493–7496, 2011.
- [176] T. M. H. Tran, B. E. Pieters, M. Siegloch, A. Gerber, C. Ulbrich, T. Kirchartz, R. Schäffler, and U. Rau, "Characterization of shunts in Cu(In,Ga)Se₂ solar modules via combined electroluminescence and dark lock-in thermography analysis," in *Proceedings of the 26th European Photovoltaic Solar Energy Conference and Exhibition*, Hambourg, Germany, 2011, pp. 2981–2985.
- [177] K. Araki, M. Yamaguchi, M. Imaizumi, T. Takamoto, and H. Kurita, "AM0 concentration operation of III-V compounds solar cells," *Conference Record of the Twenty-Eighth IEEE Photovoltaic Specialists Conference - 2000*, pp. 968–971, 2000.
- [178] P. Gleckman, J. O'gallagher, and R. Winston, "Concentration of Sunlight to Solar-Surface Levels Using Non-Imaging Optics," *Nature*, vol. 339, no. 6221, pp. 198–200, 1989.
- [179] S. Kijima and T. Nakada, "High-Temperature Degradation Mechanism of Cu(In,Ga)Se₂-Based Thin Film Solar Cells," *Applied Physics Express*, vol. 1, p. 075002, 2008.

- [180] P. Singh and N. M. Ravindra, "Temperature dependence of solar cell performance - an analysis," *Solar Energy Materials and Solar Cells*, vol. 101, pp. 36–45, 2012.
- [181] Y. P. Varshni, "Temperature dependence of the energy gap in semiconductors," *Physica*, vol. 34, no. 1, pp. 149–154, 1967.
- [182] Pilkington - Architectural Technical Bulletins, "Properties of Soda-Lime-Silica Float Glass," http://www.google.fr/url?sa=t&rct=j&q=&esrc=s&source=web&cd=1&ved=0CDIQFjAA&url=http%3A%2F%2Fwww.pilkington.com%2Fresources%2Fats129swproperties20090804.doc&ei=MGSaT7nrE-nD0QW-q_zjDg&usq=AFQjCNEKB1jkCI5QE-Mf9H3otlDnR-qTiA&sig2=jveCOL4o2BLrnnku_-Yliw. 2009.
- [183] R. P. Tye, "Preliminary measurements on the thermal and electrical conductivities of molybdenum, niobium, tantalum and tungsten," *Journal of the Less Common Metals*, vol. 3, no. 1, pp. 13–18, 1961.
- [184] M. L. Valeri-Gil and C. Rincon, "Thermal conductivity of ternary chalcopyrite compounds," *Materials Letters*, vol. 17, no. 1–2, pp. 59–62, 1993.
- [185] X. Qu, W. Wang, S. Lv, and D. Jia, "Thermoelectric properties and electronic structure of Al-doped ZnO," *Solid State Communications*, vol. 151, no. 4, pp. 332–336, 2011.
- [186] J. V. Beck, K. D. Cole, A. Haji-Sheikh, and B. Litkouhi, "Other geometries in cylindrical coordinates," in *Heat conduction using green's functions*, Hemisphere publishing corporation, 1992.
- [187] P. Thomas, "Some conduction problems in the heating of small areas on large solids," *The Quarterly Journal of Mechanics and Applied Mathematics*, vol. 10, no. 4, p. 482, 1957.
- [188] Necati Ozisik M., "Heat conduction in the cylindrical coordinate system," in *Boundary Value Problem of Heat Conduction*, Mineola, NY, USA: Dover Publications, 1989.
- [189] J. H. Tan and W. Anderson, "Current transport in copper indium gallium diselenide solar cells comparing mesa diodes to the full cell," *Solar energy materials and solar cells*, vol. 77, no. 3, pp. 283–292, 2003.
- [190] K. Miyazaki, O. Matsushima, M. Moriwake, H. Takasu, S. Ishizuka, K. Sakurai, A. Yamada, and S. Niki, "High sensitivity and wide bandwidth image sensor using CuIn_{1-x}Ga_xSe₂ thin films," *Thin Solid Films*, vol. 517, no. 7, pp. 2392–2394, 2009.
- [191] A. J. Baca, K. J. Yu, T. A. Cain, D. H. Kim,, J. Yoon, A. A. Rockett, R. G. Nuzzo, and J. A. Rogers, "Si solar microcells for modules with reduced purity requirements, high voltage outputs and mechanically stretchable designs," in *Proceedings of the 34th IEEE Photovoltaic Specialists Conference*, Philadelphia, 2009, pp. 000120 – 000123.
- [192] J. Yoon, S. Jo, I. S. Chun, I. Jung, H. S. Kim, M. Meitl, E. Menard, X. L. Li, J. J. Coleman, U. Paik, and J. A. Rogers, "GaAs photovoltaics and optoelectronics using releasable multilayer epitaxial assemblies," *Nature*, vol. 465, no. 7296, pp. 329–334, 2010.
- [193] V. P. Gupta, J. L. Cruz-Campa, M. Okandan, and G. N. Nielson, "Microsystems-enabled photovoltaics, a path to the widespread harnessing of solar energy," *Future Photovoltaics*, vol. 1, no. 1, pp. 28–36, 2010.
- [194] J. Lee, J. Wu, M. Shi, J. Yoon, S.-I. Park, M. Li, Z. Liu, Y. Huang, and J. A. Rogers, "Stretchable GaAs Photovoltaics with Designs That Enable High Areal Coverage," *Adv. Mater.*, pp. 986–991, 2011.

BIBLIOGRAPHY

- [195] A. J. Baca, K. J. Yu, J. Xiao, S. Wang, J. Yoon, J. H. Ryu, D. Stevenson, R. G. Nuzzo, A. A. Rockett, Y. Huang, and others, "Compact monocrystalline silicon solar modules with high voltage outputs and mechanically flexible designs," *Energy & Environmental Science*, vol. 3, no. 2, pp. 208–211, 2010.
- [196] J. Yoon, L. Li, A. V. Semichaevsky, J. H. Ryu, H. T. Johnson, R. G. Nuzzo, and J. A. Rogers, "Flexible concentrator photovoltaics based on microscale silicon solar cells embedded in luminescent waveguides," *Nature Communications*, vol. 2, p. 343, 2011.
- [197] R. J. Knuesel and H. O. Jacobs, "Self-Tiling Monocrystalline Silicon; a Process to Produce Electrically Connected Domains of Si and Microconcentrator Solar Cell Modules on Plastic Supports," *Advanced Materials*, vol. 23, no. 24, pp. 2727–2733, 2011.
- [198] R. Bukovnik, E. Menard, M. Meitl, S. Bonafede, R. McNeill, W. Wagner, S. Seel, and S. Burroughs, "A micro-transfer printed high efficiency flexible photovoltaic panel," in *Proceedings of the 37th IEEE Photovoltaic Specialists Conference*, Seattle, USA, 2011, pp. 001543–001547.
- [199] M. A. Green, K. Emery, Y. Hishikawa, and W. Warta, "Solar cell efficiency tables (version 37)," *Prog. Photovolt: Res. Appl.*, vol. 19, no. 1, pp. 84–92, 2011.
- [200] M. Powalla, D. Hariskos, E. Lotter, M. Oertel, J. Springer, D. Stellbogen, B. Dimmler, and R. Schöffler, "Large-area CIGS modules: processes and properties," *Thin Solid Films*, vol. 431–432, pp. 523–533, 2003.
- [201] M. Bouttemy, P. Tran-Van, I. Gerard, T. Hildebrandt, A. Causier, J. L. Pelouard, G. Dagher, Z. Jehl, N. Naghavi, G. Voorwinden, B. Dimmler, M. Powalla, J. F. Guillemoles, D. Lincot, and A. Etcheberry, "Thinning of Cu (In, Ga) S₂ solar cells: Part I: Chemical processing in acidic bromine solutions," *Thin Solid Films*, vol. 519, no. 21, pp. 7207 – 7211, 2011.
- [202] H. H. Berger, "Models for contacts to planar devices," *Solid-State Electronics*, vol. 15, no. 2, pp. 145–158, Février 1972.
- [203] C. Koechlin, S. Maine, R. Haidar, B. Trétout, A. Loiseau, and J.-L. Pelouard, "Electrical characterization of devices based on carbon nanotube films," *Applied Physics Letters*, vol. 96, no. 10, p. 103501, 2010.
- [204] U. Malm and M. Edoff, "Simulating Material Inhomogeneities and Defects in CIGS Thin-film Solar Cells," *Prog. Photovoltaics*, vol. 17, no. 5, pp. 306–314, 2009.
- [205] P. O. Grabitz, U. Rau, B. Wille, G. Bilger, and J. H. Werner, "Spatial inhomogeneities in Cu(In,Ga)Se₂ solar cells analyzed by an electron beam induced voltage technique," *Journal of Applied Physics*, vol. 100, no. 12, p. 124501, 2006.
- [206] J. R. Tuttle, A. Szalaj, and K. Beninga, "Progress towards commercialization of a 4.5-sun, flat-plate concentrating PV module and system," in *Conference Record of the Twenty-Eighth IEEE Photovoltaic Specialists Conference - 2000*, 2000, pp. 1468–1471.
- [207] I. Rey-Stolle and C. Algora, "High-irradiance degradation tests on concentrator GaAs solar cells," *Prog. Photovolt: Res. Appl.*, vol. 11, no. 4, pp. 249–254, 2003.
- [208] S. Shirakata and T. Nakada, "Photoluminescence and time-resolved photoluminescence in Cu(In,Ga)Se₂ thin films and solar cells," *Physica Status Solidi C - Current Topics in Solid State Physics*, vol. 6, no. 5, pp. 1059–1062, 2009.

- [209] A. Slobodskyy, D. Wang, T. Scherer, C. Kübel, Z.-H. Zhang, E. Müller, D. Gerthsen, M. Powalla, and U. Lemmer, "Optical and charge transport properties of a $\text{CuIn}_{1-x}\text{Ga}_x\text{Se}_2$ solar cell cross section," *Phys. Rev. B*, vol. 82, no. 20, p. 201105, 2010.
- [210] D. Abou-Ras, T. Kirchartz, and U. Rau, *Advanced Characterization Techniques for Thin Film Solar Cells*. John Wiley & Sons, 2011.
- [211] M. Wolf and H. Rauschenbach, "Series resistance effects on solar cell measurements," *Advanced Energy Conversion*, vol. 3, no. 2, pp. 455–479, 1963.
- [212] S. R. Dhariwal, R. K. Mathur, D. R. Mehrotra, and S. Mittal, "The physics of pn junction solar cells operated under concentrated sunlight," *Solar Cells*, vol. 8, no. 2, pp. 137–155, 1983.
- [213] S. M. Sze and K. K. Ng, "Physics and properties of semiconductors - a review," in *Physics of semiconductor devices*, Wiley-Interscience., John Wiley and Sons, 2007, pp. 7–78.
- [214] Z. Jehl, F. Erfurth, N. Naghavi, L. Lombez, I. Gerard, M. Bouttemy, P. Tran-Van, A. Etcheberry, G. Voorwinden, B. Dimmler, W. Wischmann, M. Powalla, J.-F. Guillemoles, and D. Lincot, "Thinning of CIGS solar cells : Part II: cell characterisations," *Thin Solid Films*, vol. 519, pp. 7212–7215, 2011.
- [215] P. Wurfel, "The chemical potential of radiation," *Journal of Physics C: Solid State Physics*, vol. 15, no. 18, p. 3967, 1982.
- [216] E. A. Katz, J. M. Gordon, W. Tassew, and D. Feuermann, "Photovoltaic characterization of concentrator solar cells by localized irradiation," *Journal of Applied Physics*, vol. 100, no. 4, p. 044514, 2006.
- [217] F. J. Vorster and E. E. van Dyk, "High saturation solar light beam induced current scanning of solar cells," *Rev. Sci. Instrum.*, vol. 78, no. 1, 2007.
- [218] M. A. Green, "Third generation photovoltaics: solar cells for 2020 and beyond," *Physica E: Low-dimensional Systems and Nanostructures*, vol. 14, no. 1–2, pp. 65–70, 2002.
- [219] T. Meyer, F. Engelhardt, J. Parisi, and U. Rau, "Spectral dependence and Hall effect of persistent photoconductivity in polycrystalline $\text{Cu}(\text{In,Ga})\text{Se}_2$ thin films," *J. Appl. Phys.*, vol. 91, no. 8, pp. 5093–5099, 2002.
- [220] S. Lany and A. Zunger, "Light- and bias-induced metastabilities in $\text{Cu}(\text{In,Ga})\text{Se}_2$ based solar cells caused by the (VSe-VCu) vacancy complex," *Journal of Applied Physics*, vol. 100, no. 11, p. 113725, 2006.
- [221] J. W. Lee, J. . Heath, J. D. Cohen, and W. N. Shafarman, "Detailed study of metastable effects in the $\text{Cu}(\text{InGa})\text{Se}_2$ alloys: Test of defect creation models.," *MRS Proceedings*, vol. 865, no. F12.4, pp. 373–377, 2005.
- [222] I. L. Eisgruber, J. E. Granata, J. R. Sites, J. Hou, and J. Kessler, "Blue-photon modification of nonstandard diode barrier in CuInSe_2 solar cells," *Solar Energy Materials and Solar Cells*, vol. 53, no. 3–4, pp. 367–377, 1998.
- [223] A. O. Pudov, J. R. Sites, M. A. Contreras, T. Nakada, and H. W. Schock, "CIGS J-V distortion in the absence of blue photons," *Thin Solid Films*, vol. 480–481, pp. 273–278, 2005.

BIBLIOGRAPHY

- [224] G. Agostinelli, E. D. Dunlop, D. L. Bätzner, A. N. Tiwari, P. Nollet, M. Burgelman, and M. Köntges, "Light dependent current transport mechanisms in chalcogenide solar cells," in *Proceedings of the 3rd World Conference on Photovoltaic Energy Conversion*, Osaka, Japan, 2003.
- [225] O. Lundberg, M. Bodegard, J. Malmstrom, and L. Stolt, "Influence of the Cu(In,Ga)Se₂ thickness and Ga grading on solar cell performance," *Prog. Photovoltaics*, vol. 11, no. 2, pp. 77–88, 2003.
- [226] M. Igalson, M. Bodegård, and L. Stolt, "Reversible changes of the fill factor in the ZnO/CdS/Cu(In,Ga)Se₂ solar cells," *Solar Energy Materials and Solar Cells*, vol. 80, no. 2, pp. 195–207, 2003.
- [227] H. Mathieu, *Physique des semiconducteurs et des composants électroniques*. Paris: Dunod, 2004.
- [228] S. H. Wei, S. B. Zhang, and A. Zunger, "Effects of Ga addition to CuInSe₂ on its electronic, structural, and defect properties," *Applied Physics Letters*, vol. 72, no. 24, pp. 3199–3201, 1998.
- [229] Garboushian, V., Stone, K. W., and Slade, A., "The Amonix High-Concentration Photovoltaic System," in *Concentrator Photovoltaics*, vol. 130, Springer-Verlag Berlin Heidelberg, 2007, pp. 253–277.
- [230] J. G. Fossum and F. A. Lindholm, "The dependence of open-circuit voltage on illumination level in p-n junction solar cells," *IEEE Transactions on Electron Devices*, vol. 24, pp. 325–329, 1977.
- [231] D. Girton, "pn diode saturation using a laser," *Proceedings of the IEEE*, vol. 51, no. 6, p. 938, 1963.
- [232] A. Luque and G. L. Araújo, *Solar cells and optics for photovoltaic concentration*, Taylor & Francis. A. Hilger, 1989.
- [233] M. A. Green, J. Zhao, and D. L. King, "Sublinear current response in high-efficiency, high-resistivity silicon solar cells: Theory and experiment," *Applied physics letters*, vol. 52, no. 16, pp. 1361–1363, 1988.
- [234] M. Cid and J. M. Ruiz, "Study of injection effects on BSF silicon solar cells," *Electron Devices, IEEE Transactions on*, vol. 36, no. 3, pp. 507–513, 1989.
- [235] T. E. Zirkle, D. K. Schroder, and C. E. Backus, "The superlinearity of the short-circuit current of low-resistivity-concentration solar cells," *Electron Devices, IEEE Transactions on*, vol. 36, no. 7, pp. 1286–1294, 1989.
- [236] M. J. Terrón and A. Luque, "Reduction of the apparent shunt resistance effect in silicon concentrator solar cells," *Progress in Photovoltaics: Research and Applications*, vol. 2, no. 3, pp. 187–202, 1994.
- [237] I. Antón, G. Sala, K. Heasman, R. Kern, and T. M. Bruton, "Performance prediction of concentrator solar cells and modules from dark IV characteristics," *Progress in Photovoltaics: Research and Applications*, vol. 11, no. 3, pp. 165–178, 2003.
- [238] S. R. Dhariwal, L. S. Kothari, and S. C. Jain, "On the recombination of electrons and holes at traps with finite relaxation time," *Solid-State Electronics*, vol. 24, no. 8, pp. 749–752, 1981.

- [239] S. J. Robinson, A. G. Aberle, and M. A. Green, "Departures from the principle of superposition in silicon solar cells," *Journal of Applied Physics*, vol. 76, no. 12, p. 7920, 1994.
- [240] G. Brown, V. Faifer, A. Pudov, S. Anikeev, E. Bykov, M. Contreras, and J. Wu, "Determination of the minority carrier diffusion length in compositionally graded Cu(In,Ga)Se₂ solar cells using electron beam induced current," *Applied Physics Letters*, vol. 96, no. 2, p. 022104, 2010.
- [241] H. J. Hovel, "Carrier collection, spectral response, and photocurrent," in *Semiconductors and semimetals*, Academic Press., vol. Solar cells, 11 vols., 1975.
- [242] Z. Jehl Li Kao, "Elaboration of ultrathin copper indium gallium diselenide based solar cells," Université Paris Sud Orsay, Orsay, France, 2012.
- [243] S. Hegedus, D. Desai, and C. Thompson, "Voltage dependent photocurrent collection in CdTe/CdS solar cells," *Prog. Photovolt: Res. Appl.*, vol. 15, no. 7, pp. 587–602, 2007.
- [244] M. Eron and A. Rothwarf, "Effects of a voltage-dependent light-generated current on solar cell measurements: CuInSe₂/Cd(Zn)S," *Appl. Phys. Lett.*, vol. 44, no. 1, pp. 131–133, 1984.
- [245] C. Jacobini, *Theory of electron transport in semiconductors*. Springer-Verlag Berlin Heidelberg, 2010.
- [246] H. K. Gummel, "A self-consistent iterative scheme for one-dimensional steady state transistor calculations," *Electron Devices, IEEE Transactions on*, vol. 11, no. 10, pp. 455–465, 1964.
- [247] Y. Rosenwaks, B. R. Thacker, R. K. Ahrenkiel, A. J. Nozik, and I. Yavneh, "Photogenerated carrier dynamics under the influence of electric fields in III-V semiconductors," *Physical Review B*, vol. 50, no. 3, p. 1746, 1994.
- [248] Chi-Kuang Sun, I-Hsing Tan, and J. E. Bowers, "Ultrafast transport dynamics of p-i-n photodetectors under high-power illumination," *Photonics Technology Letters, IEEE DOI - 10.1109/68.651137*, vol. 10, no. 1, pp. 135–137, 1998.
- [249] K. J. Williams, R. D. Esman, and M. Dagenais, "Effects of high space-charge fields on the response of microwave photodetectors," *Photonics Technology Letters, IEEE*, vol. 6, no. 5, pp. 639–641, 1994.
- [250] W. K. Metzger, R. K. Ahrenkiel, J. Dashdorj, and D. J. Friedman, "Analysis of charge separation dynamics in a semiconductor junction," *Phys. Rev. B*, vol. 71, no. 3, p. 035301, 2005.
- [251] W. K. Metzger, I. L. Repins, and M. A. Contreras, "Long lifetimes in high-efficiency Cu(In,Ga)Se₂ solar cells," *Applied Physics Letters*, vol. 93, no. 2, p. 022110, 2008.
- [252] J. Holonyak, J. A. Rossi, R. D. Burnham, B. G. Streetman, and M. R. Johnson, "An Experimental Investigation of the Maximum Photo-emf of a p-n Junction," *J. Appl. Phys.*, vol. 38, no. 13, pp. 5422–5423, 1967.
- [253] D. Cohen, "Earth's natural wealth: an audit," *New Scientist*, no. 2605, pp. 34–41, 2007.
- [254] B. A. Andersson, "Materials availability for large-scale thin-film photovoltaics," *Prog. Photovoltaics*, vol. 8, no. 1, pp. 61–76, 2000.

BIBLIOGRAPHY

- [255] C. Schönenberger, B. M. I. Van der Zande, L. G. J. Fokkink, M. Henny, C. Schmid, M. Krüger, A. Bachtold, R. Huber, H. Birk, and U. Staufer, "Template synthesis of nanowires in porous polycarbonate membranes: electrochemistry and morphology," *The Journal of Physical Chemistry B*, vol. 101, no. 28, pp. 5497–5505, 1997.
- [256] W.-H. Kim, H.-B.-R. Lee, K. Heo, Y. K. Lee, T.-M. Chung, C. G. Kim, S. Hong, J. Heo, and H. Kim, "Atomic Layer Deposition of Ni Thin Films and Application to Area-Selective Deposition," *Journal of The Electrochemical Society*, vol. 158, no. 1, p. D1, 2011.
- [257] M. N. Mullings, H.-B.-R. Lee, N. Marchack, X. Jiang, Z. Chen, Y. Gorlin, K.-P. Lin, and S. F. Bent, "Area Selective Atomic Layer Deposition by Microcontact Printing with a Water-Soluble Polymer," *Journal of The Electrochemical Society*, vol. 157, no. 12, p. D600, 2010.
- [258] P. T. Hammond, "Recent explorations in electrostatic multilayer thin film assembly," *Current Opinion in Colloid & Interface Science*, vol. 4, no. 6, pp. 430–442, 1999.
- [259] H. Minemawari, T. Yamada, H. Matsui, J. Tsutsumi, S. Haas, R. Chiba, R. Kumai, and T. Hasegawa, "Inkjet printing of single-crystal films," *Nature*, vol. 475, no. 7356, pp. 364–367, 2011.
- [260] M. Singh, H. M. Haverinen, P. Dhagat, and G. E. Jabbour, "Inkjet Printing-Process and Its Applications," *Advanced Materials*, vol. 22, no. 6, pp. 673–685, 2010.
- [261] S. D. Allen, "Laser chemical vapor deposition: A technique for selective area deposition," *Journal of Applied Physics*, vol. 52, no. 11, p. 6501, 1981.
- [262] R. Meyer, S. Hamann, M. Ehmann, D. Konig, S. Thienhaus, A. Savan, and A. Ludwig, "Small-Scale Deposition of Thin Films and Nanoparticles by Microevaporation Sources," *Journal of Microelectromechanical Systems*, vol. 20, no. 1, pp. 21–27, 2011.
- [263] E. I. Givargizov, "Fundamental aspects of VLS growth," *Journal of Crystal Growth*, vol. 31, no. 0, pp. 20–30, Dec. 1975.
- [264] B. Canava, J. F. Guillemoles, J. Vigneron, D. Lincot, and A. Etcheberry, "Chemical elaboration of well defined Cu(In,Ga)Se₂ surfaces after aqueous oxidation etching," *Journal of Physics and Chemistry of Solids*, vol. 64, no. 9, pp. 1791–1796, 2003.
- [265] C. H. Henry, R. A. Logan, and F. R. Merritt, "The effect of surface recombination on current in Al_xGa_{1-x}As heterojunctions," *Journal of Applied Physics*, vol. 49, no. 6, p. 3530, 1978.
- [266] W. K. Metzger, I. L. Repins, M. Romero, P. Dippo, M. Contreras, R. Noufi, and D. Levi, "Recombination kinetics and stability in polycrystalline Cu(In,Ga)Se₂ solar cells," *Thin Solid Films*, vol. 517, no. 7, pp. 2360–2364, 2009.
- [267] J. F. Guillemoles, J. P. Connolly, O. Ramdani, O. Roussel, D. Guimard, V. Bermudez, N. Naghavi, P. P. Grand, L. Parissi, J. Kurdi, J. Kessler, O. Kerrec, and D. Lincot, "Solution Processing Route to High Efficiency CuIn(S,Se)₂ Solar Cells," *Journal of Nano Research*, vol. 4, no. 79, pp. 79–89, 2009.
- [268] D. Lincot, J. F. Guillemoles, S. Taunier, D. Guimard, J. Sicx-Kurdi, A. Chaumont, O. Roussel, O. Ramdani, C. Hubert, J. P. Fauvarque, N. Bodereau, L. Parissi, P. Panheleux, P. Fanouillere, N. Naghavi, P. P. Grand, M. Benfarah, P. Mogensen, and O. Kerrec, "Chalcopyrite thin film solar cells by electrodeposition," *Solar Energy*, vol. 77, no. 6, pp. 725–737, 2004.

- [269] M. Paunovic and M. Schlesinger, *Fundamentals of Electrochemical Deposition, 2nd Edition*. Wiley-VCH Verlag & Co, 2006.
- [270] R. N. Bhattacharya, "Solution Growth and Electrodeposited CuInSe₂ Thin Films," *J. Electrochem. Soc.*, vol. 130, no. 10, pp. 2040–2042, 1983.
- [271] O. Roussel, O. Ramdani, E. Chassaing, P.-P. Grand, M. Lamirand, A. Etcheberry, O. Kerrec, J.-F. Guillemoles, and D. Lincot, "First Stages of CuInSe₂ Electrodeposition from Cu(II)-In(III)-Se(IV) Acidic Solutions on Polycrystalline Mo Films," *Journal of The Electrochemical Society*, vol. 155, no. 2, p. D141, 2008.
- [272] R. J. Forster, "Microelectrodes: new dimensions in electrochemistry," *Chemical Society Reviews*, vol. 23, no. 4, p. 289, 1994.
- [273] R. L. Pletcher, "Why microelectrodes?," in *Microelectrodes: Theory and Applications*, I. Montenegro, M. A. Queiros, and J. L. Daschbach, Eds. Springer, 1991.
- [274] A. M. Bond, "Past, present and future contributions of microelectrodes to analytical studies employing voltammetric detection. A review," *The Analyst*, vol. 119, no. 11, p. 1R, 1994.
- [275] O. Ramdani, J. F. Guillemoles, D. Lincot, P. P. Grand, E. Chassaing, O. Kerrec, and E. Rzepka, "One-step electrodeposited CuInSe₂ thin films studied by Raman spectroscopy," *Thin solid films*, vol. 515, no. 15, pp. 5909–5912, 2007.
- [276] L. Ribeaucourt, "Electrodeposition and selenisation of Cu-In-Ga alloys in order to form Cu(In,Ga)Se₂ thin films for solar cells," Chimie ParisTech, France, 2011.
- [277] D. W. M. Arrigan, "Nanoelectrodes, nanoelectrode arrays and their applications," *Analyst*, vol. 129, no. 12, pp. 1157–1165, 2004.
- [278] J. L. Cruz-Campa, M. Okandan, M. L. Busse, and G. N. Nielson, "Microlens rapid prototyping technique with capability for wide variation in lens diameter and focal length," *Microelectronic Engineering*, vol. 87, no. 11, pp. 2376–2381, 2010.
- [279] S. Donati, E. Randone, M. Fathi, J.-H. Lee, E. Charbon, and G. Martini, "Uniformity of Concentration Factor and Back Focal Length in Molded Polymer Microlens Arrays," in *Conference on Lasers and Electro-Optics*, 2010, p. JThE36.
- [280] M. V. Kunnavakkam, F. M. Houlihan, M. Schlax, J. A. Liddle, P. Kolodner, O. Nalamasu, and J. A. Rogers, "Low-cost, low-loss microlens arrays fabricated by soft-lithography replication process," *Appl. Phys. Lett.*, vol. 82, no. 8, pp. 1152–1154, 2003.
- [281] J. Y. Kim, N. B. Brauer, V. Fakhfour, D. L. Boiko, E. Charbon, G. Grutzner, and J. Brugger, "Hybrid polymer microlens arrays with high numerical apertures fabricated using simple ink-jet printing technique," *Optical Materials Express*, vol. 1, no. 2, pp. 259–269, 2011.
- [282] K. Lee, W. Wagermaier, A. Masic, K. P. Kommareddy, M. Bennet, I. Manjubala, S.-W. Lee, S. B. Park, H. Cölfen, and P. Fratzl, "Self-assembly of amorphous calcium carbonate microlens arrays," *Nature Communications*, vol. 3, p. 725, 2012.
- [283] F. Duerr, Y. Meuret, and H. Thienpont, "Tracking integration in concentrating photovoltaics using laterally moving optics," *Optics Express*, vol. 19, no. 103, pp. A207–A218, 2011.

LIST OF PUBLICATIONS

Publications with peer-review

Paire, M., L. Lombez, J.-F. Guillemoles, and D. Lincot. "Toward Microscale Cu(In,Ga)Se₂ Solar Cells for Efficient Conversion and Optimized Material Usage: Theoretical Evaluation." *Journal of Applied Physics* 108, no. 3 (2010) 034907.

Paire, M., L. Lombez, J.-F. Guillemoles, and D. Lincot. "Measuring Sheet Resistance of CIGS Solar Cell's Window Layer by Spatially Resolved Electroluminescence Imaging." *Thin Solid Films*, no. 519 (2011) 7493–7496.

Paire, M., L. Lombez, N. Pere-Laperne, S. Collin, J.-L. Pelouard, D. Lincot and J.-F. Guillemoles. "Microscale Solar Cells for High Concentration on Polycrystalline Cu(In,Ga)Se₂ Thin Films." *Applied Physics Letters* 98, no. 26 (2011) 264102.

Paire, M., A. Shams, L. Lombez, N. Pere-Laperne, S. Collin, J.-L. Pelouard, J.-F. Guillemoles and D. Lincot "Resistive and Thermal Scale Effects for Cu(In, Ga)Se₂ Polycrystalline Thin Film Microcells Under Concentration." *Energy Environ. Sci.* 4, no. 12 (2011) 4972–4977.

Publications without peer-review

Paire, M., A. Shams, L. Lombez, N. Pere-Laperne, S. Collin, J.-L. Pelouard, J.-F. Guillemoles and D. Lincot "Microscale Cu(In, Ga)Se₂ Solar Cells for Concentration : a Path to 30% Efficiency : Theoretical Evaluation and First Experimental Results." In *25th European Photovoltaic Solar Energy Conference, 6-11 September 2010, Valencia, Spain, 2872–2876*, (2010).

Paire, M., A. Shams, L. Lombez, N. Pere-Laperne, S. Collin, J.-L. Pelouard, J.-F. Guillemoles and D. Lincot. "Physics of Cu(In, Ga)Se₂ Solar Cells in High Injection Regime." In *Proceedings of the 37th IEEE Photovoltaic Specialists Conference*. Seattle, (2011).

Paire, M., A. Shams, L. Lombez, N. Péré-Laperne, S. Collin, A. Perona, A. Dollet, J.-L. Pelouard, J.-F. Guillemoles, and D. Lincot. "Microscale Thin Film Solar Cells: A Concept for Ultra-High Solar Concentration." In *Proceedings of the 26th European Photovoltaic Solar Energy Conference and Exhibition*, 730 – 732, (2011)

Paire, M., L. Lombez, F. Donsanti, M. Jubault, N. Péré-Laperne, S. Collin, A. Perona, et al. "Cu(In,Ga)Se₂ Photovoltaic Microcells for High Efficiency and Low Material Usage." In *Proceedings of SPIE Photonic West Conference*, 8256–18. San Francisco, CA, USA, (2012).

J.-F. Guillemoles, A. Le Bris, M. Paire, L. Lombez, S. Laribi, D. Lincot, C. Colin, S. Collin, J.-L. Pelouard, M. Laroche, R. Esteban, J.-J. Greffet, G. Boissier, and P. Christol, "Hot-carrier solar cells," *SPIE Newsroom*, (2011) DOI: 10.1117/2.1201104.003579

APPENDICES

APPENDICES	263
APPENDIX A. HEAT CONDUCTION EQUATIONS	265
1. Physical problem	265
2. Average temperature increase.....	275
APPENDIX B. TRANSMISSION LINE METHOD.....	277
APPENDIX C. PHOTOLITHOGRAPHY	281
1. Principals of photolithography	281
APPENDIX D. OPEN-CIRCUIT VOLTAGE IN THE SHOCKLEY-QUEISSER LIMIT	285
APPENDIX E. FEM PROGRAM FOR THE STUDY OF SEMICONDUCTORS UNDER HIGH INJECTION.....	287
1. Physical problem.....	287
2. Finite-Element Method (FEM).....	290
3. Results.....	295
APPENDIX F. MICROCELLS WITH LOCALIZED ABSORBERS	303
1. A top down fabrication process: study of mesa delineated microcells on co-evaporated Cu(In, Ga)Se ₂ absorbers	303
2. A bottom-up process: electrodeposition	312
APPENDIX G. ADAPTATION OF THE MICROCELL FABRICATION PROCESS TO FINISHED CELLS	317
1. Performance of microcells fabricated on complete stacks.....	317
APPENDICES BIBLIOGRAPHY	319

APPENDIX A. HEAT CONDUCTION EQUATIONS

1. Physical problem

1.1. Semi-infinite media

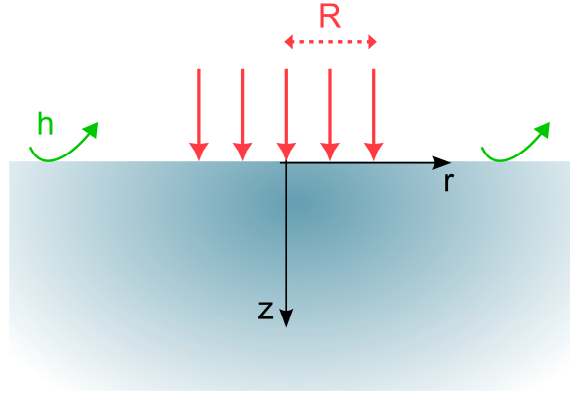


Figure A-1 : Semi-infinite media under a localized heat flux ($r < R$), with natural convection at the surface.

We consider a semi-infinite media that is uniformly heated on a small circular area of radius R at the surface. We use a cylindrical coordinates system and neglect the variation of temperature with the angle, as we suppose we have a symmetry of revolution. The temperature in the media under steady-state conditions is given by the heat conduction equation [1–3] :

$$\Delta\theta = \frac{\partial^2\theta}{\partial r^2} + \frac{1}{r} \frac{\partial\theta}{\partial r} + \frac{\partial^2\theta}{\partial z^2} = 0 \quad (\text{A-1})$$

The boundary conditions are:

$$\begin{aligned} \theta &\rightarrow 0, z \rightarrow \infty \\ h\theta - k_{th} \frac{\partial\theta}{\partial z} &= \begin{cases} Q & (r \leq R) \\ 0 & (r > R) \end{cases} \end{aligned} \quad (\text{A-2})$$

where $\theta = T - T_\infty$ is the temperature elevation from the ambient, h the coefficient of natural convection, k_{th} the thermal conductivity defined in Fourier's law and Q the heat flux incident on the disk of radius R .

We assume a separation of variables : $\theta(r, z) = R(r) \times Z(z)$. Equation (A-1) thus becomes :

$$\frac{1}{R} \left(\frac{\partial^2 R}{\partial r^2} + \frac{1}{r} \frac{\partial R}{\partial r} \right) + \frac{1}{Z} \frac{\partial^2 Z}{\partial z^2} = 0 \quad (\text{A-3})$$

The functions $R(r)$ and $Z(z)$ are independent, the only solution to satisfy this equation is if each group is equal to a constant:

$$\left(\frac{\partial^2 R}{\partial r^2} + \frac{1}{r} \frac{\partial R}{\partial r}\right) = -\lambda^2 R \quad (\text{A-4})$$

$$\frac{\partial^2 Z}{\partial z^2} = \lambda^2 Z$$

As thus temperature elevation tends to 0 when z tends to infinity, we find $Z = Z_0 \exp(-\lambda z)$.

The equation for R is the Bessel differential equation, thus the solution should be a linear combination of the Bessel function of the first and second kind of order 0. As we include the origin ($r = 0$), the Bessel function of the second kind of order 0 is excluded. Thus $R = R_0 J_0(\lambda r)$, where J_0 is the Bessel function of order 0 of the first kind.

We can define the Hankel transform of θ :

$$\bar{\theta}(\lambda, z) = \int_0^\infty \theta(r, z) J_0(\lambda r) r dr \Leftrightarrow \theta(r, z) = \int_0^\infty \bar{\theta}(\lambda, z) J_0(\lambda r) \lambda d\lambda \quad (\text{A-5})$$

After Hankel transform, the second boundary condition (A-2) is:

$$(h + k_{th}\lambda)\bar{\theta} = \int_0^R Q J_0(\lambda r) r dr = \frac{QRJ_1(\lambda R)}{\lambda} \quad (\text{A-6})$$

$$\Rightarrow \bar{\theta} = \frac{QRJ_1(\lambda R)}{\lambda(h + k_{th}\lambda)}$$

where J_1 is the Bessel function of the first kind of order 1.

Using equation (A-5) :

$$\theta(r, z) = \int_0^\infty \frac{QRJ_1(\lambda R) J_0(\lambda r) \exp(-\lambda z)}{(h + k_{th}\lambda)} d\lambda \quad (\text{A-7})$$

From that point we can derive the general solution $\theta(r, z)$ as:

$$\theta(r, z) = \frac{QR}{k_{th}} \int_0^\infty \frac{\exp(-\lambda z) J_0(\lambda r) J_1(\lambda R)}{h/k_{th} + \lambda} d\lambda \quad (\text{A-8})$$

As Bessel functions are tabulated, this expression can be used directly in a calculation software. We used MATLAB, where the Bessel functions of the first kind are called $\text{besselj}(i,x)$, where i is the order and x the variable.

At the heat source center, the temperature is :

$$\theta(0,0) = \frac{QR}{k_{th}} \int_0^{\infty} \frac{J_1(\lambda R)}{h/k_{th} + \lambda} d\lambda \quad (\text{A-9})$$

If we neglect convection ($h = 0$), it can be shown [2] that equation (A-10) becomes $\theta(0,0) = QR/k_{th}$. When $hR \rightarrow \infty$ then $\theta(0,0) \rightarrow Q/h$. This is the temperature of an infinite plane source on a semi-infinite medium.

1.2. Film of finite thickness

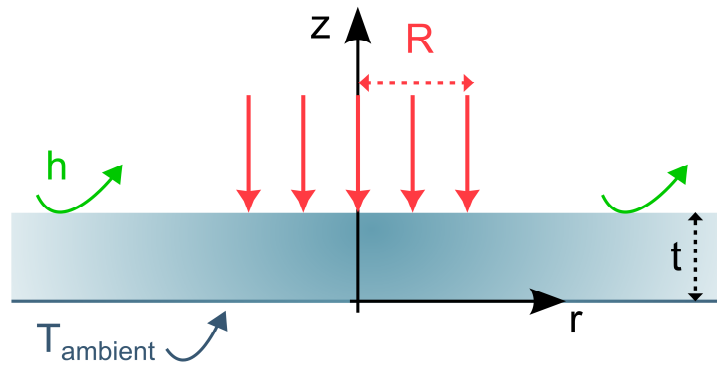


Figure A-2 : Layer of finite thickness t under a localized heat flux ($r < R$), with natural convection on the upper surface and ambient temperature maintained on the back.

Isothermal back surface

For a film of finite thickness t , we follow the same methodology as for the semi-infinite media. We consider that the film is heated on a small circular area of radius R at the surface ($z = t$). The temperature in the film under steady-state conditions is given by the heat conduction equation (A-3). The boundary conditions are:

$$\theta = 0, z = 0$$

$$h\theta + k_{th} \frac{\partial \theta}{\partial z} = \begin{cases} Q & (r \leq R) \\ 0 & (r > R) \end{cases}, z = t \quad (\text{A-10})$$

where $\theta = T - T_{\infty}$ is the temperature elevation from the ambient, h the coefficient of natural convection, k the thermal conductivity defined in Fourier's law and Q the heat flux incident on the disk of radius R . We assume a separation of variables : $\theta(r,z) = R(r) \times Z(z)$. As the temperature

elevation is 0 for $z = 0$, we find $Z = Z_0(\exp(-\lambda z) - \exp(\lambda z))$. As for the semi-infinite media, as the origin $(r, z) = (0, 0)$ is included, $R = R_0 J_0(\lambda r)$, where J_0 is the Bessel function of order 0 of the first kind.

After Hankel transform, the second boundary condition (A-10) is:

$$Z_0(h(\exp(-\lambda t) - \exp(\lambda t)) - k_{th}\lambda(\exp(-\lambda t) + \exp(\lambda t))) = \frac{QRJ_1(\lambda R)}{\lambda} \quad (\text{A-11})$$

$$\Rightarrow Z_0 = \frac{QRJ_1(\lambda R)}{\lambda(h(\exp(-\lambda t) - \exp(\lambda t)) - k_{th}\lambda(\exp(-\lambda t) + \exp(\lambda t)))}$$

Using equation (A-5) :

$$\theta(r, z) = \int_0^{\infty} \frac{QRJ_1(\lambda R)J_0(\lambda r)(\exp(-\lambda z) - \exp(\lambda z))}{(h - k_{th}\lambda)\exp(-\lambda t) - (h + k_{th}\lambda)\exp(\lambda t)} d\lambda \quad (\text{A-12})$$

From that point we can derive the general solution $\theta(r, z)$ as:

$$\theta(r, z) = \frac{-QR}{k_{th}} \int_0^{\infty} \frac{J_1(\lambda R)J_0(\lambda r)}{(\lambda + h/k_{th})} \frac{(\exp(-2\lambda z) - 1)}{\frac{\lambda - h/k_{th}}{\lambda + h/k_{th}} \exp(-2\lambda t) + 1} \exp(-\lambda(t - z)) d\lambda \quad (\text{A-13})$$

The temperature at the surface on the heat source center is:

$$\theta(0, t) = \frac{-QR}{k_{th}} \int_0^{\infty} \frac{J_1(\lambda R)}{(\lambda + h/k_{th})} \frac{\exp(-2\lambda t) - 1}{\frac{\lambda - h/k_{th}}{\lambda + h/k_{th}} \exp(-2\lambda t) + 1} d\lambda \quad (\text{A-14})$$

If we neglect the convection ($h = 0$),

$$\theta(0, t) = \frac{QR}{k_{th}} \int_0^{\infty} \frac{J_1(\lambda R)}{\lambda} \frac{1 - \exp(-2\lambda t)}{1 + \exp(-2\lambda t)} d\lambda \quad (\text{A-15})$$

$$\theta(0, t) = \frac{QR}{k_{th}} \int_0^{\infty} \frac{J_1(\lambda R)}{\lambda} \tanh(\lambda t) d\lambda$$

Note that in this case ($h = 0$), the temperature on the film surface is smaller than that of the semi-infinite media, as the factor $\tanh(\lambda t)$ is comprised between 0 and 1.

We performed simulations with the same numerical value as for the semi-infinite media. The glass has a thermal conductivity k_{th} of $9 \cdot 10^{-3}$ W/cm/K, and a thickness of 3 mm. We suppose that the

upper surface is exposed to natural convection, the coefficient of natural convection h being $25 \cdot 10^{-4}$ W/cm²/K, while the downward surface is kept at the ambient temperature. The heat flux used in our calculation is 100 W/cm², which corresponds to a $\times 1000$ illumination. We plot the temperature elevation from the ambient, θ , as a function of the dimensionless factor r/R , for a heat source radius R of 100 μ m.

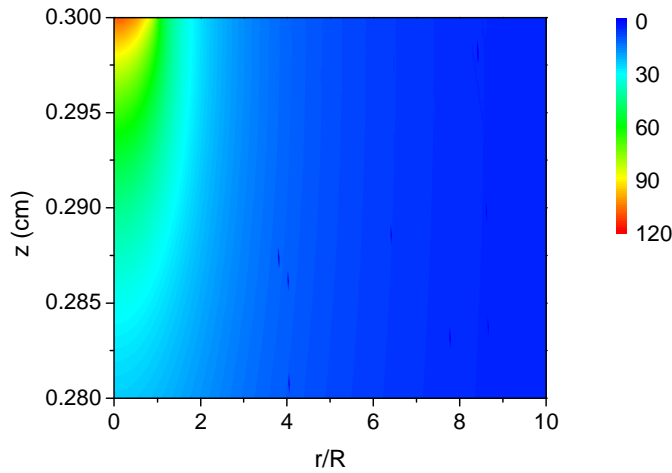


Figure A-3 : Temperature increase on a glass layer of finite thickness $t=3$ mm under a localized heat flux ($R = 100 \mu$ m, 100 W/cm²), with natural convection on the upper surface and ambient temperature maintained on the back.

One can see that for a sheet with isothermal back surface, the maximum temperature is similar to that of the infinite media (Figure III-18) , as expected from equation (A-15).

Convection at the back surface

The hypothesis of an isotherm back surface of glass is a classic textbook solution, but may not be really realistic, as no thermal element ensures that the temperature elevation at the back surface of a solar module is zero. Therefore we study the problem where the back surface is prone to conduction and convection, in the same manner as the upper surface. The boundary conditions are:

$$h\theta - k_{th} \frac{\partial \theta}{\partial z} = 0, z = 0$$

$$h\theta + k_{th} \frac{\partial \theta}{\partial z} = \begin{cases} Q & (r \leq R) \\ 0 & (r > R) \end{cases}, z = t$$
(A-16)

We can derive the temperature on the upper surface at the center of illumination as before.

After Hankel transform of the first boundary condition ($z = 0$), we obtain:

$$Z = Z_0 \left(\exp(-\lambda z) + \frac{k_{th}\lambda + h}{k_{th}\lambda - h} \exp(\lambda z) \right) \quad (\text{A-17})$$

Then with the second boundary condition ($z = t$) we obtain :

$$\Rightarrow Z_0 = \frac{QRJ_1(\lambda R)}{\lambda \left((h - k_{th}\lambda) \exp(-\lambda t) + \frac{k_{th}\lambda + h}{k_{th}\lambda - h} (h + k_{th}\lambda) \exp(\lambda t) \right)} \quad (\text{A-18})$$

Using equation (A-5) :

$$\theta(r, z) = \int_0^{\infty} \frac{QRJ_1(\lambda R)J_0(\lambda r) \left(\exp(-\lambda z) + \frac{k_{th}\lambda + h}{k_{th}\lambda - h} \exp(\lambda z) \right)}{(h - k_{th}\lambda) \exp(-\lambda t) + \frac{k_{th}\lambda + h}{k_{th}\lambda - h} (h + k_{th}\lambda) \exp(\lambda t)} d\lambda \quad (\text{A-19})$$

And thus :

$$\theta(r, z) = \frac{QR}{k_{th}} \int_0^{\infty} \frac{QRJ_1(\lambda R)J_0(\lambda r) \left(\exp(-\lambda z) + \frac{k_{th}\lambda + h}{k_{th}\lambda - h} \exp(\lambda z) \right)}{(h/k_{th} - \lambda) \exp(-\lambda t) + \frac{k_{th}\lambda + h}{k_{th}\lambda - h} (h/k_{th} + \lambda) \exp(\lambda t)} d\lambda \quad (\text{A-20})$$

The temperature at the surface on the heat source center is:

$$\theta(0, t) = \frac{QR}{k_{th}} \int_0^{\infty} \frac{J_1(\lambda R) \left(\frac{k_{th}\lambda - h}{k_{th}\lambda + h} \exp(-2\lambda t) + 1 \right)}{(h/k_{th} + \lambda) \left(- \left(\frac{k_{th}\lambda - h}{k_{th}\lambda + h} \right)^2 \exp(-2\lambda t) + 1 \right)} d\lambda \quad (\text{A-21})$$

In this case we cannot neglect convection, because then the steady state temperature would be infinite.

We performed simulation with parameters similar to that used before. We can see that with convection at the back surface the temperature increase on the surface tends to be slightly higher than with the isothermal condition, but there is less than 5% difference between both simulations. On the back surface the temperature increase is less than 3°C above the ambient for the convective condition on the back surface, compared to 0 when the ambient temperature is imposed.

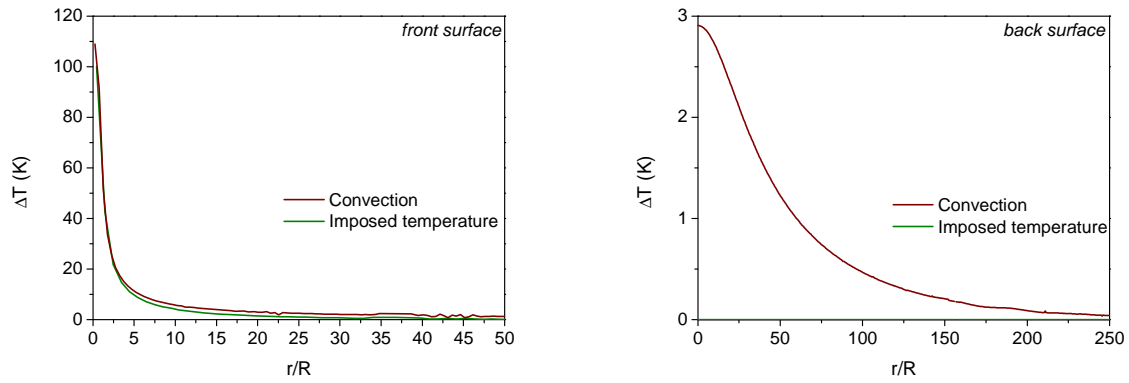


Figure A-4 : Temperature increase on a glass layer of finite thickness $t=3$ mm under a localized heat flux ($R = 100 \mu\text{m}$, 100 W/cm^2), with natural convection on the upper surface and convection (red line) or imposed ambient temperature (green line) on the back surface. (left) Temperature increase on the front surface as a function of position for the two boundary conditions. (right) Temperature increase on the back surface as a function of position for the two boundary conditions.

For a more precise simulation of thin film solar cells, we have to take into account the whole stack. The metal and semiconducting layers should be nearly isothermal as they are extremely thin and have a good thermal conductivity, but the repartition of the heat flux could result in different value of the maximum temperature.

1.3. Thermal behavior of the Cu(In,Ga)Se_2 stack

Isothermal back surface

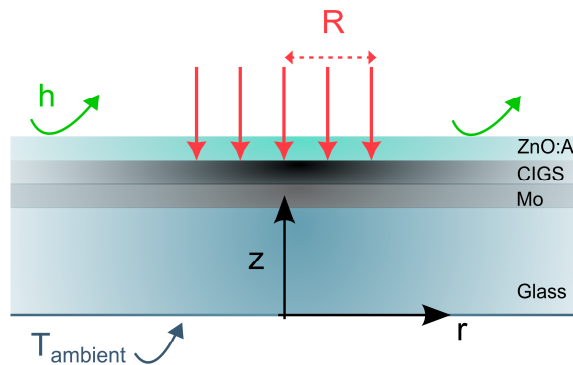


Figure A-5 : Thin film solar cell under a localized heat flux at the window/absorber interface ($r < R$), with natural convection at the upper surface and the ambient temperature imposed at the back of the substrate.

We now consider a stack of four layers: glass, molybdenum, Cu(In,Ga)Se_2 , ZnO:Al. For each layer we define a thickness and thermal coefficient. The heat source is supposed to arrive at the ZnO:Al / absorber interface, and has a radius R . The back plane of the glass substrate is kept at the ambient temperature while the upper ZnO:Al surface is prone to convection. At each of the interfaces we

ensure the continuity of the temperature and heat flux. The temperature in the film under steady-state conditions is given by the heat conduction equation (A-3). This method is very similar to that employed for LED by [4].

The boundary conditions are now for the temperature continuity:

$$\begin{aligned}\theta_{glass} &= \theta_{Mo}, & z &= t_{glass} = h_1 \\ \theta_{Mo} &= \theta_{CIGS}, & z &= t_{glass} + t_{Mo} = h_2 \\ \theta_{CIGS} &= \theta_{ZnO}, & z &= t_{glass} + t_{Mo} + t_{CIGS} = h_3\end{aligned}\tag{A-22}$$

For the heat flux continuity :

$$\begin{aligned}-k_{glass} \frac{\partial \theta_{glass}}{\partial z} &= -k_{Mo} \frac{\partial \theta_{Mo}}{\partial z}, & z &= t_{glass} \\ -k_{Mo} \frac{\partial \theta_{Mo}}{\partial z} &= -k_{CIGS} \frac{\partial \theta_{CIGS}}{\partial z}, & z &= t_{glass} + t_{Mo}\end{aligned}\tag{A-23}$$

The heat flux Q arrives at the ZnO:Al/absorber on a disk of radius R :

$$k_{CIGS} \frac{\partial \theta_{CIGS}}{\partial z} - k_{ZnO} \frac{\partial \theta_{ZnO}}{\partial z} = Q, \quad z = t_{glass} + t_{Mo} + t_{CIGS}\tag{A-24}$$

For the upper and downward surfaces :

$$\begin{aligned}\theta_{glass}(r, 0) &= 0 \\ h\theta_{ZnO} &= -k_{ZnO} \frac{\partial \theta_{ZnO}}{\partial z}, & z &= t_{glass} + t_{Mo} + t_{CIGS} + t_{ZnO} = h_4\end{aligned}\tag{A-25}$$

We assume a separation of variables for the temperature field in each layer : $\theta_i(r, z) = R_i(r) \times Z_i(z)$. The function $Z_i(z)$ is of the general form $Z_i = A_i \exp(-\lambda z) + B_i \exp(\lambda z)$. We will have now to determine all 8 (A_i, B_i) coefficients with help of the 8 boundary conditions (equations (A-25), (A-24), (A-23) and (A-22)).

The temperature in each layer i can be written as :

$$\theta(r, z) = \int_0^{\infty} (A_i \exp(-\lambda z) + B_i \exp(\lambda z)) J_0(\lambda r) \lambda d\lambda\tag{A-26}$$

Where the coefficient (A_i, B_i) are the solution of :

$$M \begin{bmatrix} A_{glass} \\ B_{glass} \\ A_{Mo} \\ B_{Mo} \\ A_{CIGS} \\ B_{CIGS} \\ A_{ZnO} \\ B_{ZnO} \end{bmatrix} = \begin{bmatrix} 0 \\ 0 \\ 0 \\ 0 \\ 0 \\ \frac{QR \exp(-\lambda h_3) J_1(\lambda R)}{\lambda} \\ 0 \\ 0 \end{bmatrix} \quad (A-27)$$

with the matrix M being:

$$M = \begin{bmatrix} 1 & 1 & 0 & 0 & 0 & 0 & 0 & 0 \\ \exp(-2\lambda h_1) & 1 & -\exp(-2\lambda h_1) & -1 & 0 & 0 & 0 & 0 \\ \exp(-2\lambda h_1) & -1 & -\frac{k_{Mo}}{k_{glass}} \exp(-2\lambda h_1) & \frac{k_{Mo}}{k_{glass}} & 0 & 0 & 0 & 0 \\ 0 & 0 & \exp(-2\lambda h_2) & 1 & -\exp(-2\lambda h_2) & -1 & 0 & 0 \\ 0 & 0 & \exp(-2\lambda h_2) & -1 & -\frac{k_{CIGS}}{k_{Mo}} \exp(-2\lambda h_2) & \frac{k_{CIGS}}{k_{Mo}} & 0 & 0 \\ 0 & 0 & 0 & 0 & \lambda k_{CIGS} \exp(-2\lambda h_3) & -\lambda k_{CIGS} & -\lambda k_{ZnO} \exp(-2\lambda h_3) & \lambda k_{ZnO} \\ 0 & 0 & 0 & 0 & \exp(-2\lambda h_3) & 1 & -\exp(-2\lambda h_3) & -1 \\ 0 & 0 & 0 & 0 & 0 & 0 & (-\lambda k_{ZnO} - h) \exp(-2\lambda h_4) & \lambda k_{ZnO} - h \end{bmatrix}$$

Therefore we can simulate the whole Cu(In,Ga)Se₂ solar cell under localized heating with an isothermal back surface (Figure (A-6)).

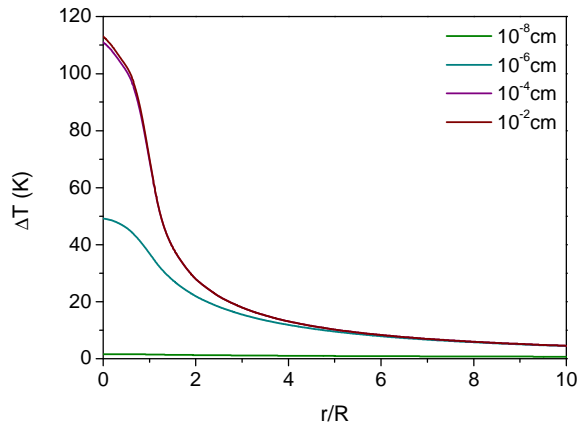


Figure A-6 : Temperature increase at the glass surface of a Cu(In,Ga)Se₂ solar cell as function of the dimensionless variable r/R , for $R=100 \mu\text{m}$, and various Mo layer thicknesses. The thickness of Cu(In,Ga)Se₂ and ZnO layers are set thin ($\ll 1 \text{ \AA}$). The back surface is kept at ambient temperature.

One can see that with increasing Mo layer thickness on top of the glass substrate, the maximum temperature increase is smaller. One can note also that for a molybdenum layer that is extremely thin, the maximum temperature increase is similar to that found on a simple film. With a $1 \mu\text{m}$ Mo the maximum temperature increase is more than divided by two compared to the bare glass

substrate. If we add ZnO and Cu(In,Ga)Se₂ layers (Figure A-7), then the maximum temperature increase is around 10K less.

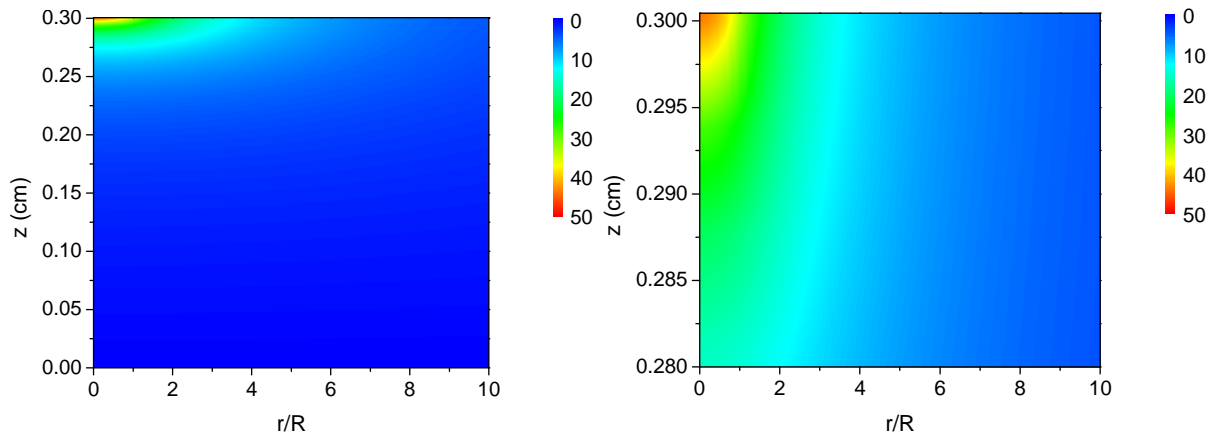


Figure A-7 : (left) Temperature elevation from the ambient in a standard Cu(In,Ga)Se₂ stack (Glass 3mm, Mo 1 μ m, Cu(In,Ga)Se₂ 3 μ m, ZnO 500 nm), with ambient temperature imposed on the back surface. (right) Zoom of the left graph on the upper surface.

Convection at the back surface

If we want to simulate the stack with convection at the back surface of glass instead of imposed temperature, the boundary condition at $z = 0$ becomes :

$$h\theta_{glass} - k_{th} \frac{\partial \theta_{glass}}{\partial z} = 0, z = 0 \quad (\text{A-28})$$

Then we have to modify the first line of the matrix M that becomes:

$$M(1,:) = [(h + \lambda k_{Glass}) \quad (h - \lambda k_{Glass}) \quad 0 \quad 0 \quad 0 \quad 0 \quad 0 \quad 0] \quad (\text{A-29})$$

We can see that there is no fundamental difference between imposing back temperature or setting a convection term. The temperature field is slightly higher with natural convection (Figure A-8), but the differences are less than 5 K.

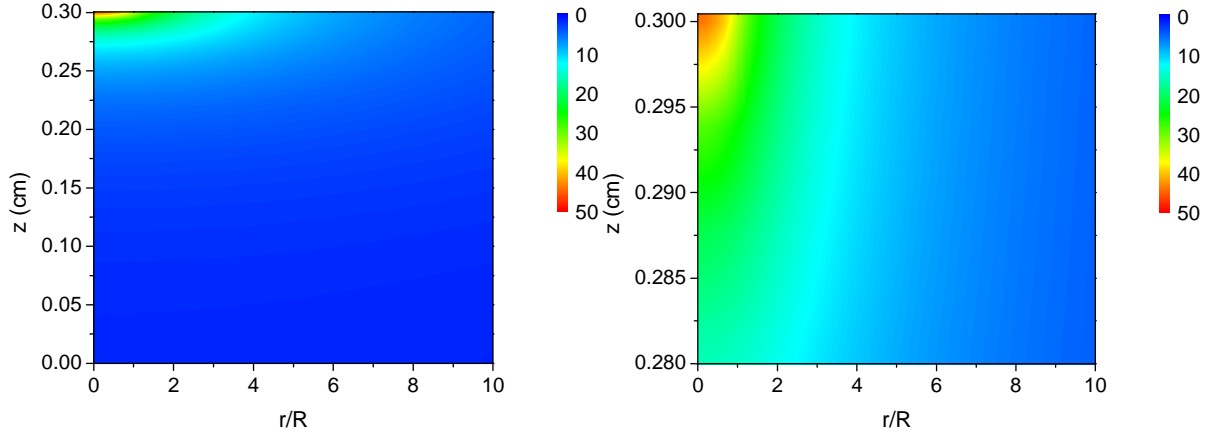


Figure A-8 : (left) Temperature elevation from the ambient in a standard Cu(In,Ga)Se₂ stack (Glass 3mm, Mo 1 μm, Cu(In,Ga)Se₂ 3 μm, ZnO 500 nm), with convection on the back surface. (right) Zoom of the left graph on the upper surface.

2. Average temperature increase

We insisted above on the maximum local temperature increase, as this value is important concerning the damage threshold and device life time span. However, from an experimental point of view, the parameter that will impact current-voltage measurement is not the maximum but the average temperature over the microcell. Therefore it is interesting to study the average temperature as a function of microcell size.

The average temperature on a microcell of radius R can be defined as the temperature given by a current-voltage measurement :

$$J_{dark} = J_0 \exp\left(\frac{qV}{AkT_{av}(R)}\right) = \frac{2J_0}{R^2} \int_0^R \exp\left(\frac{qV}{AkT(r)}\right) r dr \quad (A-30)$$

We neglected the temperature dependence over the z -coordinate as the Cu(In,Ga)Se₂ layer is essentially isothermal in this direction. Thus

$$T_{av}(R) = \frac{qV}{Ak} \frac{1}{\ln\left(\frac{2}{R^2} \int_0^R \exp\left(\frac{qV}{AkT(r)}\right) r dr\right)} \quad (A-31)$$

We suppose that the temperature $T(r)$ is of the form $T(r) = T_0 + \Delta T(r) \approx T_0 + \Delta T_{max}(1-(r/R)^2(1-\alpha))$, which is close to what we have calculated above. Thus, after careful integration, we find :

$$T_{av}(R) = \frac{qV}{nk} \frac{1}{\ln \left(\frac{-2qV}{(1-\alpha)nk\Delta T_{max}} \left[\frac{x}{2} \exp\left(\frac{1}{x^2}\right) - \frac{1}{2} E_i\left(\frac{1}{x^2}\right) \right] \frac{\sqrt{\alpha Ak \Delta T_{max}/qV}}{\sqrt{Ak \Delta T_{max}/qV}} \right)} \quad (\text{A-32})$$

where E_i is the exponential integral function, $E_i(x) = \int_{-\infty}^x \exp(t)/t dt$. We have seen that the maximum temperature increase ΔT_{max} is proportional to the microcell radius R , thus we set $\Delta T_{max} = \beta R$. Then we shall write:

$$T_{av}(R) = \frac{qV}{nk} \frac{1}{\ln \left(\frac{-2qV}{(1-\alpha)nk\beta R} \left[\frac{x}{2} \exp\left(\frac{1}{x^2}\right) - \frac{1}{2} E_i\left(\frac{1}{x^2}\right) \right] \frac{\sqrt{\alpha Ak \beta R/qV}}{\sqrt{Ak \beta R/qV}} \right)} \quad (\text{A-33})$$

The relation between $T_{av}(R)$ and R is intricate. We found that for large values of R ($R > 1$ mm), T_{av} is nearly linear with the radius. For smaller values of R there is a deviation from linearity, and the average temperature has a weaker dependence on the radius.

APPENDIX B. TRANSMISSION LINE METHOD

To determine the best metal for front contact, we conducted transmission line measurements to access the contact resistivity value between ZnO:Al and different metals: Au, Al, Pt and Ti.

Theory

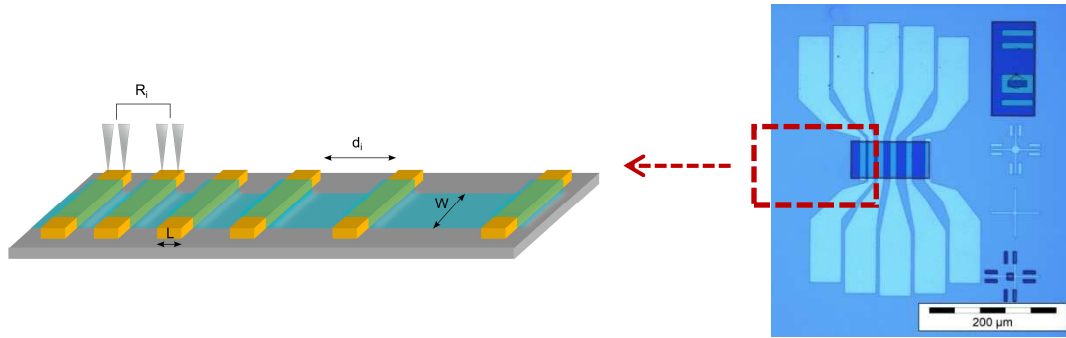


Figure B-1 : (left) Sketch of the TLM structure. (right) optical microscope image of a TLM mesa of Ti/Pt on GaAs substrate covered with ZnO:Al.

Six metal electrodes (width $L = 5 \mu\text{m}$) are deposited on an insulating GaAs substrate, defining five inter-electrode spacings d_i . On top of the metal electrodes is deposited a ZnO:Al mesa (width $W = 50 \mu\text{m}$) by sputtering. In order to improve the adhesion of the metals on the GaAs substrate, we use a thin (20 nm) Ti adhesion layer between the metal and the substrate. The resistance R_i for a given spacing d_i is [5], [6] :

$$R_i = 2 \times R_c + R_{\square} \frac{d_i}{W} \quad (\text{B-1})$$

where R_c is the contact resistance between the Au and ZnO:Al layers, and R_{\square} the ZnO:Al layer sheet resistance. The current flowing through the ZnO:Al layer is transferred to the metal electrode over a characteristic length L_T , referred to as the transfer length, and defined as [6]:

$$R_c = \frac{R_{\square} L_T}{W} \coth\left(\frac{L}{L_T}\right) \quad (\text{B-2})$$

One can determine the specific contact resistance $\rho_c = R_{\square} L_T^2$. We can also deduce the resistance associated with the front contact in a microcell. Indeed the current flowing in the window layer is transferred to the metal layer on a ring of inner radius r , the radius of the microcell, and of outer radius $r + L_T$ resulting in a contact resistance [5]:

$$R_{c,microcell} = \frac{\rho_c}{2\pi r L_T} \quad (\text{B-3})$$

Experiment

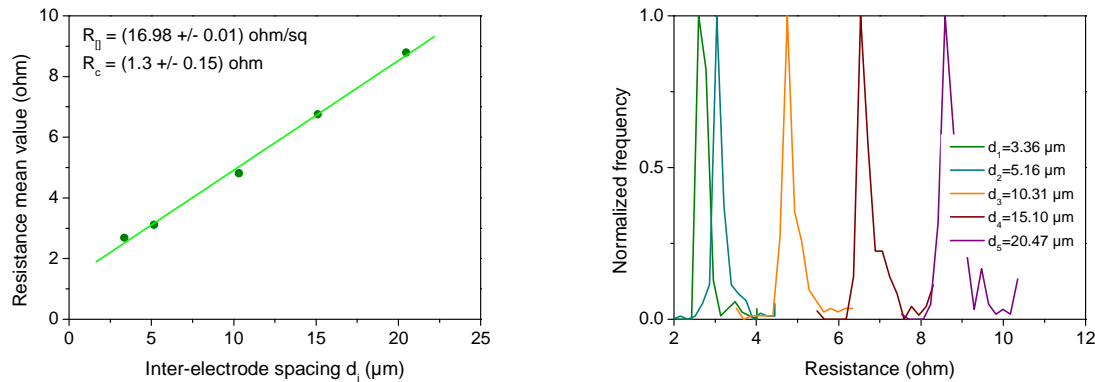


Figure B-2: (left) Resistance as a function of inter-electrode spacing for Ti/Au/ZnO:Al, average over 193 mesas. (right) Statistical repartition of the resistance for each inter-electrode spacing.

For each metal under test, we produce about 200 mesas in order to get statistical results (Figure B-2 right). We measure on each mesa the five resistances R_i in a four terminals configuration (Figure IV-7 left). We then have the value of the resistance as a function of the spacing, averaged over around 200 mesas (Figure B-2), and can extract the transfer length and contact resistivity, as shown in Table IV-1.

Table B-1 : Transfer length and contact resistivity between 5 metals and sputtered ZnO:Al, calculated according to equations (B-1) and (B-2). The contact Ti/Al/ZnO:Al is so resistive that a proper analysis of the TLM was made impossible.

Metal	Ti/Au	Ti/Al	Ti/Ni	Ti/Pt	Ti
L_T (μm)	2	/	7	7	16
ρ_c (ohm.cm^2)	$5 \cdot 10^{-7}$	/	$7 \cdot 10^{-6}$	$9 \cdot 10^{-6}$	$6 \cdot 10^{-5}$

It is clear that gold is the best contact to ZnO:Al in our experiment. Resistance is found linear with inter-electrode spacing and the statistical repartition of the measures show small standard deviation. For the other metals, the contact is not as good as gold, and a slightly non-linear behavior of the resistance as a function of inter-electrode spacing is found for small inter-electrode distance. The Ti/Al/ZnO:Al contact is so resistive that interpretation of the results is hazardous, probably because of the formation of an Al_2O_3 insulating phase at the surface of Al that was not removed before the sputtering of the Al doped ZnO layer.

We chose gold as the front contact metal for microcells for the rest of our study. The contact resistance of the front contact, $R_{c,microcell}$, for a microcell of diameter 50 μm is 0.2 ohm or $4 \cdot 10^{-6}$ ohm. cm^2 (equation (B-3)). The front contact has therefore a resistance that is sufficiently low to be neglected compared to the other sources of resistance in a solar cell. (See chapter III). Therefore with gold the front contact resistance is never limiting to the device.

APPENDIX C. PHOTOLITHOGRAPHY

1. Principals of photolithography

1.1. Basis

Photolithography is a patterning technique that relies on the use of photoresist, i.e. photosensitive polymers. The properties of the photoresist change upon exposure to light (usually UV-light). They are classified in two categories. Positive photoresists have the properties to be highly soluble after exposure to UV. On the opposite, negative photoresists are less soluble in the developer after exposure than before (Figure C-1).

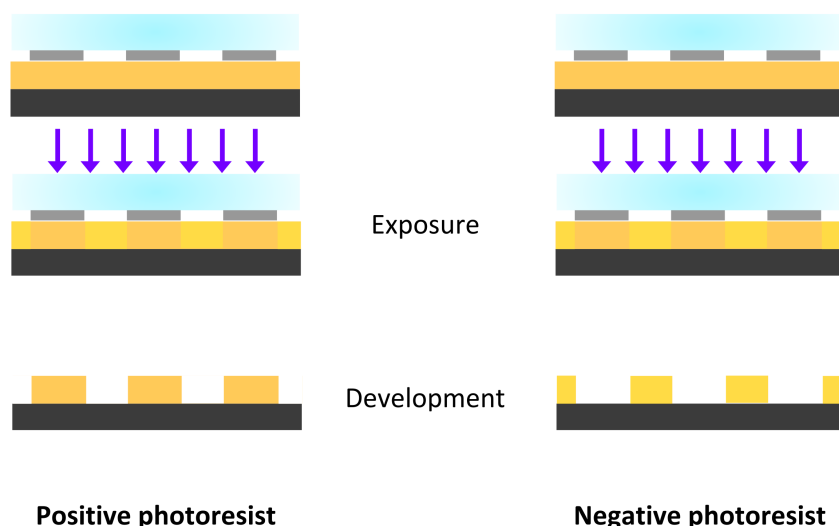


Figure C-1 : Definition of a positive or negative photoresist. The two types of photoresists differs by the high development rate of either exposed or unexposed area.

After exposure to UV-light, patterns can be created by the difference in development rates of exposed/unexposed zones. The photoresist are made of three principal components: a polymer, a photoactive compound and a solvent. The chemistry of AZ[®] photoresists, which are the one used in this thesis, is described briefly hereafter. More details can be found in MicroChemicals booklet [7].

1.2. Chemistry of photoresist

The resin of AZ[®] photoresists is Novolak, a mixture of phenol and formaldehyde. The photoactive compound of AZ[®] photoresists is a product of the family of diazonaphthoquinone-sulphonates (DNQ). The presence of the DNQ compound reduces the alkaline solubility of the resist by several orders of magnitude. During exposure to UV light of desired wavelength (<440 nm), the DNQ compound transforms into a carboxylic acid. This transformation leads to the creation of nitrogen

and adsorption of water. After exposure the photoresist is highly solvable in alkaline solution, the development rate being several orders of magnitude higher than unexposed resist (positive resist).

Negative resists such as AZ[®] 2070 contain a crosslinker that is activated during exposure and crosslink the resist during post-bake making it poorly soluble in developer.

1.3. Process

1.3.1. Spin-coating

The spin coating parameters (time, speed, acceleration) define the resin homogeneity and thickness. The last two digits of the AZ[®] photoresist name represent the thickness ($\times 100\text{nm}$) of the resin spin-coated at 4000 rpm. The thickness is inversely proportional to the square root of spinning speed, therefore thickness of the resin layer can be adjusted if needed.

1.3.2. Prebake

The prebake reduces the solvent content of the resin (concentration drops from more than 50% to less than 5%). This step has several consequences, such as lowering bubbles formation during exposure, increasing adhesion of the film to the substrate or lowering dark erosion (development of unexposed resist in the developer). Prebake also decomposes the photoactive compound. Therefore a long/hot prebake will result in a longer development time for constant exposure.

1.3.3. Exposure

Exposure to UV-light enables the reaction of the photoactive compound. The structure resolution is limited by diffraction. Diffraction increases with the gap between the sample and photomask. The lateral resolution of an image d is linked to the gap g and exposure wavelength by $= \sqrt{g\lambda}$. This gap can be important in case of a rough substrate for example. In our case it is therefore not possible to have well defined structures that are smaller than $1\ \mu\text{m}$.

1.3.4. Post-exposure bake

Post-exposure bakes are not compulsory. They are needed in case of negative crosslinking resists, such as AZ[®] 2070. The post-bake completes the cross-linking mechanism initiated during exposure. A post-bake step can also relax mechanical stress in the resist in thick films.

1.3.5. Development

Developer selectively etches exposed/unexposed resists. In case of a positive photoresist the ratio between the development of unexposed resist to that of exposed zone decreases with developer concentration. A proper dilution is the equilibrium between sufficient etching rate and good selectivity.

1.3.6. Image reversal

Image reversal resists can be processed either in positive or negative tone. The first exposure dose can control profile of the structure sidewalls. If the exposure dose is low, the near-substrate resist is not much exposed, which makes it very soluble, and favors undercut. The resist can be directly developed and forms a positive pattern. If one wants to reverse the structure, more process steps are needed. The image reversal bake makes the exposed resist area insoluble, whereas unexposed areas are unchanged. A flood exposure, i.e. exposure of the entire sample without a mask, makes the area unexposed up to now developable. Then the sample is developed, a long development time ensure a good undercut of the structures, which is of extreme importance for lift-off.

1.3.7. Etch and lift-off

Once the photoresist pattern is created on the substrate one can either use it to etch the substrate or to protect the substrate from the deposition of a new layer and then dissolve the resist. The later process is called lift-off.

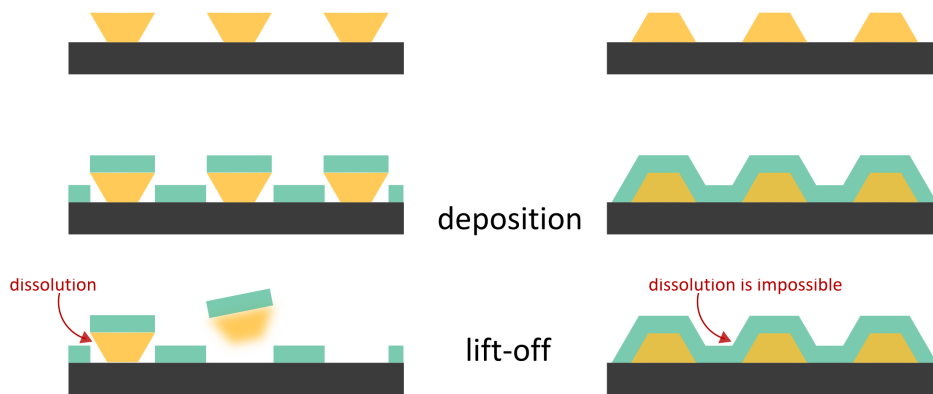


Figure C-2 : Lift-off for undercut profile structures or problem of badly shaped structures.

The profiles of the structure sidewalls are very important in case of a lift-off (Figure C-2). Indeed the resist is used to protect the substrate during deposition of an additional layer. For the resist to be dissolved in the lift-off step, the sidewalls of the structures have to be cleared, and a good undercut profile is necessary.

APPENDIX D. OPEN-CIRCUIT VOLTAGE IN THE SHOCKLEY-QUEISSER LIMIT

The Shockley Queisser limit [8] described an ideal solar cell with perfect absorption for energies above the bandgap E_g , internal quantum efficiency equal to 1 (each incident photon with energy above the bandgap creates an electron-hole pair), and perfect collection (or infinite mobility).

The Shockley Queisser limit is based on detailed balance, i.e. under equilibrium the flux incoming on a cell is equal to the flux emitted by the cell.

If the cell is considered as a black-body at temperature T , under an applied voltage V , it emits a flux that can be estimated in the limit of $E - qV \gg kT$, by a Boltzmann distribution :

$$\phi(V, E) = a(E)\phi_{bb}(E)\exp\left(\frac{qV}{kT}\right) = a(E)\frac{2\pi E^2}{h^3 c^2}\exp\left(\frac{-E}{kT}\right)\exp\left(\frac{qV}{kT}\right) \quad (\text{D-1})$$

Where $\phi_{bb}(E)$ is the black-body radiation $\frac{2\pi E^2}{h^3 c^2}\exp\left(\frac{-E}{kT}\right)$. This flux is emitted by radiative recombination, the only recombination mechanism considered in the ideal Shockley-Queisser limit. In the absence of applied voltage and illumination, no current flows in the solar cell, and recombination current equals current photogenerated by the black-body radiation of the environment at temperature T . Thus the recombination current is:

$$J_{rad} = J_{0,rad}\left(\exp\left(\frac{qV}{kT}\right) - 1\right) \quad (\text{D-2})$$

$$\text{with } J_{0,rad} = q \int_{E_g}^{\infty} \phi_{bb}(E)dE$$

Under illumination and applied bias, the current in an ideal cell is :

$$J = J_{0,rad}\left(\exp\left(\frac{qV}{kT}\right) - 1\right) - J_{sc} \quad (\text{D-3})$$

Where J_{sc} is the photogenerated current density under an illumination photon flux $\phi_{sun}(E)$:

$$J_{sc} = q \int_{E_g}^{\infty} \phi_{sun}(E)dE \quad (\text{D-4})$$

OPEN-CIRCUIT VOLTAGE IN THE SHOCKLEY-QUEISSER LIMIT

Combining equations (D-2),(D-3) and (D-4), the open-circuit voltage in the Shockley-Queisser limit is :

$$V_{oc,SQ} = \frac{kT}{q} \ln \left(\frac{J_{sc}}{J_{0,rad}} + 1 \right) \quad (D-5)$$

More details on the detailed balance theory and Shockley-Queisser limit can be found in references [8], [9].

APPENDIX E. FEM PROGRAM FOR THE STUDY OF SEMICONDUCTORS UNDER HIGH INJECTION

1. Physical problem

1.1. Hypothesis and context

In order to study semiconductors under high light fluxes, continuity and Poisson equations have to be solved self-consistently. We study a 1D problem, with a semiconductor of length L , for the sake of simplicity.

The electron j_n and hole j_p current densities are :

$$j_n = -q\mu_n n \frac{dv}{dx} + qD_n \frac{dn}{dx} = q\mu_n nE + qD_n \frac{dn}{dx} \quad (\text{E-1})$$

$$j_p = -q\mu_p p \frac{dv}{dx} - qD_p \frac{dp}{dx} = q\mu_p pE - qD_p \frac{dp}{dx} \quad (\text{E-2})$$

where q is the elementary charge, μ the mobility, n and p respectively the electron and hole concentrations, v the electrostatic potential, E the electric field ($E = -\frac{dv}{dx}$).

The continuity equations are :

$$-\frac{1}{q} \text{div}(j_n) = g_n(x) - r_n(x) = g(x) - r(x) = \mu_n \frac{d}{dx} \left(n \frac{dv}{dx} \right) - D_n \frac{d^2 n}{dx^2} \quad (\text{E-3})$$

$$\frac{1}{q} \text{div}(j_p) = g_p(x) - r_p(x) = g(x) - r(x) = -\mu_p \frac{d}{dx} \left(p \frac{dv}{dx} \right) - D_p \frac{d^2 p}{dx^2} \quad (\text{E-4})$$

where g is the generation rate and r the recombination rate, that are equal for holes and electrons. We choose an only source of recombination that is the radiative recombination.

$$r(x) = b(np - n_i^2) \quad (\text{E-5})$$

where b is the radiative recombination coefficient, and n_i^2 the value of the product $n \times p$ at equilibrium.

An other recombination mechanism, such as Shockley-Read, could be employed as well. It should be noted that here b is supposed to be independent on the carrier concentration, i.e. on the illumination intensity. This hypothesis will not be valid under ultra-high illumination, where Auger recombination is non-negligible, leading to a coefficient b that is dependent on illumination.

Based on equations (VI-15) and (VI-16), $j_n + j_p$ is a constant for all positions. The electric potential v is linked to the carrier concentrations through Poisson's equation :

$$-\frac{d^2v}{dx^2} = \frac{q}{\epsilon}(p - n + \rho) \quad (\text{E-6})$$

It is important to note that no simplifications are made concerning majority or minority carrier. Indeed our aim is to study a regime where the incident light flux generates carriers in a quantity close to or superior to the doping. In this regime no carrier type can be consider in majority (or minority) and the complete form of equations (III-8)and (E-2) has to be kept.

In order to solve equations (III-8), (E-2) and (VI-18), proper boundary conditions have to be determined. At the surface the bulk current have to be equal to the surface current.

$$j_n(0) = q\mu_n nE(0) + qD_n \frac{dn}{dx}(0) = q(n(0) - n_{eq})S_{nf} \quad (\text{E-7})$$

$$j_p(0) = q\mu_p nE(0) - qD_p \frac{dp}{dx}(0) = -q(p(0) - p_{eq})S_{pf} \quad (\text{E-8})$$

where n_{eq} and p_{eq} are the electron and hole concentration at equilibrium, without illumination.

We considered in equations (VI-19) and (VI-20) that the electric fields can be neglected at the surface, which represents a situation where the surfaces are ideal in the sense that no defect can induce a charging of the interface. The only source of electric field considered here is the charge carriers and doping of the bulk semiconductor.

For $x = 0$, that will be called "front" position, the boundary condition writes :

$$v(0) = 0$$

$$j_n(0) = q(n(0) - n_{eq})S_{nf} \quad (\text{E-9})$$

$$j_p(0) = -q(p(0) - p_{eq})S_{pf}$$

For $x = L$, that is called “back” position, the boundary condition writes :

$$v(L) = v_0$$

$$j_n(L) = -q(n(L) - n_{eq})S_{nb} \quad (\text{E-10})$$

$$j_p(L) = q(p(L) - p_{eq})S_{pb}$$

1.2. Dimensionless problem

The problem presented here will be solved numerically. Therefore the variables to be handled during the numerical resolution have to be of comparable value, in order to prevent a lack of accuracy stemming from the use of parameters differing from several orders of magnitude.

In order to numerically work on similar values, we use dimensionless variables, as shown in Table E-1.

Table E-1 : Dimensionless variables for FEM program

Variable	Classical	Dimensionless
position	x	$X = x/L$
electric potential	v	$V = v/V_{th}$, where $V_{th} = kT/q$ is the thermal voltage
carrier concentration	n, p	$N = n / (\epsilon V_{th} / qL^2), P = p / (\epsilon V_{th} / qL^2)$
charge concentration	ρ	$\Sigma = \rho / (\epsilon V_{th} / qL^2)$
electron current density	j_n	$J_n = -j_n / (D_n \epsilon V_{th} / L^3)$
hole current density	j_p	$J_p = j_p / (D_n \epsilon V_{th} / L^3)$
generation rate	g	$G_{n/p} = g / ((\epsilon D_{n/p} V_{th}) / qL^4)$
recombination rate	r	$R_{n/p} = r / ((\epsilon D_{n/p} V_{th}) / qL^4)$
recombination coefficient	b	$B_n = b \times (\epsilon V_{th} / qD_n), B_p = b \times (\epsilon V_{th} / qD_p)$
surface recombination velocity	$S_{(f/b)(n/p)}$	$S_{\left(\frac{f}{b}\right)\left(\frac{n}{p}\right)} = S_{(f/b)(n/p)} L / (D_{n/p})$

The dimensionless system to be solved is :

$$-V'' = (P - N + \Sigma) \quad (\text{E-11})$$

$$\text{div}(J_n) = G_n - R_n(N, P) = G_n - B_n(NP - N_i^2) = -N'' + (NV)'' \quad (\text{E-12})$$

$$\text{div}(J_p) = G_p - R_p(N, P) = G_p - B_p(NP - N_i^2) = -P'' - (PV)'' \quad (\text{E-13})$$

where $J_n = -N' + NV'$ and $J_p = -P' + PV'$

The boundary conditions become:

For $X = 0$

$$V(0) = 0$$

$$J_n(0) = -q(N(0) - N_{eq})S_{nf} \quad (\text{E-14})$$

$$J_p(0) = -q(P(0) - P_{eq})S_{pf}$$

For $X = 1$

$$V(1) = V_0$$

$$J_n(1) = q(N(1) - N_{eq})S_{nb} \quad (\text{E-15})$$

$$J_p(1) = q(P(1) - P_{eq})S_{pb}$$

2. Finite-Element Method (FEM)

In order to solve equations (E-11), (E-12) and (E-13), we build a finite element method program. The idea is to find V , N and P self-consistently, by multiple iterations. V at the step $k + 1$, V^{k+1} , is calculated based on N^k and P^k through the Poisson's equation (E-11). Then $N^{k+1}(x)$ is calculated by equation (E-12), with V^{k+1} and P^k . Finally P^{k+1} is calculated with equation (E-13), with V^{k+1} and $N^{k+1}(x)$. The convergence is obtained when the solution (V, N, P) at two consecutive steps are very close, i.e. $\left\| \frac{N^{k+1}(x) - N^k(x)}{N^{k+1}(x)} \right\| + \left\| \frac{P^{k+1}(x) - P^k(x)}{P^{k+1}(x)} \right\|$ is inferior to the convergence criteria (set to 10^{-6}).

Despite of rather simple equations, the numerical convergence of the problem is not easily found. In order to stabilize the solution during the iteration steps, a relaxation scheme is employed. It states that instead of going directly from the solution at the step k , $(N, P)^k$ to the solution at step $k + 1$, $(N, P)^{k+1}$, the data used for the next iteration will be a linear combination of the two : $\alpha(N, P)^k + (1 - \alpha)(N, P)^{k+1}$, with α between 0 and 1, and as close to 1 as necessary to ensure convergence.

2.1. Weak formulation and stiffness matrices

We want to solve equations (E-11), (E-12) and (E-13) on the interval $[0,1]$. We discretize $[0,1]$ in $n-1$ sub-intervals of length h , that define n nodes $(x_i)_{1 \leq i \leq n}$. We choose a finite element basis in one dimension $(\varphi_i)_{1 \leq i \leq n}$, based on piecewise linear functions ϕ_i that equal 1 at x_i and equal 0 for $x_{j \neq i}$, also called tent functions.

We can express V , N and P on the finite-element basis :

$$V_i = \sum_{i=1}^n V_i \varphi_i \text{ with } V_1 = 0 \text{ and } V_n = V_0 \text{ imposed due to boundary conditions.}$$

$$N_i = \sum_{i=1}^n N_i \varphi_i \text{ and } P_i = \sum_{i=1}^n P_i \varphi_i$$

2.2. Determining the potential V^{k+1} for given carrier concentrations N^k and P^k

For each $\varphi_j \in (\varphi)_{2 \leq j \leq n-1}$, equation (E-11) can be written as: $-V'' \varphi_j = (P - N + \Sigma) \varphi_j$.

We integrate on $]0,1[$, ($(\varphi)_{2 \leq j \leq n-1}$ are zeros for $X = 0$ and $X = 1$).

$$\int_0^1 -V'' \varphi_j = \int_0^1 (P - N + \Sigma) \varphi_j$$

$$\Rightarrow \int_0^1 V' \varphi_j' = \int_0^1 (P - N + \Sigma) \varphi_j$$

$$\Rightarrow \sum_{i=1}^n V_i \int_0^1 \varphi_i' \varphi_j' = \int_0^1 (P - N + \Sigma) \varphi_j$$

$$\Rightarrow \sum_{i=2}^{n-1} V_i \int_0^1 \varphi_i' \varphi_j' = \int_0^1 (P - N + \Sigma) \varphi_j - \int_0^1 V_1 \varphi_1' \varphi_j' - \int_0^1 V_n \varphi_n' \varphi_j'$$

V^{k+1} is thus a solution of the linear problem $K_v \times V^{k+1} = b$, where the second term b depends on the solutions N^k and P^k found on the previous iteration step. The stiffness matrix K_v is a tridiagonal matrix included in $(\mathbb{R}^{n-2})^2$ such that $K_v(i, j) = \int_0^1 \varphi_i' \varphi_j'$. Therefore given the form of the tent functions ϕ , we have:

$$K_v = \frac{1}{h} \begin{bmatrix} 2 & -1 & & 0 \\ -1 & \dots & \dots & \\ & \dots & \dots & -1 \\ 0 & & -1 & 2 \end{bmatrix}$$

and b , vector of (\mathbb{R}^{n-2}) is :

$$b = \begin{bmatrix} \frac{0}{h} + \int_{x_1=0}^{x_3=2h} (P^k - N^k + \Sigma)\varphi_2 \\ \int_{x_{i-1}}^{x_{i+1}} (P^k - N^k + \Sigma)\varphi_i \\ \dots \\ \frac{V_0}{h} + \int_{x_{n-2}=1-2h}^{x_n=1} (P^k - N^k + \Sigma)\varphi_{n-1} \end{bmatrix} = \begin{bmatrix} \frac{0}{h} + h(P^k(h) - N^k(h) + \Sigma(h)) \\ h(P^k(x_i) - N^k(x_i) + \Sigma(x_i)) \\ \dots \\ \frac{V_0}{h} + h(P^k(1-h) - N^k(1-h) + \Sigma(1-h)) \end{bmatrix}$$

The solution of the linear problem, the vector V^{k+1} is determined by $V_{2 \leq i \leq n-1}^{k+1} = K_v^{-1}b$ and $V_1=0$ and $V_n=V_0$, imposed by boundary conditions.

2.3. Determining the electron concentration N^{k+1} for given V^{k+1} and P^k

For each $\varphi_j \in (\phi)_{1 \leq j \leq n}$, we can write equation (E-12) in the weak form :

$$\int_0^1 \text{div}(J_n)\varphi_j = \int_0^1 (-N'' + (NV'))'\varphi_j = \int_0^1 (G_n - R_n)\varphi_j$$

$$\Rightarrow - \int_0^1 J_n \varphi_j' + \int_{\partial\Omega} J_n \varphi_j = \int_0^1 (G_n - R_n)\varphi_j$$

soit avec la C.L. de Robin $J_n(x) = \lambda_n(x)(N - N_{eq}) \vec{n}$

$$\Rightarrow - \int_0^1 (-N' + (NV'))\varphi_j' + \int_{\partial\Omega} \lambda_n(x)(N - N_{eq}) \vec{n} \varphi_j = \int_0^1 (G_n - R_n)\varphi_j$$

$$\Rightarrow - \sum_{i=1}^n N_i \int_0^1 (-\varphi_i' + (\varphi_i V'))\varphi_j' + \sum_{i=1}^n N_i \int_{\partial\Omega} \lambda_n(x) \vec{n} \varphi_i \varphi_j = \int_0^1 (G_n - R_n)\varphi_j + \int_{\partial\Omega} \lambda_n(x) \vec{n} N_{eq} \varphi_j$$

$$\Rightarrow \sum_{i=1}^n N_i \int_0^1 \varphi_i' \varphi_j' - \sum_{i=1}^n N_i \int_0^1 (\varphi_i V')\varphi_j' + \sum_{i=1}^n N_i \int_{\partial\Omega} \lambda_n(x) \vec{n} \varphi_i \varphi_j$$

$$= \int_0^1 (G_n - R_n)\varphi_j + \int_{\partial\Omega} \lambda_n(x) \vec{n} N_{eq} \varphi_j$$

The recombination term R_n depends on both carrier concentration N and P , therefore we implicit this term.

$$\begin{aligned} \Rightarrow \sum_{i=1}^n N_i \int_0^1 \varphi_i' \varphi_j' - \sum_{i=1}^n N_i \int_0^1 (\varphi_i V') \varphi_j' + \sum_{i=1}^n N_i \int_{\partial\Omega} \lambda_n \vec{n} \varphi_i \varphi_j \\ = \int_0^1 (G_n - B_n(NP - N_i^2)) \varphi_j + \int_{\partial\Omega} \lambda_n \vec{n} N_{eq} \varphi_j \\ \Rightarrow \sum_{i=1}^n N_i \int_0^1 \varphi_i' \varphi_j' - \sum_{i=1}^n N_i \int_0^1 (\varphi_i V') \varphi_j' + \sum_{i=1}^n N_i \int_{\partial\Omega} \lambda_n \vec{n} \varphi_i \varphi_j + \sum_{i=1}^n N_i \int_0^1 B_n(\varphi_i P) \varphi_j \\ = \int_0^1 (G_n + B_n(N_i^2)) \varphi_j + \int_{\partial\Omega} \lambda_n \vec{n} N_{eq} \varphi_j \end{aligned}$$

The solution at the $k+1^{\text{th}}$ iteration, N^{k+1} , is solution of the linear problem $N^{k+1} = K_n^{-1}c$, where c and the stiffness matrix K_n depends on V^{k+1} and P^k . We divide K_n in the sum of several matrices:

$K_n = A - B + C_1 + I_1 \in (\mathbb{R}^n)^2$, where :

$A(i, j) = \int_0^1 \varphi_i' \varphi_j'$ tridiagonal matrix

$$A(i, j) = \frac{1}{h} \begin{bmatrix} 1 & -1 & & 0 \\ -1 & 2 & \dots & \\ & \dots & 2 & -1 \\ 0 & & -1 & 1 \end{bmatrix}$$

$B(i, j) = \int_0^1 \varphi_i V' \varphi_j'$, thus

$$B = \frac{1}{h} \begin{bmatrix} -\frac{1}{2}(V^{k+1}(h) - V^{k+1}(0)) & \frac{1}{2}(V^{k+1}(h) - V^{k+1}(0)) & & 0 \\ -\frac{1}{2}(V^{k+1}(h) - V^{k+1}(0)) & -\frac{1}{2h}(V^{k+1}(x_{i-1}) + V^{k+1}(x_{i+1}) - 2V^{k+1}(x_i)) & \frac{1}{2}(V^{k+1}(x_{i+1}) - V^{k+1}(x_i)) & \\ & -\frac{1}{2}(V^{k+1}(x_{i+1}) - V^{k+1}(x_i)) & \dots & \frac{1}{2}(V^{k+1}(1) - V^{k+1}(1-h)) \\ 0 & & -\frac{1}{2}(V^{k+1}(1) - V^{k+1}(1-h)) & \frac{1}{2}(V^{k+1}(1) - V^{k+1}(1-h)) \end{bmatrix}$$

$C_1(i, j) = \int_{\partial\Omega} \lambda_n \varphi_i \varphi_j \vec{n}$, thus

$$C_1 = \begin{bmatrix} -\lambda_n(0) & 0 & 0 \\ 0 & 0 & \\ 0 & \ddots & 0 \\ & 0 & \lambda_n(1) \end{bmatrix}$$

$I_1(i, j) = \sum_{i=1}^n N_i \int_0^1 B_n(\varphi_i P) \varphi_j$, thus

$$I_1 = \frac{h}{D_n} B_n \begin{bmatrix} P^k(0) & 0 & 0 \\ 0 & P^k(h) & \\ 0 & \ddots & 0 \\ & 0 & P^k(1) \end{bmatrix}$$

c is the second term vector: $\int_0^1 (G_n + B_n(N_i^2)) \varphi_j + \int_{\partial\Omega} \lambda_n \vec{n} N_{eq} \varphi_j$

$$c = \begin{bmatrix} -\lambda_n(0) N_{eq} + h(G_n(x_2) + B_n(N_i^2)) \\ h(G_n(x_i) + B_n(N_i^2)) \\ \dots \\ \lambda_n(1) N_{eq} + h(G_n(x_n) + B_n(N_i^2)) \end{bmatrix}$$

N^{k+1} is found as the solution of $K_n N^{k+1} = c$, i.e $N^{k+1} = K_n^{-1} c$

2.4. Determining the hole concentration P^{k+1} for given V^{k+1} and N^{k+1}

The determination of P^{k+1} is similar to that of N^{k+1} . The stiffness matrix $K_p = A + B + C_2 + I_2 \in (\mathbb{R}^n)^2$, with :

$C_2(i, j) = \int_{\partial\Omega} \lambda_p \varphi_i \varphi_j \vec{n}$, thus

$$C_1 = \begin{bmatrix} -\lambda_p(0) & 0 & 0 \\ 0 & 0 & \\ 0 & \ddots & 0 \\ & 0 & \lambda_p(1) \end{bmatrix}$$

$I_2(i, j) = \sum_{i=1}^n N_i \int_0^1 B_p(\varphi_i P) \varphi_j$, thus

$$I_2 = \frac{h}{D_p} B_p \begin{bmatrix} N^{k+1}(0) & 0 & 0 \\ 0 & N^{k+1}(h) & \\ 0 & \ddots & 0 \\ & 0 & N^{k+1}(1) \end{bmatrix}$$

d is the second term vector: $\int_0^1 (G_p + B_p(N_i^2)) \varphi_j + \int_{\partial\Omega} \lambda_p \vec{n} N_{eq} \varphi_j$

$$d = \begin{bmatrix} -\lambda_p(0)P_{eq} + h(G_p(x_2) + B_p(N_i^2)) \\ h(G_p(x_i) + B_p(N_i^2)) \\ \dots \\ \lambda_p(1)P_{eq} + h(G_p(x_n) + B_{np}(N_i^2)) \end{bmatrix}$$

P^{k+1} is found as the solution of $K_p P^{k+1} = d$, i.e $P^{k+1} = K_p^{-1} d$

As mentioned previously, in order to ensure convergence for a large set of input parameters, a relaxation scheme is used. Indeed equations (E-12) and (E-13) enable to find self-consistently the carrier concentrations, knowing generation, recombination and potential. If the carrier concentrations change too much between two iteration steps, instability can occur. Instead of using directly the solution $(N, P)^{k+1}$ calculated from $(N, P)^k$ as described, the $k + 2^{\text{th}}$ iteration uses as input data the linear combination $\alpha (N, P)^k + (1 - \alpha) (N, P)^{k+1}$, with α close to 1, instead of using directly $(N, P)^{k+1}$ ($\alpha=0$). The resolution of equation (E-11) being easier, a relaxation scheme is not employed for the electric potential.

3. Results

3.1. Validation of our model

In order to assess the validity of the results found by our simulations, we compare our results with solution from SCAPS software (see box n°2). We simulate a symmetric homojunction, under low illumination levels.

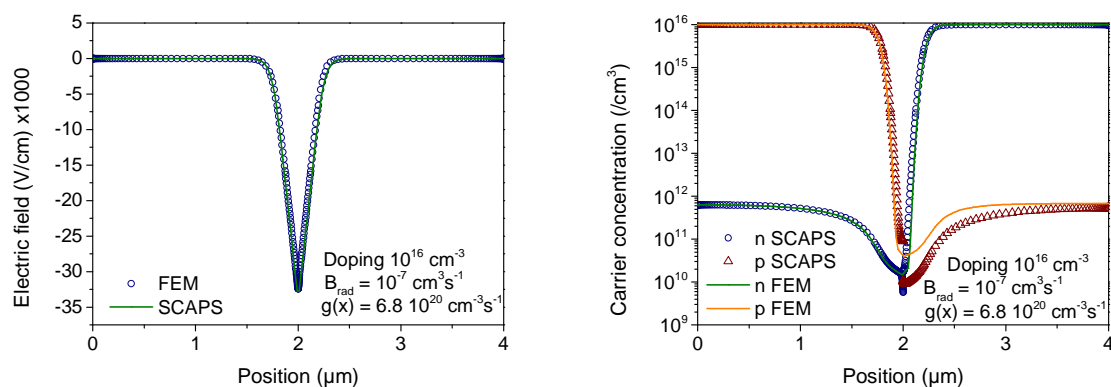


Figure E-1 : Abrupt homojunction between semiconductors of 10^{16} cm^{-3} doping and a recombination coefficient b of $10^{-7} \text{ cm}^3 \text{ s}^{-1}$, under zero applied voltage. The generation is set to I_0 , which is equivalent to a constant generation rate of $6.8 \cdot 10^{20} \text{ cm}^{-3} \cdot \text{s}^{-1}$. Simulations are done by both SCAPS (dots) and our FEM program (line). (left) Electric field as a function of position. (right) Carrier concentration as a function of position.

It can be seen that the results of our program are very close to that of the well-known SCAPS simulation software (See box n°2) for low generation rates (Figure E-1). It confirms the correctness of

our calculations. Interestingly, in SCAPS software, the user has no influence on the convergence criteria. It can be seen that the carrier concentration are discontinuous at the junction in SCAPS, which is probably the sign of a lack of convergence. On the contrary our results, which are however obtained with greater computational time, give continuous carrier concentrations.

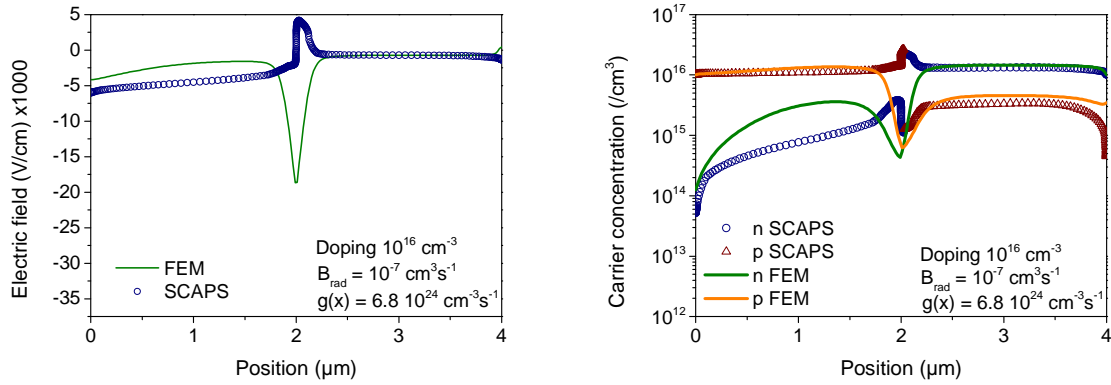
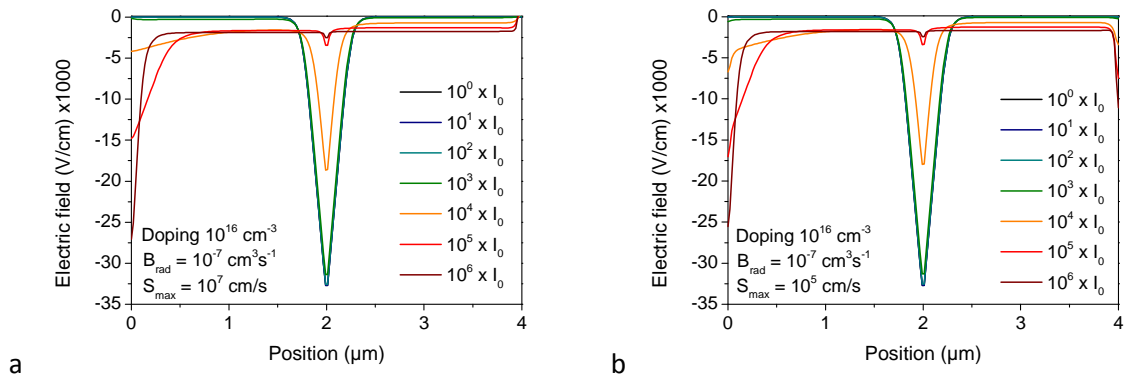


Figure E-2 : Abrupt homojunction between semiconductors of 10^{16} cm^{-3} doping and a recombination coefficient b of $10^{-7} \text{ cm}^3 \text{ s}^{-1}$, under zero applied voltage. The generation is set to $10^4 \times I_0$, which is equivalent to a constant generation rate of $6.8 \cdot 10^{24} \text{ cm}^{-3} \cdot \text{s}^{-1}$. Simulations are done by both SCAPS (dots) and our FEM program (line). (left) Electric field as a function of position. (right) Carrier concentration as a function of position.

At higher illumination levels, i.e. higher generation rate, SCAPS simulation software gives results that are aberrant. The discontinuities in the carrier densities are more pronounced.

3.2. Impact of boundary conditions



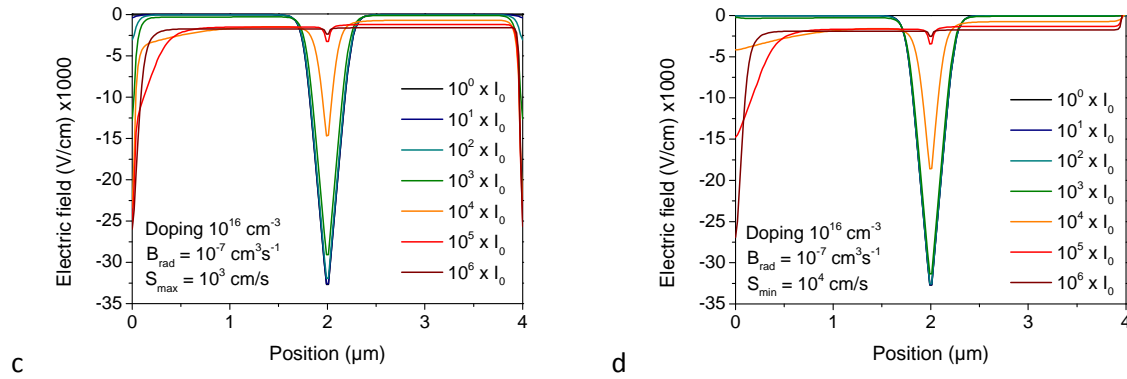
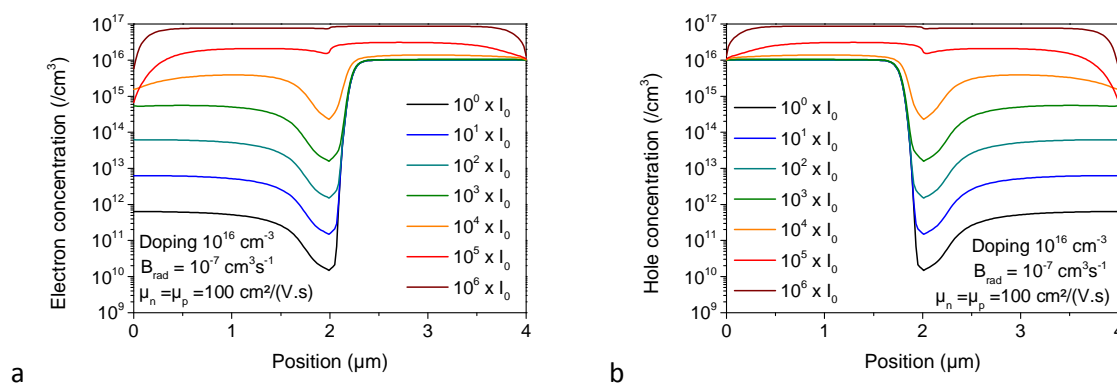


Figure E-3 : Electric field as a function of position, for a homojunction between semiconductors of 10^{16} cm^{-3} doping and a recombination coefficient b of $10^{-7} \text{ cm}^3 \text{ s}^{-1}$. (a) (b) (c) The “minority” carrier transfer velocity 10^2 cm/s at the boundaries (d) The minority carrier velocity is 10^4 cm/s . The boundary conditions for “majority” carriers: (a) (d) transfer velocity at the boundaries 10^7 cm/s , (b) 10^5 cm/s , (c) 10^3 cm/s . Majority (minority) carriers refers to electrons (holes) in the n-type doped part of the homojunction and vice-versa in the p-type part, independently of the injection level.

Boundary conditions only influence the carrier repartition at the extreme surfaces. They do not impact carrier repartition in the bulk, nor the electric field or current densities. Thus the conclusions drawn in this work on the screening of the homojunction electric field under illumination are very general.

3.3. Impact of the mobilities

We simulated the same abrupt p-n junction with symmetric doping of 10^{16} cm^{-3} under increasing illumination as before, but we equalize the carrier mobilities. We chose $\mu_n = \mu_p = 100 \text{ cm}^2/(\text{V.s})$.



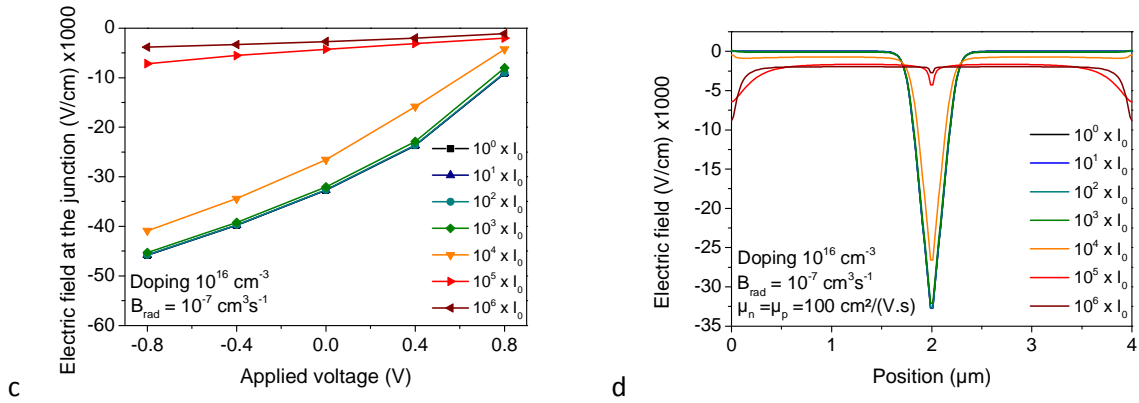


Figure E-4 : Homojunction between semiconductors of 10^{16} cm^{-3} doping and a recombination coefficient b of $10^{-7} \text{ cm}^3 \text{ s}^{-1}$, and equal carrier mobilities, set to $100 \text{ cm}^2 / (\text{V.s})$. (a) Electron concentration as a function of position and illumination, at zero applied voltage. (b) Hole concentration as a function of position and illumination, at zero applied voltage. (c) Electric field at the junction as a function of applied voltage and illumination. (d) Electric field at zero applied voltage as a function of position and illumination.

We can see that with equal mobilities, the carrier concentration are perfectly symmetric (Figure E-4 a and b), which is not the case otherwise. As a consequence, the electric field is also perfectly symmetric (Figure E-4 d). However no drastic change in the modulation of the electric field with applied voltage and position can be seen (Figure E-4 c). Thus we can say that the electric field screening is not due to a Dember effect, which requires unequal mobilities.

In order to understand the physical origin of the field screening, we take the electric field calculated above for a homojunction between semiconductors of 10^{16} cm^{-3} doping and a recombination coefficient b of $10^{-7} \text{ cm}^3 \text{ s}^{-1}$, and equal carrier mobilities, set to $100 \text{ cm}^2 / (\text{V.s})$, for a uniform illumination of $10^6 I_0$. This configuration is the simplest as no Dember term is involved. We calculate the ohmic component of the electric field, according to equation (VI-1). This component can be visualized on Figure E-5.

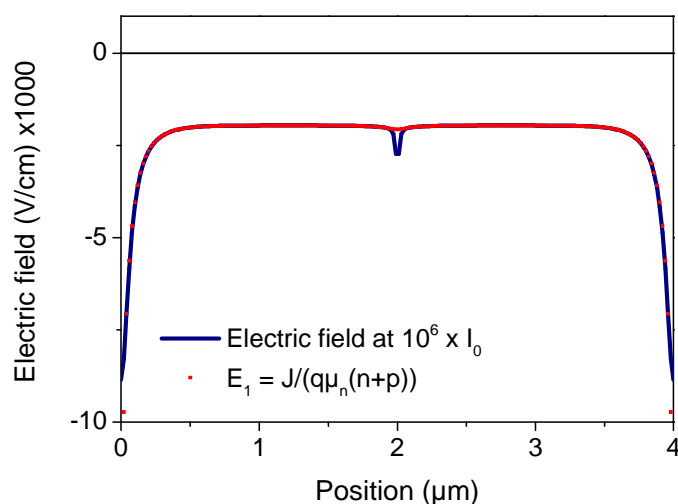
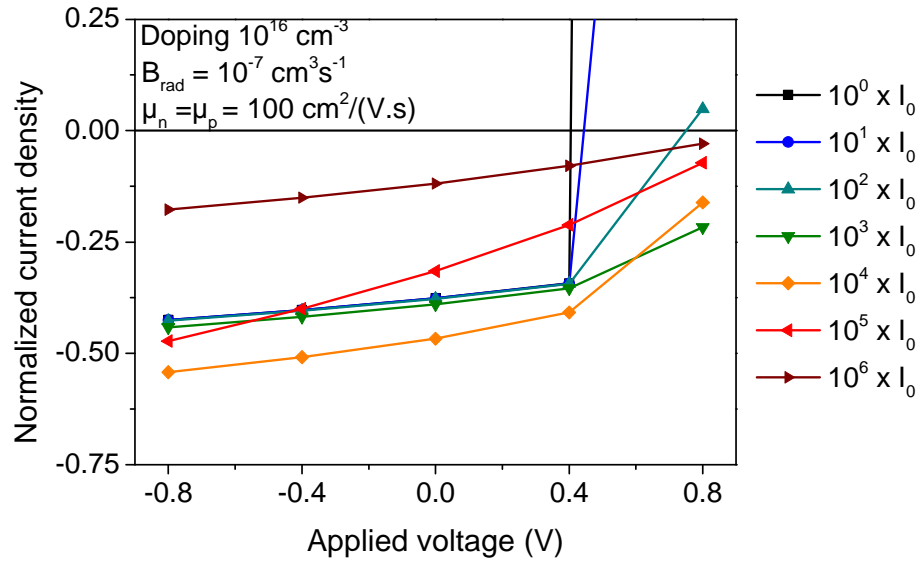


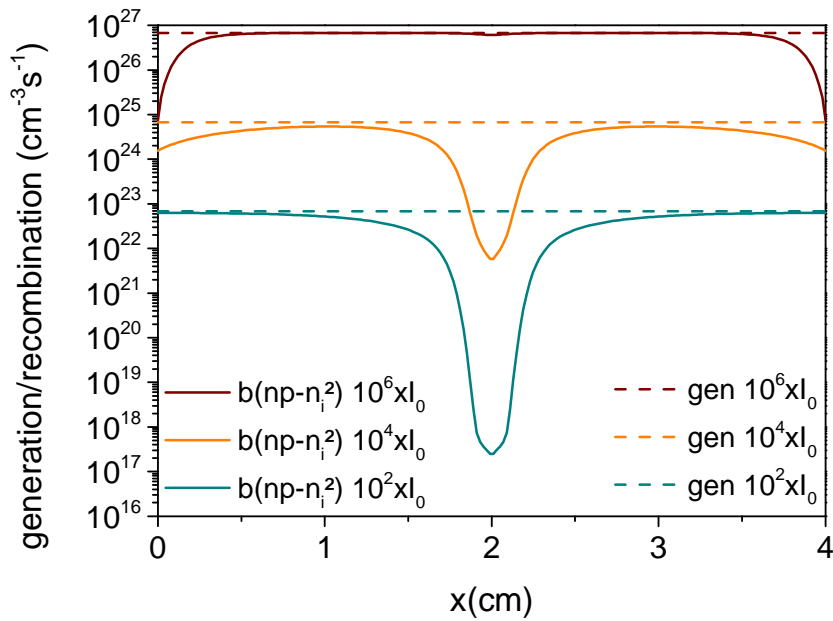
Figure E-5 : Electric field in a homojunction between semiconductors of 10^{16} cm^{-3} doping and a recombination coefficient b of $10^{-7} \text{ cm}^3 \text{ s}^{-1}$, and equal carrier mobilities, set to $100 \text{ cm}^2 / (\text{V} \cdot \text{s})$ at an illumination of $10^6 \times I_0$. The ohmic component of equation (VI-1) is displayed.

One can see that the increase of the electric field far from the junction is due to an ohmic term. There is still a slight contribution of the junction to the electric field, but completely screened from its original low illumination value. More generally, we can see that the value of the electric field in the “quasi-neutral” region, or more precisely outside of the space charge region, is fixed by this ohmic component.

In spite of the constant decrease of the electric field at the junction, we can observe in the case modeled here a slight superlinearity of the current, with increasing illumination (Figure E-6 a). This case is very similar to that found for different electron and hole mobility (Figure VI-13). If we look at the generation and recombination rate in the junction, at three different illumination intensities, we can highlight interesting facts (Figure E-6 a). At low illumination intensity ($10^2 \times I_0$), the band-to-band recombination, described by equation (VI-19), is strong in the quasi-neutral region and decrease at the junction, due to the low carrier concentration. At this illumination intensity, the diffusion length of electrons is $0.5 \mu\text{m}$, which is small compared to the thickness, and explains the low collection. At higher illumination intensity, i.e. higher generation rate, the recombination rate decreases proportionally at the junction edge. This is due to the gradient in the minority carrier concentration (Figure E-4), due to the creation of an ohmic electric field (Figure E-5). The collection is therefore increased, which results in higher current density proportionally to the generation rate. When the illumination intensity is increased further the ohmic electric field at the edge cannot compensate for the increased recombination at the junction, due to decreased electric field, and the collection drops, giving a strong current sub-linearity.



a



b

Figure E-6 : (a) Current-voltage curve in a homojunction between semiconductors of 10^{16} cm^{-3} doping and a recombination coefficient b of $10^{-7} \text{ cm}^3 \text{ s}^{-1}$, and equal carrier mobilities, set to $100 \text{ cm}^2/(\text{V}\cdot\text{s})$ at various illumination levels. (b) generation and recombination rate as a function of position for three illumination intensities.

3.4. Non constant generation rate

We have performed so far simulations with a constant generation rate. This choice was done to avoid artifacts due to strong generation at the samples edge, as we performed simulations on symmetric homojunction. We tested however simulations with a generation profile of the Beer-Lambert form.

The screening effect is still visible. However the non uniform generation produces carrier concentration gradients that influence the electric field.

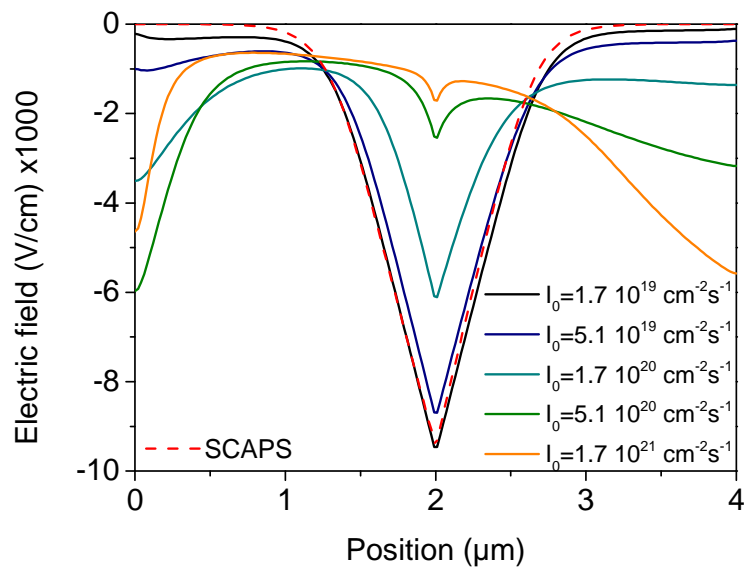


Figure E-7 : Electric as a function of position in a homojunction between semiconductors of 10^{15} cm^{-3} doping and a recombination coefficient b of $10^{-7} \text{ cm}^3 \text{ s}^{-1}$, electron mobility of $100 \text{ cm}^2/(\text{V}\cdot\text{s})$, hole mobility $25 \text{ cm}^2/(\text{V}\cdot\text{s})$, and a generation profile of the form $g(x) = \alpha I_0 \exp(-\alpha x)$.

APPENDIX F. MICROCELLS WITH LOCALIZED ABSORBERS

1. A top down fabrication process: study of mesa delineated microcells on co-evaporated Cu(In, Ga)Se₂ absorbers

1.1. Fabrication process

Overview of the process

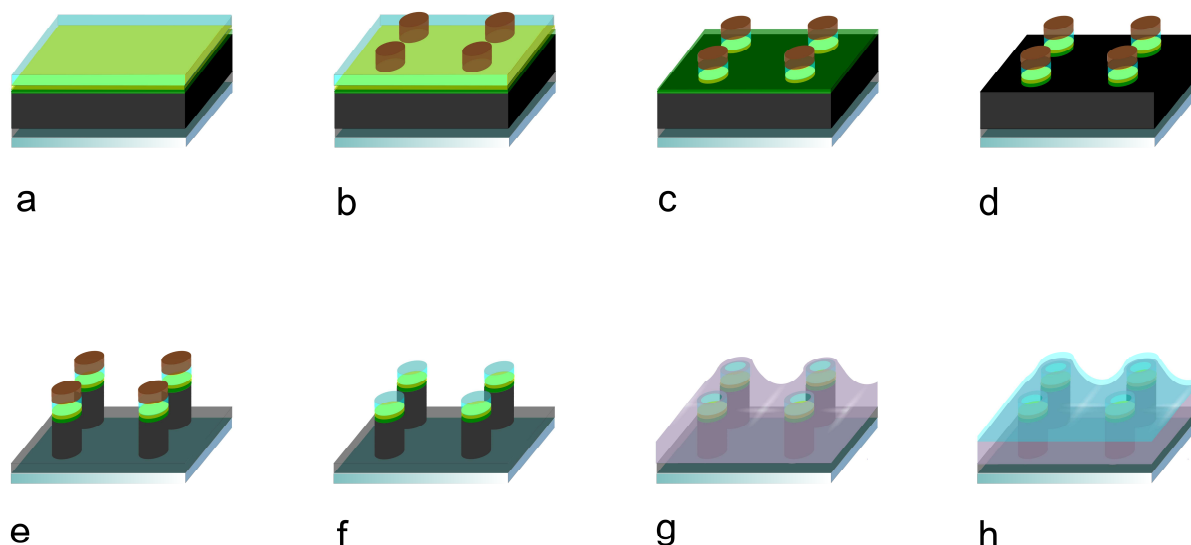


Figure F-1 : Sketch of the top-down Cu(In,Ga)Se₂ microcell process.

In order to create these “micro-blocks” solar cells, the process is as follows. A standard Cu(In,Ga)Se₂ solar cell is created (Figure VII-2 a). We chose to start from finished solar cells in order to avoid degradation of Cu(In,Ga)Se₂ surface before buffer deposition. It is known in Cu(In,Ga)Se₂ community that the best devices are created when the time elapsed between the end of the coevaporation process and buffer deposition is minimum [10]. For this study we use solely co-evaporated substrates coming from Würth Solar. Then we proceed to a first photolithography. A photoresist (AZ®5214 resist or AZ®4533, AZ Electronics Materials) is deposited on the samples and spun at 4000 rpm (Karl Süss CT62) for 30 s. The resist is pre-bake at 128°C, exposed (365nm - 435nm light, through Karl Süss MJB mask aligner), bake at 128°C and then developed (developer MIF 726). An array of photoresist blocks is thus created (Figure VII-2 b). Then the front window is etched with a 5.10⁻² mol/L hydrochloric acidic solution. Both ZnO and CdS are etched due to the low pH of the solution (Figure VII-2 c and d). Then the Cu(In,Ga)Se₂ layer is etched. Two different processes were tested and are described hereafter: ion beam etching and wet chemical etching. Then the photoresist is dissolved in acetone (Figure VII-2 f). As such the micro-block solar cells can be tested with a probe on the top of the cell,

and one on the Mo back substrate. However it can be interesting to contact the micro-blocks array (Figure VII-2 h). This step is described hereafter.

Ion beam etching

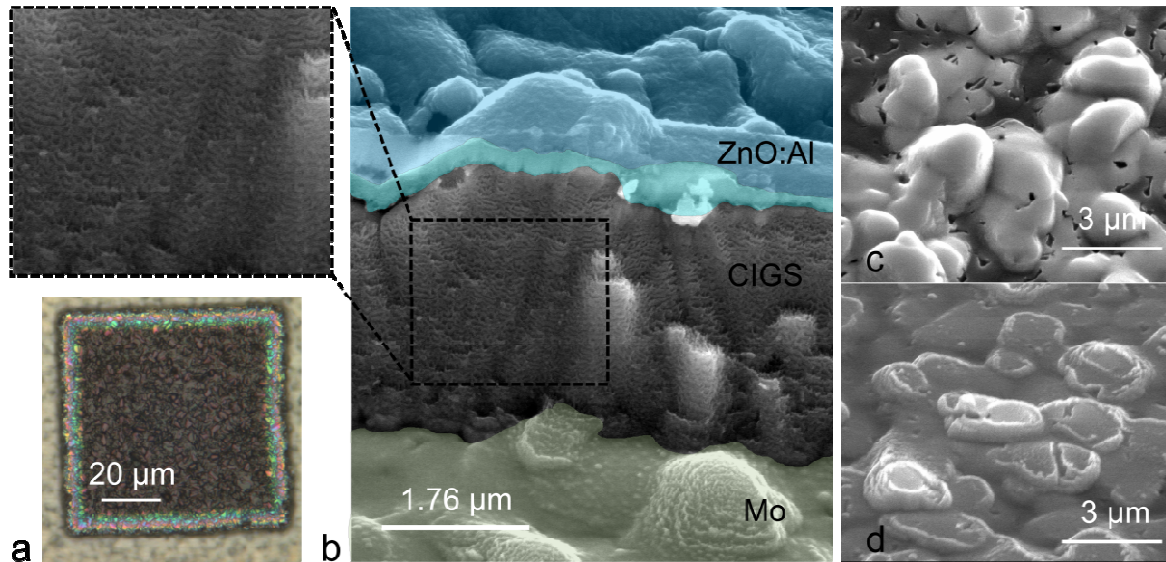


Figure F-2 : (a) optical microscope image of a Cu(In,Ga)Se_2 micro-blocks after hydrochloric and 75' IBE etching (b) Colorized SEM image of a Cu(In,Ga)Se_2 micro-block solar cell after IBE etching of 98'. Highly structured Cu(In,Ga)Se_2 edge is visible. A zoom of the structure is displayed on the inset. SEM view of the substrate between the micro-blocks after (c) 60' of etching and (d) after 98'. The difference in roughness is due to the difference in etching rates, which is higher for Cu(In,Ga)Se_2 (40nm/mn) than for Mo (≈ 5 nm/mn).

Ion beam etching was used to pattern Cu(In,Ga)Se_2 through a patterned photoresist layer. The ion beam etching is based on the bombardment of the sample by Ar^+ ions generated in a Ar plasma. A mass spectrometer detects the elements etched from the sample, and enables in-situ monitoring. Due to the ion bombardment and low thermal conductivity of the glass substrate, etching was done by steps of 30' to avoid excessive heating. The sample is fixed on an aluminum holder with high vacuum grease on the back surface to ensure a good thermal contact and metallic clamps on the surface. Between steps, the sample was cooled, through cooling of the aluminum sample holder. However even if the temperature of the sample holder was maintained below 10°C during etching and cooling, it is difficult to know the maximum temperature attained on the sample surface, and degradation may be possible. The sample holder is rotating during the etch (10 rpm) and the line perpendicular to the sample plane is inclined from 20° with respect to the direction of the ion bombardment.

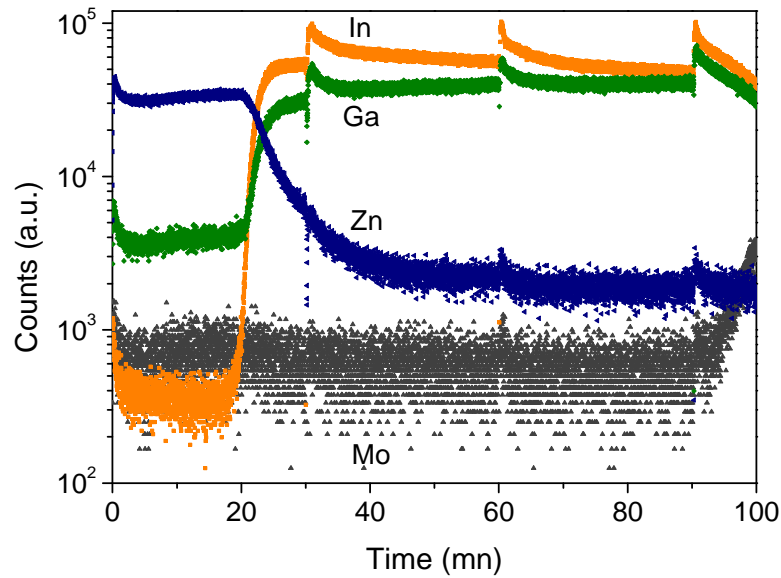


Figure F-3 : Detection of Mo, Zn In and Ga by a mass spectrometer during ion beam etching of a $\text{Cu}(\text{In},\text{Ga})\text{Se}_2$ sample. Etching steps of 30mn are done and the etch is stopped when the signal from $\text{Cu}(\text{In},\text{Ga})\text{Se}_2$ decreases and that of Mo increases. Exceptionally the window layer were not chemically etched before the IBE for this sample to follow the etch of the complete cell.

The etch rate in these conditions is found to be 40 nm/mn. Thus the etches are long and possible overheating of the sample may become problematic. The etches are stopped when the Mo signal become important at the spectrometer (Figure F-3). Due to the difference in etching rates of $\text{Cu}(\text{In},\text{Ga})\text{Se}_2$ and Mo, we can control easily the thickness of $\text{Cu}(\text{In},\text{Ga})\text{Se}_2$ that we leave on the substrate, and we can decide to etch away all $\text{Cu}(\text{In},\text{Ga})\text{Se}_2$ (Figure F-2 d). The remaining roughness on the Mo layer depends on the roughness of the $\text{Cu}(\text{In},\text{Ga})\text{Se}_2$ at the beginning, as ion beam etching tends to conserve the sample topography. It is interesting to note from a material point of view that we observe an important density of holes on the sample in the last 200 nm of absorber, tending to show that $\text{Cu}(\text{In},\text{Ga})\text{Se}_2$ grains are not perfectly coalescent at their base (Figure F-2 c). This confirms studies showing multi-stage growth induce formation of microvoids at the grain boundary due to species diffusion and consequently coalescence of vacancies [11].

Ion beam etching was successful in creating $\text{Cu}(\text{In},\text{Ga})\text{Se}_2$ micro-blocks (Figure F-2 a). The edges of the $\text{Cu}(\text{In},\text{Ga})\text{Se}_2$ layer present a specific texture (Figure F-2 b and inset). This texture is found on all etched samples, and is resistant to acetone cleaning, and thus is unlikely due to photoresist residuals. It may come from the rotation of the sample, inclined with respect to the plasma direction, which exposed periodically the edges to the ion bombardment and thus create trenches.

Chemical etching

Table F-1 : Properties of the two bromide solutions used for chemical patterning of Cu(In,Ga)Se₂ micro-blocks solar cells.

	Br ₂ (mol.L ⁻¹)	KBr (mol.L ⁻¹)	KOH (mol.L ⁻¹)	pH	Etch rate (μm/mn)
Solution 1	4 10 ⁻²	1	9.5 10 ⁻⁴	7.1	1
Solution 2	8 10 ⁻²	2	9.5 10 ⁻⁴	7.2	4

In order to pattern Cu(In,Ga)Se₂ micro-blocks by a wet chemical process we chose to use a solution of the bromide family[12], [13]. As we are processing on complete solar cells, the pH of the solution has to be quasi-neutral to prevent the etch of both ZnO and CdS layers, during the etch of the 2 to 3 μm Cu(In,Ga)Se₂ layer. Thus we prepared solutions of bromine and potassium bromide, and adjusted the pH with potassium hydroxide. We prepared two solutions (Table VII-1). The first was 4 10⁻² mol/L of Br₂, and 1 mol/L of KBr. The second one was 8 10⁻² mol/L of Br₂ and 2 mol/L of KBr. The as-prepared KBr/Br₂ solutions are acidic, with pH around 4. The pH of the solutions was thus adjusted by step-by-step addition of KOH. The solution preparation was done in collaboration with the Institut Lavoisier de Versailles, which has a strong know-how on bromide etching and has equipment dedicated to direct bromine handling that is forbidden in our laboratories due to the toxicity of this product.

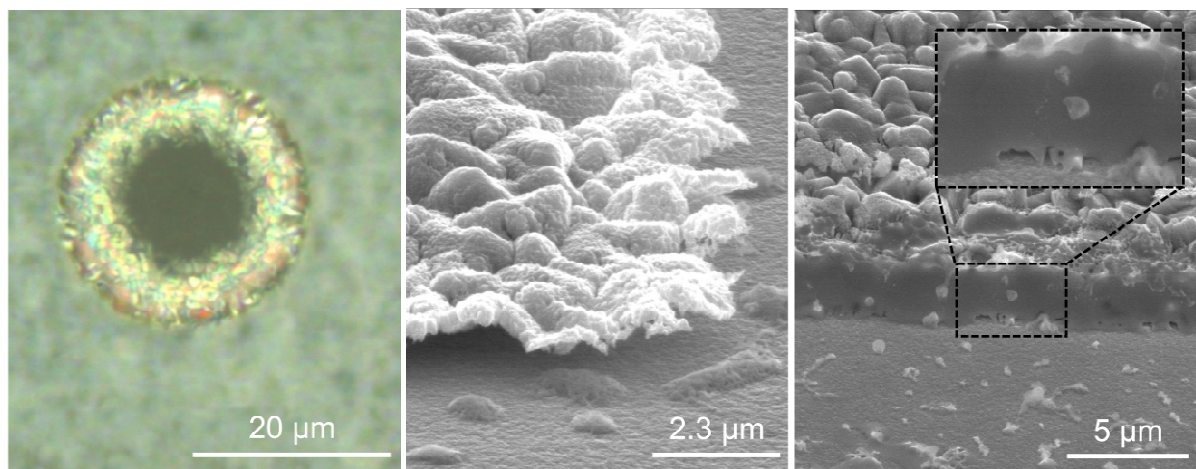


Figure F-4 : (left) optical image of a microcell 25 μm of diameter after Cu(In,Ga)Se₂ chemical etch. Under-etching of 5 μm is visible. (middle) SEM image of a microcell after Cu(In,Ga)Se₂ chemical etch. Under-etching of Cu(In,Ga)Se₂ compared to ZnO is visible. (right) SEM image of a microcell where ZnO has been sufficiently etched to observe the Cu(In,Ga)Se₂ edge. On the inset one can see that the edge surface is smooth.

We follow the chemical etch of Cu(In,Ga)Se₂ solar cells. We proceed by successive steps. The etching rate is dependent on the solution concentration (Figure F-5). Trenching occurs, i.e. etching is faster close to the patterns. Moreover etching is not unidirectional. Thus there is under-etching of the patterns, i.e. Cu(In,Ga)Se₂ is etched under the ZnO and photoresist layer (Figure F-4 left and middle).

The under-etched length is of the order of the $\text{Cu}(\text{In}, \text{Ga})\text{Se}_2$ layer thickness. It should be noted that an evolution of etching rate was observed with aging of the solutions. After a few weeks the etching rate of solution 1 was found three times that of the fresh solution.

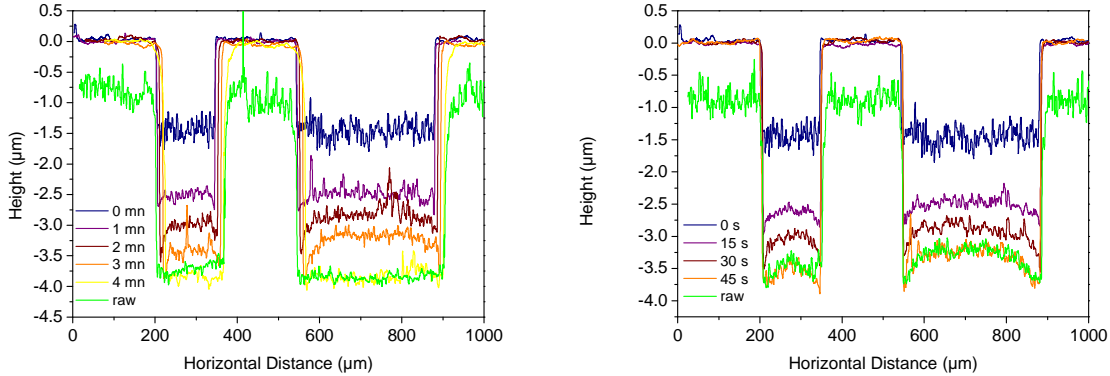


Figure F-5 : Profile of the etching in solution 1 (left) and solution 2 (right) as a function of time. Measured by profilometer on the same pattern.

Contacting microcells

With the two etching procedures we create micro-block solar cells (Figure VII-2 f). We can measure them by contacting the Mo back contact and $\text{ZnO}:\text{Al}$ window layers with micro-probes. If this technique is satisfactory for dark characterization, we need to have a better connection if we want to measure the devices under illumination. Indeed the probe placed on the $\text{ZnO}:\text{Al}$ will an important shading, especially for the smallest devices.

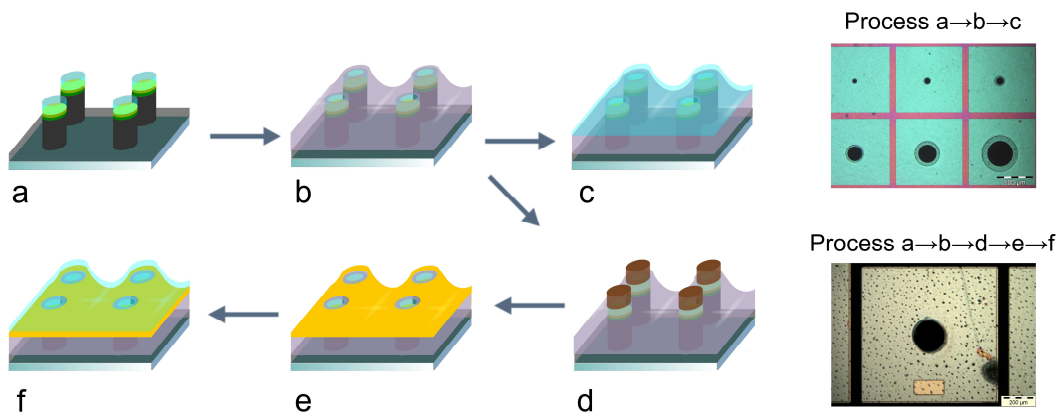


Figure F-6 : (left) Contacting process. Two different processes (a → b → c) or (a → b → d → e → f) can be done depending on the need for a metallic layer. (right) optical images of a sample at the end of the two processes. The squares are $1 \times 1 \text{ mm}^2$.

We developed two procedures for contacting the micro-blocks. The simplest one, noted (a → b → c) on Figure F-6, contacts all the microblocks through an insulation with a polymer (Figure F-6 b) that

lets the top of the micro-block unprotected and a subsequent ZnO:Al deposition on the whole substrate that connects all the micro-blocks surfaces (Figure F-6 c). If a peripheral contact with gold is desirable, two more steps are needed. A lithography is done to protect the top of the micro-blocks (Figure F-6 d) from the deposition of Au (Figure F-6 e). Then ZnO is deposited on the whole substrate (Figure F-6 f).

The insulation is done with SU-8 photoresist, an epoxy based photoresist that is highly cross-linked after exposure and development. Thus SU-8 is stable and can be left on the substrate for subsequent processing. It is referred to as permanent photoresist. SU-8 is electrically insulating ($2.8 \cdot 10^{16}$ ohm.cm) [14] and will prevent shunts between Mo back contact and the front contact. SU-8-2002 (2 μ m thick) is spin coated at 4000 rpm (Karl Süss CT62) for 30 s. The resist is pre-bake at 95°C for 5', exposed for 20'' (365nm - 435nm light, through Karl Süss MJB mask aligner), bake at 125°C for 10' and then developed 15'' in SU-8-developer. Geometrically, the surface that is not protected at step b is a disk that is concentric to that of the micro-block with slightly smaller diameter. Thus the SU-8 covers the periphery of the micro-blocks surface to prevent shunts, and gives us a margin for the lithographic alignments.

ZnO:Al can be deposited on SU-8 without pre-treatments. If a gold layer needs to be deposited, a lithography with AZ5214® is carried out to protect the micro-blocks surfaces. Adhesion of metals on SU-8 is difficult due to the low energy of cross-linked SU-8 surfaces, and thus strong hydrophobicity [15]. A pre-treatment of the resist before deposition of the Au layer was found necessary. The sample is etched by reactive ion etching for 10 s to modify the surface properties of the cross-linked SU-8. The etching is carried out with a plasma of dioxygen and trifluoromethane. Oxygen treatment is known to render the SU-8 surfaces hydrophilic for a few weeks, by creation of C=O and COO groups on SU-8 surface, and to increase surface roughness [15], [16]. After the Ti/Au deposition, the AZ5214 photoresist is lifted-off in acetone (Figure F-6 e). Despite the oxygen treatment the adhesion of the Ti/Au bilayer on SU-8 can be problematic, and the metal can be lifted-off along with the resist during this process step. Finally a 400 nm thick ZnO:Al is sputtered on the substrate (Figure F-6 f). In order to test the cells individually the front contact layers are etched. Metallization, ZnO deposition and microcell separation are carried out as described in Chapter IV.

In order to evaluate the impact of the different fabrication processes, we test the current-voltage characteristic of micro-blocks solar cells in the dark and under AM1.5 illumination.

1.2. Electrical characterization

IBE etched samples

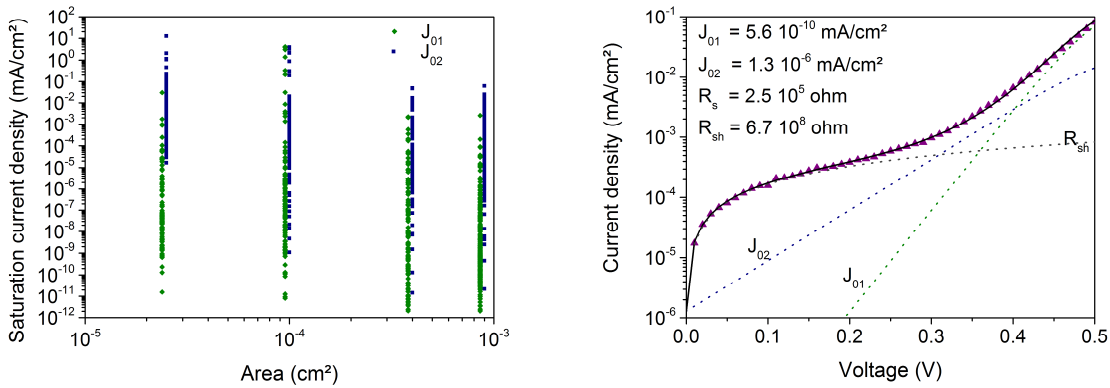


Figure F-7 : (left) Saturation current densities J_{01} and J_{02} (mA/cm²) as a function of cell area in a two-diodes model. The data are separated by an offset to enable better visualization. Sample is etched in IBE during 60 mn. (right) Current voltage characteristic of a IBE etched square microblock with 300 µm lateral dimension. The experimental data are displayed as purple dots, the fit as a black line. The different components of the fits are detailed in dotted lines.

The dark current-voltage characteristics are measured on the setup described in Chapter IV. The data are fitted in a two-diodes model (Figure F-7). However, there is a strong dispersion in the measurements, especially for the component of ideality 1, which fit is not accurate as most devices are dominated by the current of ideality 2. The data for saturation current densities are dispersed on more than six orders of magnitude. Some devices have rather good dark characteristics with small saturation currents (Figure F-7 right). Unfortunately there are too few good working device to draw solid conclusions.

In order to clean the edges of Cu(In,Ga)Se₂ that may have been modified by ion beam etching, we try different surface treatments. We cleaned the substrate in a acidic bromine solution that is known to etch Cu(In,Ga)Se₂ [12], [13], [17]. The acidic bromine solution is an aqueous solution with 0.75 mol/L of hydrogen bromide HBr, 0.35 mol/L of hydrochloric acid HCl, and 5.8 · 10⁻² mol/L of hydrogen peroxide H₂O₂. Br₂ forms in solution due to the reaction of HBr with H₂O₂, and is the oxidizing agent that etches the chalcopyrite. This solution is acidic and attacks ZnO and CdS layers. We thus need to have very short etch steps, which is sufficient, as we are intended to clean the extreme surface. We also implemented cyanide solution (KCN) etch that cleans the surface from elemental Se and eventual Cu_xSe binaries [13], [18]. However in spite of these different chemical treatments, the dark current-voltage characteristic of the sample stays alike and the dispersion does not diminish.

It is found that for samples with longer ion beam etching time, the devices are shunted, and stay so in spite of chemical treatments. We conclude that for these devices, Mo etched between the micro-block partially covers the blocks edge surface and thus create shunts. Etching time thus need to be limited, and it is preferable to leave a ultrathin layer of Cu(In,Ga)Se₂ between the blocks.

Samples with chemical etching

Then we test samples realized by chemical etching. No difference was found between samples etched in solution 1 or 2, thus we presented samples etched in solution 1 that have about 5µm under-etching. As both J_{01} and J_{02} signals can be detected, we analyze our device in the two-diode model (See Chapter II).

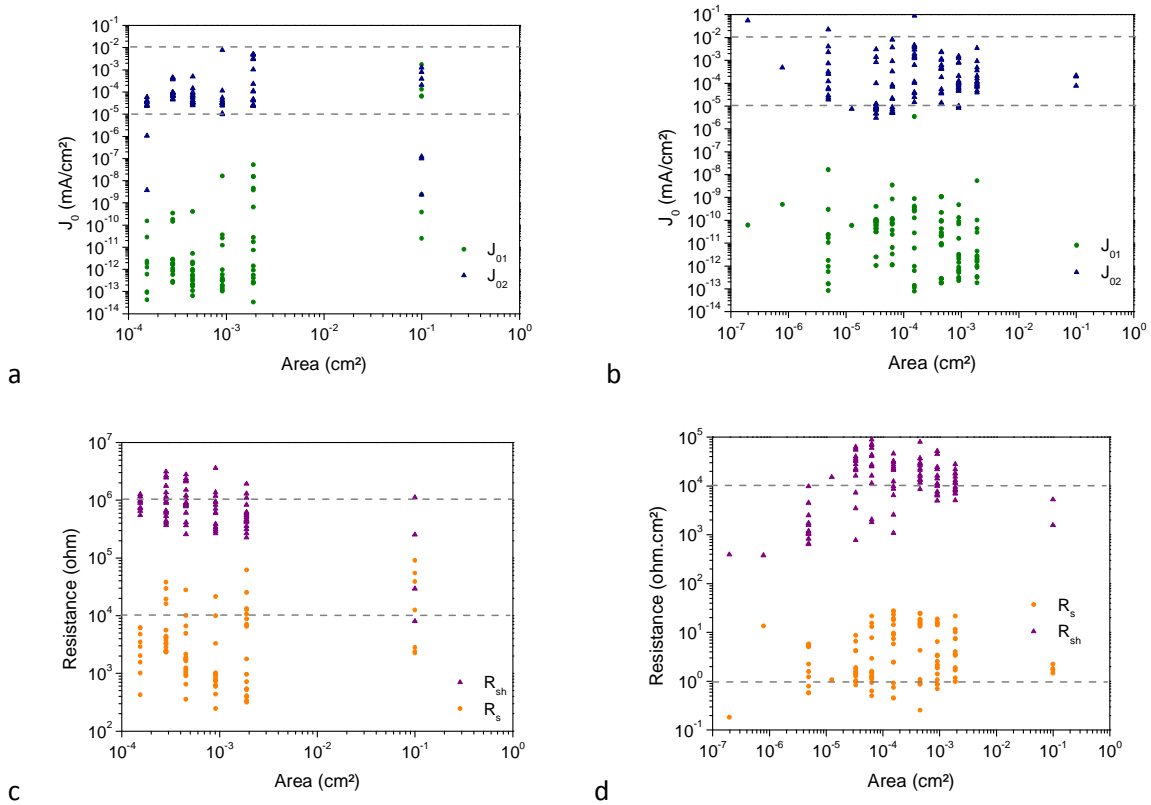


Figure F-8 : (above) Saturation currents J_{01} and J_{02} as a function of size for a micro-blocks sample patterned by chemical etching before (a) and after (b) contacting with procedure a→b→c. (below) Shunt and series resistance as a function of micro-blocks size before (c) and after (d) contacting with procedure a→b→c. Samples are etched in solution 1. Samples with shunt resistance smaller than 100 ohm.cm² are not displayed.

We can see that, as for microcells presented in the last chapters, the saturation current J_{02} of ideality 2 is predominant. It is comprised between 10^{-5} and 10^{-2} mA/cm². The saturation current J_{01} is comprised between 10^{-13} and 10^{-9} mA/cm² (Figure VII-4 a and b). One can see that the contacting process (Figure F-6 a→b→c) does not modify the dark saturation currents, but enables the measurement of devices that are too small to be directly contacted by a probe. Thus measurements after contacting concern a more important number of devices. If we look at the series resistances, we can see that it is roughly proportional to the cell surface, i.e. the value in ohm.cm² is roughly constant. The values of series resistance are higher compared to previous microcell devices (Figure VII-4 c and d). This is probably due to a bad contact between the probe tip and the ZnO at the micro-

block surface. After contacting, series resistance does not decrease significantly (Figure VII-4 d), as we are still doing our measurements with a probe on the ZnO surface. It is comprised between 1 and 10 ohm.cm^2 . The shunt resistance is roughly proportional to the cell surface. Thus the area around the micro-blocks, covered in SU-8, seems correctly isolated. We can see however that for small devices the shunt resistance is low, due to shunts between ZnO and Mo layer. Indeed the alignment between the micro-blocks and the lithographic step of Figure F-6 b is done with an uncertainty of 2 to 5 μm . Misalignment occurs and is more critical on small devices. Shunts between ZnO:Al and Mo are possible for the smallest devices.

We studied the effect of the surface ageing. We fabricated a sample and stored it for a week. Then it was measured in the dark. Afterwards the edge surfaces were cleaned by a short 5 s etch in solution 1, and the current-voltage characteristics were acquired shortly after. One can see on Figure F-9 that the differences between the two measurements are very limited. The saturation current J_{02} after surface cleaning tends to be slightly higher on average, but the dispersion of the data is smaller. The average saturation current density over the devices which size are comprised between $5 \cdot 10^{-5}$ and $1 \cdot 10^{-3} \text{ cm}^2$, after eliminating the 20% highest and 20% smallest values, is $8 \cdot 10^{-6} \text{ mA/cm}^2$ for the sample before cleaning and $16 \cdot 10^{-6} \text{ mA/cm}^2$ after cleaning.

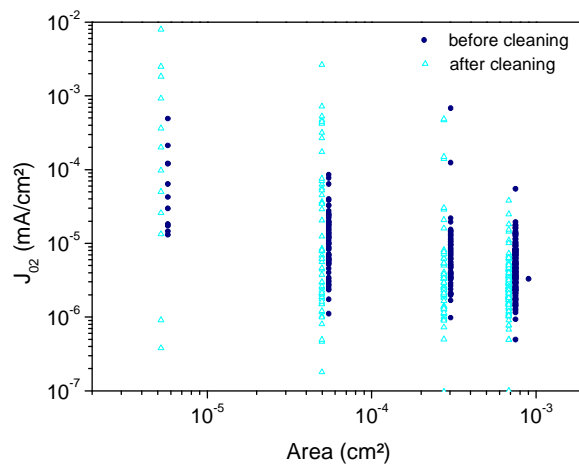


Figure F-9 : Saturation current J_{02} as a function of size for a micro-blocks sample patterned by chemical etching after 1 week of storage without cleaning, and after cleaning by a short etch in KBr/Br_2 solution. The data points after cleaning are translated by a negative x-offset to enable good visualization.

Current voltage characterization of contacted microcells under AM1.5 illumination

For the sample we contacted with procedure $a \rightarrow b \rightarrow c$, we can measure AM1.5 current-voltage characteristic as the probe, positioned outside the micro-blocks, does not provoke shading. The

average short circuit current density J_{SC} for cell bigger than $1 \cdot 10^{-5} \text{ cm}^2$ is $27.7 \pm 0.3 \text{ mA/cm}^2$ and V_{OC} is $620 \pm 11 \text{ mV}$.

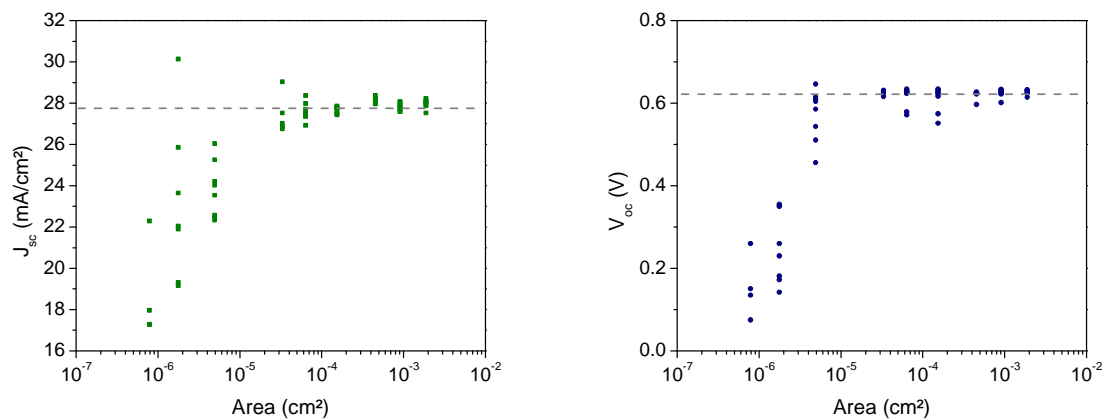


Figure F-10 : (left) Short circuit current density as a function of cell size for micro-blocks solar cell under AM1.5. (right) Open-circuit voltage as a function of micro-blocks solar cell size. In both graphs, the micro-block size accounts for a $5 \mu\text{m}$ under-etch. The lines are guides for the eye to situate the average over the devices bigger than 10^{-5} cm^2

The short-circuit current and open-circuit voltage are stable for devices bigger than 10^{-5} cm^2 . For devices smaller, J_{SC} and V_{OC} drop. The decrease of V_{OC} comes partly from increased shunts for smaller devices. The decrease in J_{SC} may be due to different sources. In our analysis, we consider that the devices have on average $5 \mu\text{m}$ under-etch as observed by optical microscopy. However the under-etch is found slightly higher for smaller devices as the etch is not perfectly homogeneous, which results in an underestimation of the J_{SC} of the smallest micro-blocks.

2. A bottom-up process: electrodeposition

Fabrication of electrodeposited CuInSe_2 microcells

Principle

The fabrication of electrodeposited microcells consists in different steps. First a molybdenum layer is sputtered on a soda-lime glass substrate (Figure VII-8 a). The molybdenum is $0.7 \mu\text{m}$ thick, and was optimized for electrodeposition [19]. For the substrate structuring, a Al_2O_3 layer is deposited by atomic layer deposition (ALD) (Figure VII-8 b). The optimization of deposition temperature is described in paragraph 0. A photolithography with AZ5214® is carried out to protect the Al_2O_3 layer from chemical etch (Figure VII-8 c). Then Al_2O_3 is etched in an orthophosphoric acidic solution (Figure VII-8 d). On those structured substrates co-electrodeposition of CuInSe_2 is carried out (Figure VII-8 e).

Annealing is done on this precursor layer. Then a cyanide etch is performed to removed possible binaries. The cells are completed by deposition of CdS layer by chemical bath deposition (Figure VII-8 f), of intrinsic ZnO (Figure VII-8 g) and of ZnO:Al (Figure VII-8 h) by radio-frequency sputtering. To isolate the cells from each other, lithography and subsequent HCl etching can be done as described in Chapter IV.

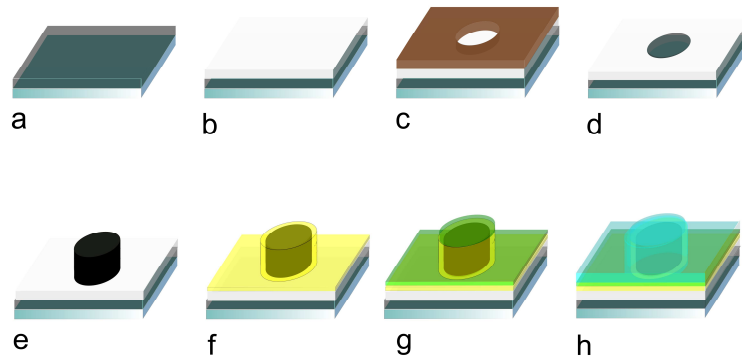


Figure F-11 : Micro-block solar cell electrodeposition process.

Substrate structuration

One of the most important steps in the realization of electrodeposited microcells is the fabrication of an adapted structured substrate. We chose Al_2O_3 as the insulating layer due to its high thermal and chemical stability. Several points have to be optimized: thermal stability of the glass/Mo/ Al_2O_3 stack during annealing, the etching process for Al_2O_3 and the design of a pattern that is convenient for electrodeposition. These points are tackled hereafter.

Atomic layer deposition of Al_2O_3

Al_2O_3 is deposited at IRDEP by atomic layer deposition (ALD). Al_2O_3 is a material commonly deposited by ALD [20]. The reactive gases are trimethylaluminum $\text{Al}(\text{CH}_3)_3$ and water. The deposition is done at a given chamber temperature, usually comprised between 150°C and 300°C . Atomic layer deposition consists in the sequential injection of reactive gazes in a chamber. During a cycle a first gas is introduced and molecules adsorb on the substrate's surface. The chamber is then emptied before the introduction of the second gas. Finally the chamber is pumped once again. Thus when the second gas is introduced, the other reactive is only present as adsorbed molecules on the substrate. Chemical reaction occurs on the substrate's surface and the growth progresses atomic layer by atomic layer. Due to this atomic layer growth, control of the layer thickness is accurate, but deposition time can be important.

Thermal stability

Due to the difference in coefficient of thermal expansion of Mo ($5 \cdot 10^{-6} \text{ K}^{-1}$) [21] and Al_2O_3 ($8 \cdot 10^{-6} \text{ K}^{-1}$), optimization is needed to avoid peel off of the Al_2O_3 layer after annealing. We synthesize two Al_2O_3 layers one at 200°C (430 nm) and one at 300°C (200 nm). The layer synthesized at 200°C does not withstand annealing steps at 400°C or higher, needed for the electrodeposition process. Delamination occurs. For the layer synthesized at 300°C , peel off occurs for temperatures of 650°C or higher. Thus we conclude that the synthesis of Al_2O_3 at high temperature is favorable. Indeed due to the high temperature growth, the Al_2O_3 layer is under tensile strain at ambient temperature. Strain diminishes upon annealing. It should be noted that the layer grown at 300°C is thinner, which makes it also more resistant to peel off. Indeed according to the Stoney equation [22], the strain in a layer subjected to a fixed external force is inversely proportional to its thickness.

Table F-2 : Annealing stability of glass/Mo/ Al_2O_3 stack.

Maximum temperature during annealing ($^\circ\text{C}$)	Al_2O_3 - 200°C 430 μm	Al_2O_3 - 300°C 200 μm
400	delamination	adherence
450	delamination	adherence
500	delamination	adherence
550	delamination	adherence
600	/	adherence
650	/	delamination
700	/	delamination

Etching procedure

Once the Al_2O_3 is deposited, we need to structure it. We proceed to a lithography to protect parts of the substrate (Figure VII-8 c). The etch of Al_2O_3 is done with orthophosphoric acid. This acid is a known etchant of alumina [23] that does not attack Mo. This selectivity makes this acid suitable for our process, contrary to ammonia and hydrogen peroxide solution for example, that etches Al_2O_3 but has a higher etching rate on Mo, which makes etching control difficult.

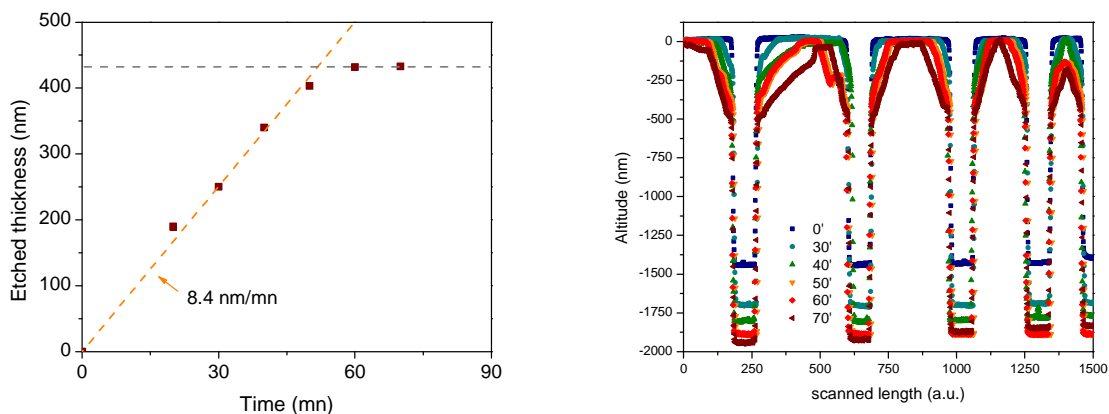


Figure F-12 : (right) Al_2O_3 etched thickness vs. time for a orthophosphoric solution of 7.4 mol.L^{-1} at 50°C . (left) Profile of tests samples at different etching time measured by profilometer.

The orthophosphoric H_3PO_4 solution is an aqueous solution of 7.4 mol.L^{-1} . The etch is done at 50°C to improve the kinetics. In these conditions the etch rate is 8.4 nm/mn . Thus it takes nearly 50 mn to etch 430 nm of Al_2O_3 (Figure F-12 right). We can verify that molybdenum is not attacked by H_3PO_4 , as a plateau is seen in the etched thickness for etching times over 60 mn. However, when etching times are superior to 60 mn, the under-etching of the Al_2O_3 structure continues (Figure F-12 left) and the patterns are deteriorated. The etch is not perfectly homogeneous and stirring of the etching solution may be necessary in the future.

Electrodeposition processes

The bath is an aqueous solution containing 0.1 mol.L^{-1} of $\text{Na}_2(\text{SO}_4)$ as supporting electrolyte, $10^{-3} \text{ mol.L}^{-1}$ of $\text{Cu}(\text{SO}_4)$, $3 \cdot 10^{-3} \text{ mol.L}^{-1}$ of $\text{In}_2(\text{SO}_4)_3$ and $1.7 \cdot 10^{-3} \text{ mol.L}^{-1}$ of SeO_2 . The pH is fixed at 2.2 by addition of hydrochloric acid. The substrates are cleaned during 10' in ammonia before deposition.

The electrodeposition is done with an applied potential at the working electrode of -0.9V (or -1V) with respect to mercury/mercurous sulfate reference electrode (potentiostatic control). Agitation is provided by a magnetic stirring bar rotating between 300 and 500 rpm. The duration of electrodeposition is fixed by the charge exchanged, in order to attain a precursor layer thickness between 1 and $3 \mu\text{m}$.

Annealing

As-deposited films are microcrystalline. The deposits are referred to as precursor layers. In order to have polycrystalline films, an annealing step is mandatory. Annealing is done either by rapid thermal annealing in a flash system, or longer processes in a tubular heater. Different maximum

MICROCELLS WITH LOCALIZED ABSORBERS

temperatures were tested, as well as annealing time. Annealings are done in a selenium overpressure atmosphere.

APPENDIX G. ADAPTATION OF THE MICROCELL FABRICATION PROCESS TO FINISHED CELLS

The microcell process can be adapted in order to fabricate microcell on a complete glass / Mo / Cu(In,Ga)Se₂ / CdS / ZnO / ZnO:Al solar cell. The window layer can be etched by IBE or chemically in a HCl aqueous solution. We present briefly hereafter the performance of such microcells.

1. Performance of microcells fabricated on complete stacks

1.1. Current-voltage characteristics

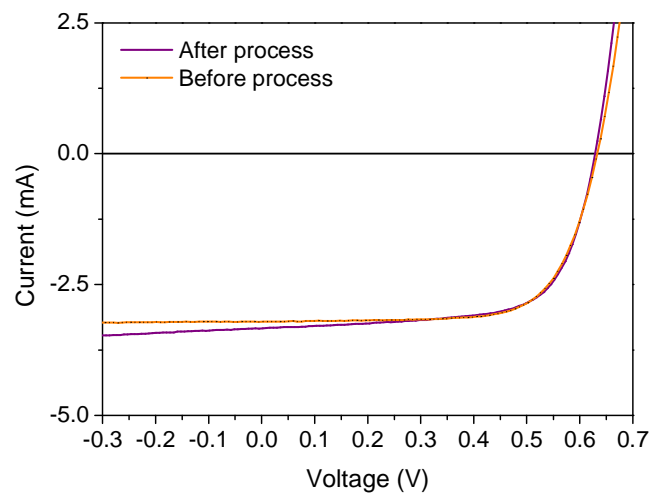


Figure G-1: AM1.5 current voltage characteristic of 0.1 cm² solar cells. Before the process a 0.1 cm² solar cell is mechanically scribed on a finished Cu(In,Ga)Se₂ stack. After the process, a microcell of 0.1 cm² on the same stack is tested (that was fabricated by IBE etching of the window layer).

It is interesting to note that the microcell process does not decrease the efficiency of 0.1 cm² solar cells. Indeed we performed AM1.5 current-voltage measurements before the process, on a cell mechanically scribed on the complete stack, and compared the result with a 0.1 cm² cell created on the same stack by the microcell process. It should be noted however that the microcell tested here after the process present a slightly higher shunt conductance.

1.2. Laser tests

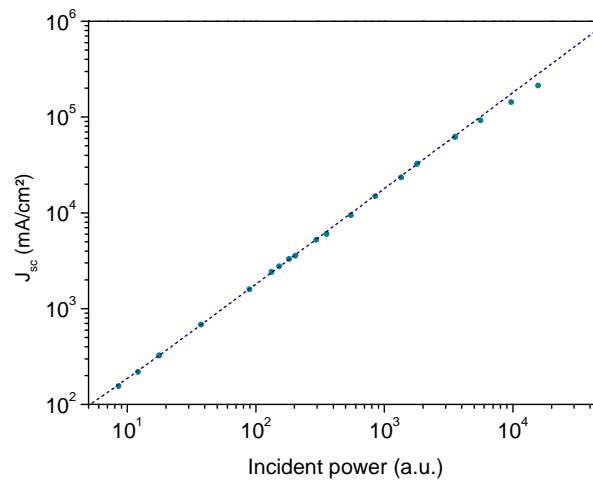


Figure G-2: Short-circuit current density as a function of incident power (measured in situ by a powermeter from the signal deviates by the beam splitter). Test under 532 nm laser.

The linearity of the short-circuit current density is observed up to high concentration ratios (Figure G-2), as on standard microcells. The smallest microcells generally present a decrease in efficiency at low concentration ratios due to high shunt conductance. However bigger microcells (75 μm) have efficiency at one sun that are similar to the macro 0.1 cm^2 solar cells. An increase in efficiency is observed in the sample under concentration. The efficiency saturates around $\times 100$ (Figure G-3).

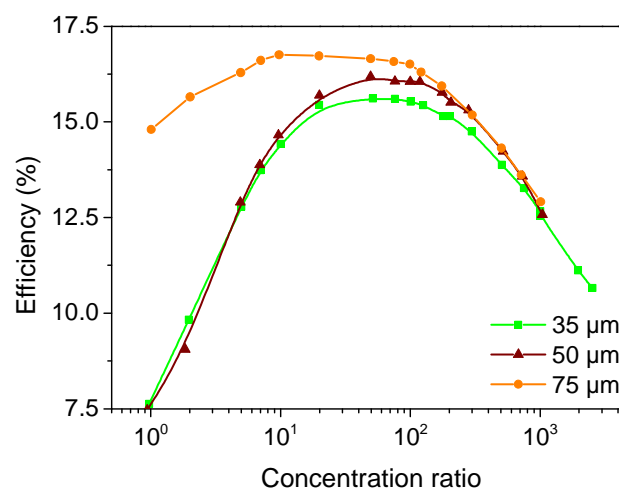


Figure G-3: Efficiency as a function of concentration of microcells of different diameters (indicated in the legend).

This process has not been studied extensively. It appears however that microcells fabricated on finished $\text{Cu}(\text{In,Ga})\text{Se}_2$ stack have good properties. Thus we can expect to use them as feedback tools, on the quality of the process.

APPENDICES BIBLIOGRAPHY

- [1] J. V. Beck, K. D. Cole, A. Haji-Sheikh, and B. Litkouhi, "Other geometries in cylindrical coordinates," in *Heat conduction using green's functions*, Hemisphere publishing corporation, 1992.
- [2] P. Thomas, "Some conduction problems in the heating of small areas on large solids," *The Quarterly Journal of Mechanics and Applied Mathematics*, vol. 10, no. 4, p. 482, 1957.
- [3] Necati Ozisik M., "Heat conduction in the cylindrical coordinate system," in *Boundary Value Problem of Heat Conduction*, Mineola, NY, USA: Dover Publications, 1989.
- [4] H. Kim, E. Brueckner, J. Song, Y. Li, S. Kim, C. Lu, J. Sulkin, K. Choquette, Y. Huang, R. G. Nuzzo, and others, "Unusual strategies for using indium gallium nitride grown on silicon (111) for solid-state lighting," *Proceedings of the National Academy of Sciences*, vol. 108, no. 25, p. 10072, 2011.
- [5] H. H. Berger, "Models for contacts to planar devices," *Solid-State Electronics*, vol. 15, no. 2, pp. 145–158, Février 1972.
- [6] C. Koechlin, S. Maine, R. Haidar, B. Trétout, A. Loiseau, and J.-L. Pelouard, "Electrical characterization of devices based on carbon nanotube films," *Applied Physics Letters*, vol. 96, no. 10, p. 103501, 2010.
- [7] "Lithography - Theory and applications of photoresists, developers, solvents and etchants." MicroChemicals GmbH, 2009-2008.
- [8] W. Shockley and H. J. Queisser, "Detailed Balance Limit of Efficiency of p-n Junction Solar Cells," *Journal of Applied Physics*, vol. 32, no. 3, p. 510, 1961.
- [9] T. Kirchartz, *Generalized Detailed Balance Theory of Solar Cells*. Forschungszentrum Jülich, 2009.
- [10] W. K. Metzger, I. L. Repins, and M. A. Contreras, "Long lifetimes in high-efficiency Cu(In,Ga)Se₂ solar cells," *Applied Physics Letters*, vol. 93, no. 2, p. 022110, 2008.
- [11] A. Rockett, "Surface analysis of chalcopyrite materials for photovoltaics," *Progress in Photovoltaics: Research and Applications*, p. n/a–n/a, 2012.
- [12] M. Bouttemy, P. Tran-Van, I. Gerard, T. Hildebrandt, A. Causier, J. L. Pelouard, G. Dagher, Z. Jehl, N. Naghavi, G. Voorwinden, B. Dimmler, M. Powalla, J. F. Guillemoles, D. Lincot, and A. Etcheberry, "Thinning of Cu (In, Ga) S₂ solar cells: Part I: Chemical processing in acidic bromine solutions," *Thin Solid Films*, vol. 519, no. 21, pp. 7207 – 7211, 2011.
- [13] B. Canava, J. F. Guillemoles, J. Vigneron, D. Lincot, and A. Etcheberry, "Chemical elaboration of well defined Cu(In,Ga)Se₂ surfaces after aqueous oxidation etching," *Journal of Physics and Chemistry of Solids*, vol. 64, no. 9, pp. 1791–1796, 2003.
- [14] MicroChem, "SU-8 Permanent Photoresists, Technical documentation." .

- [15] F. Walther, P. Davydovskaya, S. Zürcher, M. Kaiser, H. Herberg, A. M. Gigler, and R. W. Stark, "Stability of the hydrophilic behavior of oxygen plasma activated SU-8," vol. 17, no. 3, pp. 524–531, 2007.
- [16] F. Walther, T. Drobek, A. M. Gigler, M. Hennemeyer, M. Kaiser, H. Herberg, T. Shimitsu, G. E. Morfill, and R. W. Stark, "Surface hydrophilization of SU-8 by plasma and wet chemical processes," *Surf. Interface Anal.*, vol. 42, no. 12–13, pp. 1735–1744, 2010.
- [17] R. W. Birkmire and B. E. McCandless, "Specular CuInSe₂ films for solar cells," *Applied Physics Letters*, vol. 53, no. 2, p. 140, 1988.
- [18] C. Guillen and J. Herrero, "Effects of Thermal and Chemical Treatments on the Composition and Structure of Electrodeposited CuInSe₂ Thin Films," *J. Electrochem. Soc.*, vol. 141, no. 1, pp. 225–230, 1994.
- [19] M. Jubault, L. Ribeaucourt, E. Chassaing, G. Renou, D. Lincot, and F. Donsanti, "Optimization of molybdenum thin films for electrodeposited CIGS solar cells," *Solar Energy Materials and Solar Cells*, vol. 95, Supplement 1, no. 0, pp. S26–S31, 2011.
- [20] A. Rahtu, T. Alaranta, and M. Ritala, "In Situ Quartz Crystal Microbalance and Quadrupole Mass Spectrometry Studies of Atomic Layer Deposition of Aluminum Oxide from Trimethylaluminum and Water," *Langmuir*, vol. 17, no. 21, pp. 6506–6509, 2001.
- [21] F. C. Nix and D. MacNair, "The Thermal Expansion of Pure Metals. II: Molybdenum, Palladium, Silver, Tantalum, Tungsten, Platinum, and Lead," *Physical Review*, vol. 61, pp. 74–79, 1942.
- [22] G. G. Stoney, "The tension of metallic films deposited by electrolysis," *Proceedings of the Royal Society of London. Series A, Containing Papers of a Mathematical and Physical Character*, vol. 82, no. 553, pp. 172–175, 1909.
- [23] B. Zhou and W. F. Ramirez, "Kinetics and Modeling of Wet Etching of Aluminum Oxide by Warm Phosphoric Acid," *Journal of The Electrochemical Society*, vol. 143, no. 2, pp. 619–623, 1996.

Résumé

Dans cette thèse nous évaluons le potentiel de cellules solaires micrométriques pour une utilisation sous flux concentré. Le but de l'étude est de mettre au point une technologie photovoltaïque à haut rendement, basée sur des technologies de grandes surfaces pour obtenir de fortes productivités, qui soit en même temps économe en matières premières pour respecter les contraintes imposées par un développement du photovoltaïque à l'échelle du terawatt. La miniaturisation des cellules solaires permet d'obtenir une architecture peu résistive, qui évacue efficacement la chaleur. Les microcellules sont donc adaptées à la concentration lumineuse. Des prototypes sont fabriqués, grâce à des techniques de photolithographie. Leur test permet d'évaluer leur rendement. Un gain absolu de 5% de rendement a été mesuré; un rendement maximum de 21.3% sur une cellule de 50 μm de diamètre à une concentration de $\times 475$ est atteint. Les caractéristiques du régime de forte illumination sont étudiées pour la première fois sur Cu(In,Ga)Se_2 . La photoconductivité de cet absorbeur est examinée. L'écrantage du champ électrique de l'hétérojonction Cu(In,Ga)Se_2 sous fort flux est simulé numériquement et semble expliquer l'influence de l'intensité lumineuse sur la collecte des porteurs, mise en évidence expérimentalement. La possibilité d'une application industrielle est envisagée grâce à la fabrication de microcellules à absorbeur localisé, qui a permis de déterminer une faible vitesse de recombinaison sur les surfaces latérales des cellules ($< 4 \cdot 10^3 \text{ cm/s}$). Une technique de dépôt sélective, l'électrodépôt, a permis la synthèse de CuInSe_2 sur des microélectrodes.

Mots-clés : photovoltaïque, micro- cellules solaires, concentration, forte injection, Cu(In,Ga)Se_2

Abstract

In this thesis we explored the potential of thin film microscale concentrator solar cells. The aim of the study is to develop a highly efficient photovoltaic technology, based on large-area processes for high throughput, and which is raw-material thrifty to meet the constraints of terawatt development. The miniaturization of thin film solar cells leads to a low resistive architecture, with easy thermal management, which is therefore adapted to the concentrating regime. The scale effects are studied from an analytical and numerical point of view. Prototype Cu(In,Ga)Se_2 solar cells are fabricated with help of photolithography techniques and tested to evaluate the performance of the microcells. A 5% absolute efficiency increase was measured, which led to a 21.3% efficiency of a 50 μm diameter microcell at a concentration of $\times 475$. The influence of the incident spectra is highlighted. The specific features of the high illumination regime are studied for the first time on Cu(In,Ga)Se_2 . The photoconductive behavior of Cu(In,Ga)Se_2 is analyzed. The screening of the electric field in the Cu(In,Ga)Se_2 heterojunction under high light fluxes is evidenced by simulation and may explain the influence of the illumination level on the collection efficiency observed experimentally. The possibility of an industrial application is tackled via the fabrication of mesa delineated microcells, which proves that the edge surface of the microcells have a low recombination velocity ($< 4 \cdot 10^3 \text{ cm/s}$). A bottom-up approach is studied via electrodeposition. This selective deposition technique enables the synthesis of CuInSe_2 on microelectrodes.

Keywords : photovoltaics, microscale solar cell, concentration, high injection, Cu(In,Ga)Se_2